**Title**
Internal Wave Generation by Convection



**Author**
Lecoanet, Daniel

**Publication Date**
2016

Peer reviewed|Thesis/dissertation

# Internal Wave Generation by Convection

By

Daniel Michael Lecoanet

A dissertation submitted in partial satisfaction of the

requirements for the degree of

Doctor of Philosophy

in

Physics

in the

Graduate Division

of the

University of California, Berkeley

Committee in charge:

Professor Eliot Quataert, Chair
Professor Edgar Knobloch
Professor Philip Marcus

Spring 2016

Internal Wave Generation by Convection

Abstract

Internal Wave Generation by Convection

by

Daniel Michael Lecoanet

Doctor of Philosophy in Physics

University of California, Berkeley

Professor Eliot Quataert, Chair

In nature, it is not unusual to find stably stratified fluid adjacent to convectively unstable fluid. This can occur in the Earth's atmosphere, where the troposphere is convective and the stratosphere is stably stratified; in lakes, where surface solar heating can drive convection above stably stratified fresh water; in the oceans, where geothermal heating can drive convection near the ocean floor, but the water above is stably stratified due to salinity gradients; possible in the Earth's liquid core, where gradients in thermal conductivity and composition diffusivities maybe lead to different layers of stable or unstable liquid metal; and, in stars, as most stars contain at least one convective and at least one radiative (stably stratified) zone. Internal waves propagate in stably stratified fluids. The characterization of the internal waves generated by convection is an open problem in geophysical and astrophysical fluid dynamics.

Internal waves can play a dynamically important role via nonlocal transport. Momentum transport by convectively excited internal waves is thought to generate the quasi-biennial oscillation of zonal wind in the equatorial stratosphere, an important physical phenomenon used to calibrate global climate models. Angular momentum transport by convectively excited internal waves may play a crucial role in setting the initial rotation rates of neutron stars. In the last year of life of a massive star, convectively excited internal waves may transport even energy to the surface layers to unbind them, launching a wind. In each of these cases, internal waves are able to transport some quantity—momentum, angular momentum, energy—across large, stable buoyancy gradients. Thus, internal waves represent an important, if unusual, transport mechanism.

This thesis advances our understanding of internal wave generation by convection. Chapter 2 provides an underlying theoretical framework to study this problem. It describes a detailed calculation of the internal gravity wave spectrum, using the Lighthill theory of wave excitation by turbulence. We use a Green's function approach, in which we convolve a convective source term with the Green's function of different internal gravity waves. The remainder of the thesis is a circuitous attempt to verify these analytical predictions.

I test the predictions of Chapter 2 via numerical simulation. The first step is to identify a code suitable for this study. I helped develop the Dedalus code framework to study internal wave gen-

eration by convection. Dedalus can solve many different partial differential equations using the pseudo-spectral numerical method. In Chapter 3, I demonstrate Dedalus' ability to solve different equations used to model convection in astrophysics. I consider both the propagation and damping of internal waves, and the properties of low Rayleigh number convective steady states, in six different equation sets used in the astrophysics literature. This shows that Dedalus can be used to solve the equations of interest.

Next, in Chapter 4, I verify the high accuracy of Dedalus by comparing it to the popular astrophysics code Athena in a standard Kelvin–Helmholtz instability test problem. Dedalus performs admirably in comparison to Athena, and provides a high standard for other codes solving the fully compressible Navier–Stokes equations. Chapter 5 demonstrates that Dedalus can simulate convective adjacent to a stably stratified region, by studying convective mixing near carbon flames. The convective overshoot and mixing is well-resolved, and is able to generate internal waves.

Confident in Dedalus' ability to study the problem at hand, Chapter 6 describes simulations inspired by water experiments of internal wave generation by convection. The experiments exploit water's unusual property that its density maximum is at 4°C, rather than at 0°C. We use a similar equation of state in Dedalus, and study internal gravity waves generation by convection in a water-like fluid. We test two models of wave generation: bulk excitation (equivalent to the Lighthill theory described in Chapter 2), and surface excitation. We find the bulk excitation model accurately reproduces the waves generated in the simulations, validating the calculations of Chapter 2.

I dedicate this dissertation to Jia.

# Contents

**List of Figures** v

**List of Tables** vii

**Acknowledgments** viii

**1 Introduction** 1
- 1.1 The Importance of "Sub-Grid Scale" Dynamics . . . 1
- 1.2 Outline . . . 2

**2 Internal Gravity Wave Excitation by Turbulent Convection** 6
- 2.1 Introduction . . . 6
- 2.2 Background State and Perturbation Equations . . . 7
- 2.3 Wave Generation by Turbulent Convection . . . 10
  - 2.3.1 Green's Function for Discontinuous $N^2$ . . . 10
  - 2.3.2 Green's Function for Smooth $N^2$ . . . 11
  - 2.3.3 Amplitude Equation . . . 13
  - 2.3.4 Model of Turbulent Convection . . . 14
  - 2.3.5 Energy Generation Rates and IGW Fluxes . . . 15
  - 2.3.6 Wave Excitation Within the Overshoot Region . . . 18
- 2.4 Pressure Perturbation Balance . . . 21
- 2.5 Comparison with Previous Work . . . 22
- 2.6 Discussion & Conclusions . . . 24
- 2.A tanh Profile Eigenfunctions . . . 26
  - 2.A.1 Numerical Verification . . . 30
- 2.B Piecewise Linear $N^2$ . . . 30
- 2.C Mode Projection Formalism (GK90) . . . 34

**3 Conduction in Low Mach Number Flows: Linear & Weakly Nonlinear Regimes** 37
- 3.1 Introduction . . . 37
- 3.2 Preliminaries . . . 39
  - 3.2.1 Motivation . . . 39
  - 3.2.2 Model Equations . . . 40

3.3 Linear Wave Modes: Numerics . . . 43
3.4 Linear Wave Modes: Analytics . . . 46
3.4.1 Large Wavenumber Limit . . . 46
3.4.2 Damping Rates & the Weak Dissipation Limit . . . 47
3.4.3 FC & PI equations . . . 49
3.5 Steady Nonlinear Convective Solutions . . . 49
3.6 Conclusion . . . 56
3.A Eigenvalue Equations and Damping Rates for Fully Compressible Equations . . . 58
3.B Eigenvalue Equations and Damping Rates for PI Equations . . . 60
3.C Thermal Conduction and Sound Waves . . . 60
3.D Equation Implementation in Dedalus . . . 62
3.D.1 Fully Compressible Equations . . . 63
3.D.2 Pseudo-Incompressible Equations . . . 64
3.D.3 Anelastic Equations . . . 66

**4 A Validated Nonlinear Kelvin-Helmholtz Benchmark for Numerical Hydrodynamics 67**
4.1 Introduction . . . 67
4.2 Methods . . . 69
4.2.1 Equations and Initial Conditions . . . 69
4.2.2 Numerical Methods . . . 71
4.3 Results . . . 72
4.3.1 Unstratified simulations ($\Delta\rho/\rho_0 = 0$) . . . 72
4.3.2 Simulations with a density jump ($\Delta\rho/\rho_0 = 1$) . . . 79
4.4 Conclusion . . . 89
4.A Interpolation to a Common Grid . . . 94
4.B Convergence to a "True" Solution . . . 94
4.C Lyapunov exponent calculation . . . 97

**5 Turbulent Chemical Diffusion in Convectively Bounded Carbon Flames 99**
5.1 Introduction . . . 99
5.2 Carbon Flame Properties . . . 100
5.3 Problem Setup . . . 102
5.3.1 Equations & Numerics . . . 102
5.3.2 Passive Tracer Field . . . 104
5.4 Results . . . 104
5.4.1 Self-Similar Solution . . . 104
5.4.2 Effective Diffusivity Model . . . 107
5.4.3 Diffusion Profiles . . . 108
5.4.4 Flame Disruption in MESA . . . 109
5.5 Conclusions . . . 109

**6 Numerical Simulations of Internal Wave Generation by Convection in Water 111**
6.1 Introduction . . . . . 111
6.2 Full simulation . . . . . 112
6.2.1 Numerical implementation . . . . . 112
6.2.2 Characteristics of convectively generated waves . . . . . 114
6.3 Linear damping rates . . . . . 118
6.4 Bulk excitation: Reynolds stress forcing . . . . . 121
6.5 Interface forcing: Mechanical oscillator effect . . . . . 124
6.6 Conclusions . . . . . 125

**Bibliography 128**

# List of Figures

2.1 Schematic of problem setup . . . 8
2.2 Representation eigenfunction and buoyancy frequency squared near the radiative-convective transition . . . 19
2.3 Normalized eigenfunction at the radiative-convective interface . . . 31

3.1 Damping rates and oscillation frequencies of gravity wave modes . . . 44
3.2 Error in oscillation frequencies and damping rates between different equations and conduction models . . . 45
3.3 Steady convective states for FC equations . . . 53
3.4 Steady convective states for different equations and conduction models . . . 54
3.5 Root-mean-square Reynolds number of convective steady states . . . 55
3.6 Damping rates and oscillation frequencies of sound wave modes . . . 61

4.1 Snapshots of dye concentration field in simulations with $\Delta\rho/\rho_0 = 0$ . . . 73
4.2 Norm of errors for $\Delta\rho/\rho_0 = 0$ and $\mathrm{Re} = 10^5$ . . . 74
4.3 Dye entropy for simulations with $\mathrm{Re} = 10^5$ . . . 75
4.4 Norm of errors for $\Delta\rho/\rho_0 = 0$ and $\mathrm{Re} = 10^6$ . . . 76
4.5 Dye entropy for simulations with $\mathrm{Re} = 10^6$ . . . 76
4.6 Dye entropy for resolved simulations with $\Delta\rho/\rho_0 = 0$ . . . 77
4.7 Zoom-in of dye concentration field for $\Delta\rho/\rho_0 = 0$ . . . 78
4.8 Snapshots of dye concentration field in simulations with $\Delta\rho/\rho_0 = 1$ . . . 80
4.9 Norm of errors for $\Delta\rho/\rho_0 = 1$ . . . 81
4.10 Schematic phase-space diagram for Kelvin–Helmholtz instability simulations . . . 82
4.11 Dye entropy for simulations with $\Delta\rho/\rho_0 = 1$ . . . 83
4.12 Assorted quantities in D4096 with $\Delta\rho/\rho_0 = 1$ . . . 85
4.13 Snapshots of dye concentration field in a Dedalus simulation restarted with an Athena simulation . . . 86
4.14 Snapshots of dye concentration field using different initial conditions . . . 88
4.15 Snapshots of dye concentration field in simulations without explicit diffusion . . . 90
4.16 Dye entropy for simulations without explicit diffusion . . . 91
4.17 Differences between different solutions for $\mathrm{Re} = 10^6$ and $\Delta\rho/\rho_0 = 0$ . . . 96

5.1 Buoyancy frequency squared near a carbon flame . . . 101

5.2 Vertical slices of temperature and passive scalar fields . . . . . 105
5.3 Horizontal average of the passive scalar field . . . . . 106
5.4 Horizontal average of reinitialized passive tracer field . . . . . 107
5.5 Effective diffusivity as a function of height . . . . . 108

6.1 Snapshots of water experiment simulations . . . . . 115
6.2 Spectrogram of the kinetic energy density . . . . . 117
6.3 Wave flux spectrum . . . . . 118
6.4 Spectrograms of kinetic energy testing different damping formulas . . . . . 120
6.5 Snapshots of vertical velocity in the full simulation and two simplified simulations . . 122
6.6 Spectrograms of vertical velocity squared in the full simulation and two simplified simulations . . . . . 123

# List of Tables

4.1 List of Kelvin–Helmholtz simulations with $\Delta\rho/\rho_0 = 0$ . . . . . 73
4.2 List of Kelvin–Helmholtz simulations with $\Delta\rho/\rho_0 = 1$ . . . . . 79

5.1 List of carbon flame simulations . . . . . 103

6.1 Parameter values used in the water simulations . . . . . 113
6.2 Dimensionless numbers characterizing the convection . . . . . 114

# Acknowledgments

This work was supported by the Hertz Foundation, a National Science Foundation Graduate Research Fellowship under Grant No. DGE 1106400, a Kavli Institute for Theoretical Physics Graduate Student Fellowship, a Woods Hole Oceanographic Institute Geophysical Fluid Dynamics Summer Fellowship, and the Labex program MEC (ANR-11-LABX-0092).

Many computers were harmed in the making of this thesis, including computers at: the Texas Advanced Computing Center (TACC) at The University of Texas at Austin; the Extreme Science and Engineering Discovery Environment (XSEDE allocations TG-AST140039, TG- AST140047, and TG-AST140083), which is supported by National Science Foundation grant number ACI-1053575; and, the NASA High-End Computing (HEC) Program through the NASA Advanced Supercomputing (NAS) Division at Ames Research Center and the NASA Center for Climate Simulation (NCCS) at Goddard Space Flight Center.

Part of this work was completed at the Kavli Institute of Theoretical Physics programs on Wave-Mean Flow Interaction, and Star Formation (Grant No. NSF PHY11-25915).

It takes a village to raise a graduate student. The papers comprising this thesis share thirteen co-authors, with each paper having a different second author. I am grateful to all of my collaborators for making graduate school more interesting. I am particularly grateful to the other members of the Dedalus team: Ben Brown, Keaton Burns, Jeff Oishi, & Geoff Vasil. Dedalus became a core focus and tool of my thesis work, and I have enjoyed our collaboration. Finally, I am very grateful to Eliot Quataert for all his support during my PhD.

This dissertation was typeset using the ucastrothesis LaTeX template.

# Chapter 1

# Introduction

## 1.1 The Importance of "Sub-Grid Scale" Dynamics

An important characteristic of fluid dynamics is that features on small length scales can influence features on large length scales. For example, in two dimensional flows, small vortices merge to form large vortices, concentrating energy on large scales (e.g., Pedlosky 1992). Small-scale turbulent fluctuations can generate large-scale magnetic fields via the $\alpha$-effect (Moffatt 1978). The release of magnetic energy in small magnetic reconnection regions is thought to drive coronal mass ejections (e.g., van Driel-Gesztelyi et al. 2014). A significant portion of the ocean's tidal dissipation is due to rough topography of the ocean floor (Egbert & Ray 2000). The convective heat flux in the Earth's core may be limited by Ekman boundary layers (Julien et al. 2016). Stellar outflows and explosions play a crucial role in galactic gas dynamics (Hopkins et al. 2014).

One is often most interested in the large scale features of a system. The influence of small scale phenomena means the large scales cannot be studied in isolation. It is infeasible to capture the full range of scales in astrophysical and geophysical systems using either experiments or numerical simulations. For this reason, small-scale effects are always described using a model. In numerical simulations, these are known as "sub-grid scale" models, as they describe effects not captured by the chosen numerical discretization.

The goal of this thesis is to develop a sub-grid scale model of convective excitation of internal waves. Although, as described in Chapter 2, internal waves are most efficiently excited on length scales comparable to the dominant length scale of convection (i.e., large length scales), Chapter 6 shows that these waves are strongly damped. The waves which might have important dynamical consequences are instead excited by small scale, high frequency convective motions. These small scale fluctuations must be modeled, as it is currently infeasible to study their properties either experimentally or numerically.

A sub-grid scale model of convective excitation of internal waves can be coupled with a model for wave propagation, wave damping, and wave-mean flow interaction to study the effects the waves have on their surroundings. The quasi-biennial oscillation (QBO) is thought to caused by the interaction of convective excited internal gravity waves with a mean flow (Baldwin et al. 2001). However, I am not aware of any model demonstrating that a realistic wave spectrum can interact

with a zonal wind to produce the amplitude and period of the QBO. In fact, simplified models find the mean flow is not robust, and depends sensitively on the parameters describing wave excitation and damping (e.g., Rogers et al. 2008).

Quataert & Shiode (2012) and Shiode & Quataert (2014) suggest internal waves generated by convection may drive mass-loss in the last year of a star's life. At the end of a star's life, oxygen and neon burning lead to extremely vigorous core convection. This convection excites internal waves, which propagate outward, tunneling through a region of the star, and eventually becoming sound waves near the surface. These waves damp in near the surface of the star, sometimes depositing enough energy to launch a wind (Quataert et al. 2016). This could help explain observations of some luminous supernovae (e.g., Smith & McCray 2007). However, the waves which could reach high enough amplitudes to launch a wind are hypothesized to be excited by small-scale convective eddies. The amplitudes of these waves are highly uncertain, and can only be predicted with sub-grid scale models.

In addition to the lead author papers contained in this thesis and summarized in section 1.2, I also collaborated with Jim Fuller on two papers studying the astrophysical implications of internal waves generated by convection. In Fuller et al. (2014), we calculate the angular momentum transport by internal waves in red giant branch (RGB) stars. The *Kepler* and *CoRoT* telescopes have identified rotational mode splitting in the global oscillation modes of RGB stars. These measurements suggest the stably stratified core rotates more slowly than predicted by models which assume no angular momentum transport between the core and convective envelope. Whether or not internal waves can efficiently transport angular momentum depends on the assumed excitation spectrum: the spectrum predicted by the analytic arguments in Chapter 2 does not contain enough wave power to yield much angular momentum transport; however, other proposed spectra (e.g., Rogers et al. 2013) do contain enough wave power.

In Fuller et al. (2015), we calculate the angular momentum transport by internal waves in evolved massive stars, similar to those studied in Quataert & Shiode (2012) and Shiode & Quataert (2014). Instead of studying the outward propagating waves, we instead study the inward propagation of waves excited by convective shells. In contrast to Fuller et al. (2014), we found the wave transport of angular momentum in late burning phases does not depend sensitively on the assumed wave spectrum. In particular, we predict the waves may be able to spin up the core during oxygen or silicon shell burning. The predicted rotation rates are consistent with the observed rotation rates of young neutron stars, assuming negligible angular momentum transport out of the core during the subsequent supernova.

The sensitivity of large-scale phenomena on the details of how small-scale convection excites internal waves underscores the importance of developing and validating a sub-grid scale parameterization of these waves.

## 1.2 Outline

The remainder of this thesis is divided into five chapters, which represent the majority of my first author papers as a graduate student (one additional first author paper is sufficiently unrelated

that it is not included here; Lecoanet et al. 2012). In addition to these first author papers, I have three second author papers and two third author paper that are described briefly in this introduction but that are not included as part of the thesis. I also contributed to Marcus et al. (2015), which is unrelated to the work presented in this thesis.

In Chapter 2, I propose a sub-grid scale model of internal gravity wave generation by convection. This extends and clarifies a similar calculation in Goldreich & Kumar (1990). I use the Lighthill theory of wave excitation by turbulence, in which I convolve a Green's function associated with the internal gravity wave of interest with a source term related to the convective turbulence. Goldreich & Kumar (1990) calculates the wave eigenfunctions and Green's function assuming a discontinuous boundary between the convective and stably stratified regions. In this Chapter, I consider two parameterizations of a continuous boundary, assuming the Brunt–Väisälä (buoyancy) frequency profile is either piece-wise linear, or is given by a tanh near the edge of the convection zone. I find that the waves couple more efficiently to the convection for smooth transitions than for the discontinuous boundary studied in Goldreich & Kumar (1990). The work in Chapter 2 has previously been published in Lecoanet & Quataert (2013).

The next four chapters build and test computational machinery necessary to verify the predictions of Chapter 2 via numerical simulation. I helped develop the pseudo-spectral simulation framework, Dedalus (Burns et al. 2017), to study internal wave generation by convection. Dedalus can solve nearly arbitrary partial differential equations, which are specified in plain text. I contributed to the derivation of new numerical methods for implementation in pseudo-spectral codes like Dedalus. Vasil et al. (2015) presents a new Jacobi polynomial basis that can represent arbitrary tensors on a disk. Linear operators such as differentiation act sparsely on this basis. I am currently working to derive a similar Jacobi polynomial basis to represent the radial direction in spherical simulations which extend to $r = 0$ (Vasil et al. 2016). This uses the properties of spin-weighted spherical harmonics to represent the angular dependence of arbitrary tensors.

Chapter 3 demonstrates Dedalus can solve many different sets of equations used to model astrophysical and geophysical fluid dynamics. I solve three classes of equations: the fully-compressible Navier–Stokes equations, the pseudo-incompressible equations, and the anelastic equations; each using either a temperature diffusion or entropy diffusion model of thermal conduction. The pseudo-incompressible simulations use the energy-conserving formulation that I helped develop in Vasil et al. (2013). In each case, I calculate internal gravity wave eigenmodes and low Rayleigh number convective steady states. Although the equations are formulated in very different ways, they should give similar solutions in the limit of a nearly adiabatic background (and low Mach number), or for perturbations with wavelength $\lambda$ much smaller than the local pressure scale height $H$. I find excellent agreement between the different solutions when the corresponding equations should be equivalent. However, the pseudo-incompressible equations with temperature diffusion give much different solutions (especially convective steady states) than the other equations. This is because the approximation to the equation of state employed by the pseudo-incompressible equations is not valid for low Mach number flows. The work in Chapter 3 has previously been published in Lecoanet et al. (2014).

In Chapter 4 I study the accuracy of Dedalus. I run a series of two dimensional Kelvin–Helmholtz (KH) instability test problems in both Dedalus and Athena, a popular Godunov code

used in the astrophysics community (Gardiner & Stone 2008; Stone et al. 2008). I use the same fully-compressible Navier–Stokes equations in the two codes, using the formulation in Dedalus developed in Chapter 3. Simulations which start with constant initial density are easy for both codes to resolve. In all cases, both codes arrive at very similar solutions. Dedalus converges spatially very rapidly, with errors dominated by temporal discretization at high resolutions. However, Athena and Dedalus get different answers when the initial density changes by a factor of two. In this case, Athena develops a secondary instability not present in the Dedalus simulations. This secondary instability diminishes in amplitude as the resolution of the Athena simulations increases. At very high resolutions, the secondary instability disappears from Athena, and I find similar accuracy to Dedalus (although at eight times higher resolution). The secondary instability is a physical instability which also occurs in Dedalus simulations reinitialized at intermediate times with data from the Athena simulations. Most striking, however, are Athena simulations with no explicit diffusion, which are characterized by excessive irreversible mixing. Increasing the resolution of the simulation causes more irreversible mixing. This is counter to the expectation that one should approach the ideal hydrodynamic result of no irreversible mixing as the resolution increases. The work in Chapter 4 has previously been published in Lecoanet et al. (2016).

Next, in Chapter 5, I demonstrate that Dedalus can simulate a convective region adjacent to a stably stratified region. I initialize a Boussinesq simulation with a buoyancy frequency profile inspired by a 1D MESA simulation (Paxton et al. 2015) of a carbon flame that develops in the course of evolving a $9.5 M_\odot$ zero-age main sequence star. The heating from nuclear burning within the flame (implemented with a constant-in-time volumetric heating term) drives convection above the flame. The Chapter focuses on the mixing of the flame region via convective overshoot. I evolve a passive tracer field which quickly approaches a self-similar solution. This self-similar solution can be inverted to solve for an effective diffusion profile, which is the sum of the microphysical diffusion we use for numerical stability, and an effective convective diffusion. Surprisingly, the convective diffusion drops by orders of magnitude within the convection zone itself. This means there is little diffusion due to convective mixing within the flame. Although the convection generates internal waves in the stable region, the steep rise of the buoyancy frequency into the stable region causes the waves to damp very quickly, making it difficult to study the waves themselves in these simulations. The work in Chapter 5 has been submitted for publication in Astrophysical Journal Letters.

Finally, in Chapter 6 I simulate internal wave generation by convection in Dedalus. The simulations are inspired by a series of water experiments I helped analyze (Le Bars et al. 2015). The experiments exploit water's usual equation of state: Water's density maximum is at 4°C, rather than 0°C. In the experiment, a narrow tank is filled with water near 4°C, then the bottom is cooled to 0°C and the top is heated to 25°C. Between 0°C and 4°C the water is convective, and above 4°C the water is stably stratified. The system evolves into a self-consistent convective steady state, and the convection excites internal gravity waves in stably stratified region. The convection and waves are studied using particle imaging velocity and with sensitive thermistors. Chapter 6 describes Dedalus simulations similar to these experiments. A major difference between the simulations and experiments is the lack of heat losses on the side boundaries in the simulations. This causes the large scale circulation in the convection zone of the simulation to be oriented differently than the

large scale circulation in the experiments. However, the wave spectra are similar enough in the simulations and experiment to believe the Dedalus results.

The main result of Chapter 6, and indeed of this thesis, is that the Lighthill theory of wave excitation by turbulence (used in Chapter 2) is an effective description of internal wave generation by convection. To demonstrate this, I run a model simulation of the simulation inspired by the water experiment. The model simulation solves the linearized wave equation with a source term related to Reynolds stresses in the convection zone. In Chapter 2, I guess the form of this source term, but now I can use the actual value of the Reynolds stresses from the full simulation. At every time step and position in the simulation, I calculate the Reynolds stresses in the full simulation, and use them as a source term for the simplified simulation. This then makes a prediction of the wave field in the stable region. The predicted wave field matches the true wave field in the full simulation very closely. This validates the analytic approach developed in Chapter 2. The work in Chapter 6 has previously been published in Lecoanet et al. (2015).

Ongoing work includes an effort to recover the wave excitation spectrum derived in Chapter 2 in numerical simulations. This is very difficult because the prediction is only valid for waves with frequencies much lower than the buoyancy frequency, and on length scales much smaller than the convective driving length scale. The former requires long integrations due to the disparate time scales in the problem, while the latter requires low diffusivities and high resolutions to resolve small scale convective turbulence. Our phenomenological turbulence model is only valid in 3D. I have run a series of fully-compressible simulations (using the results of Chapter 3) with convection zones comprising multiple density scale heights, and have generated preliminary wave excitation spectra. However, it is difficult to compare these to the predictions in Chapter 2 because we can only study frequencies close to the buoyancy frequency, and the convection has a limited "inertial range." Nevertheless, I find the sub-grid scale model of Chapter 2 promising given experimental work showing that our assumption of a Kolmogorov spectrum holds at small scales in high Rayleigh number experiments (Niemela et al. 2000).

# Chapter 2

# Internal Gravity Wave Excitation by Turbulent Convection

## 2.1 Introduction

Internal gravity waves (hereafter, IGWs) are a class of waves in a stably stratified background in which buoyancy serves as a restoring force. IGWs propagate in radiative zones in stars and can influence composition, angular momentum, and energy transport within stars. IGWs could also be important diagnostics of stellar structure—the detection of standing IGWs ($g$-modes) has been a long-standing goal of helioseismology (Severnyi et al. 1976; Brookes et al. 1976), as $g$-modes provide better information about the core of the Sun than the more easily observed global sound waves ($p$-modes) (e.g., Turck-Chièze et al. 2001). However, IGWs are evanescent in the convection zone, so their surface manifestation is expected to be small.

IGWs have been invoked to explain the observation that F-stars have a smaller than expected Li abundance (e.g., Talon & Charbonnel 1998). Garcia Lopez & Spruit (1991), hereafter GLS91, first suggested that mixing from IGWs could enhance diffusion of Li, leading to lower Li abundances. Charbonnel & Talon (2005) invoke IGWs to explain both the Li abundances of solar-type stars and the rotation of the solar interior. When propagating through a differentially rotating star, selective damping of modes can deposit the wave's angular momentum and modify the star's rotation profile (e.g., Kumar & Quataert 1997; Zahn et al. 1997; Talon et al. 2002). Note, however, that IGWs generally have an anti-diffusive effect, accentuating angular velocity gradients. This anti-diffusive behavior leads to the quasi-biennial oscillation (QBO) in the Earth's atmosphere, and has been studied extensively by the atmospheric science community (Baldwin et al. 2001; Fritts & Alexander 2003).

Massive stars have convective cores surrounded by a radiative envelope. Quataert & Shiode (2012) suggested that extremely vigorous convection within the last $\sim$ year of a massive star's life could generate a super-Eddington IGW flux and drive significant mass loss. Earlier in a massive star's life, the angular momentum carried by IGWs may generate substantial differential rotation, perhaps mirroring the QBO in the Earth's atmosphere (Rogers et al. 2012).

In some stars, IGWs are linearly unstable, driven by, e.g., the $\epsilon$ or $\kappa$ mechanisms (Unno 1979).

Even absent such linear driving, however, IGWs are thought to be generated by turbulent convection. Although IGWs are evanescent in a convective region, they can be excited by Reynolds stresses or entropy fluctuations associated with the convection. A related excitation mechanism is IGW generation by overshooting convective plumes which penetrate into the radiative region. Numerical simulations of a radiative zone adjacent to a convection zone find efficient generation of IGWs (e.g., Rogers & Glatzmaier 2005a; Meakin & Arnett 2007; Brun et al. 2011). Although simulations reported in Rogers & Glatzmaier (2005a) & Meakin & Arnett (2007) show power distributed over a wide range of frequencies and wavelengths, the power spectra in Brun et al. (2011) exhibit ridges corresponding to discrete $g$-modes.[1] Simulations often require artificially high diffusivities in the radiative zone to maintain a strong convective flux, and thus IGWs are artificially strongly damped in the radiative zone. This complicates estimating IGW fluxes or quantitatively studying the effects of IGWs on the stellar structure.

There have been several efforts to analytically estimate the flux of IGWs stochastically excited by turbulent convection. These models are essential for determining the resulting efficiency of the mixing, angular momentum transport, or mass-loss produced by IGWs. Press (1981, hereafter P81) and GLS91 match pressure perturbations in the convective region to pressure perturbations in the waves, whereas Goldreich & Kumar (1990, hereafter GK90) and Belkacem et al. (2009, hereafter B09) calculate eigenmodes and derive how their amplitudes change using an inhomogeneous wave equation. P81, GLS91, and GK90 all model the convective region using mixing length theory, assuming a Kolmogorov turbulence spectrum. B09 uses an energy spectrum calculated from a direct numerical simulation of the solar convection zone. Each of these papers predicts a different IGW power spectrum.

In this chapter, we calculate the IGW flux generated by turbulent convection and clarify the relationship between different predictions in the literature. In Section 2.2, we state our assumptions regarding the background state, and describe some properties of IGWs. Our main calculation is in Section 2.3, where we introduce our formalism for calculating the IGW flux. Our formalism relies on calculating a Green's function using the eigenmodes of the system (also discussed in P81). We relate our method to GK90's in Appendix 2.C. In Section 2.3.5 we calculate the IGW flux and rms wave displacements for both smooth and discontinuous radiative-convective transitions. Next, we show that our results for a discontinuous transition can be derived more heuristically using pressure balance arguments (Section 2.4); we also make detailed comparisons to previous results (Section 2.5). Finally, in Section 2.6 we show how our results increase the predicted IGW flux in stars, and discuss some implications of this increased wave flux.

## 2.2 Background State and Perturbation Equations

In this chapter we consider a simple model of a radiative zone adjacent to a convection zone. We assume that the length scales of interest are small in comparison to the stellar radius, i.e., we are

[1] The simulations of Rogers & Glatzmaier (2005a) and Brun et al. (2011) solve the anelastic equations, which do not conserve energy (Brown et al. 2012). This could potentially produce errors in the IGW amplitudes and/or power spectra.

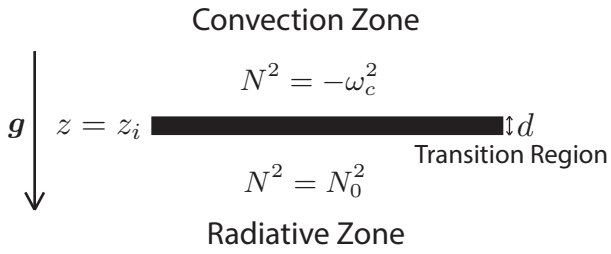


*Figure 2.1*: A schematic of our problem setup. The radiative-convective interface is at $z = z_i$, where $z_i$ is close to zero, and has width $d$. Gravity points downward in the $z$ direction. The convection zone is the region $z > z_i$ and the radiative zone is the region $z < z_i$. We will use $\xi_{z,\text{rad}}$ to denote the part of the vertical displacement within the radiative zone. If $d$ is small, the waves see the radiative-convective transition as discontinuous; we will use superscript $D$ to denote results for a discontinuous transition. If $d$ is large, the waves see the radiative-convective transition as smooth. In this case, the results depend on the $N^2$ profile very close to $z_i$. We consider $N^2$ parameterized by a tanh profile, which is a very smooth transition; we will use superscript $T$ to denote results for the tanh profile. We also consider a piecewise linear $N^2$ profile, which is the most abrupt possible continuous transition; we will use superscript $L$ to denote results for the piecewise linear profile. Eqns. 2.46, 2.58, & 2.59 give our IGW flux estimates for discontinuous, tanh, and piecewise-linear $N^2$, respectively.

in the local limit, so we use cartesian geometry, where $\boldsymbol{e}_z$ is the direction of gravity. In our model, the radiative zone is the region $-L < z < z_i$, and the convection zone is the region $z_i < z < L$, where $z_i$ is the location of the radiative-convective interface, and both regions have a horizontal area $\mathcal{A}$. We take $L$ and $\sqrt{\mathcal{A}}$ to be much larger than any other length scale in the problem, and will assume $z_i$ is close to zero. In Figure 4.10 we sketch a schematic of our model. Using a domain with finite vertical extent provides simpler boundary conditions, but yields the same results as an infinite domain.

Furthermore, we employ the Boussinesq approximation. This is appropriate if the wave generation occurs close to the radiative-convective boundary, and if we are only concerned with IGWs near this boundary. We will see that the wave generation primarily occurs in a region with height approximately equal to the size of the energy bearing convective motions, which we assume is $\sim H$ the pressure scale height. Although the Boussinesq approximation is only rigorously valid on length scales smaller than $H$, we recover results similar to those presented in GK90 who used the fully compressible equations. We thus believe that our results would not change significantly if we used the fully compressible equations.

We model the radiative region as a stably stratified atmosphere with a squared buoyancy frequency $N_0^2$. The convective region is much more complicated due to turbulent motions. We decompose the fluid properties in the convection zone into time averaged and fluctuating components. We assume the time averaged velocity is zero, and there is a very small mean stratification with squared buoyancy frequency $-\omega_c^2$. Because the convective region is nearly adiabatic, $\omega_c \ll N_0$. We treat the fluctuating components of the velocity and entropy in the convective region as source

terms in the wave equation. In practice, we only include source terms due to the Reynolds stress in our analysis; source terms due to entropy fluctuations are of the same size or smaller than the Reynolds stress terms (P81, GK90).

With these assumptions, the equation for the evolution of the vertical displacement $\xi_z$ is

$$\nabla^2 \frac{\partial^2}{\partial t^2}\xi_z + N_0^2 \nabla_\perp^2 \xi_z = 0, \tag{2.1}$$

in the radiative region, and

$$\nabla^2 \frac{\partial^2}{\partial t^2}\xi_z - \omega_c^2 \nabla_\perp^2 \xi_z = S = -\nabla^2 F_z + \frac{\partial}{\partial z}\nabla \cdot \boldsymbol{F}, \tag{2.2}$$

in the convective region. We take $\nabla_\perp = \partial_x \boldsymbol{e}_x + \partial_y \boldsymbol{e}_y$ to be the horizontal part of the gradient operator (perpendicular to gravity), and $S$ to be the source term due to the Reynolds stress $\boldsymbol{F}$.

There are three parts of the Reynolds stress $\boldsymbol{F}$ on the RHS of eqn. 2.2: the convection-convection term, $\nabla \cdot (\boldsymbol{u}_c \boldsymbol{u}_c)$; the wave-convection terms, $\boldsymbol{u}_c \cdot \nabla \partial_t \boldsymbol{\xi} + (\partial_t \boldsymbol{\xi}) \cdot \nabla \boldsymbol{u}_c$; and the wave-wave term, $(\partial_t \boldsymbol{\xi}) \cdot \nabla (\partial_t \boldsymbol{\xi})$. In this chapter, we will only consider the convection-convection term, taking

$$\boldsymbol{F} = \nabla \cdot (\boldsymbol{u}_c \boldsymbol{u}_c). \tag{2.3}$$

Nonlinearities from the wave-wave term are only important if $k_z \xi_z \gtrsim 1$. We will find later that this condition is not satisfied in the convection zone, although wave breaking does occur within the radiative zone. The first wave-convection interaction term, $\boldsymbol{u}_c \cdot \nabla \partial_t \boldsymbol{\xi}$, is the advection of wave energy by convection, and thus does not change the wave energy. The second part, $(\partial_t \boldsymbol{\xi}) \cdot \nabla \boldsymbol{u}_c$, gives the effect of the strain associated with the convection on the wave, and can contribute to wave generation. However, we find that the wave flux is smaller than the convective flux, so the wave velocities are smaller than the convective velocities. Furthermore, one can check that the $(\partial_t \boldsymbol{\xi}) \cdot \nabla \boldsymbol{u}_c$ is also smaller than the other linear (in $\boldsymbol{\xi}$) terms in our eigenvalue equation (e.g., using eqn. 2.29 or eqn. 2.30). Thus, it is consistent to take $\boldsymbol{F} = \nabla \cdot (\boldsymbol{u}_c \boldsymbol{u}_c)$.

We now discuss the wave solutions to the homogeneous equations, i.e., taking $S = 0$. Because the equations are autonomous in $x, y, t$, we can Fourier transform in these directions. Thus, we can take the solutions to be

$$\xi_z(x, y, z, t) = \xi_z(z) \exp(i k_x x + i k_y y - i\omega t), \tag{2.4}$$

and define the horizontal wavenumber $k_\perp = \sqrt{k_x^2 + k_y^2}$, i.e., the wavenumber perpendicular to gravity. Throughout this chapter we will assume $N_0 \gg \omega$. The solutions to eqns. 2.1,2.2 are

$$\xi_z = B_1 \cos(N_0 k_\perp z/\omega) + B_2 \sin(N_0 k_\perp z/\omega), \tag{2.5}$$

$$\xi_z = C_1 \exp(-k_\perp z) + C_2 \exp(k_\perp z), \tag{2.6}$$

respectively, where we have assumed $\sqrt{\omega^2 + \omega_c^2} \sim \omega$. The horizontal displacement $\boldsymbol{\xi}_\perp$ and pressure perturbation $\delta p$ are related to $\xi_z$ by

$$\xi_\perp \sim i(N_0/\omega)\xi_z, \tag{2.7}$$

$$\delta p \sim i\rho_0 (N_0 \omega / k_\perp)\xi_z, \tag{2.8}$$

in the radiative region, and

$$\xi_\perp \sim \xi_z, \tag{2.9}$$
$$\delta p \sim \rho_0(\omega^2/k_\perp)\xi_z, \tag{2.10}$$

in the convective region. The background density is $\rho_0$, which is constant to lowest order in the Boussinesq approximation.

To solve for the coefficients in eqns. 2.5 & 2.6 and the eigenvalues $\omega$, we must impose four boundary conditions and a normalization condition (the latter is discussed in Section 2.3.3). Two of the boundary conditions are on the behavior of $\xi_z$ at $z = \pm L$. The physical solution requires that $\xi_z = 0$ at the top and bottom boundaries. The other two boundary conditions are set at the radiative-convective interface, $z = z_i$. These depend on the nature of the boundary between the radiative and convective regions, and determine which $\omega$ satisfy the eigenvalue problem. Assume that $N^2$ varies from $N_0^2$ to $-\omega_c^2$ in a thin layer with height $d$, as illustrated in Figure 4.10. If there is a sharp transition between the radiative and convective regions, i.e., $(k_\perp N_0/\omega)d \ll 1$, we can make the approximation that $N^2$ is discontinuous at $z_i$, which we take to be at $z = 0$. However, if $N^2$ varies slowly, i.e., $(k_\perp N_0/\omega)d \gg 1$, then interesting behavior can take place in the transition region. As we discuss in Section 2.6, we expect the most efficiently excited waves in the Sun to fall under this latter regime. We will discuss both the discontinuous and smooth $N^2$ limits below.

## 2.3 Wave Generation by Turbulent Convection

Because the wave generation and wave propagation regions are distinct, we use a Green's function (or equivalently, variation of parameters), as in P81. Once we have a Green's function $G(z, t; \zeta, \tau)$, we can write the vertical displacement in the radiative region as

$$\xi_{z,\mathrm{rad}} = \int_{-\infty}^{t} d\tau \int_{z_i}^{L} d\zeta \; G(z, t; \zeta, \tau) \; S(x, y, \zeta, \tau), \tag{2.11}$$

where we assume that $\xi_{z,\mathrm{rad}}$ is zero at $t \to -\infty$. The Green's function depends on whether $N^2$ can be modeled as discontinuous or smooth at the radiative-convective boundary. In Section 2.3.1 we calculate the Green's function assuming $N^2$ is discontinuous (as was assumed in GLS91 and GK90) and then in Section 2.3.2 we treat the smooth $N^2$ case. As we shall argue, the latter is more appropriate for the low frequency waves which dominate the IGW flux. In Appendix 2.C we show that the Green's function method is formally equivalent to GK90's method of expanding $\xi_z$ into normal modes to solve eqns. 2.1, 2.2.

### 2.3.1 Green's Function for Discontinuous $N^2$

To calculate the Green's function, we need two linearly independent solutions, one which satisfies $\xi_z(-L) = 0$, and one that satisfies $\xi_z(+L) = 0$. The boundary conditions at $z_i$, which we take

to be at $z = 0$, when $N^2$ is discontinuous, are that $\xi_z$ and $\delta p$ are continuous at $z = 0$. The first solution, which we call $\eta_z^D$, satisfies the boundary condition at $z = +L$:

$$\eta_z^D = \begin{cases} B_1 \cos(N_0 k_\perp z/\omega + \omega/N_0) & z < 0, \\ B_1 \exp(-k_\perp z) & z > 0. \end{cases} \tag{2.12}$$

Here we use *superscript D* to denote the eigenfunction when $N^2$ is *discontinuous* at the interface. Below, we will use *superscript T* to denote quantities for a smooth $N^2$ parameterized by a tanh profile, and *superscript L* to denote quantities for a smooth piecewise linear $N^2$. The second linearly independent solution, which we call $\xi_z^D$, satisfies the boundary condition at $z = -L$:

$$\xi_z^D = \begin{cases} B_2 \sin(N_0 k_\perp z/\omega) & z < 0, \\ B_2 \frac{N_0}{2\omega} \left(\exp(k_\perp z) - \exp(-k_\perp z)\right) & z > 0. \end{cases} \tag{2.13}$$

The eigenvalues $\omega$ must satisfy $\sin(N_0 k_\perp L/\omega) = 0$. Later we will project the total vertical displacement in the radiative zone onto the basis $\{\xi_z\}_\omega$. The vertical displacement in the radiative zone is approximately orthogonal to $\{\eta_z\}_\omega$ in the radiative zone. Thus, it is important that our second linearly independent solution is also approximately orthogonal to $\{\eta_z\}_\omega$, as is the case for eqns. 2.12 & 2.13.

The general expression for the Green's function, assuming $z < \zeta$, is

$$G(z,t;\zeta,\tau) = \int d\omega' \, \frac{\delta(f(\omega'))}{\omega'^2} \frac{\xi_z(z;\omega')\eta_z(\zeta;\omega')}{W(\zeta)} \exp(-i\omega'(t-\tau)), \tag{2.14}$$

where we label the eigenfunctions with their frequency $\omega'$, $\delta$ denotes the Dirac delta function, and $W(\zeta)$ denotes the Wronskian of $\xi_z$ and $\eta_z$. $f(\omega')$ is a function which is zero if and only if $\omega'$ is an eigenvalue. For the discontinuous case, we have $f(\omega') = \sin(N_0 k_\perp L/\omega')$. We thus can simplify eqn. 2.14 to

$$G(z,t;\zeta,\tau) = \sum_{\omega'} \frac{1}{N_0 k_\perp L} \frac{\xi_z(z;\omega')\eta_z(\zeta;\omega')}{W(\zeta)} \exp(-i\omega'(t-\tau)), \tag{2.15}$$

where the sum is over the eigenvalues $\omega'$. For the discontinuous $N^2$ problem, assuming $z < 0$ and $\zeta > 0$, the Green's function is

$$G^D(z,t;\zeta,\tau) = \sum_{\omega'} \frac{\omega'}{N_0^2 k_\perp^2 L} \frac{1}{B_2} \xi_z^D(z;\omega') \exp(-k_\perp \zeta - i\omega'(t-\tau)). \tag{2.16}$$

### 2.3.2 Green's Function for Smooth $N^2$

If $N^2$ varies smoothly from $N_0^2$ to $-\omega_c^2$, then a WKB type approximation can be used, provided that $N_0 k_\perp d/\omega \gg 1$. Our motivation for studying this limit is that the largest scale waves in stars satisfy $N_0 k_\perp d/\omega \gg 1$ (see Section 2.6). We would like to develop an approximate solution which is valid within the transition region, allowing us to connect the solution in the radiative region (eqn. 2.5) to the solution in the convective region (eqn. 2.6).

The solution in the transition region depends on the form of $N^2(z)$ near the radiative-convective interface. In this section, we will provide some details of the calculation for a tanh profile. An eigenmode with frequency $\omega$ transitions from oscillatory behavior to exponential behavior at a point $z_t$ (where $N^2 = \omega^2$), which is lower than the the radiative-convective interface, $z_i$ (where $N^2 = 0$). For a tanh profile, $z_t$ does not change very much as $\omega$ changes; although it is smooth, it is not *too* smooth. Thus, we believe that the tanh profile is the smoothest physically relevant $N^2$ profile.

In Appendix 2.B, we also consider a piecewise linear $N^2$ profile. In contrast to the smooth tanh profile, this is the most abrupt continuous transition possible. Thus, we believe that any actual stellar $N^2$ profile should lie somewhere between these two limits. Although we focus on the tanh profile in this section, we will also describe the IGW fluxes for the piecewise linear $N^2$ profile in Section 2.3.5.

One might be tempted to appeal to WKB analysis to solve for the eigenfunction on either side of the interface, and then match across the interface by expanding $N^2$ to linear order near the wave's turning point (as is standard in, e.g., quantum mechanics). Roughly, a WKB solution is valid if the local wavelength of the eigenfunction is small compared to the scale on which the wavenumber of the eigenfunction varies, which for us is $d$. For smooth $N^2$ we have assumed $N_0 k_\perp d/\omega \gg 1$, so the WKB solution in the radiative zone is valid. However, the WKB solution might break down near the convection zone if $k_\perp d \ll 1$. For the piecewise linear $N^2$ profile, a version of WKB matching is valid (see Appendix 2.B). For the tanh profile, however, the eigenfunction is poorly approximated by the WKB solution when $k_\perp d \ll 1$. Moreover, because $d/H \leq 1$ and IGWs with $k_\perp H \sim 1$ dominate the wave flux (see Section 2.3.5; $H$ here is the pressure scale height which we assume is the largest scale of the turbulence), the WKB solution fails for the most efficiently excited IGWs. Instead, we need to develop a different method to solve for the eigenfunctions. The details of this calculation are given in Appendix 2.A.

We assume $N^2(z)$ is given by

$$N^2(z) = \frac{N_0^2 + \omega_c^2}{2}\left(\tanh\left(-\frac{z}{d}\right) + 1\right) - \omega_c^2. \tag{2.17}$$

In Appendix 2.A, we derive approximate forms for two independent eigenfunctions, and show that there is excellent agreement between the numerical solutions to the eigenvalue problem and our asymptotic Bessel function solutions. We are interested in the behavior of the eigenfunctions near the radiative-convective interface $z_i$. The interface is at

$$\exp\left(-2\frac{z_i}{d}\right) \sim \frac{\omega_c^2}{N_0^2 + \omega_c^2}. \tag{2.18}$$

The two independent solutions are

$$\eta_z^T \sim \begin{cases} B_1 \cos(N_0 k_\perp z/\omega + \pi/4) & z \gtrsim -d \\ B_1 \left(\frac{N_0 k_\perp d}{\omega}\right)^{1/2} \left(\frac{\omega}{\bar{\omega}}\right)^{k_\perp d} J_{\bar{d}}\left[\frac{\omega_c k_\perp d}{\omega} \exp\left(-\frac{z-z_i}{d}\right)\right] & z \lesssim d \end{cases} \tag{2.19}$$

$$\xi_z^T \sim \begin{cases} B_2 \sin(N_0 k_\perp z/\omega + \pi/4) & z \gtrsim -d \\ B_2 \left(\frac{N_0 k_\perp d}{\omega}\right)^{1/2} \left(\frac{\bar{\omega}}{\omega}\right)^{k_\perp d} Y_{\bar{d}}\left[\frac{\omega_c k_\perp d}{\omega} \exp\left(-\frac{z-z_i}{d}\right)\right] & z \lesssim d \end{cases} \tag{2.20}$$

where $\bar{\omega}^2 = \omega_c^2 + \omega^2$ and $\bar{\omega}/\omega$ ranges between $\sqrt{2}$ and 1 for $\omega \gtrsim \omega_c$, and $\bar{d} = \bar{\omega} k_\perp d/\omega$. In eqns. 2.19 & 2.20 we have dropped several factors of order unity from the equations derived in Appendix 2.A. The eigenvalues for this problem are the frequencies $\omega$ which satisfy $\sin(-N_0 k_\perp L/\omega + \pi/4) = 0$. In Figure 2.2 we plot $\eta_z^T$ for parameters representative of the energy-bearing waves in the sun.

Given eqns. 2.19 & 2.20, the Green's function, for $z < 0$ and $\zeta > 0$ is

$$G^T(z,t;\zeta,\tau) \sim \sum_{\omega'} \left(\frac{\omega' d}{N_0 k_\perp}\right)^{1/2} \left(\frac{\omega'}{\bar{\omega}'}\right)^{k_\perp d} (B_2 N_0 k_\perp L)^{-1} \times J\, \xi_z^T(z;\omega') \exp(-k_\perp \zeta - i\omega'(t-\tau)), \tag{2.21}$$

where we introduce the shorthand

$$J \equiv J_{\bar{\omega} k_\perp d/\omega}\left(\frac{\omega_c k_\perp d}{\omega}\right). \tag{2.22}$$

Using series expansions from Abramowitz & Stegun (2012), we can approximate

$$J \sim \begin{cases} 1 & \text{if } k_\perp d \ll 1, \\ (k_\perp d)^{-1/2} \exp(-k_\perp d) & \text{if } k_\perp d \gg 1. \end{cases} \tag{2.23}$$

Note that although the Green's function for a tanh profile is equal to the discontinuous Green's function when $N_0 k_\perp d/\omega \sim 1$, the Green's function in eqn. 2.21 is no longer valid when $N_0 k_\perp d/\omega \ll 1$ (see Appendix 2.A.1). Instead, eqn. 2.16 must be used in this limit.

### 2.3.3 Amplitude Equation

Now that we have the Green's function, we can calculate mode excitation. First, we will expand $\xi_{z,\mathrm{rad}}$ (in eqn. 2.11) into eigenmodes $\xi_{z,\mathrm{rad}}(z;\omega)$. We use the subscript rad to denote the $z < z_i$ part of the eigenfunctions (eqns. 2.13, 2.20). We write

$$\xi_{z,\mathrm{rad}} = \frac{1}{\sqrt{\mathcal{A}}} \sum_{\omega'} A(t;\omega')\, \xi_{z,\mathrm{rad}}(z;\omega') \exp(ik_x x + ik_y y - i\omega' t), \tag{2.24}$$

where the $\xi_{z,\mathrm{rad}}$ are the $z < z_i$ part of the eigenmodes. Using this representation in eqn. 2.11, we take the inner product with $\xi_{z,\mathrm{rad}}(z;\omega)$, multiply by $\exp(-ik_x x - ik_y y + i\omega t)$, and integrate over $dxdy$ to find

$$A(t;\omega) = \frac{1}{\sqrt{\mathcal{A}}} \int_{-\infty}^{t} d\tau \int dxdy \int_{z_i}^{L} d\zeta \frac{1}{N_0 k_\perp L} \frac{\eta_z(\zeta;\omega)}{W(\zeta)} \times S(x,y,\zeta,\tau) \exp(-ik_x x - ik_y y + i\omega\tau). \tag{2.25}$$

This procedure is discussed more thoroughly in Appendix 2.C.

At this point we must pick a normalization condition for our eigenfunctions. The energy in the perturbation is

$$\int d^3x\rho_0 \left|\frac{\partial}{\partial t}\boldsymbol{\xi}_{\rm rad}(z)\right|^2 = \sum_{\omega}\sum_{\omega'} A(\omega)\, A^*(\omega') \left(\omega\omega' \int dz\, \rho_0 \boldsymbol{\xi}_{\rm rad}(z,\omega)\cdot\boldsymbol{\xi}^*_{\rm rad}(z,\omega')\right). \tag{2.26}$$

We want to identify $\sum_\omega |A(\omega)|^2$ with the energy, so our normalization condition is

$$\omega\omega' \int dz\, \rho_0 \boldsymbol{\xi}_{\rm rad}(z;\omega)\cdot\boldsymbol{\xi}^*_{\rm rad}(z;\omega') = \delta_{\omega\omega'}, \tag{2.27}$$

where $\delta$ is the Kronecker delta. Using the eigenfunctions (eqns. 2.12, 2.13, 2.19, 2.20) and the polarization relation (eqn. 2.7), the normalization condition implies

$$B^2 \sim B_1^2 \sim B_2^2 \sim \frac{1}{N_0^2 L\rho_0}, \tag{2.28}$$

for all the $N^2$ profiles considered in this chapter. Using this normalization in eqn. 2.25, the amplitude equations are

$$A^D(t;\omega) = \frac{1}{\sqrt{\mathcal{A}}}\int_{-\infty}^{t} d\tau \int dxdy\ \exp(-ik_x x - ik_y y + i\omega\tau) \times \frac{\omega}{N_0 k_\perp^2}\sqrt{\frac{\rho_0}{L}}\int_{z_i}^{L} d\zeta \exp(-k_\perp\zeta)\, S(x,y,\zeta,\tau), \tag{2.29}$$

$$A^T(t;\omega) = \frac{1}{\sqrt{\mathcal{A}}}\int_{-\infty}^{t} d\tau \int dxdy \exp(-ik_x x - ik_y y + i\omega\tau) \times \left(\frac{J\sqrt{\omega\rho_0 d}}{\sqrt{N_0 L k_\perp^3}}\right)\left(\frac{\omega}{\bar{\omega}}\right)^{k_\perp d}\int_{z_i}^{L} d\zeta \exp(-k_\perp\zeta) S(x,y,\zeta,\tau). \tag{2.30}$$

It is straightforward to derive the analogous amplitude equation for the piecewise linear $N^2$ profile using the Green's function given in eqn. 2.118.

### 2.3.4 Model of Turbulent Convection

To make further progress, we need to specify the source term $S$. We assume that the convective turbulence is composed of a large number of incoherent eddies, estimate the wave generation due to a single eddy in isolation, and then find the total wave generation by summing over all eddies. We model the statistical properties of stellar convection using Kolmogorov turbulence (see, e.g., Goldreich & Keeley 1977): the convective velocity on the outer-scale $H$ is $u_c$ and the associated convective turnover frequency is $\omega_c \sim u_c/H$. The convective energy flux is $F_{\rm conv} \sim \rho_0 u_c^3$. On scales

$h$ sufficiently small compared to $H$, the turbulent power-spectrum is given by the Kolmogorov scaling:

$$u_h \simeq u_c\,(h/H)^{1/3} \simeq u_c(\omega_e/\omega_c)^{-1/2} \tag{2.31}$$

where we have used the fact that smaller eddies have higher frequencies, i.e., shorter turnover times, with $\omega_e \simeq u_h/h \propto h^{-2/3}$ and thus $h \propto \omega_e^{-3/2}$. A given convective eddy characterized by its frequency $\omega_e$ can excite waves having frequencies $\omega$ and horizontal wavenumbers $k_\perp$ that satisfy

$$\omega \lesssim \omega_e \quad \text{and} \quad k_\perp \lesssim k_\perp^{max} \simeq H^{-1}(\omega_e/\omega_c)^{3/2}. \tag{2.32}$$

### 2.3.5 Energy Generation Rates and IGW Fluxes

In this section we calculate the IGW fluxes for discontinuous, tanh, and piecewise linear convective-radiative transitions. We begin by estimating the energy generation due to a single eddy with size $h$ and turnover frequency $\omega_e$. The source term contains three spatial derivatives which we can integrate by parts. The contribution due to the source term is

$$S \sim k_\perp^3 u_h^2. \tag{2.33}$$

Assuming the eddy has volume $h^3$ and lasts for a time $\omega_e^{-1}$, we can estimate the change in the amplitude due to a single eddy

$$\Delta A^D(\omega) \sim \sqrt{\frac{\rho_0}{\mathcal{A}L}}\frac{\omega}{N_0}k_\perp h^4 u_h, \tag{2.34}$$

$$\Delta A^T(\omega) \sim \sqrt{\frac{N_0}{\omega}}\left(J\sqrt{k_\perp d}\right)\left(\frac{\omega}{\bar{\omega}}\right)^{k_\perp d}\Delta A^D(\omega), \tag{2.35}$$

$$\Delta A^L(\omega) \sim \left(\frac{N_0 k_\perp d}{\omega}\right)^{1/6}\Delta A^D(\omega). \tag{2.36}$$

The total energy generation rate due to all eddies is then

$$\cdot E^D(\omega) \sim \frac{\left(\Delta A^D\right)^2}{\omega_e^{-1}}\left(\frac{\mathcal{A}k_\perp^{-1}}{h^3}\right) \sim \frac{\rho_0}{L}\left(\frac{\omega}{N_0}\right)^2 u_h^3 h^3\ (k_\perp h), \tag{2.37}$$

$$\cdot E^T(\omega) \sim \frac{N_0}{\omega}\left(J^2 k_\perp d\right)\left(\frac{\omega}{\bar{\omega}}\right)^{2k_\perp d}\cdot E^D(\omega), \tag{2.38}$$

$$\cdot E^L(\omega) \sim \left(\frac{N_0 k_\perp d}{\omega}\right)^{1/3}\cdot E^D(\omega). \tag{2.39}$$

The factor of $\mathcal{A}k_\perp^{-1}/h^3$ in eqn. 2.37 counts the number of eddies with size $h$ which excite IGWs with frequency $\omega$. We have assumed excitation happens in a region with thickness $dz \sim k_\perp^{-1}$ (because the IGW eigenfunction decreases in the convection zone over a characteristic lengthscale $\sim k_\perp^{-1}$). Because of the random phases of the convective eddies, the excitations due to different eddies are assumed to be uncorrelated, and the energy increases only linearly with the number of eddies.

In the case of smooth $N^2$, the flux decreases exponentially for $k_\perp d \gg 1$. The dominant contribution to the flux is from $k_\perp d \lesssim 1$, so for the rest of this section, we will assume $k_\perp d \lesssim 1$. The IGW flux is then given by

$$\frac{dF^D}{d\log\omega\, d\log k_\perp} \sim \frac{\cdot E^D(\omega)}{\mathcal{A}} \left(\mathcal{A}k_\perp^2 L k_\perp \frac{N_0}{\omega}\right)$$
$$\sim \rho_0 u_h^3 \frac{\omega}{N_0}(k_\perp h)^4 \sim \rho_0 u_c^3 \mathcal{M}(k_\perp H)^4 \left(\frac{\omega}{\omega_c}\right)^{-13/2}, \tag{2.40}$$
$$\frac{dF^T}{d\log\omega\, d\log k_\perp} \sim \rho_0 u_c^3 (k_\perp H)^4 \left(\frac{\omega}{\omega_c}\right)^{-15/2} (k_\perp d), \tag{2.41}$$
$$\frac{dF^L}{d\log\omega\, d\log k_\perp} \sim \rho_0 u_c^3 \mathcal{M}^{2/3} (k_\perp H)^4 \left(\frac{\omega}{\omega_c}\right)^{-41/6} (k_\perp d)^{1/3}. \tag{2.42}$$

where $\mathcal{M} = \omega_c/N_0$ is the convective Mach number. The term in parentheses in the first equality of eqn. 2.40 is the density of states. There are $\mathcal{A}k_\perp^2$ modes in the horizontal direction, and $Lk_\perp N_0/\omega$ modes in the vertical direction, with wavenumber $\sim k_\perp$ and frequency $\sim \omega$, which each contribute a flux $\cdot E(\omega)/\mathcal{A}$. Recall that eqns. 2.40-2.42 only apply for $\omega \gtrsim \omega_c$ and $k_\perp \lesssim k_\perp^{\max}(\omega) \sim H^{-1}(\omega/\omega_c)^{3/2}$, and eqns. 2.41 & 2.42 assume $k_\perp d \lesssim 1$.

Integrating over $k_\perp$, we find

$$\frac{dF^D}{d\log\omega} \sim \rho_0 u_c^3 \mathcal{M} \left(\frac{\omega}{\omega_c}\right)^{-1/2}, \tag{2.43}$$
$$\frac{dF^T}{d\log\omega} \sim \rho_0 u_c^3 \left(\frac{d}{H}\right), \tag{2.44}$$
$$\frac{dF^L}{d\log\omega} \sim \rho_0 u_c^3 \mathcal{M}^{2/3} \left(\frac{\omega}{\omega_c}\right)^{-1/3} \left(\frac{d}{H}\right)^{1/3}. \tag{2.45}$$

Finally, we find that the total flux is

$$F^D \sim \rho_0 u_c^3 \mathcal{M} \sim F_{\rm conv}\mathcal{M}, \tag{2.46}$$
$$F^T \sim \rho_0 u_c^3 \left(\frac{d}{H}\right) \sim F_{\rm conv}\left(\frac{d}{H}\right), \tag{2.47}$$
$$F^L \sim \rho_0 u_c^3 \mathcal{M}^{2/3} \left(\frac{d}{H}\right)^{1/3} \sim F_{\rm conv}\mathcal{M}^{2/3}\left(\frac{d}{H}\right)^{1/3}. \tag{2.48}$$

This estimate predicts, for a tanh $N^2$ profile, an IGW flux only slightly smaller than the convective flux. However, as we now show, energy-bearing waves in the smooth $N^2$ case (both tanh and piecewise linear profiles) will undergo vigorous wave-breaking within the radiative zone (see Figure 2.2). This process occurs concurrently with overshooting convective plumes, but is much more spatially localized (in $z$) than overshooting convection.

To quantify this argument, we calculate the typical size of the perturbations in the radiative zone using

$$\frac{dF}{d\log\omega\, d\log k_\perp} \sim \rho_0(\omega\xi_\perp)^2 u_{g,z}, \tag{2.49}$$

where $u_{g,z} \sim \omega/k_z \sim \omega^2/(N_0 k_\perp)$ is the vertical group velocity, and we have assumed $\xi_\perp \gg \xi_z$ (eqn. 2.7). From this, we find

$$\xi_z^D \sim H\frac{\omega}{N_0}(k_\perp H)^{5/2}\left(\frac{\omega}{\omega_c}\right)^{-21/4}, \tag{2.50}$$

$$\xi_z^T \sim H\sqrt{\frac{\omega}{N_0}}(k_\perp H)^3\left(\frac{\omega}{\omega_c}\right)^{-21/4}\left(\frac{d}{H}\right)^{1/2}, \tag{2.51}$$

$$\xi_z^L \sim H\left(\frac{\omega}{N_0}\right)^{5/6}(k_\perp H)^{8/3}\left(\frac{\omega}{\omega_c}\right)^{-21/4}\left(\frac{d}{H}\right)^{1/6}, \tag{2.52}$$

and

$$k_z\xi_z^D \sim (k_\perp H)^{7/2}\left(\frac{\omega}{\omega_c}\right)^{-21/4}, \tag{2.53}$$

$$k_z\xi_z^T \sim \mathcal{M}^{-1/2}(k_\perp H)^4\left(\frac{\omega}{\omega_c}\right)^{-23/4}\left(\frac{d}{H}\right)^{1/2}, \tag{2.54}$$

$$k_z\xi_z^L \sim \mathcal{M}^{-1/6}(k_\perp H)^{11/3}\left(\frac{\omega}{\omega_c}\right)^{-65/12}\left(\frac{d}{H}\right)^{1/6}, \tag{2.55}$$

where we have used $k_z = k_\perp N_0/\omega$ which holds in the radiative zone for $|z| \ll d$. Recall that the condition for wave breaking is $k_z\xi_z \sim 1$. For the case of discontinuous $N^2$, the most efficiently excited waves are marginally susceptible to wave breaking. However, for both tanh and piecewise linear $N^2$, the most efficiently excited waves will break in the radiative zone.

The only waves that successfully propagate in the radiative zone have $k_z\xi_z \lesssim 1$. Thus, to find the IGW flux for smooth $N^2$, we must integrate the flux only over the regions of $(k_\perp, \omega)$ space in which $k_z\xi_z \lesssim 1$. This implies

$$(H\mathcal{M}/d)^{1/2} \lesssim (k_\perp H)^4\left(\frac{\omega}{\omega_c}\right)^{-23/4} \quad \text{(tanh)} \tag{2.56}$$

$$(H\mathcal{M}/d)^{1/6} \lesssim (k_\perp H)^{11/3}\left(\frac{\omega}{\omega_c}\right)^{-65/12} \quad \text{(piecewise linear)} \tag{2.57}$$

and, as before, $\omega \gtrsim \omega_c$, $k_\perp \lesssim H^{-1}(\omega/\omega_c)^{3/2}$, and $k_\perp d \lesssim 1$. We find that the waves that are marginally susceptible to wave breaking, and which maximize the flux for the tanh profile are at the convective turnover frequency, $\omega \sim \omega_c$, but have small wave numbers, $k_\perp H \sim (\mathcal{M}H/d)^{1/8}$. For the piecewise linear profile, the spatial scale is $k_\perp H \sim 1$, but the waves have higher frequencies,

$\omega \sim \omega_c(\mathcal{M}H/d)^{-2/65}$. The resulting IGW flux in waves that do not break is given by

$$F^T \sim F_{\rm conv}\mathcal{M}^{5/8}\left(\frac{d}{H}\right)^{3/8}, \tag{2.58}$$

$$F^L \sim F_{\rm conv}\mathcal{M}^{57/65}\left(\frac{d}{H}\right)^{8/65}. \tag{2.59}$$

These results are only valid if these waves see a smooth $N^2$ profile, i.e.,

$$\mathcal{M}H/d \ll 1. \tag{2.60}$$

If this condition is satisfied, then the IGW flux is larger than that predicted by the discontinuous result by $(\mathcal{M}H/d)^{-3/8}$ for the tanh profile and $(\mathcal{M}H/d)^{8/65}$ for the piecewise linear profile. Note that if $d/H \sim \mathcal{M}$, then the discontinuous and smooth $N^2$ limits give the same wave flux.

### 2.3.6 Wave Excitation Within the Overshoot Region

In the previous sections, we have considered the efficiency of IGW excitation by turbulent motions in the convection zone. However, convective overshoot and wave breaking produce turbulent motions within the radiative zone, near the radiative-convective interface. We can estimate the wave excitation within the radiative zone by convolving the Reynolds stress associated with turbulent motions due to convective overshoot with the appropriate Green's functions (see, e.g., Section 2.3.2).

The principal difficulty in calculating the wave generation in the overshoot region is in accurately describing the turbulent motions near the radiative-convective interface. Although convective overshoot has been investigated via simulations (e.g., Rogers & Glatzmaier 2005b), it is currently computationally infeasible to employ a realistic Mach number and interface stiffness. To roughly estimate the IGW generation due to turbulent motions within the overshoot region, we will assume that the motions can be decomposed into incoherent eddies with the statistical properties of Kolmogorov turbulence, as above. However, instead of taking the outer-scale of the cascade to be $H$, we will assume it is given by the size of the overshoot region $\sim d\log(N_0/\omega_c)$. We assume the typical velocity on this outer-scale is still $u_c$.

To predict where turbulent eddies can most effectively excite IGWs, it is helpful to consider the structure of the Green's function in the transition region. In Figure 2.2, we plot the eigenfunction $\eta_z^T(z)$ when $N^2$ is given by a tanh profile, with $\omega_c/N_0 = 10^{-3}$ and $d/H = 0.1$, as we might expect for the energy-bearing eddies in the Sun (see Section 2.6).

If an eddy is much larger than the local wavelength of the eigenfunction, then it will not be able to efficiently couple to the mode, as its convolution with the Green's function will to first order average out to zero. The most efficient wave excitation in the overshoot region for the example mode in Figure 2.2 will be for eddies filling the region between $z_i$ and the first zero of $\eta_z$; we define this distance to be $\Delta z_{\rm os}$. This eddy has size $\sim 0.3H$, smaller than the energy-bearing eddies of size $H$ in the convection zone.

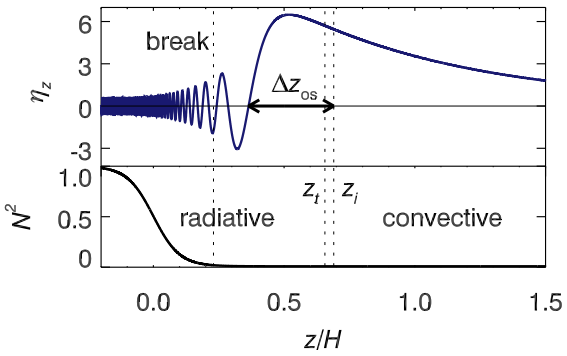


*Figure 2.2*: Representative eigenfunction and buoyancy frequency squared near the radiative-convective transition. See Appendix 2.A.1 for details on the calculation of the eigenfunction. The top panel shows the numerically calculated vertical perturbation eigenfunction normalized to have amplitude one in the radiative zone, for the parameters $\omega_c/N_0 = 10^{-3}$, $d/H = 0.1$, and $k_\perp H = 1$. The bottom panel shows the buoyancy frequency squared normalized to one in the radiative zone, which we have assumed follows a tanh profile. The vertical dotted lines, from left to right, correspond to the point at which $k_z\xi_z = 1$ where we expect the mode to break; the transition point $z_t$ (defined by $N^2 = \omega^2$), where this mode transitions from exponential to oscillatory behavior, and gives a typical amplitude of $\eta_z$ within the overshoot region; and the radiative-convective interface $z_i$ (defined by $N^2 = 0$). We have also labelled the distance between the radiative-convective interface and the first zero of the eigenfunction, $\Delta z_{\rm os}$. Turbulent eddies associated with convective overshoot cannot efficiently couple to this mode unless they have vertical size less or equal to $\Delta z_{\rm os}$.

Wave excitation in the overshoot region differs from wave excitation in the convection zone in several ways. First, because we assume the outer-scale of the turbulence is $d\log(N_0/\omega_c)$ instead of $H$, the turbulent velocities on any length scale $h < H$ are larger than the turbulent velocities on that length scale in the convection zone (see Section 2.3.4). We will assume that the excitation within the overshoot region is given by eddies with size at most $\Delta z_{\rm os}$. Thus, there are $\mathcal{A}\Delta z_{\rm os}/h^3$ eddies with size $h$ which excite IGWs with frequency $\omega$ (see eqn. 2.37 and accompanying text). Because the vertical length scale of $\eta_z$ is $\Delta z_{\rm os}$ in the overshoot region, the typical size of the Reynolds stress source term in eqn. 2.2 is

$$S \sim \frac{k k_\perp u_h^2}{\Delta z_{\rm os}}, \tag{2.61}$$

where $k$ is the total wavenumber defined by

$$k^2 = k_\perp^2 + \Delta z_{\rm os}^{-2}. \tag{2.62}$$

If $k_\perp \gg \Delta z_{\rm os}^{-1}$, then $k \approx k_\perp$, and if $\Delta z_{\rm os}^{-1} \gg k_\perp$ then $k \approx \Delta z_{\rm os}^{-1}$. When we derived the Green's functions above (e.g., Section 2.3.2), we took $\eta_z(z_i)$ as a typical value of $\eta_z$ in the convection zone. Here, we will take $\eta_z(z_t)$ as a typical value of $\eta_z$ in the overshoot region.

The exact form of the IGW wave flux depends on the background $N^2$ profile. As an illustrative example, we will sketch the results for the tanh profile. Broadly speaking, our estimates for wave excitation in the overshoot region are comparable to, but mostly smaller than, the wave excitation in the convection zone, except for high wavenumber waves with $k_\perp d \gg 1$ which are strongly suppressed in the convection zone. Note that these results are predicated on our assumptions regarding the turbulence within the overshoot region, which are uncertain. More detailed calculations likely require input from numerical simulations of plumes in the overshoot region.

For the tanh profile, the distance between the radiative-convective interface and the first zero of the eigenfunction, $\Delta z_{\rm os}$, is given by

$$\Delta z_{\rm os} \approx d\log\left(\frac{\omega}{\omega_c k_\perp d}\left(\frac{3\pi}{4} + \frac{\bar{\omega} k_\perp d}{\omega}\frac{\pi}{2}\right)\right). \tag{2.63}$$

We also have

$$\eta_z(z_t) \sim \left(\frac{N_0 k_\perp d}{\omega}\right)^{1/2}\left(\frac{\omega}{\bar{\omega}}\right)^{\bar{\omega} k_\perp d/\omega}\overline{J}, \tag{2.64}$$

where we use the shorthand

$$\overline{J} = J_{\bar{\omega} k_\perp d/\omega}\left(\frac{\bar{\omega} k_\perp d}{\omega}\right) \sim \begin{cases} 1 & \text{if } k_\perp d \ll 1, \\ 0.45(k_\perp d)^{-1/3} & \text{if } k_\perp d \gg 1. \end{cases} \tag{2.65}$$

Note that $\overline{J}$ falls off much less steeply for $k_\perp d \gg 1$ than the associated convection zone quantity, $J$ (eqn. 2.23).

Using these results, we can calculate the IGW power spectrum. Because the result depends sensitively on our assumptions regarding the turbulence within the overshoot region, we will only highlight the general properties of the excitation power spectrum. The IGW flux in the energy

bearing mode, which has $k_\perp \sim H^{-1}$ and $\omega \sim \omega_c$, is smaller in the overshoot region by a factor of $(\Delta z_{\rm os}/H)^2(H/(d\log(N_0/\omega_c))$; if we take $d/H \sim 0.1$ and $\omega_c/N_0 = 10^{-3}$ (see Section 2.6), this factor is $\sim 0.2$. For higher frequency waves with $\omega/\omega_c = (H/\Delta z_{\rm os})^{3/2}$, the excitation is larger in the overshoot region by a factor of $(H/(d\log(N_0/\omega_c))$, which is $\sim 1.5$ for the parameters given above. Excitation is significantly more efficient in the overshoot region for modes with $k_\perp d \gg 1$.

As pointed out in Section 2.3.5, there is a significant flux of IGWs which break in the radiative zone. The breaking occurs where the local $k_z$ becomes comparable to $\xi_z^{-1}$. As can be seen in Figure 2.2, this occurs when $k_z$ is large (for higher frequency waves, the breaking would occur for even larger $k_z$). If the turbulence associated with the wave breaking is isotropic, then only very small eddies would efficiently couple to the eigenfunction, leading to negligible wave excitation. However, the wave will be very anisotropic when it breaks, possibly leading to more efficient wave excitation. The details of wave generation by wave breaking are beyond the scope of this chapter.

## 2.4 Pressure Perturbation Balance

A more heuristic way to derive the IGW flux is to compare the pressure perturbation on either side of the radiative-convective boundary. This argument is not sufficiently precise to treat the smooth $N^2$ case—hence, we will assume $N^2$ is discontinuous, and thus that the pressure perturbation is continuous at the radiative-convective interface at $z = 0$. The pressure perturbation associated with a convective eddy with a turnover frequency $\omega_e$ and size $h$ is

$$\delta p_{\rm conv} \sim \rho_0 v_h^2 \sim \rho_0 u_c^2 (\omega_e/\omega_c)^{-1}. \tag{2.66}$$

The polarization condition (eqn. 2.8) relates the pressure perturbation in the radiative zone to the vertical displacement,

$$\delta p_{\rm rad} \sim \rho_0 \frac{N_0 \omega \xi_z}{k_\perp}. \tag{2.67}$$

We assume the convective eddy can only effectively couple to an IGW if the frequencies and horizontal wavelengths match, which requires $\omega_e \sim \omega$ and $k_\perp \sim h^{-1}$.

A large number of convective eddies contribute to driving a given standing IGW. This is particularly true for $k_\perp H \gg 1$ and/or $\omega \gg \omega_c$ because then small eddies with sizes $h \ll H$ are responsible for the driving. The number of eddies contributing to the excitation of a given standing wave is

$$\mathcal{N} \sim \frac{\mathcal{A} dz}{h^3} \sim (\mathcal{A} H^{-2})\ (k_\perp H)^{-1} \left(\frac{\omega}{\omega_c}\right)^{9/2} \tag{2.68}$$

where we have assumed $\omega \gtrsim \omega_c$ and that the excitation happens in a region with thickness $dz \sim k_\perp^{-1}$ (see also eqn. 2.37). Because an individual IGW is excited by many uncorrelated eddies, the effective pressure fluctuation driving a wave is reduced by a factor of $\sqrt{\mathcal{N}}$ relative to that given in eqn. 2.66.

When $N^2$ is discontinuous at $z = 0$ one of the boundary conditions is that $\delta p$ is continuous at $z = 0$, so that $\delta p_{\rm rad} \sim \delta p_{\rm conv}$. Using eqns. 2.66-2.68, we find that the amplitude of a mode with

frequency $\sim \omega$ and wavenumber $\sim k_\perp$ is

$$\xi_z^D \sim \frac{\delta p_{\rm conv} k_\perp}{\rho_0 N_0 \omega \sqrt{\mathcal{N}}} \sim H^2 k_\perp \frac{\omega_c^3}{N_0 \omega^2} \mathcal{N}^{-1/2}. \tag{2.69}$$

However, there are $\mathcal{A} k_\perp^2$ such modes in the domain (we have already implicitly summed over the vertical modes in deriving eqns. 2.66, 2.67), so the typical rms vertical displacement is

$$\xi_z^D \sim H^2 k_\perp \frac{\omega_c^3}{N_0 \omega^2} \sqrt{\frac{\mathcal{A} k_\perp^2}{\mathcal{N}}} \sim H \frac{\omega}{N_0} (k_\perp H)^{5/2} \left(\frac{\omega}{\omega_c}\right)^{-21/4}, \tag{2.70}$$

the same result as in the inhomogeneous wave equation calculation (eqn. 2.50).

## 2.5 Comparison with Previous Work

In this section, we discuss the relationship between our results and previous calculations in the literature. We begin with GK90, who only consider the discontinuous $N^2$ case. GK90 solved the fully compressible inhomogeneous wave equation by expanding the perturbation in terms of normal modes and then deriving an amplitude equation. This is equivalent to our Green's function method (see Appendix 2.C). Their end result is very similar to our own; for $k_\perp H \ll 1$ they find

$$\frac{dF}{d\log\omega\, d\log k_\perp} \sim \mathcal{M} \rho_0 u_c^3 (k_\perp H)^3 \left(\frac{\omega}{\omega_c}\right)^{-13/2} \quad \text{(GK90; eq. 73)} \tag{2.71}$$

This differs from our result (eqn. 2.40) by a factor of $k_\perp H$.[2] We arrive at a different IGW flux because in the Boussinesq approximation $\partial_z \xi_z \sim k_\perp \xi_z$, whereas for the fully compressible system, $\partial_z \xi_z \sim \xi_z / H$ when $k_\perp H \ll 1$. Accounting for both $k_\perp H \gtrsim 1$ and $k_\perp H \lesssim 1$, the correct scaling of the IGW flux with $k_\perp H$ is $F \sim (k_\perp H)^3 (1 + k_\perp H)$. This does not influence the flux of IGWs which do not break in our smooth $N^2$ calculations.

Because GK90 solve the fully compressible equations, they include multiple scale heights in their convection zone. They find that the most efficient excitation of waves with frequency $\omega$ is at the height where the turnover frequency of the energy bearing eddies is about equal to $\omega$. This effect would be straightforward to include in our model—one would need to derive a Green's function based on the fully compressible eigenfunctions, and then convolve with a vertically varying source term.

GLS91 use a pressure balance argument to study the discontinuous $N^2$ case. Their power spectrum agrees with eqn. 2.40 when $\omega \sim \omega_c$ and $k_\perp H \sim 1$, but not at higher frequencies or wave

[2] Although our final results are similar, there are some ambiguities in GK90's derivation. In deriving their eqn. 48 from their eqn. 45, GK90 appear to assume that the $\delta p$ are orthogonal under the weighting function $c^{-2}$ and that $\int dz \rho_0 c^{-2} |\delta p|^2 \sim 1$. Both of these are true for sound waves, the main focus of their paper. However, for IGWs, $\int dz \rho_0 c^{-2} |\delta p|^2 \sim \mathcal{M}^2$, and the $\delta p$ are only orthogonal under the weighting function 1 (see Appendix 2.C for further discussion on orthogonality).

numbers. They assume that the pressure perturbation in the convection zone equals the pressure perturbation in the radiative zone. They take $\delta p_{\rm conv} \sim \rho_0 u_h^2$, and $\delta p_{\rm rad} \sim \rho_0 (\omega \xi_\perp)^2$. This expression for the pressure perturbation in the radiative zone does not satisfy the polarization condition $\delta p_{\rm rad} \sim \rho_0 (N_0 \omega / k_\perp) \xi_z$ (eqn. 2.8), unless $\xi_\perp \sim k_\perp^{-1}$. Because many eddies contribute to the excitation of a single IGW mode, GLS91 also decrease their IGW amplitude by a factor of $1/\sqrt{\mathcal{N}}$. However, they only account for the incoherent sum of small eddies at the interface producing perturbations on large spatial scales. This gives $\mathcal{N}_{\rm GLS91} \sim (k_\perp h)^{-2}$, where $k_\perp h \ll 1$. In our analysis, we include eddies which are a distance $k_\perp^{-1}$ above the interface, and we take into account that IGWs excited in different parts of the domain incoherently interfere with each other as they propagate in the radiative zone. These additional effects yield $\mathcal{N} \sim \mathcal{A} k_\perp^{-1} / h^3$.

P81 uses two different techniques to calculate the IGW flux. The first uses a pressure balance argument. Press uses that $\delta p_{\rm conv} \sim \rho_0 u_h^2$, and that $\delta p_{\rm rad} \sim (\rho_0 N_0 \omega / k_\perp) \xi_z$, and that these pressure perturbations are about equal at the interface. Throughout his analysis, Press assumes $k_\perp^{-1} \sim h$. Thus, Press finds

$$\xi_z \sim \frac{(k_\perp h)^2}{k_z} \sim \frac{1}{k_z}, \qquad \text{(P81; eq. 75)} \tag{2.72}$$

This is the same result given by GLS91, and is consistent with our own assuming $k_\perp h \sim 1$. This is because $\mathcal{A} k_\perp^2 / \mathcal{N} \sim 1$ when $k_\perp h \sim 1$.

Press also derives this result more rigorously using the method of variation of parameters, which is equivalent to using a Green's function. In addition, Press considers the case in which $N^2$ is continuous at the interface. He only treats this case in the limit in which $\omega \sim N_0$, and finds

$$\xi_z \sim \frac{1}{k}, \qquad \text{(P81; eq. 88)} \tag{2.73}$$

the same result as eqn. 2.72. However, note that if $\omega \sim N_0$, then $N_0 k_\perp d / \omega \ll 1$, and the smooth result cannot be used (these waves see the interface as discontinuous). In addition, Press's use of standard WKB matching to treat the smooth $N^2$ profile is generally not applicable (see Appendix 2.A).

Finally, we consider the work of B09. In their paper, Belkacem et al. numerically calculate the eigenfunctions for a solar structure model, use a convection simulation to specify the source term, and solve an amplitude equation in the same way as GK90. It is unclear whether the $N^2$ profile in their solar structure model has a smooth transition between the radiative and convection zones—if their $N^2$ profile is discontinuous (Section 2.3.1) or has an abrupt transition (Appendix 2.B), they will derive different eigenfunctions than for a tanh profile (Appendix 2.A). These eigenfunctions will produce a smaller flux (eqns. 2.46, 2.59) than we predict for a very smooth radiative-convective transition (eqn. 2.58).

Another key difference is that Belkacem et al. use an eddy-time correlation function $\chi_{\boldsymbol{k}}(\omega)$, which in the notation of this chapter can be written as $\chi(\omega; \omega_e)$. This function describes how efficiently an eddy with size $1/k$ and turn-over frequency $\omega_e = u_{\boldsymbol{k}} k$ excites a wave with frequency $\omega$. Our analysis implicitly assumes $\chi(\omega; \omega_e) \sim \exp(-\omega^2/\omega_e^2)$. This Gaussian eddy-time correlation function implies that eddies with turn-over frequencies $\omega_e$ only excite waves with frequencies

$\omega$. However, the turbulence in the convection simulation in B09 is not well described by a Gaussian eddy-time correlation function. Instead, Belkacem et al. find that a Lorentzian distribution, $\chi(\omega;\omega_e) \sim (1 + 2(\omega/\omega_e)^2)^{-1}$, is more accurate. This indicates that waves with frequency $\omega$ can be excited by a broad range of eddies. In general, this makes wave excitation more efficient. It would be straightforward to generalize our results to this Lorentzian expression for $\chi(\omega;\omega_e)$.

## 2.6 Discussion & Conclusions

In this chapter we have calculated the excitation of internal gravity waves (IGW) by turbulent convection, motivated by the application to stellar convection. We assume that the source term exciting the IGWs can be modeled by Reynolds stresses associated with uncorrelated eddies in a Kolmogorov turbulent cascade. Our main results are the IGW fluxes, eqns. 2.46, 2.58 & 2.59. In particular, we predict a *larger wave flux than previous calculations for low frequency waves* which satisfy $N_0 k_\perp d/\omega \gg 1$, where $N_0$ is the buoyancy frequency in the radiative zone, $k_\perp$ and $\omega$ are the horizontal wavenumber and frequency of the IGW, respectively, and $d$ is the thickness of the transition region between the radiative and convection zones. We also reconcile somewhat disparate claims in the literature by showing that different methods, such as pressure balance arguments and solving the inhomogeneous wave equation, predict the same IGW power spectrum when using the same assumptions (Section 2.4).

An IGW with frequency $\omega$ sees the transition between the radiative and convection zones as discontinuous if $N_0 k_\perp d/\omega \ll 1$. In this case, the total flux is $F^D \sim F_{\rm conv}\,\mathcal{M}$ (eqn. 2.46), as derived in past work, where $F_{\rm conv}$ is the convective flux and $\mathcal{M}$ is the convective Mach number. The most efficiently excited waves have frequencies $\omega \sim \omega_c$, the eddy turn-over frequency of the largest turbulent eddies, and $k_\perp \sim H^{-1}$, the inverse of the pressure scale height. These most efficiently excited waves are marginally susceptible to wave breaking when they enter the radiative region.

If, however, the transition between radiative and convective regions is smooth (i.e., $N_0 k_\perp d/\omega \gg 1$), the problem becomes more complicated. The IGW flux depends on the structure of the buoyancy frequency $N^2(z)$ near the transition between the radiative and convective regions. We parameterize the transition using both a tanh profile, which is we believe represents the smoothest possible transition, and a piecewise linear profile, which is the most abrupt transition possible. These two examples bound the physical possibilities, and we expect real $N^2$ profiles in stars to be somewhere in between. The wave excitation is more efficient when $N^2$ is smooth because the IGW eigenfunctions change amplitude rapidly near the interface (as originally discussed by P81).

The total IGW fluxes for the tanh and piecewise linear profiles are $F^T \sim F_{\rm conv}(d/H) \gg F^D$ (eqn. 2.47), and $F^L \sim F_{\rm conv}\mathcal{M}^{2/3}(d/H)^{1/3} \gg F^D$ (eqn. 2.48), respectively. Again, the most efficiently excited waves have frequencies $\omega \sim \omega_c$ and $k_\perp \sim H^{-1}$. However, these waves are extremely prone to wave breaking, as $k_z\xi_z \gg 1$ in the radiative region (e.g., P81). These waves will break in the transition region between the radiative and convection zones. The flux of IGWs that are marginally susceptible to wave breaking (i.e., have $k_z\xi_z \sim 1$) is $F^T \sim F_{\rm conv}\mathcal{M}^{5/8}(d/H)^{3/8}$ (eqn. 2.58) and $F^L \sim F_{\rm conv}\mathcal{M}^{57/65}(d/H)^{8/65}$ (eqn. 2.59). This is larger than the discontinuous $N^2$ flux by $(\mathcal{M}H/d)^{-3/8}$ for the tanh profile, and by $(\mathcal{M}H/d)^{-8/65}$ for the piecewise linear profile.

In the Sun, $\omega_c \sim 10^{-3} N_0$, so $\mathcal{M} \sim 10^{-3}$ (e.g., Brown et al. 2012), and $d$ is estimated to be $\sim 0.1H$ (Christensen-Dalsgaard et al. 2011). IGWs produced by the energy bearing eddies have $N_0 k_\perp d/\omega \sim 10^2$, and thus the transition region must be treated as smooth. This suggests that the IGW flux in the Sun is somewhere between

$$F^T \sim F_{\rm conv} \mathcal{M}^{5/8} \left(\frac{d}{H}\right)^{3/8} \sim 5 \times 10^{-3}\ F_{\rm conv}, \tag{2.74}$$

$$F^L \sim F_{\rm conv} \mathcal{M}^{57/65} \left(\frac{d}{H}\right)^{8/65} \sim 2 \times 10^{-3}\ F_{\rm conv}, \tag{2.75}$$

about two to five times larger than the flux in the discontinuous $N^2$ case. In both cases, the flux is dominated by waves with frequencies near $\omega_c$, and wave numbers near $H^{-1}$.

We expect the $N^2$ profile in stars to be somewhere between the tanh profile and the piecewise linear profile. Real $N^2$ profiles are likely to have continuous derivatives, which precludes the piecewise linear profile. However, a piecewise linear function can be smoothed over an arbitrarily small length scale to form an infinitely differentiable function. Indeed, in simulations of penetrative convection, the time and spatially averaged $N^2$ profile appears similar to a tanh profile (e.g., Fig. 3 in Rogers et al. 2006 and Fig. 7 in Rogers & Glatzmaier 2005b). Specifically, these simulations find that $dN^2/dz|_{z_i} \ll N_0^2/d$, i.e., the slope of $N^2$ near $N^2 = 0$ is much less than in a simple piecewise linear model. This suggests that even if real $N^2$ profiles look closer to piecewise linear, the appropriate value for $d$ might be much larger than expected. For these reasons, we expect IGW generation in stars to more closely follow the tanh profile results than the piecewise linear results.

In this chapter we have also briefly considered IGW excitation due to turbulence driven by overshooting convective plumes (Section 2.3.6). These results depend sensitively on our assumptions regarding the turbulence within the overshoot region, which is poorly understood. However, our calculations suggest that IGW excitation is about as efficient in the overshoot region as in the convection zone. The flux in the energy-bearing mode, using solar parameters, is smaller in the overshoot region by a factor of 0.2, but the flux in some higher frequency modes can be slightly larger in the overshoot region. These higher frequency IGWs are the ones most likely to be observed in main sequence stars (e.g. Shiode et al. 2013), making it important to understand excitation in the overshoot region in more detail in future work. Modes which have $k_\perp d \gg 1$ are excited much more efficiently in the overshoot region than in the convection zone, where they are exponentially suppressed. It is difficult to excite the large, energy-bearing modes in the overshoot region, because $k_z$ is larger in the overshoot region than in the convection zone. Thus, only smaller eddies can couple to the large modes, decreasing the IGW flux produced in the overshoot region.

The increase in wave flux due to a smooth radiative-convective interface is only for waves with $N_0 k_\perp d/\omega \gg 1$, i.e., for low frequency waves. For certain applications (e.g., helioseismology), the flux of low frequency waves is unimportant. In particular, low frequency $g$-modes in the Sun and massive stars are strongly damped by radiative diffusion and are unlikely to be seen at the surface. Thus, the increase in wave flux we predict for low frequency waves does not change the expected amplitudes of potentially observable $g$-modes in main sequence stars.

However, low frequency waves are important for the angular momentum transport, mixing, and/or mass loss due to IGWs excited by stellar convection. For example, a larger IGW flux may

increase the predicted mass loss in the final stages of the life of a massive star (Quataert & Shiode 2012) and in Type Ia supernova progenitors (Piro 2011). This will be studied in detail in future work.

We have shown that there is significant wave breaking near the radiative-convective interface if $N^2$ is smooth. Wave breaking produces turbulence and can lead to additional IGW generation (Fritts et al. 2009). When $N^2$ is smooth, the flux in modes which are unstable to breaking is a significant fraction of $F_{\rm conv}$; thus the breaking process has the potential to excite a non-negligible flux of IGWs. In addition, wave breaking could redistribute energy in $(k_\perp, \omega)$ space, thus potentially modifying the IGW power spectrum from that calculated here.

In order to make a more accurate prediction of the wave flux and spectrum, one would need to use a stellar structure model with a realistic radiative-convective interface and a better representation of the convective turbulence, as in B09. Our results highlight the importance of adequately resolving the smooth transition between the radiative and convective regions in such calculations. A discontinuous or abrupt transition will give a different IGW flux than a smooth transition. We note that the radiative-convective transition seen in numerical simulations of penetrative convection is significantly smoother than the transition in typical 1D stellar models (e.g., Rogers et al. 2006).

Perhaps the most promising way to test the results of this chapter is through comparison with direct numerical simulations of a radiative zone adjacent to a convection zone (e.g., Rogers & Glatzmaier 2005a; Brun et al. 2011). Although such simulations typically require artificially high conduction in the radiative zone, and it is unclear how to best identify IGWs (Dintrans et al. 2005), this is probably the simplest system in which one can quantify the IGW flux generated by convection. We hope that analysis of such simulations can provide a quantitative test of the theory derived in this chapter in the near future.

## 2.A tanh Profile Eigenfunctions

We will derive the eigenfunctions for the equation

$$\frac{\partial^2}{\partial z^2}\xi_z + \left(\frac{N^2(z)}{\omega^2} - 1\right)k_\perp^2 \xi_z = 0, \tag{2.76}$$

where

$$N^2(z) = \frac{N_0^2 + \omega_c^2}{2}\left(\tanh\left(-\frac{z}{d}\right) + 1\right) - \omega_c^2. \tag{2.77}$$

The transition between oscillatory behavior and exponential behavior (where $N^2(z) = \omega^2$) is at $z_t$ given by

$$\frac{\omega^2 + \omega_c^2}{N_0^2 + \omega_c^2} \sim \exp\left(-2\frac{z_t}{d}\right). \tag{2.78}$$

The eigenfunction in the radiative zone is well approximated by the WKB solution,

$$\xi_z = B_1 \left(N_0 k_\perp/\omega\right)^{1/2} \; k_z(z)^{-1/2} \cos\left(\int dz k_z(z) + \pi/4\right)$$
$$+B_2 \left(N_0 k_\perp/\omega\right)^{1/2} \; k_z(z)^{-1/2} \sin\left(\int dz k_z(z) + \pi/4\right), \tag{2.79}$$

where we define the vertical wavenumber to be

$$k_z^2(z) = k_\perp^2 \left(N^2(z)/\omega^2 - 1\right). \tag{2.80}$$

Near $z_t$, the WKB solution in the radiative region diverges. We wish to derive a new set of functions which closely approximate the eigenfunctions for $z > z_t$.

In many problems, the WKB solutions near a turning point can be asymptotically matched onto Airy functions, which provide a connection between exponentially decaying and oscillatory WKB solutions. However, we cannot use this approach when $k_\perp d < 1$; in this parameter regime $k_z^2(z)$ cannot be well approximated as linear near $z_t$. Instead, we will show that when $k_\perp d < 1$ the eigenfunctions can be well approximated in terms of Bessel functions. Furthermore, these Bessel function solutions are also a good approximation when $k_\perp d \geq 1$.

To show this, first note that if $\exp(-2z/d) \ll 1$, we can approximate

$$N^2(z) \approx \left(N_0^2 + \omega_c^2\right) \exp\left(-\frac{2z}{d}\right) - \omega_c^2. \tag{2.81}$$

The solutions to the wave equation (eqn. 2.76) for this approximate $N^2(z)$ function are

$$\xi_z = C_1 J_{\bar{\omega} k_\perp d/\omega}\left(k_\perp d \frac{\sqrt{N_0^2 + \omega_c^2}}{\omega} \exp\left(-\frac{z}{d}\right)\right)$$
$$+C_2 Y_{\bar{\omega} k_\perp d/\omega}\left(k_\perp d \frac{\sqrt{N_0^2 + \omega_c^2}}{\omega} \exp\left(-\frac{z}{d}\right)\right), \tag{2.82}$$

where $J$ and $Y$ are the Bessel functions of the first and second kind, respectively. We have also defined $\bar{\omega}^2 = \omega^2 + \omega_c^2$, where $\bar{\omega}/\omega$ ranges between $\sqrt{2}$ and 1. These approximate the solution for large positive $z$. We can asymptotically match the Bessel functions onto the WKB solution in the radiative zone (eqn. 2.79). We will make use of the following asymptotic forms for $J$ and $Y$:

$$J_\alpha(x) \sim \frac{1}{\Gamma(\alpha+1)}\left(\frac{x}{2}\right)^\alpha, \tag{2.83}$$
$$Y_\alpha(x) \sim -\frac{\Gamma(\alpha)}{\pi}\left(\frac{2}{x}\right)^\alpha, \tag{2.84}$$

provided that $0 < x \ll \sqrt{\alpha + 1}$, and

$$J_\alpha(x) \sim \sqrt{\frac{2}{\pi x}} \cos\left(x - \frac{\alpha\pi}{2} - \frac{\pi}{4}\right), \tag{2.85}$$

$$Y_\alpha(x) \sim \sqrt{\frac{2}{\pi x}} \sin\left(x - \frac{\alpha\pi}{2} - \frac{\pi}{4}\right), \tag{2.86}$$

provided that $x \gg |\alpha^2 + 1/4|$.

We must consider two regimes, depending on the size of $k_\perp d$. First consider $k_\perp d \ll 1$. We can use the asymptotic formula for large arguments provided that

$$k_\perp d \frac{\sqrt{N_0^2 + \omega_c^2}}{\omega} \exp\left(-\frac{z}{d}\right) \gg \frac{1}{4}. \tag{2.87}$$

This constraint can be satisfied simultaneously with $\exp(-2z/d) \ll 1$, implying that the asymptotic form of the Bessel functions are good approximations to the eigenfunctions. If we approximate $k_z^2(z)$ as

$$k_z^2(z) \approx k_\perp^2 \frac{N_0^2 + \omega_c^2}{\omega^2} \exp\left(-\frac{2z}{d}\right), \tag{2.88}$$

we can approximate eqn. 2.82 by

$$\begin{aligned}\xi_z \approx C_1 \sqrt{\frac{2}{\pi d}} \left(k_z^2(z)\right)^{-1/4} \cos\left(-d\left(k_z^2(z)\right)^{1/2} + \frac{\pi\bar{\omega}k_\perp d}{2\omega} + \frac{\pi}{4}\right) \\ -C_2 \sqrt{\frac{2}{\pi d}} \left(k_z^2(z)\right)^{-1/4} \sin\left(-d\left(k_z^2(z)\right)^{1/2} + \frac{\pi\bar{\omega}k_\perp d}{2\omega} + \frac{\pi}{4}\right).\end{aligned} \tag{2.89}$$

This matches onto the WKB solution in the radiative region since $k_\perp d$ is small. The amplitudes are

$$C_1 = B_1 \left(\frac{\pi N_0 k_\perp d}{2\omega}\right)^{1/2}, \tag{2.90}$$

$$C_2 = -B_2 \left(\frac{\pi N_0 k_\perp d}{2\omega}\right)^{1/2}. \tag{2.91}$$

Now assume $k_\perp d \gg 1$. In this case, the asymptotic form of the Bessel functions for small argument is only valid when $\exp(-z/d) \gg 1$, i.e., for positions where the Bessel functions themselves are not a good approximation to the eigenfunctions ($N^2(z)$ cannot be simplified as in eqn. 2.81 if $\exp(-z/d) \gg 1$). However, in this limit we can use the WKB approximation in the convective region, and connect the two WKB solutions with Airy functions. Thus, in the convective region, we have

$$\begin{aligned}\xi_z \sim (B_1/2)\,(N_0 k_\perp/\omega)^{1/2} k_z(z)^{-1/2} \exp\left(-\int_{z_t}^{z} dz' |k_z(z')|\right) \\ +B_2 (N_0 k_\perp/\omega)^{1/2} k_z(z)^{-1/2} \exp\left(+\int_{z_t}^{z} dz' |k_z(z')|\right).\end{aligned} \tag{2.92}$$

For $z$ much larger than $z_t$, this becomes

$$\xi_z \sim \frac{B_1}{2}\left(\frac{N_0}{\omega}\right)^{1/2}\left(\frac{e}{2}\right)^{\bar{\omega}k_\perp d/\omega}\exp(-(z-z_t)k_\perp\bar{\omega}/\omega) + B_2\left(\frac{N_0}{\omega}\right)^{1/2}\left(\frac{2}{e}\right)^{\bar{\omega}k_\perp d/\omega}\exp(+(z-z_t)k_\perp\bar{\omega}/\omega), \tag{2.93}$$

For $z$ much larger than $z_t$, the Bessel functions are a good approximation to the eigenfunction. In the limit of large $z$, the Bessel functions become

$$\xi_z \sim C_1\left(\frac{1}{e\pi k_\perp d}\right)^{1/2}\left(\frac{e\bar{\omega}}{2\omega}\right)^{\bar{\omega}k_\perp d/\omega+1/2}\exp\left(-\frac{(z-z_t)k_\perp\bar{\omega}}{\omega}\right) - C_2\left(\frac{4}{e\pi k_\perp d}\right)^{1/2}\left(\frac{2\omega}{e\bar{\omega}}\right)^{\bar{\omega}k_\perp d/\omega+1/2}\exp\left(+\frac{(z-z_t)k_\perp\bar{\omega}}{\omega}\right). \tag{2.94}$$

Thus, the Bessel function solution matches onto the WKB solution in the convective region when

$$C_1 = B_1\left(\frac{\pi N_0 k_\perp d}{2\omega}\right)^{1/2}\left(\frac{\omega}{\bar{\omega}}\right)^{\bar{\omega}k_\perp d/\omega+1/2}, \tag{2.95}$$

$$C_2 = -B_2\left(\frac{\pi N_0 k_\perp d}{2\omega}\right)^{1/2}\left(\frac{\bar{\omega}}{\omega}\right)^{\bar{\omega}k_\perp d/\omega+1/2}. \tag{2.96}$$

Using eqns. 2.90, 2.91 & 2.95, 2.96, we can approximate $\xi_z$ by

$$\xi_z \sim B_1\left(\frac{\pi N_0 k_\perp d}{2\omega}\right)^{1/2}\left(\frac{\omega}{\bar{\omega}}\right)^{\bar{d}} J_{\bar{d}}\left(k_\perp d\frac{\sqrt{N_0^2+\omega_c^2}}{\omega}\exp\left(-\frac{z}{d}\right)\right) + B_2\left(\frac{\pi N_0 k_\perp d}{2\omega}\right)^{1/2}\left(\frac{\bar{\omega}}{\omega}\right)^{\bar{d}} Y_{\bar{d}}\left(k_\perp d\frac{\sqrt{N_0^2+\omega_c^2}}{\omega}\exp\left(-\frac{z}{d}\right)\right), \tag{2.97}$$

where we have defined $\bar{d} = \bar{\omega}k_\perp d/\omega$. This will be a good approximation for $\xi_z(z)$ as long as $\exp(-z/d) \ll 1$.

For the purposes of determining the convective excitation of IGWs, we are interested in evaluating $\xi_z$ between $z_i$ and $z_i + 1/k_\perp$, where $z_i$ is the location of the interface between the radiative and convective regions. Since

$$\frac{\omega_c^2}{N_0^2+\omega_c^2} \sim \exp\left(-2\frac{z_i}{d}\right), \tag{2.98}$$

the argument of the Bessel functions varies from $\omega_c k_\perp d/\omega$ to $\exp(-(k_\perp d)^{-1})\omega_c k_\perp d/\omega$. Within this range, the Bessel functions change by about a factor of $e$. It is thus within the accuracy of our

calculation to take $\xi_z$ to be about constant within this range: at $z = z_i$, we have that

$$\xi_z \sim B_1 \left(\frac{\pi N_0 k_\perp d}{2\omega}\right)^{1/2} \left(\frac{\omega}{\bar{\omega}}\right)^{\bar{\omega}k_\perp d/\omega} J_{\bar{\omega}k_\perp d/\omega}\left(\omega_c k_\perp d/\omega\right) + B_2 \left(\frac{\pi N_0 k_\perp d}{2\omega}\right)^{1/2} \left(\frac{\bar{\omega}}{\omega}\right)^{\bar{\omega}k_\perp d/\omega} Y_{\bar{\omega}k_\perp d/\omega}\left(\omega_c k_\perp d/\omega\right). \tag{2.99}$$

In evaluating eqn. 2.99, we need to calculate $J_x(xa)$, where $x = \bar{\omega}k_\perp d/\omega$, and $a = \omega_c/\bar{\omega} < 1/\sqrt{2}$. A good set of approximations for the Bessel functions for $x \ll 1$ and $x \gg 1$ is given in eqn. 2.23 of the main text (based on expansions of $J_x(xa)$ from Abramowitz & Stegun (2012)).

## 2.A.1 Numerical Verification

Here we will present numerical verification of our approximate solutions in the above subsection. We numerically integrated the homogeneous differential equation (eqn. 2.76) with $N^2$ given by eqn. 2.77 in Mathematica using the "ImplicitRungeKutta" method, and solved for a physical solution, satisfying $\xi_z \to 0$ as $z \to \infty$ (see Fig. 2.2 in the main text for a representative eigenfunction). We pick the right boundary to be a point $b$ deep within the convective region, where $k_z^2(b) = -k_\perp^2$, specify $\xi_z(b) = 1$, $\xi_z'(b) = -k_\perp$, and integrate $\xi_z$ leftwards into the radiative region. This ensures that $\xi_z$ satisfies the boundary condition $z \to +\infty$. We find that our calculations are insensitive to the value of $b$, provided that it is sufficiently larger than $z_t$.

To test the approximations described in the above subsection, we calculate the value of the physical eigenfunction at the interface between the radiative and convective regions $\xi_z(z_i)$. Because any multiple of the eigenfunction is also an eigenfunction, we normalize by $B_1$ (see eqn. 2.79), which is the amplitude of the oscillations deep in the radiative zone. Equation 2.99 predicts

$$\xi_z(z_i)/B_1 = \left(\frac{\pi N_0 k_\perp d}{2\omega}\right)^{1/2} \left(\frac{\omega}{\bar{\omega}}\right)^{\bar{\omega}k_\perp d/\omega} J_{\bar{\omega}k_\perp d/\omega}\left(k_\perp d \frac{\omega_c}{\omega}\right). \tag{2.100}$$

Our analysis is only valid if we are in the smooth $N^2$ limit, i.e., if $N_0 k_\perp d/\omega \gg 1$.

In Figure 2.3 we compare our numerical results to the analytic predictions. In Figure 2.3 (top panel) we vary $\omega/N_0$ for two different values of $k_\perp d$. The numerical solutions agree with our prediction when $N_0 k_\perp d/\omega \gg 1$. In the opposite limit, when $N_0 k_\perp d/\omega \ll 1$, we can treat $N^2$ as discontinuous, so $\xi_z$ is continuous across the interface, and $\xi_z(z_i)/B_1 = 1$, as is the case for the lower curve in Figure 2.3 (top panel). In Figure 2.3 (bottom panel) we vary $k_\perp d$, fixing $\omega/N_0 = 0.01$, for two values of $\omega_c/N_0$. In this case, we have $N_0 k_\perp d/\omega = 1$ when $k_\perp d = 0.01$. The normalized eigenfunctions approach one as $k_\perp d$ decreases, and the numerical solutions begin to deviate slightly from the analytic prediction near $k_\perp d = 0.01$. These results indicate that our analytic solution for $\xi_z$ near $z_i$ is accurate provided we are in the smooth $N^2$ limit. The numerical solutions also show how the eigenfunctions transition between the smooth and discontinuous $N^2$ limits.

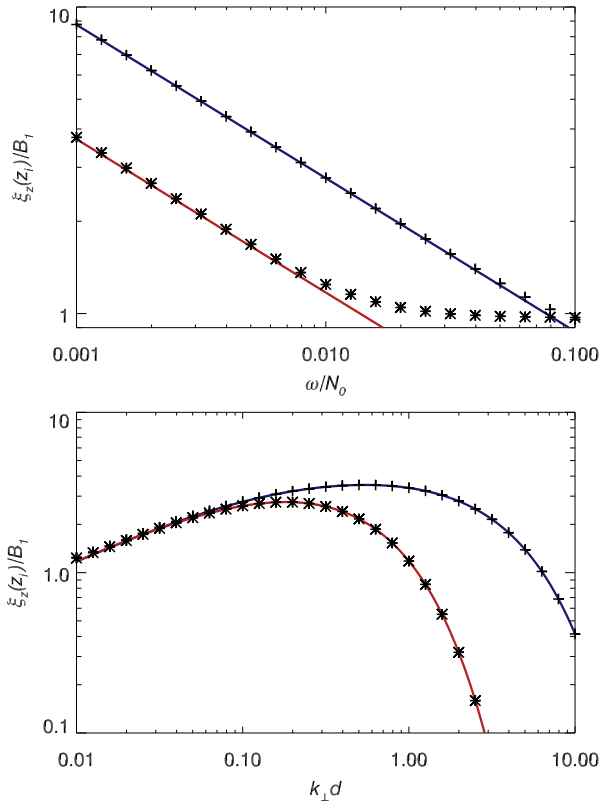


*Figure 2.3*: The normalized eigenfunction at the radiative-convective interface $z_i$. The symbols denote the numerical solution, and the lines denote the analytic prediction, eqn. 2.99. In the top panel, we vary $\omega/N_0$, fixing $\omega_c = \omega$. The blue line and crosses have $k_\perp d = 0.1$, and the red line and asterisks have $k_\perp d = 0.01$. The numerical solution matches the analytic prediction for smooth $N^2$ when $N_0 k_\perp d/\omega \gg 1$, and approaches one (the discontinuous $N^2$ solution) when $N_0 k_\perp d/\omega \ll 1$. In the bottom panel, we vary $k_\perp d$, fixing $\omega/N_0 = 0.01$ and setting $\omega_c/N_0 = 0.01$ (blue curve, crosses) or $\omega_c/N_0 = 0.002$ (red curve, asterisks). Again, there is good agreement between the numerical solution and the analytic prediction.

## 2.B Piecewise Linear $N^2$

In the limit of smooth $N^2$, the eigenfunctions, Green's function, and IGW flux all depend on the nature of the transition between radiative and convective regions. In this chapter, we focus on the case of a tanh profile (Appendix 2.A), as we think it is the best simple model of this transition region. However, in this appendix, we consider another analytically tractable transition—a piecewise linear $N^2$ profile. This is the most abrupt transition possible, and thus provides a lower limit to the efficiency of wave excitation for a "smooth" radiative-convective transition.

We assume $N^2$ is given by

$$N^2(z) = \begin{cases} N_0^2 & \text{if } z \le -d/2, \\ (N_0^2 - \omega_c^2)/2 - (N_0^2 + \omega_c^2)\,(z/d) & \text{if } -d/2 < z < d/2, \\ -\omega_c^2 & \text{if } z \ge d/2. \end{cases} \tag{2.101}$$

We have that $N^2(z) = \omega^2$ at the point

$$z_t = \frac{N_0^2 - 2\omega^2 - \omega_c^2}{N_0^2 + \omega_c^2}\left(\frac{d}{2}\right), \tag{2.102}$$

and that $N^2(z) = 0$ at

$$z_i = \frac{N_0^2 - \omega_c^2}{N_0^2 + \omega_c^2}\left(\frac{d}{2}\right). \tag{2.103}$$

The solutions in each region are

$$\xi_z = B_1 \cos(N_0 k_\perp (z + d/2)/\omega) + B_2 \sin(N_0 k_\perp (z + d/2)/\omega), \tag{2.104}$$
$$\text{for } z < -d/2,$$
$$\xi_z = C_1 \exp(-k_\perp (z - d/2)) + C_2 \exp(k_\perp (z - d/2)), \tag{2.105}$$
$$\text{for } z > d/2,$$
$$\xi_z = D_1 \mathrm{Ai}\left(K_1^{1/3}(z - z_t)\right) + D_2 \mathrm{Bi}\left(K_1^{1/3}(z - z_t)\right), \tag{2.106}$$
$$\text{for } -d/2 < z < d/2,$$

where Ai, Bi are the Airy functions of the first and second kind, and

$$K_1 = \left.\frac{dk_z^2(z)}{dz}\right|_{z_t} = \frac{k_\perp^2}{d}\frac{N_0^2 + \omega_c^2}{\omega^2}. \tag{2.107}$$

We can relate the six coefficients in eqns. 2.104-2.106 to one another using four boundary conditions: $\xi_z$ and $\xi_z'$ must be continuous at $z = \pm d/2$.

First consider the boundary at $z = +d/2$. The argument of the Airy functions at this boundary is

$$(k_\perp d)^{2/3}\left(\frac{\omega^2 + \omega_c^2}{\left(N_0^2 + \omega_c^2\right)^{2/3}(\omega^2)^{1/3}}\right) \sim \left(\frac{\omega^2 k_\perp d}{N_0^2}\right)^{2/3}. \tag{2.108}$$

This is much smaller than one unless $k_\perp d$ is extremely large. One can check that IGW excitation is exponentially suppressed when $\omega^2 k_\perp d/N_0^2 \gg 1$. Thus, we will assume that $\omega^2 k_\perp d/N_0^2 \ll 1$. This implies that $\mathrm{Ai}|_{d/2}, \mathrm{Bi}|_{d/2}, \mathrm{Ai}'|_{d/2}, \mathrm{Bi}'|_{d/2}$ are all of order one, where we have introduced the shorthand $\mathrm{Ai}|_z = \mathrm{Ai}(K_1^{1/3}(z - z_t))$, and similarly for the other functions. To order of magnitude, we have that

$$C_1 + C_2 \sim D_1 \mathrm{Ai}|_{d/2} + D_2 \mathrm{Bi}|_{d/2}, \tag{2.109}$$

and

$$C_1 - C_2 \sim \frac{K_1^{1/3}}{k_\perp} \left(D_1 \mathrm{Ai}'|_{d/2} + D_2 \mathrm{Bi}'|_{d/2}\right). \tag{2.110}$$

Notice that

$$K_1^{1/3}/k_\perp \sim \left(\frac{1}{k_\perp d} \frac{N_0^2 + \omega_c^2}{\omega^2}\right)^{1/3} \gg 1. \tag{2.111}$$

Now consider the boundary at $z = -d/2$. The argument of the Airy functions at this boundary is

$$(k_\perp d)^{2/3} \left(\frac{N_0^2 + \omega_c^2}{\omega^2}\right)^{1/3} \sim \left(\frac{N_0 k_\perp d}{\omega}\right)^{2/3} \gg 1, \tag{2.112}$$

where the last inequality follows from assuming that we are in the smooth $N^2$ limit. We thus have

$$\begin{aligned} \xi_z|_{-d/2} &\sim \left(\frac{N_0 k_\perp d}{\omega}\right)^{-1/6} \\ &\times \left[D_1 \cos\left(\frac{2}{3}\frac{N_0 k_\perp d}{\omega} + \frac{\pi}{4}\right) + D_2 \sin\left(\frac{2}{3}\frac{N_0 k_\perp d}{\omega} + \frac{\pi}{4}\right)\right], \end{aligned} \tag{2.113}$$

implying

$$B_1 \sim \left(\frac{N_0 k_\perp d}{\omega}\right)^{-1/6} \left(D_1 \cos(\phi) + D_2 \sin(\phi)\right), \tag{2.114}$$

where $\phi = (2/3)(N_0 k_\perp d/\omega) + \pi/4$. Similarly, by comparing $\xi_z'$ on either side of $z = -d/2$ we find

$$B_2 \sim \left(\frac{N_0 k_\perp d}{\omega}\right)^{-1/6} \left(-D_1 \sin(\phi) + D_2 \cos(\phi)\right). \tag{2.115}$$

Using these boundary conditions, we find that the physical eigenfunction is

$$\eta_z^L \sim \begin{cases} B_1 \cos\left(\frac{N_0 k_\perp (z+d/2)}{\omega}\right) + B_2 \sin\left(\frac{N_0 k_\perp (z+d/2)}{\omega}\right) & z < -d/2, \\ \tilde{B}_1 \left(\frac{N_0 k_\perp d}{\omega}\right)^{1/6} \exp(-k_\perp (z - d/2)) & z > d/2, \end{cases} \tag{2.116}$$

where we use *superscript L* to denote the eigenfunction for the *piecewise linear* $N^2$ profile, and $\tilde{B}_1 \sim B_2 \sim B_1$. An unphysical eigenfunction is

$$\xi_z^L \sim \begin{cases} B_2 \sin\left(\frac{N_0 k_\perp (z+d/2)}{\omega}\right) & z < -d/2, \\ \left(\frac{N_0 k_\perp d}{\omega}\right)^{-1/6} \frac{N_0}{\omega} \times & \\ \left(\tilde{B}_1 \exp(-k_\perp (z - d/2)) + \tilde{B}_2 \exp(k_\perp (z - d/2))\right) & z > d/2, \end{cases} \tag{2.117}$$

where $\tilde{B}_2 \sim \tilde{B}_1 \sim B_2$. Note that the constants $B_1, B_2$ in $\eta_z^L$ and $\tilde{B}_1, \tilde{B}_2$ in $\xi_z^L$ vary sinusoidally with $d$ (as well as the other parameters of the problem). Thus, although for most values of $d$ they are the same size, there are specific values of $d$ for which one term is much larger than the other.

The Green's function for $z < 0$ and $\zeta > 0$ is then

$$G^L(z,t,\zeta,\tau) \sim \sum_{\omega'} \frac{\omega' \sqrt{\rho_0}}{N_0 k_\perp^2 \sqrt{L}} \left(\frac{N_0 k_\perp d}{\omega'}\right)^{1/6} \times \xi_z^l(z;\omega') \exp(-k_\perp \zeta - i\omega'(t-\tau)). \tag{2.118}$$

## 2.C Mode Projection Formalism (GK90)

In GK90, an amplitude equation is derived by projecting the inhomogeneous wave equation onto specific modes. We will show that their approach gives the same result as our Green's function approach, provided that the correct inner product is used.

First start with the inhomogeneous equation for $\xi_z$ in the Boussinesq approximation

$$\boldsymbol{\nabla}^2 \frac{\partial^2}{\partial t^2} \xi_z + N^2 \boldsymbol{\nabla}_\perp^2 \xi_z = S. \tag{2.119}$$

In the mode projection formalism, we decompose $\xi_z$ as

$$\xi_z = \frac{1}{\sqrt{\mathcal{A}}} \sum_{\omega'} A(t;\omega') \eta_z(z;\omega') \exp(ik_x x + ik_y y - i\omega' t), \tag{2.120}$$

where $\eta_z(z;\omega')$ are the physical solutions satisfying the homogeneous wave equation. Substituting this into the inhomogeneous wave equation, multiplying by $\rho_0 \eta_z^*(z;\omega) \exp(-ik_x x - ik_y y + i\omega t)$ and integrating over $d^3x dt$, we find

$$|A(t;\omega)| = \frac{\omega}{2k_\perp^2 \sqrt{\mathcal{A}}} \int_{-\infty}^{t} d\tau \int dx dy \exp(-ik_x x - ik_y y + i\omega\tau) \times \int_{z_i}^{L} d\zeta \rho_0 S(x,y,\zeta,\tau) \eta_z^*(\zeta;\omega). \tag{2.121}$$

A crucial step in deriving this is using

$$\int dz \rho_0 \partial_z \eta_z(z;\omega') \partial_z \eta_z^*(z;\omega) = \delta_{\omega\omega'} \frac{k_\perp^2}{\omega\omega'}. \tag{2.122}$$

That is, the $\eta_z(z;\omega)$ are orthogonal with respect to the inner product $\langle a, b\rangle = \int dz \rho_0 \partial_z a \partial_z b^*$. This follows from our normalization equation (eqn. 2.27) and the polarization conditions (eqn. 2.7).

Although we use $\xi_z$ as our perturbation variable in this chapter, GK90 uses $\delta p$. The inhomogeneous wave equation for $\delta p$ in the Boussinesq approximation is

$$\boldsymbol{\nabla}^2 \frac{\partial^2}{\partial t^2} \delta p + N^2 \boldsymbol{\nabla}_\perp^2 \delta p = \bar{S}, \tag{2.123}$$

where $\bar{S} \sim (\rho_0\omega^2/k_\perp)\, S$. As above, we can decompose $\delta p$ into eigenmodes

$$\delta p = \frac{1}{\sqrt{\mathcal{A}}} \sum_{\omega'} A(t;\omega')\delta p(z;\omega') \exp(ik_x x + ik_y y - i\omega' t), \tag{2.124}$$

where $\delta p(z;\omega')$ are the physical solutions satisfying the homogeneous wave equation. When we put this into the inhomogeneous wave equation, multiply by $\rho_0 \delta p^*(z;\omega)\exp(-ik_x x - ik_y y + i\omega t)$, and integrate over $d^3x dt$, one might think that

$$\begin{aligned} |A(t;\omega)| \stackrel{?}{=} &\int_{-\infty}^{t} d\tau \int dx dy \exp(-ik_x x - ik_y y + i\omega t) \\ &\times \frac{1}{2\omega N_0^2 \rho_0^2 \sqrt{\mathcal{A}}} \int_{z_i}^{L} d\zeta \rho_0 \bar{S}(x,y,\zeta,\tau)\delta p^*(\zeta;\omega). \end{aligned} \tag{2.125}$$

Using $\delta p(\zeta;\omega) \sim (\rho_0\omega^2/k_\perp)\eta_z(\zeta;\omega)$ (eqn. 2.10), we see that this estimate of $|A(t;\omega)|$ differs from our estimate using $\xi_z$ (eqn. 2.121) by $\omega^2/N_0^2$. This leads to an underestimation of the flux in IGWs by $\sim \mathcal{M}^4$.

The discrepancy is due to using the incorrect inner product. Implicit in the derivation of eqn. 2.125 is the assumption that the $\delta p$ are orthogonal under the same inner product as the $\xi_z$, i.e.,

$$\int dz \rho_0 \partial_z \delta p(z;\omega')\partial_z \delta p^*(z;\omega) \stackrel{?}{=} \delta_{\omega\omega'}\, \rho_0^2 N_0^2. \tag{2.126}$$

However, one can check that the $\delta p$ are not orthogonal with respect to this inner product.[3] Rather, they are orthogonal with respect to $\langle a, b\rangle = \int dz \rho_0^{-1} a b^*$, i.e.,

$$\int dz \rho_0^{-1} \delta p(z;\omega')\delta p^*(z;\omega) = \delta_{\omega\omega'} \frac{\omega^2}{k_\perp^2}. \tag{2.127}$$

Thus, if we integrate the inhomogeneous wave equation twice with respect to $z$, multiply by $\rho_0^{-1}\delta p^*(z;\omega)\exp(-ik_x x - ik_y y + i\omega t)$, and integrate over $d^3x dt$, we get

$$\begin{aligned} |A(t;\omega)| = \frac{1}{2\omega^3 \sqrt{\mathcal{A}}} &\int_{-\infty}^{t} d\tau \int dx dy \exp(-ik_x x - ik_y y + i\omega t) \\ &\times \int_{z_i}^{L} d\zeta \rho_0^{-1} \bar{S}(x,y,\zeta,\tau)\delta p^*(\zeta;\omega). \end{aligned} \tag{2.128}$$

One can check that this is consistent with the calculation using $\xi_z$.

[3] Using the properties of Hermitian operators, one can show that the $\delta p$ IGW eigenfunctions of eqn. 2.123 are orthogonal under the inner product defined in eqn. 2.126. However, for the mode projection to be well defined, we must work in a complete basis, and the IGWs alone do not form a complete basis (in the convection zone). Our resolution of this apparent inconsistency is to note that the eigenfunctions of the full non-Boussinesq wave equation *do* form a complete basis (this includes sound waves in addition to IGWs). Moreover, one can show that the $\delta p$ eigenfunctions for the non-Boussinesq equations are only orthogonal under the inner product defined in eqn. 2.127.

If one uses a Green's function this issue of orthogonality under different inner products becomes trivial. Using the expansions in Sec. 2.3.3, we have

$$\frac{1}{\sqrt{\mathcal{A}}}\sum_{\omega'} A(t;\omega')\xi_{z,\mathrm{rad}}(z;\omega')\exp(ik_x x + ik_y y - i\omega' t) = \int_{-\infty}^{t} d\tau \int_{z_i}^{L} d\zeta \sum_{\omega'} \frac{\xi_{z,\mathrm{rad}}(z;\omega')\eta_z(\zeta;\omega')}{N_0 k_\perp L W(\zeta)} S\exp(-i\omega'(t-\tau)), \tag{2.129}$$

where $z < z_i$. Since both the left and right hand sides are in the span of $\{\xi_{z,\mathrm{rad}}\}_\omega$, we can simply use the inner product defined by

$$\langle \xi_{z,\mathrm{rad}}(z;\omega), \xi_{z,\mathrm{rad}}(z;\omega')\rangle = \delta_{\omega\omega'}. \tag{2.130}$$

Taking $\langle \xi_{z,\mathrm{rad}}(z;\omega), \cdot\rangle$ of eqn. 2.129, multiplying by $\exp(-ik_x x - ik_y y + i\omega t)$, and integrating in the horizontal directions, we get

$$A(t;\omega) = \frac{1}{\sqrt{\mathcal{A}}}\int_{-\infty}^{t} d\tau \int dxdy \int_{z_i}^{L} d\zeta \frac{1}{N_0 k_\perp L}\frac{\eta_z(\zeta;\omega)}{W(\zeta)} \times S(x,y,\zeta,\tau)\exp(-ik_x x - ik_y y + i\omega\tau). \tag{2.131}$$

This is eqn. 2.25, which can easily be manipulated into eqns. 2.29, 2.30 using the eigenfunctions. Note that we cannot use such an inner product in the mode decomposition formalism because we need to calculate terms like $\langle \delta p^*(\zeta;\omega), S(x,y,\zeta,\tau)\rangle$, and thus need an explicit formula for the inner product in terms of integrals over $\zeta$.

Finally, we will demonstrate that the mode projection formalism—when done correctly—and the Green's function formalism give the same result. Specifically, we will show that eqns. 2.121 and 2.131 are equivalent. First note that $W(\zeta)$ is a constant for our wave equation. We want to show that

$$\frac{1}{N_0 k_\perp L W} = \frac{\rho_0 \omega}{2k_\perp^2}. \tag{2.132}$$

We can evaluate $W$ in the radiative zone, and find

$$W = \frac{2N_0 k_\perp B_1 B_2}{\omega} \sim \frac{2k_\perp}{N_0 \omega L \rho_0}, \tag{2.133}$$

where we have used eqn. 2.28. This proves that the two formulations are equivalent.

# Chapter 3

# Conduction in Low Mach Number Flows: Linear & Weakly Nonlinear Regimes

## 3.1 Introduction

In astrophysical fluid dynamics, important processes routinely occur on very disparate length and time scales. Often, systems are driven on length scales orders of magnitude larger than the dissipation length scale. Astrophysicists have turned to numerical simulations to attempt to gain insight into these complicated, nonlinear systems. The inability to simulate the full range of spatial and temporal scales of a system has led to an ever-growing set of approximations, each of which has its own advantages and disadvantages.

For instance, the Navier–Stokes equations admit fast sound waves, which place strong restrictions on the time step of low Mach number flow when using an explicit time-integration scheme. However, by removing the sound waves from the system of fluid equations, a "sound-proof" set of equations need not resolve the fast sound time scale. These approximations range from the Boussinesq approximation, which assumes a constant density fluid; to the anelastic equations (Batchelor 1953; Ogura & Phillips 1962), which assume small thermodynamic perturbations about a background state; to the pseudo-incompressible equations (Durran 1989; Almgren et al. 2006), which allow for order unity thermodynamic perturbations in all quantities except the pressure. In Brown et al. (2012, hereafter B12) & Vasil et al. (2013, hereafter V13), we show that certain ideal formulations of the anelastic (e.g., Lantz 1992; Braginsky & Roberts 1995) and pseudo-incompressible (e.g., Durran 1989) equations reproduce internal gravity wave eigenfunctions and frequencies better than other formulations.

In this chapter, we turn to non-ideal behavior in these different equation sets, focusing on thermal conduction. Thermal conduction plays a role in damping internal gravity waves in the radiative zones of stars, and in setting the ferocity of convection (presumably related to the Rayleigh number, the ratio of driving to damping on large scales) in the convection zone of stars. However, thermal conduction in convection is most important on length scales much smaller than the driving scale. Thus, simulations either replace thermal conduction by algorithmic numerical conduction (e.g., the Athena code, Gardiner & Stone 2008; Stone et al. 2008), or an explicit conduction term which

acts on much larger length scales than in the physical system (e.g., Clune et al. 1999; Brun et al. 2004; Nonaka et al. 2010). Simulations with a reduced dynamic range are feasible with current computational resources.

When increasing the strength of thermal conduction (and similarly viscosity) to remove small scales from the system, one has to decide how to model the neglected small scales. One perspective is to run a direct numerical simulation (DNS), in which one uses the real damping processes that act on small scales. In this case, thermal conduction is modeled by Fourier's law of conduction (Fourier 1822),

$$\boldsymbol{Q}_T = -\kappa_T \boldsymbol{\nabla} T, \tag{3.1}$$

where $\boldsymbol{Q}$ is the heat flux, $\kappa_T$ is the conductivity, and $T$ is the temperature. This leads to temperature diffusion. However, it is computationally infeasible to use the microscopic diffusivities of many physical systems, so the diffusivities must be artificially increased. Thus, even a DNS employs a certain sub grid-scale (SGS) model of thermal conduction.

Another perspective is to use a SGS model to describe how the unresolved small scales influence thermal conduction. In this case, the unresolved *convective* heat flux can represented by a *conductive* heat flux. Although there are many SGS models (e.g., Lesieur 1990), one particularly popular model is the entropy diffusion model (used extensively in anelastic simulations, e.g., Clune et al. 1999, and also occasionally in fully compressible simulations, Chan & Sofia 1986, 1989),

$$\boldsymbol{Q}_S = -\kappa_S \boldsymbol{\nabla} S, \tag{3.2}$$

where $S$ is the entropy. In this chapter we compare the temperature diffusion and entropy diffusion models. Glatzmaier (1984) argues that the heat liberated by an eddy is given by the local entropy gradient. Braginsky & Roberts (1995) argue for the "engineering approach" that the flux of entropy should be linear in the entropy gradient (though not necessarily parallel to it). Practically speaking, perhaps the most important feature of entropy diffusion is that it does not require the calculation of the pressure perturbation, which can be advantageous for the anelastic equations.

Calkins et al. (2015) has recently calculated the onset of convection in anelastic simulations with either temperature diffusion or entropy diffusion, as well as in fully compressible Navier–Stokes simulations with temperature diffusion. They find that the anelastic and Navier–Stokes equations with temperature diffusion have almost identical behavior, provided the background entropy gradient is close to adiabatic. However, they only find "qualitative" rather than "quantitative" agreement between the temperature diffusion and entropy diffusion models.

The remainder of the chapter is structured as follows. First, in section 3.2.1, we show that entropy diffusion can lead to non-monotonicity of entropy. We state the various equations we use in section 3.2.2 (and describe their numerical implementation in appendix 3.D). Next we study thermal damping of internal gravity waves, both numerically (section 3.3) and analytically (section 3.4). In section 3.5 we describe convective steady states for each of our equation sets with either temperature or entropy diffusion. Finally, section 3.6 summarizes our results, discusses its connection with other work, and suggests future paths of inquiry.

## 3.2 Preliminaries

### 3.2.1 Motivation

A fundamental law of equilibrium statistical mechanics is that the total entropy of a closed system increases monotonically with time. This is encapsulated in the entropy equation for a fully compressible fluid,

$$\rho T \frac{dS}{dt} = \boldsymbol{\nabla} \cdot \kappa_T \boldsymbol{\nabla} T, \tag{3.3}$$

where $\rho, T, S$ are the density, temperature, and specific entropy of the fluid, and $d/dt = \partial_t + \boldsymbol{u} \cdot \boldsymbol{\nabla}$ denotes the material derivative where $\boldsymbol{u}$ is the fluid velocity. We will assume that the heat flux is proportional to $\boldsymbol{\nabla} X$, for $X = S, T$, and take $\kappa_X$ to be the constant of proportionality: $\boldsymbol{Q} = -\kappa_X \boldsymbol{\nabla} X$. For temperature diffusion ($X = T$), $\kappa_T$ is the conductivity. Using the continuity equation, this can be rewritten as

$$\frac{\partial \rho S}{\partial t} = -\boldsymbol{\nabla} \cdot \left[ \rho S \boldsymbol{u} - \frac{\kappa_T}{T} \boldsymbol{\nabla} T \right] + \kappa_T \frac{|\boldsymbol{\nabla} T|^2}{T^2}. \tag{3.4}$$

Assuming boundary conditions that ensure that the term in the total divergence on the RHS of equation 3.4 is zero on the boundaries (e.g., no penetration and no heat flux), the volume integral of equation 3.4 shows entropy increases monotonically with time,

$$\frac{\partial}{\partial t} \int_V \rho S \, dV = \int_V \kappa_T \frac{|\boldsymbol{\nabla} T|^2}{T^2} \, dV \geq 0. \tag{3.5}$$

However, if we instead use entropy diffusion in equation 3.3,

$$\rho T \frac{dS}{dt} = \boldsymbol{\nabla} \cdot \kappa_S \boldsymbol{\nabla} S, \tag{3.6}$$

the entropy per volume instead evolves according to

$$\frac{\partial \rho S}{\partial t} = -\boldsymbol{\nabla} \cdot \left[ \rho S \boldsymbol{u} - \frac{\kappa_S}{T} \boldsymbol{\nabla} S \right] + \kappa_S \frac{\boldsymbol{\nabla} S \cdot \boldsymbol{\nabla} T}{T^2}. \tag{3.7}$$

Again assuming boundary conditions such that the term in the total divergence is zero on the boundaries, the volume integral of equation 3.7 is

$$\frac{\partial}{\partial t} \int_V \rho S \, dV = \int_V \kappa_S \frac{\boldsymbol{\nabla} S \cdot \boldsymbol{\nabla} T}{T^2} \, dV. \tag{3.8}$$

The $\boldsymbol{\nabla} S \cdot \boldsymbol{\nabla} T$ term is not positive definite, so there is no guarantee that entropy increases monotonically with time. Although we focus only on thermal diffusion and entropy diffusion, the only heat flux which will monotonically increase entropy is proportional to $\boldsymbol{\nabla} T$ (Landau & Lifshitz 2013)[1].

[1]The most general heat flux which monotonically increases entropy is $Q_i \sim -M_{ij} \partial T / \partial x_j$, where $M_{ij}$ is a symmetric rank-2 tensor. For instance, in relatively collisionless plasmas, the heat flux is carried by electrons which follow magnetic field lines. Thus, the heat flux is in the direction of the local magnetic field, $\boldsymbol{Q} \sim -\boldsymbol{b}\boldsymbol{b} \cdot \boldsymbol{\nabla} T$, where $\boldsymbol{b}$ is the unit vector in the direction of the magnetic field (e.g., Spitzer 2013; Balbus 2000). In this case, $M_{ij} = b_i b_j$ is symmetric, so entropy will increase monotonically.

This chapter investigates the effects of this modification of the second law of thermodynamics for linear waves and weakly nonlinear convective equilibria.

### 3.2.2 Model Equations

We break the thermodynamic variables into background and fluctuating parts, e.g., $S = \overline{S} + S'$. The background fields are time independent and satisfy hydrostatic and thermal equilibrium,

$$\boldsymbol{\nabla}\overline{P} = \boldsymbol{g}\overline{\rho}, \tag{3.9}$$
$$\boldsymbol{\nabla}\cdot\overline{\boldsymbol{Q}} = 0, \tag{3.10}$$

where $P$ is the pressure, $\boldsymbol{g}$ is the gravitational acceleration, and $\boldsymbol{Q}$ is the heat flux. This chapter studies the effects of varying the form of $\boldsymbol{Q}$. To simplify the problem, we assume the fluid to be an ideal gas with constant ratio of specific heats $\gamma$. We make extensive use of the linearized thermodynamic relations,

$$\frac{P'}{\overline{P}} = \frac{\rho'}{\overline{\rho}} + \frac{T'}{\overline{T}}, \tag{3.11}$$
$$\frac{S'}{C_P} = \frac{P'}{\gamma\overline{P}} - \frac{\rho'}{\overline{\rho}}. \tag{3.12}$$

#### Full Compressible Equations

The fully compressible (FC) equations are

$$\rho\left(\partial_t\boldsymbol{u} + \boldsymbol{u}\cdot\boldsymbol{\nabla}\boldsymbol{u}\right) + \boldsymbol{\nabla}P = \boldsymbol{g}\rho - \boldsymbol{\nabla}\cdot\Pi, \tag{3.13}$$
$$\partial_t\rho + \boldsymbol{u}\cdot\boldsymbol{\nabla}\rho + \rho\boldsymbol{\nabla}\cdot\boldsymbol{u} = 0, \tag{3.14}$$
$$\partial_t S + \boldsymbol{u}\cdot\boldsymbol{\nabla}S = -\frac{1}{\rho T}\boldsymbol{\nabla}\cdot\boldsymbol{Q} - \frac{1}{\rho T}\Pi_{ij}\partial_{x_i}u_j, \tag{3.15}$$

where repeated indices are summed over, $\Pi_{ij}$ is the viscous stress tensor,

$$\Pi_{ij} = -\mu\left(\partial_{x_i}u_j + \partial_{x_j}u_i - \frac{2}{3}\delta_{ij}\boldsymbol{\nabla}\cdot\boldsymbol{u}\right), \tag{3.16}$$

and $\delta_{ij}$ is the Kronecker delta.

To study waves, we solve the linearized, inviscid, FC equations. We subtract off hydrostatic equilibrium and thermal equilibrium (equations 3.9 & 3.10), and linearize the thermodynamic variables (equations 3.11 & 3.12). To use notation consistent with B12, we pick $S'$ and $\varpi' = P'/\overline{\rho}$

as our thermodynamic variables. Then the FC equations take the form

$$\partial_t \boldsymbol{u} + \boldsymbol{\nabla}\varpi' - \varpi'\boldsymbol{\nabla}\left(\frac{\overline{S}}{C_P}\right) = -\boldsymbol{g}\frac{S'}{C_P}, \tag{3.17}$$

$$\partial_t S' + \boldsymbol{u}\cdot\boldsymbol{\nabla}\overline{S} = -\frac{1}{\overline{\rho}\overline{T}}\boldsymbol{\nabla}\cdot\boldsymbol{Q}', \tag{3.18}$$

$$\boldsymbol{u}\cdot\boldsymbol{\nabla}\left(\frac{\overline{S}}{C_P}\right) + \boldsymbol{u}\cdot\boldsymbol{\nabla}\log\overline{\rho} + \boldsymbol{\nabla}\cdot\boldsymbol{u} = -\frac{1}{\overline{c_s}^2}\partial_t\varpi' - \frac{1}{\overline{\rho}\overline{T}C_P}\boldsymbol{\nabla}\cdot\boldsymbol{Q}', \tag{3.19}$$

where $\overline{c_s}^2 = \gamma\overline{P}/\overline{\rho}$ is the adiabatic sound speed. These equations support sound waves because they include the $\partial_t\varpi'/\overline{c_s}^2$ term in equation 3.19. Also note that thermal conduction appears in both thermodynamic equations.

### Pseudo-Incompressible Equations

The pseudo-incompressible (PI) equations (see V13) assume that sound waves rapidly equilibrate pressure fluctuations, so that pressure fluctuations are small ($O(\overline{P}\mathrm{Ma}^2)$, where Ma is the Mach number) when averaged over a sound crossing time. The pressure fluctuations must be retained in the pressure gradient term in the momentum equation to keep the flow from building large pressure fluctuations, but must be dropped everywhere else. The PI equations are

$$\rho\left(\partial_t\boldsymbol{u} + \boldsymbol{u}\cdot\boldsymbol{\nabla}\boldsymbol{u}\right) + \overline{\beta}\boldsymbol{\nabla}\left(\frac{\pi'}{\overline{\beta}}\right) = \boldsymbol{g}\rho' - \boldsymbol{\nabla}\cdot\Pi, \tag{3.20}$$

$$\partial_t\rho + \boldsymbol{u}\cdot\boldsymbol{\nabla}\rho + \rho\boldsymbol{\nabla}\cdot\boldsymbol{u} = 0, \tag{3.21}$$

$$\boldsymbol{u}\cdot\boldsymbol{\nabla}\overline{P} + \gamma\overline{P}\boldsymbol{\nabla}\cdot\boldsymbol{u} = -\frac{1}{C_V}\boldsymbol{\nabla}\cdot\boldsymbol{Q} - \frac{1}{C_V}\Pi_{ij}\partial_{x_i}u_j, \tag{3.22}$$

where $\overline{\beta} = \overline{P}^{1/\gamma}$ and $C_V$ is the specific heat at constant volume. In the equation of state, $P$ is replaced by $\overline{P}$, i.e., $T = T(\rho, \overline{P})$ and $s = s(\rho, \overline{P})$. The variable $\pi'$ is the $O(\overline{P}\mathrm{Ma}^2)$ correction to the background pressure.

The linearized, inviscid PI equations are very closely related to the linearized, inviscid FC

equations: the $\varpi'$ term in equation 3.19 is dropped,

$$\partial_t \boldsymbol{u} + \boldsymbol{\nabla}\varpi' - \varpi'\boldsymbol{\nabla}\left(\frac{\overline{S}}{C_P}\right) = -\boldsymbol{g}\frac{S'}{C_P}, \tag{3.23}$$

$$\partial_t S' + \boldsymbol{u}\cdot\boldsymbol{\nabla}\overline{S} = -\frac{1}{\overline{\rho}\overline{T}}\boldsymbol{\nabla}\cdot\boldsymbol{Q}', \tag{3.24}$$

$$\boldsymbol{u}\cdot\boldsymbol{\nabla}\left(\frac{\overline{S}}{C_P}\right) + \boldsymbol{u}\cdot\boldsymbol{\nabla}\log\overline{\rho} + \boldsymbol{\nabla}\cdot\boldsymbol{u} = -\frac{1}{\overline{\rho}\overline{T}C_P}\boldsymbol{\nabla}\cdot\boldsymbol{Q}', \tag{3.25}$$

and the PI equations use the modified equation of state (compare to equation 3.12),

$$\frac{S'}{C_P} = -\frac{\rho'}{\overline{\rho}}. \tag{3.26}$$

### Anelastic Equations

The anelastic (AN) equations (see B12) were first used in astrophysics to remove sound waves from convection simulations. Efficient convection almost entirely erases an unstable entropy gradient. Thus, the anelastic equations are derived in the limit that $\boldsymbol{\nabla}(\overline{S}/C_P) \sim O(\mathrm{Ma}^2/L_z) \ll 1$, where $L_z$ is the vertical (or radial) length of the convection zone. Furthermore, the AN equations assume that all thermodynamic fluctuations are $O(\mathrm{Ma}^2)$, and thus the linearized thermodynamic relations (equations 3.11 & 3.12) can be used. The AN equations can be written

$$\partial_t \boldsymbol{u} + \boldsymbol{u}\cdot\boldsymbol{\nabla}\boldsymbol{u} + \boldsymbol{\nabla}\varpi' = -\boldsymbol{g}\frac{S'}{C_P} - \boldsymbol{\nabla}\cdot\Pi, \tag{3.27}$$

$$\partial_t S' + \boldsymbol{u}\cdot\boldsymbol{\nabla}S' + \boldsymbol{u}\cdot\boldsymbol{\nabla}\overline{S} = -\frac{1}{\overline{\rho}\overline{T}}\boldsymbol{\nabla}\cdot\boldsymbol{Q}' - \frac{1}{\overline{\rho}\overline{T}}\Pi_{ij}\partial_{x_i}u_j, \tag{3.28}$$

$$\boldsymbol{u}\cdot\boldsymbol{\nabla}\log\overline{\rho} + \boldsymbol{\nabla}\cdot\boldsymbol{u} = 0. \tag{3.29}$$

Having already linearized the thermodynamics, these equations bear striking similarity to the linearized FC & PI equations, although they include the nonlinear $\boldsymbol{u}\cdot\boldsymbol{\nabla}\boldsymbol{u}$ and $\boldsymbol{u}\cdot\boldsymbol{\nabla}S'$ terms. The $\boldsymbol{\nabla}\overline{S}/C_P$ terms in the momentum equation and constraint equation have been dropped, as well as the heating terms on the RHS of the constraint equation (which can be justified by dimensional analysis).

The linearized, inviscid AN equations are

$$\partial_t \boldsymbol{u} + \boldsymbol{\nabla}\varpi' = -\boldsymbol{g}\frac{S'}{C_P}, \tag{3.30}$$

$$\partial_t S' + \boldsymbol{u}\cdot\boldsymbol{\nabla}\overline{S} = -\frac{1}{\overline{\rho}\overline{T}}\boldsymbol{\nabla}\cdot\boldsymbol{Q}' \tag{3.31}$$

$$\boldsymbol{u}\cdot\boldsymbol{\nabla}\log\overline{\rho} + \boldsymbol{\nabla}\cdot\boldsymbol{u} = 0. \tag{3.32}$$

## 3.3 Linear Wave Modes: Numerics

We solve for internal gravity wave (IGW) eigenmodes with different thermal conduction models using Dedalus[2] (Burns et al. 2014). Dedalus is a general framework for studying partial differential equations, including eigenvalue problems, boundary value problems, and initial value problems (i.e., simulations). It uses the $\tau$ spectral method to solve nearly arbitrary equation sets including algebraic constraints and complex boundary conditions. This flexibility allows us to specify the linear eigenvalue problem for IGWs in all three equation sets discussed above, with different thermal conduction models, all within the same code. In all cases, we use a 2D Cartesian domain with a Fourier grid in the horizontal ($x$) and a Chebyshev grid in the vertical ($z$) directions. In section 3.5, we use Dedalus to evolve the nonlinear versions of these equation sets in time, and in appendix 3.D we specify the exact equations as entered into the code.

We use a polytrope background field:

$$\overline{T} = T_0 \frac{L_z + H - z}{H}, \tag{3.33}$$

$$\overline{\rho} = \rho_0 \left( \frac{L_z + H - z}{H} \right)^n, \tag{3.34}$$

$$\overline{P} = P_0 \left( \frac{L_z + H - z}{H} \right)^{n+1}, \tag{3.35}$$

where $\rho_0, T_0, P_0$ are constants satisfying $\rho_0 T_0 = P_0$, $L_z$ is the box height, and $H$ is the local scale height at the top of the box. $n$ is the polytropic index, and satisfies $\boldsymbol{g} = -T_0(n+1)/H\boldsymbol{e}_z$. We nondimensionalize the system by setting $\rho_0 = T_0 = P_0 = H = 1$. We take $\gamma = 5/3$, so any $n > 1.5$ corresponds to stable stratification—we pick $n = 2$. We take the box size to be $(L_x, L_z) = (78.3, 26.1)$, which corresponds to $\approx 6.6$ density scale heights, the number of density scale heights in the solar radiative zone. The vertical resolution is typically 128 grid points & modes (no dealiasing is needed for linear calculations).

This background satisfies thermal equilibrium only when using temperature diffusion with a constant $\overline{\kappa_T}$. We assume that the background fields and the perturbation fields conduct heat differently. Various authors (e.g., Braginsky & Roberts 1995; Clune et al. 1999; Jones et al. 2009) have argued that the heat conduction acting on the perturbation fields is actually a SGS effect from unresolved turbulent motions, and thus different from the microphysical heat conduction acting on the background fields. In our calculations, the background fields conduct heat using temperature diffusion with a constant $\overline{\kappa_T}$; we use different choices for the conduction model for the perturbation fields. The equations remain consistent as the perturbations never feed back onto the background fields.

The wave perturbations evolve according to the equations described in sections 3.2.2–3.2.2. We use two forms for $\boldsymbol{Q}'$,

$$\boldsymbol{Q}'_T = -\chi_T \overline{\rho} \boldsymbol{\nabla} T', \tag{3.36}$$

$$\boldsymbol{Q}'_S = -\chi_S \overline{\rho}\,\overline{T} \boldsymbol{\nabla} \frac{S'}{C_P}, \tag{3.37}$$

[2]For more information and links to the source code, see `dedalus-project.org`.

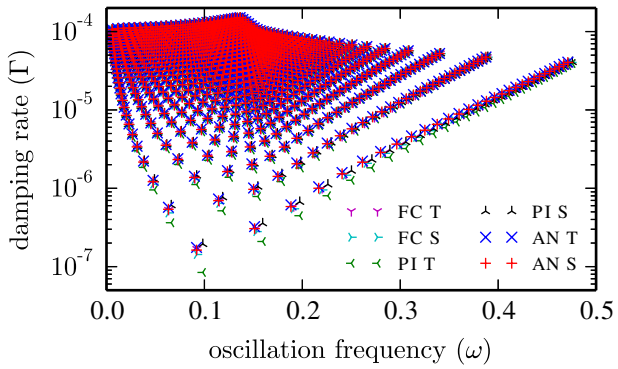


*Figure 3.1*: Damping rates and oscillation frequencies of gravity wave modes of the FC, PI, and AN equations, using either $T$- or $S$- diffusion. The first thirty radial and horizontal modes are shown for each equation set. The modes with lowest mode number are at the bottom of the plot. Moving up and to the left corresponds to increasing the vertical mode number ($m$), and moving up and to the right corresponds to increasing the horizontal mode number ($n$).

where $\chi_T = \chi_S = 10^{-5}$ are taken to be constant, which implies a constant diffusivity throughout the domain. Such a small diffusivity ensures all modes are weakly damped. We will refer to these two thermal conduction models as $T$-diffusion and $S$-diffusion. Our boundary conditions are $w = 0$ (the vertical velocity) and $Q_z = 0$ at $z = 0$ and $z = L_z$, and periodic in the horizontal direction. The eigenmodes depend on horizontal and vertical wave numbers. We define the $(n, m)$ mode to be the mode with horizontal wavenumber $k_x = 2\pi n/L_x$, and $m$ extrema in the vertical direction (with vertical wavenumber defined as $k_z = 2\pi m/L_z$). $n$ and $m$ are the mode's horizontal and vertical mode number respectively. The total wavenumber of a mode is $k = \sqrt{k_x^2 + k_z^2}$.

The linear modes vary in time as $\exp(-i\omega t - \Gamma t)$, where $\omega$ is the oscillation frequency and $\Gamma$ is the damping rate. Figure 3.1 shows eigenvalues of the different equation sets with either $T$- or $S$- diffusion. To ensure the accuracy of the eigenvalues, we compare the damping rate, $\Gamma$, to the analytic expression of the damping rate given in equations 3.47 & 3.48 and the analogous expressions in appendices 3.A & 3.B. In all cases, the discrepancy is less than 1%, and typically is less than 0.01%.

The damping rates and oscillation frequencies match very well for the different equation sets and conduction models, particularly for large $kH$. For small $kH$, there are some discrepancies in both damping rates and oscillation frequencies. Figure 3.2 shows the percent error in the oscillation frequency and damping rate with respect to the eigenvalues of the FC equations with $T$-diffusion. The relative errors are plotted for the modes $(1, m)$, with $m$ ranging from one to thirty.

The largest errors in damping rate occur for the PI equations with $T$-diffusion, where the damping rate is underestimated by half for the $(1, 1)$ mode—interestingly, the PI equations with $S$-diffusion seem to agree more closely with the true damping rate. This may be because the PI equations do not use the full linearized equation of state to calculate the temperature (compare

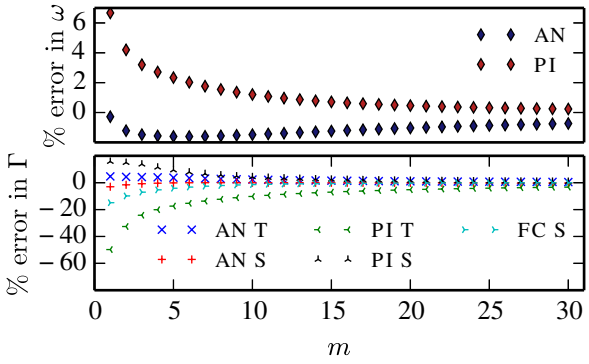


*Figure 3.2*: Percent error in oscillation frequencies and damping rates between different equations and thermal conduction models and the FC equations with $T$-diffusion, e.g., $(\omega_{AN;T} - \omega_{FC;T})/\omega_{FC;T}$. The modes have $n = 1$, but with varying vertical mode number $m$—these are the modes with the largest errors. The percent error in oscillation frequency depends only on the equation set, not on the model of thermal conduction.

equations 3.11 & 3.12 to equation 3.26).

For the AN equations, the error in damping rate is always less than twenty percent. For all the models described here, the relative errors are less than 10% for mode numbers greater than ten (or four if we neglect the PI equations with $T$-diffusion). The FC equations with $S$-diffusion have relative errors of less than 1% for mode numbers greater than eleven, whereas the AN equations with $S$-diffusion have relative errors of less than 1% for mode numbers greater than nine (which is much better than the AN equations with $T$-diffusion).

Overall, there is little difference in the damping rates between $T$-diffusion and $S$-diffusion. We will explain this by studying the linear problem analytically in section 3.4.

In addition to errors in damping rates, there are also small (several percent) errors in oscillation frequency associated with using different equation sets. Although the PI equations have the largest relative error (almost seven percent) for the $(1, 1)$ mode, the AN equations have more persistent errors as the vertical mode number increases.

As shown in B12 & V13, the ideal linear eigenvalues differ more among the different equation sets in spherical geometry than in plane parallel geometry. Furthermore, in spherical geometry, the eigenfunctions also differ between equation sets. These suggest that differences between damping rates (which depend on the eigenfunctions, as shown in section 3.4) and oscillation frequencies will be larger in spherical geometry than in plane parallel geometry. However, the differences in spherical geometry will also become small for $kH \gg 1$.

Nonlinear damping can also be an important damping mechanism, especially for modes with low linear damping rates. Via nonlinear interactions, low wavenumber gravity waves can couple and transfer energy to higher wavenumber gravity waves (e.g., Weinberg et al. 2012). The energy in high wavenumber modes can then be damped via dissipative effects, e.g., thermal conduction.

Thus, it is possible that the low wavenumber modes which have the largest discrepancies in linear damping rates could still be damped at the correct rate in fully nonlinear simulations—if the damping is dominated by nonlinearities.

## 3.4 Linear Wave Modes: Analytics

In the previous section, we demonstrated that IGWs have very similar damping rates with either $T$- or $S$- diffusion. To better understand why this is the case, we study the linear IGW problem analytically. We use different approximations to render the problem tractable. First, we derive the eigenvalue equation in the large wavenumber limit. Second, we assume dissipation is weak, and derive an expression for the damping rate. The numerical results presented above in section 3.3 satisfy this weak dissipation assumption. We only include the details of the calculations for the AN equations; the (similar) main results for the FC & PI equations can be found in appendices 3.A & 3.B, respectively. We find that $T$- and $S$- diffusion give the same damping rate because $T$ and $S$ are approximately proportional to one another in the large wavenumber limit.

### 3.4.1 Large Wavenumber Limit

We derive the eigenvalue equation for the AN equation (see appendices 3.A & 3.B for the eigenvalue equations for the FC and PI equations, respectively), for both $T$- and $S$- diffusion. In the limit of $kH \gg 1$, these eigenvalue equations are equivalent, which implies that $T$- and $S$- diffusion will give the same eigenfunctions and eigenvalues.

To simplify the expressions, we will drop all terms with derivatives on background quantities, which are order $(kH)^{-1} \ll 1$. In this limit, the eigenvalue equation for the AN equations using $T$-diffusion is

$$\left[1 + \frac{i\overline{\kappa_T}}{\overline{\rho} C_P \omega}\nabla^2 + \frac{i\overline{\kappa_T}}{\overline{\rho} C_P \omega}\frac{\gamma - 1}{\gamma}\frac{g}{\overline{T}}\partial_z\right]\nabla^2 w = -\frac{k_\perp^2 \overline{N}^2}{\omega^2} w, \tag{3.38}$$

where $\overline{N}^2 = g\partial_z \overline{S}/C_P$ is the squared buoyancy (Brunt–Väisälä) frequency. The eigenvalue equation using $S$- diffusion is

$$\left[1 + \frac{i\overline{\kappa_S}}{\overline{\rho}\,\overline{T}\omega}\nabla^2\right]\nabla^2 w = -\frac{k_\perp^2 \overline{N}^2}{\omega^2} w. \tag{3.39}$$

Note that $\nabla^2 \gg (g/\overline{T})\partial_z$, because $g/\overline{T} \sim H^{-1}$. Thus, the two eigenvalue equations are equivalent under the identification $\overline{\kappa_S} = \overline{\kappa_T}\,\overline{T}/C_P$. This shows that $T$- and $S$- diffusion will have the same eigenfunctions and eigenvalues in the limit of large $kH$, as can be seen in figure 3.1.

### 3.4.2 Damping Rates & the Weak Dissipation Limit

By manipulating the equations of motion, the damping rate can be expressed as a ratio of volume averages of the eigenfunctions. In this section, we focus on the AN equations; the analogous results for FC & PI equations are in appendices 3.A & 3.B, respectively. Dotting the momentum equation (3.30) with $\overline{\rho}\boldsymbol{u}$ gives an energy equation,

$$\partial_t\left(\frac{1}{2}\overline{\rho}|\boldsymbol{u}|^2\right) = \boldsymbol{\nabla}\cdot(\overline{\rho}\boldsymbol{u}\varpi') + \frac{g\overline{\rho}}{C_P}S'w. \tag{3.40}$$

The vertical velocity is given by the entropy equation (3.31),

$$w = -\frac{\partial_t S'}{\partial_z \overline{S}} - \frac{1}{\overline{\rho}\overline{T}\partial_z\overline{S}}\boldsymbol{\nabla}\cdot\boldsymbol{Q}'. \tag{3.41}$$

Using this relation, we can rewrite the energy equation in the form

$$\partial_t E + \boldsymbol{\nabla}\cdot\boldsymbol{F} = -\theta, \tag{3.42}$$

where

$$E = \frac{1}{2}\overline{\rho}|\boldsymbol{u}|^2 + \frac{1}{2}\frac{g\overline{\rho}}{C_P}\left(\partial_z\overline{S}\right)^{-1}S'^2, \tag{3.43}$$

$$\boldsymbol{F} = \overline{\rho}\boldsymbol{u}\varpi' + \frac{g}{\overline{T}\partial_z\overline{S}}\frac{S'}{C_P}\boldsymbol{Q}, \tag{3.44}$$

$$\theta = -\boldsymbol{Q}\cdot\boldsymbol{\nabla}\left(\frac{g}{\overline{T}\partial_z\overline{S}}\frac{S'}{C_P}\right), \tag{3.45}$$

are the wave energy, the energy flux, and the change of wave energy due to thermal conduction, respectively.

The damping rate (of the perturbations) $\Gamma$ is

$$\Gamma = \frac{\langle\theta\rangle}{2\langle E\rangle}, \tag{3.46}$$

where $\langle\cdot\rangle$ denotes a volume average. For $T$- and $S$- diffusion, the expressions for $\theta$ are

$$\theta_T = \overline{\kappa_T}\boldsymbol{\nabla}\left(\frac{gS'}{C_P\overline{T}\partial_z\overline{S}}\right)\cdot\boldsymbol{\nabla}\left(\overline{T}\frac{S'}{C_P} + \frac{\gamma-1}{\gamma}\varpi'\right), \tag{3.47}$$

$$\theta_S = \overline{\kappa_S}\boldsymbol{\nabla}\left(\frac{gS'}{C_P\overline{T}\partial_z\overline{S}}\right)\cdot\boldsymbol{\nabla}S'. \tag{3.48}$$

These expressions follow directly from the equations of motion and contain no approximations. They are used to check the numeric damping rates calculated in figure 3.1.

In equation 3.47, we have rewritten $T'$ as a function of $S'$ and $\varpi'$ using the linearized equation of state (equations 3.11 & 3.12). $T'$ is comprised of a part that is proportional to $S'$ and a part that

is proportional to $\varpi'$. We will show below that if $kH \gg 1$, the $\varpi'$ term is much smaller than the $S'$ term. Thus, $T'$ and $S'$ are well aligned, and give the same damping rate.

If we assume $g/(\overline{T}\partial_z\overline{S})$ is constant (as is the case for a plane-parallel polytrope atmosphere), then $\theta_S$ is positive definite, proving there are no overstable modes with $S$-diffusion. By contrast, $\theta_T$ cannot be shown to be positive definite, leaving open the possibility of overstable IGWs. For the FC & PI equations, neither $\theta_S$ nor $\theta_T$ can be shown to be positive definite (see appendices 3.A & 3.B). Lou (1990) searched extensively for overstable IGWs using the FC equations with temperature diffusion in a polytrope atmosphere, but found none. We also have not found any overstable IGWs.

Next we calculate the relative sizes of the different terms in equations 3.47 & 3.48 by solving for the eigenfunctions. To simplify the calculation, we will use the weak dissipation limit. For sufficiently small dissipation, the eigenfunctions are very well approximated by the ideal eigenfunctions, which can be solved for analytically if we use the WKB approximation (assuming $kH \gg 1$).

The ideal eigenvalue equation (see, e.g., B12) is

$$\omega^2\left(k_\perp^2 - \partial_z^2\right)w - \omega^2\partial_z\left((\partial_z \log\overline{\rho})w\right) = \overline{N}^2 k_\perp^2 w, \tag{3.49}$$

The lowest order WKB approximation to the solution is

$$w \approx \frac{A}{\sqrt{\overline{\rho}k_z}}\exp\left(-\int_{z_0}^{z} k_z(z')\,dz'\right), \tag{3.50}$$

where $A = w(z_0)\sqrt{\overline{\rho}k_z}$ is the amplitude and $k_z(z)$ satisfies

$$k_z^2 = k_\perp^2\left(\frac{\overline{N}^2}{\omega^2} - 1\right). \tag{3.51}$$

The entropy and pressure perturbations are related to one another via

$$S' = -i\frac{w\partial_z\overline{S}}{\omega}, \tag{3.52}$$

$$\varpi' = \frac{i\omega}{k_\perp^2}\left(\partial_z w + w\partial_z\log\overline{\rho}\right) \approx \frac{\omega^2 - \overline{N}^2}{\omega k_z}w, \tag{3.53}$$

where the approximation is dropping terms of order $(k_z H)^{-1}$ and smaller.

The ratio of the $S'$ contribution to $\theta_T$ to the $\varpi'$ contribution to $\theta_T$ is

$$\left|\frac{\overline{T}S'}{C_P}\right|\left|\frac{\varpi'}{\gamma}\right|^{-1} = \left(\frac{\overline{c_s}^2 k_\perp^2}{\omega^2}\right)\left(\frac{\partial_z\left(\frac{\overline{S}}{C_P}\right)}{k_z}\right). \tag{3.54}$$

Using that $\overline{c_s}^2 \sim \overline{N}^2 H^2$ and that $\omega \le \overline{N}$ for gravity waves, one can show that this ratio is of order $kH$, which is assumed to be much larger than one[3]. Thus, $\theta_T$ is dominated by entropy diffusion.

[3]Near the cores of stars we instead have $\overline{c_s}^2 \sim \overline{N}^2 r^2$. In this case, the ratio is of order $k_z r \gg 1$.

Furthermore, the leading order (in $k_z H$) expressions for $\varpi'$ and $S'$ are out of phase, so upon volume integration, cross terms such as $\boldsymbol{\nabla}\varpi' \cdot \boldsymbol{\nabla} S'$ are smaller than the leading order term $|\boldsymbol{\nabla} S'|^2$ by $(k_z H)^{-2}$. Similarly, the volume average of terms like $S' \boldsymbol{\nabla}\overline{T} \cdot \boldsymbol{\nabla} S'$ are also of order $(k_z H)^{-2}$ because $S'$ and $\partial_z S'$ are out of phase to leading order.

The leading order contributions to $\theta_T$ and $\theta_S$ are

$$\theta_T \approx \frac{g\overline{\kappa_T}}{C_P^2 \partial_z \overline{S}} |\boldsymbol{\nabla} S'|^2 , \tag{3.55}$$

$$\theta_S \approx \frac{g\overline{\kappa_S}}{C_P \overline{T} \partial_z \overline{S}} |\boldsymbol{\nabla} S'|^2 . \tag{3.56}$$

For perturbations with $k_z H \gg 1$, we have that thermal diffusion and entropy diffusion are equivalent under the identification $\overline{\kappa_S} = \overline{\kappa_T}\,\overline{T}/C_P$.

A key assumption in the above argument is that $\omega \leq \overline{N}$, which was used to show that the ratio of the $S'$ contribution to $\theta_T$ to the $\varpi'$ contribution to $\theta_T$ (equation 3.54) is order $kH \gg 1$. This is satisfied for gravity waves, but not for sound waves. For sound waves, the first term on the RHS of equation 3.54 is order one, so the $\varpi'$ contribution to $\theta_T$ is *larger* than the $S'$ contribution to $\theta_T$ by order $kH$. This suggests that $T$- and $S$- diffusion give very different results for sound waves (see appendix 3.C).

### 3.4.3 FC & PI equations

Although we have only shown the results for the AN equations, similar results hold for the FC & PI equations. In appendix 3.A, we show that for the FC equations the $T$- and $S$- diffusion eigenvalue equations reduce to one another if we assume $kH \gg 1$ *and* that damping is weak. Unlike the AN equations, there are differences between $T$- and $S$- diffusion for strongly damped modes (which are no longer waves). We also derive analytic expressions for the damping rates.

In appendix 3.B, we carry out the same analysis as above for the PI equations. It is straightforward to show that the PI equations will give the same damping rates using either $T$- or $S$- diffusion, assuming $kH \gg 1$. This is because $T$- and $S$- diffusion in the PI equations only differ by a factor of $\overline{T}$, which can be absorbed into $\overline{\kappa}$ in the limit $kH \gg 1$.

## 3.5 Steady Nonlinear Convective Solutions

We present nonlinear simulations of convection using the FC, PI, & AN equations with both $T$- and $S$- diffusion models. Near the onset of convection, unstable modes saturate as steady convective rolls. For sufficiently small driving (Ra), these are stable. However, as the driving of the system (Ra) increases, the rolls become unstable to oscillatory motions. The accuracy of the stable convection states is an important nonlinear test of the different equation sets and thermal conduction models. We restrict our investigation to 2D because the convection solutions are more susceptible to oscillatory motions in 3D.

We solve for convective steady states using Dedalus by integrating the equations of motion forward in time. The background state is a polytrope (equations 3.33-3.35) with polytropic index

$$n = 1.5 - \epsilon. \tag{3.57}$$

Recall that an adiabatic background has $n = 1.5$; by setting $n$ slightly smaller than 1.5, we are imposing a slightly superadiabatic stratification. We set $\epsilon = 10^{-5}$. This implies the background entropy gradient is

$$\partial_z\left(\frac{\overline{S}}{C_P}\right) = -\frac{\epsilon}{L_z + 1 - z}. \tag{3.58}$$

Mixing length theory suggests that the Mach number squared is proportional to the entropy gradient, so we choose to fix the entropy gradient in order to fix the Mach number. The convective steady states described in this chapter have Mach numbers of about $10^{-3}$.

As above, we assume that the perturbation fields conduct heat differently from the background fields. To satisfy thermal equilibrium, we assume that the background fields are acted upon by temperature diffusion with a constant $\overline{\kappa_T}$. Again, it is consistent to use a different conduction model for the perturbations, provided that the perturbation fields never feed back onto the background fields.

For the perturbation fields, we use a constant diffusivity $\chi$,

$$\boldsymbol{Q}'_T = -\chi_T \rho \boldsymbol{\nabla} T', \tag{3.59}$$

$$\boldsymbol{Q}'_S = -\chi_S \rho \overline{T} \boldsymbol{\nabla} \frac{S'}{C_P}. \tag{3.60}$$

Similarly, for viscosity, we use a constant diffusivity $\nu$,

$$\mu = \rho\nu. \tag{3.61}$$

In both cases, $\rho$ is replaced by $\overline{\rho}$ for the AN equations.

We can now define the Rayleigh number: the ratio of driving to dissipation in the system,

$$\mathrm{Ra} = \frac{\Delta\overline{S}\, g L_z^3}{C_P \nu \chi}, \tag{3.62}$$

where $\Delta\overline{S}/C_P = \epsilon \log(L_z + 1)$ is the entropy jump across the domain (recall that in our non-dimensionalization $g = n + 1$). Below, we study how convective steady states vary as a function of Ra. All simulations have $\mathrm{Pr} = \nu/\chi = 1$. We find that when $\mathrm{Pr} < 1$, there are very few convective steady states, as the convection is strongly susceptible to oscillatory instabilities. Thus, to compare the convection for $\mathrm{Pr} < 1$ in different models would require a study of the (temporal) statistical properties of the flow, which is beyond the scope of this chapter. However, we do not expect our results to change qualitatively for low Pr convection (note that our linear wave results are at a $\mathrm{Pr} = 0$). Recent work by Calkins et al. (2014) shows substantial differences between the onset

of rapidly-rotating convection in the FC and AN equations with Pr $<$ 1. However, there is no indication that such differences persist in the non-rotating limit.

For simulations at fixed Ra with Pr $>$ 1, we do find some convective steady states. In this case viscosity is a more dominant damping mechanism than thermal conduction, so we expect smaller differences between the conduction models. For sufficiently high Pr, the thermal boundary layers become unstable and there are no longer steady convective states.

To maintain the background entropy gradient, we use the boundary conditions $S' = 0$ on the top and bottom. Our other boundary conditions are $\boldsymbol{u} = 0$ on the top and bottom, and all variables are periodic in the horizontal direction. Our vertical boundary conditions are artificial—a more physical boundary condition would be to add stably stratified layers on either side of the convection zone. We do not implement this type of background state because it greatly complicates the problem. In real systems, convective plumes penetrate into the stably stratified regions, which in turn affects the whole convective state. However, for stiff interfaces, the penetration is small (Rogers & Glatzmaier 2005a; Brummell et al. 2002), suggesting that there might not be significant differences between a convective–radiative boundary and a solid wall.

Note that $w = 0$ on the top and bottom are redundant equations for the horizontally averaged ($n = 0$) mode when using the AN equations. Furthermore, there is a gauge freedom in the definition of $\pi'$ for the PI equations and $\varpi'$ for the AN equations. Thus, when using the PI or AN equations, for the horizontally averaged mode ($n = 0$), we use the boundary conditions $w = 0$ on the bottom boundary, and $\pi'$ or $\varpi' = 0$ on the top boundary. In fact, the PI equations are inconsistent for $\boldsymbol{u} = 0$ on the top and bottom, and periodic in the horizontal directions. This can be verified by integrating the constraint equation—the LHS is zero for these boundary conditions, but the RHS is generally non-zero. Physically, this is because heating causes the fluid to expand, so there must be a way for the fluid to leave the box.

The simulations are run in a box with aspect ratio three, i.e., $L_x = 3L_z$, with three different heights: $L_z = 10, 30, 100$. This corresponds to about $3, 5, 7$ density scale heights, respectively. We use a resolution of 96 grid points in each direction, with 2/3 dealiasing (i.e., 64 modes). We represent the solution as a Fourier series in the $x$ direction and a Chebyshev series in the $z$ direction. For several cases, we ran with a resolution of 192 grid points (128 modes) in each direction, and found that the results were virtually identical. To timestep the equations, we use an implicit–explicit, SBDF2 method (Ascher et al. 1995; Wang & Ruuth 2008). The time step is given by the smaller of the $0.3\boldsymbol{u} \cdot \Delta\boldsymbol{x}^{-1}$, where $\Delta\boldsymbol{x}^{-1}$ is the inverse local grid spacing, and $5 \times 10^{-5}\ \chi/L_z^2$. The latter time scale almost always sets the time step, and was chosen to ensure the simulations are extremely well resolved temporally.

We do not base our CFL on the sound speed for the simulations of the FC equations (all equation sets are solved with the same time step size). This is because we are able to implicitly timestep the sound waves, and are thus not limited by the sound speed CFL. A similar approach was used by Viallet et al. (2011, 2013), although they use an iterative, nonlinear implicit solve, whereas we only treat linear terms implicitly. This is significant as the typical rms Mach number of our nonlinear strongly stratified convection is $10^{-3}$, and explicitly following the sound waves would increase the computation cost by approximately $10^3$, which would make low-Mach number convection prohibitively expensive to simulate. The greater complexity of the FC equations (see appendix 3.D)

makes them a factor of two slower than the AN simulations (the PI equations run at about the same speed as the FC equations).

The simulations are initialized by random, low amplitude density perturbations (FC & PI equations) or entropy perturbations (AN equations). The system is evolved forward in time until a convective steady state is found. We assume we are in a steady state if the volume-averaged kinetic energy changes by less than a factor of $10^{-4}$ over one thousand iterations. For higher Ra, we sometimes did not find a steady state solution—instead, the system evolves into a periodically varying state. In this case, we restart the simulation with different random initial conditions. If several different random initial conditions lead to periodically varying states, we stop the search. Of course, our limited search of initial conditions does not prove that there is no steady state for certain parameters, but it does suggest that the basin of attraction of a hypothetical steady state solution is likely limited.

Sometimes we found multiple convective steady states. The most common state consists of two pairs of convective rolls. To facilitate comparison between different states, we only consider steady states consisting of two pairs of convective rolls (see figures 3.3 & 3.4). If we changed the horizontal periodicity of the domain, the aspect ratio of the convective cells would likely stay close to the aspect ratio described here, as this is the preferred aspect ratio of the system.

Figure 3.3 plots several convective steady states using the FC equations. We do not calculate the critical Rayleigh number for the onset of instability, but expect similar values for all equation sets. We vary Ra in panels (*a*)–(*c*), fixing $L_z = 100$ and using $T$-diffusion. As Ra increases, the boundary layer at the top of the domain decreases in size, and the flow and entropy become more asymmetric. The down flows between convective rolls become sharper as Ra increases. At Ra somewhat higher than $4 \times 10^5$, the down flows become so sharp that they become unstable to an oscillatory instability.

In the bulk of the fluid, up flows carry high entropy fluid, and down flows carry low entropy fluid. However, things become more complicated in the upper boundary layer for highly stratified convection, where sometimes high entropy fluid rests above down flows, and low entropy fluid rests above up flows (see panel (*a*)). This could be due to two effects. First, viscous heating increases the entropy near the down flows where there are sharp velocity gradients. Second, due to large stratification near the top of the box, up flows produce diverging flows which dilute entropy, whereas down flows produce converging flows which concentrate entropy.

Panels (*d*)–(*f*) show convective steady states with $S$-diffusion for fixed $\mathrm{Ra} = 4 \times 10^4$, but with increasing $L_z$. Increasing $L_z$ also decreases the thickness of the boundary layer (relative to the box size) at the top of the domain. Note that as $L_z$ increases, the critical Ra (at which convection begins) also increases. Thus, $\mathrm{Ra}/\mathrm{Ra}_c$ is decreasing with increasing $L_z$, which might naively lead one to believe that the boundary layer thickness should *increase* with increasing $L_z$, the opposite of what we find.

However, these convective steady states are in some ways consistent with the idea that convection only occurs on the local scale height. In all cases, the local scale height is $\approx 1$ near the top of the box. This corresponds to $1/10$ of the domain when $L_z = 10$, but $1/100$ of the domain when $L_z = 100$. Thus, the upper boundary layer might be influenced by the local scale height near the top of the box. The convective rolls also seem to have size $\sim L_z$, which is similar to the scale

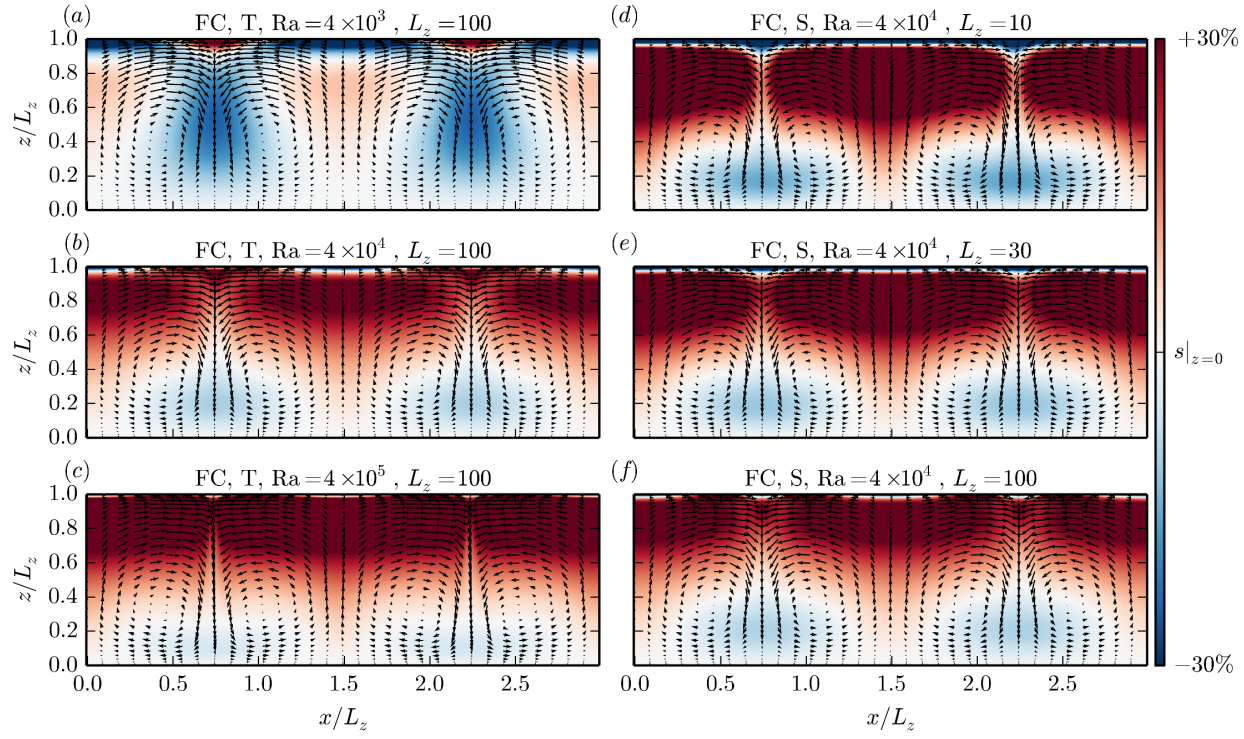


*Figure 3.3*: Steady convective states for the FC equations, varying the thermal conduction model, Ra, and $L_z$. The color depicts the total entropy (background plus perturbations)—the convective layers are fairly adiabatic, with a sharp boundary layer at the top of the domain. The color scale is chosen such that white corresponds to the entropy at the bottom of the domain, and red (blue) is thirty percent greater (less) than this value. The arrows show the flow field. Each steady state is labelled with the equation set, the thermal conduction model ($T$- or $S$- diffusion), the Rayleigh number, and the vertical length of the domain. In all cases, $L_x = 3L_z$. Panels (*a*)–(*c*) use the FC equations with $T$-diffusion and $L_z = 100$, but vary Ra from $4\times10^3$ to $4\times10^5$. Panels (*d*)–(*f*) use the FC equations with $S$-diffusion and Ra = $4\times10^4$, but vary $L_z$ from 10 to 100.

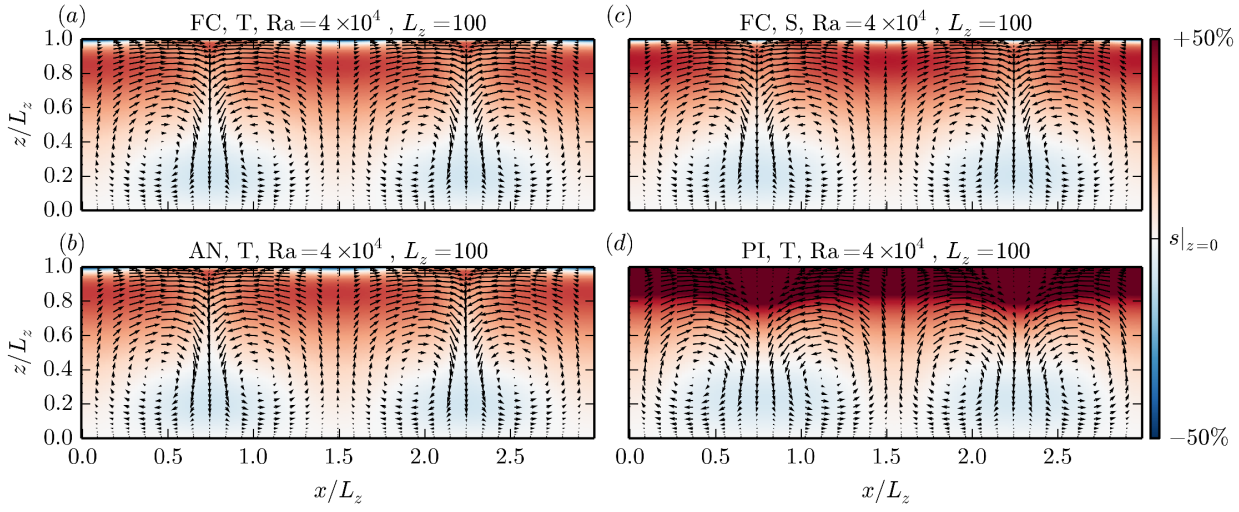


*Figure 3.4*: Steady convective states for different equations and thermal conduction models, with Ra = $4 \times 10^4$ and $L_z = 100$. The quantities plotted and labeling are the same as for figure 3.3, except that the red (blue) colors correspond to fifty percent greater (less) than the entropy value at $z = 0$. In all cases, $L_x = 3L_z$. Panels (*a*) & (*b*) use the $T$-diffusion with the FC & AN equations, respectively. These plots are virtually identical. Panel (*c*) shows the convective steady state for the FC equations with $S$-diffusion; the results for the AN & PI equation equations with $S$-diffusion are virtually identical and not shown. Panel (*d*) shows the convective steady state for the PI equations with $T$-diffusion.

height at the bottom of the domain. However, there are no features on intermediate scales, even for $L_z = 100$ which contains seven density scale heights.

In figure 3.4, we vary the equations and thermal conduction model, fixing Ra = $4 \times 10^4$ and $L_z = 100$. Panels (*a*) & (*c*) correspond to panels (*b*) & (*f*) in figure 3.3. The FC & AN equations with $T$-diffusion (panels (*a*) & (*b*)) look virtually identical. There are slight differences between the FC equations with $T$- and $S$- diffusion (panels (*a*) & (*c*))—the upper boundary layer is slightly thinner for $S$-diffusion.

However, there are substantial differences between the steady state for the PI equations with $T$-diffusion (panel (*d*)) and the other three steady states. The entropy variation with height is very different for the PI steady state—the entropy is much larger at the top of the box than the rest of the domain. It might appear that the convective steady state does not satisfy the $S' = 0$ boundary condition at the top of the domain. However, this is only because there is an extremely thin boundary layer at the top of the domain which is well resolved in the simulation, but is smaller than the resolution of the image. Also, the flow pattern looks very different, with less asymmetry between the up flows and down flows than in the FC & AN simulations. The convective steady states were virtually identical for the FC & AN equations using $T$-diffusion, and all three equation sets with $S$-diffusion. The only equations which show strong differences from the others are the PI

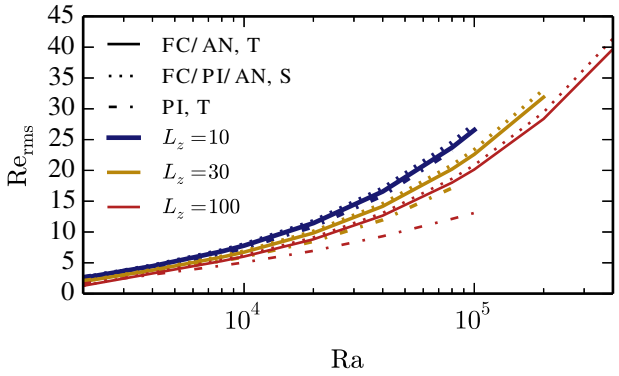


*Figure 3.5*: $\mathrm{Re}_{\mathrm{rms}}$ (equation 3.63) of convective steady states as a function of Ra (equation 3.62) for different equation sets, thermal conduction models, and box sizes $L_z$. Solid lines show results for the FC & AN equations with $T$-diffusion, dotted lines show results for the FC, PI, & AN equations with $S$-diffusion, and dot-dashed lines show results for the PI equations with $T$-diffusion. Blue, yellow, and red lines show results for $L_z = 10$, 30, and 100 respectively (recall that $L_x = 3L_z$). The different equation sets which have been grouped together have differences in $\mathrm{Re}_{\mathrm{rms}}$ of less than 1% (and typically less than 0.01%) for each Ra and $L_z$ shown. Although the $T$- and $S$- diffusion models track each other fairly well for the FC & AN equations, the PI equations with $T$-diffusion have convective steady states with low $\mathrm{Re}_{\mathrm{rms}}$, especially for highly stratified domains.

equations with $T$-diffusion.

To more quantitatively compare the different convective steady states, we plot the rms Re in figure 3.5. We define the rms Re to be

$$\mathrm{Re}_{\mathrm{rms}} = \frac{\sqrt{\langle |\boldsymbol{u}|^2 \rangle} L_z}{\nu}. \tag{3.63}$$

Note that we were not able to find convective steady states for high Ra for some of the low $L_z$ boxes, and with the PI equations with $T$-diffusion.

The $T$- and $S$- diffusion models produced very similar results for the FC & AN equations. For all three $L_z$, the difference in $\mathrm{Re}_{\mathrm{rms}}$ at the lowest Ra was less than 1%, and at the highest Ra was $\approx 4\%$. In contrast, the PI equations with $T$-diffusion has convective steady states which are rather different (note that the PI equations with $S$-diffusion give results practically indistinguishable from the FC or AN equations with $S$-diffusion). Although the differences in $\mathrm{Re}_{\mathrm{rms}}$ between the FC and PI equations with $T$-diffusion are $< 5\%$ for all Ra for $L_z = 10$, at high Ra, the differences grow to 15% for $L_z = 30$ and 35% for $L_z = 100$. These results are consistent with the similarity and differences between the convective steady states shown in figure 3.4.

It might seem odd that the PI equations seem to be substantially different from the FC & AN equations with $T$-diffusion, but virtually identical to the FC & AN equations with $S$-diffusion. The difference lies in the PI equation of state (equation 3.26), in which $P$ is replaced by $\overline{P}$. For low

Mach number convection, $\rho'/\overline{\rho}$, $P'/\overline{P}$, and $S'/C_P$ are all $O(\mathrm{Ma}^2)$. However, the PI equation of state assumes that $\rho'/\overline{\rho}$ and $S'/C_P$ are $O(1)$, but that $P'/\overline{P} \sim O(\mathrm{Ma}^2)$. Thus, the PI equation of state introduces inaccuracies in thermodynamic variables.

When using $S$-diffusion, the equation of state is in some sense "not used." Summing the PI continuity equation (3.21) and the PI constraint equation (3.22), and using the PI equation of state (3.26), one can show that $S'_{\mathrm{PI}}$ and $S'_{\mathrm{AN}}$ satisfy the same equation. However, when using $T$-diffusion, the equation of state must be used to relate $T'_{\mathrm{PI}}$ to other thermodynamic quantities. In this case, there are differences in $T'_{\mathrm{PI}}$ and $T'_{\mathrm{AN}}$ because the latter depends on the pressure perturbation.

## 3.6 Conclusion

This chapter examines the differences between the temperature diffusion and entropy diffusion models of thermal conduction, for three different equations sets: the fully compressible equations, the pseudo-incompressible equations, and the anelastic equations. We study both damping rates of linear internal gravity wave modes, and the properties of low Rayleigh number convective steady states.

Overall, we find little difference between temperature diffusion and entropy diffusion, provided that the conductivities are related by

$$\overline{\kappa_T} = \overline{T}\,\overline{\kappa_S}/C_P. \tag{3.64}$$

Using a different relation between $\overline{\kappa_T}$ and $\overline{\kappa_S}$ will cause differences between the temperature and entropy diffusion models, just as there are differences between temperature diffusion using two different conductivities. Although entropy diffusion could lead to non-monotonicity of the total entropy, in practice, it generally does not, as the $\boldsymbol{\nabla} S$ field is often aligned with the $\boldsymbol{\nabla} T$ field (section 3.4.2). The only way to ensure that entropy will increase monotonically is to use temperature diffusion (Landau & Lifshitz 2013).

Temperature and entropy diffusion give the same linear internal gravity wave damping rates for all three equation sets, provided that $kH \gg 1$, i.e., that the wavelength is shorter than the density scale height. For $kH \lesssim 1$, we find modest differences between damping rates for different equation sets and thermal conduction models (see figure 3.1). The longest wavelength modes we studied ($\approx 6.6$ density scale heights) have damping rate errors of $\sim 20\%$ for the anelastic equations (with either thermal conduction model) and pseudo-incompressible equations with entropy diffusion, but errors of $\sim 50\%$ for the pseudo-incompressible equations with temperature diffusion. We believe the large errors in the pseudo-incompressible equations with temperature diffusion are due to inaccuracies in the pseudo-incompressible equation of state (which assumes that the pressure perturbations are much smaller than the density and entropy perturbations, and can be dropped).

We also calculate convective steady states using Dedalus (section 3.5). The flexibility of Dedalus allows us to study the fully compressible, anelastic, and pseudo-incompressible equations all within the same framework. Furthermore, by implicitly timestepping sound waves, we are able to take the same time step in fully compressible calculations as the anelastic and pseudo-incompressible calculations (despite having Mach numbers of $10^{-3}$). Because the implementation

of the fully compressible equations is more complicated than the implementation of the anelastic equations, we find that the fully compressible simulations run about half as fast as the anelastic simulations. The pseudo-incompressible simulations run at about the same speed as the fully compressible simulations.

For Rayleigh numbers above the instability threshold of convection, but below the onset of oscillatory instabilities, we find many convective steady states for box sizes ranging from three density scale heights to seven density scale heights. The convective steady states are essentially identical for the fully compressible equations and anelastic equations with temperature diffusion; similarly, the convective steady states are essentially identical for the all three equation sets using entropy diffusion. Furthermore, these two classes of steady states are very similar (figure 3.5). However, the pseudo-incompressible equations with temperature diffusion find convective steady states with much lower rms Reynolds number than the other equations, and with very different convection patterns (figure 3.4). We again attribute the difference to the incorrect equation of state, which does not correctly calculate the temperature perturbation for low Mach number convection. The differences are largest for the most strongly stratified domains, as the convective rolls have longest wavelengths ($kH \lesssim 1$).

In a similar analysis, Calkins et al. (2015) calculate the critical Rayleigh number for the onset of convection for the fully compressible equations (with temperature diffusion) and the anelastic equations with both temperature and entropy diffusion, also including the effects of rotation. They also find that the anelastic and fully compressible equations with temperature diffusion give nearly identical results in the low Mach number limit (when the background is very close to adiabatic). They find much larger differences between entropy and temperature diffusion than we do. This is likely because their entropy diffusion model diffuses $\overline{T}S'$, unlike our own which diffuses $S'$. Diffusing $\overline{T}S'$ is equivalent to using temperature diffusion in the pseudo-incompressible equations, which we have shown can produce substantial errors for highly stratified domains.

Although we find only minor differences between temperature and entropy diffusion for linear internal waves and low Rayleigh number convective steady states, there is no guarantee that these different thermal conduction models will continue to give similar results in the strongly nonlinear regime. In the future, we plan to investigate the effects of different thermal conduction models on strongly nonlinear wave breaking and high Rayleigh number convection. Our present results show that the differences between temperature and entropy diffusion in convective steady states grows as the Rayleigh number increases, with entropy diffusion overestimating the velocities in the convective steady states. Perhaps this indicates that at the very high Rayleigh numbers of stellar convection, there are substantial and important differences between temperature and entropy diffusion.

## 3.A Eigenvalue Equations and Damping Rates for Fully Compressible Equations

The eigenvalue equations for the FC equations are somewhat more complicated than for the AN equations. We again drop all terms of order $(kH)^{-1} \ll 1$. The eigenvalue equation for $T$-diffusion

is

$$\left[\omega^2\left(1-i\frac{\overline{\kappa_T}\nabla^2}{\omega C_P}\right)^2\nabla^2+\frac{\omega^4}{\overline{c_s}^2}\left(1-i\frac{\chi_T\nabla^2}{\overline{\rho}C_P\omega}\right)\left(1-i\frac{\gamma\overline{\kappa_T}\nabla^2}{\overline{\rho}C_P\omega}\right)\right.$$
$$\left.-\frac{g}{C_P}\left(1-i\frac{\overline{\kappa_T}\nabla^2}{\overline{\rho}C_P\omega}\right)\left(\partial_z\overline{S}\left(\nabla_\perp^2+\frac{\omega^2}{\overline{c_s}^2}\right)+i\omega\frac{\gamma-1}{\overline{c_s}^2}\frac{\overline{\kappa_T}}{\overline{\rho}}\nabla^2\partial_z\right)\right]w=0. \tag{3.65}$$

The eigenvalue equation for $S$-diffusion is

$$\left[\omega^2\left(1-i\frac{\overline{\kappa_S}\nabla^2}{\overline{\rho}\overline{T}\omega}\right)\left(\nabla^2+\frac{\omega^2}{\overline{c_s}^2}\right)-g\frac{\partial_z\overline{S}}{C_P}\left(\nabla_\perp^2+\frac{\omega^2}{\overline{c_s}^2}\right)\right]w=0. \tag{3.66}$$

Unlike the eigenvalue equations for the AN equations, these are not equivalent. This is partially because sound waves are affected differently by temperature and entropy diffusion. IGWs with $kH\gg 1$ have the property

$$k^2\gg\frac{\omega^2}{\overline{c_s}^2}. \tag{3.67}$$

If we use this relation, the eigenvalue equation with $T$-diffusion is

$$\left[\omega^2\left(1-i\frac{\overline{\kappa_T}\nabla^2}{\overline{\rho}C_P\omega}\right)\nabla^2-\frac{g}{C_P}\left(\partial_z\overline{S}\nabla_\perp^2+i\omega\frac{\gamma-1}{\overline{c_s}^2}\frac{\overline{\kappa_T}}{\overline{\rho}}\nabla^2\partial_z\right)\right]w=0, \tag{3.68}$$

while the eigenvalue equation with $S$-diffusion is

$$\left[\omega^2\left(1-i\frac{\overline{\kappa_S}\nabla^2}{\overline{\rho}\overline{T}\omega}\right)\nabla^2-g\frac{\partial_z\overline{S}}{C_P}\nabla_\perp^2\right]w=0. \tag{3.69}$$

These equations are still not equivalent, due to the last term in equation 3.68. It cannot be shown to be small in comparison to $\partial_z\overline{S}\nabla_\perp^2$ unless $\overline{\kappa_T}$ is assumed to be small. For weakly damped waves, the eigenvalue equations are equivalent under the identification $\overline{\kappa_S}=\overline{T}\overline{\kappa_T}/C_P$. However, for strongly damped modes (which are no longer wave-like), we expect larger differences.

One can show that the perturbation energy for the FC equations is

$$E=\frac{1}{2}\overline{\rho}|\boldsymbol{u}|^2+\frac{1}{2}\frac{g\overline{\rho}}{C_P\partial_z\overline{S}}S'^2+\frac{1}{2}\frac{\overline{\rho}}{\overline{c_s}^2}\varpi'^2, \tag{3.70}$$

and the $T$- and $S$- diffusion damping terms are

$$\theta_T = \overline{\kappa_T}\boldsymbol{\nabla}\left(\frac{gS'}{C_P\overline{T}\partial_z\overline{S}}+\frac{\varpi'}{\overline{T}C_P}\right)\cdot\boldsymbol{\nabla}\left(\overline{T}\frac{S'}{C_P}+\frac{\gamma-1}{\gamma}\varpi'\right), \tag{3.71}$$

$$\theta_S = \overline{\kappa_S}\boldsymbol{\nabla}\left(\frac{gS'}{C_P\overline{T}\partial_z\overline{S}}+\frac{\varpi'}{\overline{T}C_P}\right)\cdot\boldsymbol{\nabla}S'. \tag{3.72}$$

For weak dissipation, both $S'$ and $\varpi'$ can be related to $w$ by

$$S' = -i\frac{w\partial_z\overline{S}}{\omega}, \tag{3.73}$$

$$\varpi' = i\omega\frac{\partial_z w + \frac{1}{\gamma}\left(\partial_z \log\overline{p}\right)w}{\frac{\omega^2}{\overline{c_s}^2} + k_\perp^2} \approx \frac{\omega^2 - \overline{N}^2}{\omega k_z}w, \tag{3.74}$$

where the approximation is dropping terms of order $(k_z H)^{-1}$ and smaller. This implies the $S'$ contribution is much larger than the $\varpi'$ contribution to $\theta_T$ and $\theta_S$,

$$\left|\frac{\overline{T}S'}{C_P}\right|\left|\frac{\varpi'}{\gamma}\right|^{-1} = \left(\frac{\overline{c_s}^2 k_z^2}{\omega^2 - \overline{N}^2}\right)\left(\frac{\partial_z\left(\frac{\overline{S}}{C_P}\right)}{k_z}\right), \tag{3.75}$$

$$\left|\frac{gS'}{\partial_z\overline{S}}\right||\varpi'|^{-1} = \frac{gHk_z^2}{\omega^2 - \overline{N}^2}\frac{1}{k_z H}. \tag{3.76}$$

Using the IGW eigenvalue equation, and that $\overline{c_s}^2 \sim \overline{N}^2 H^2$, one can show that both these terms are order $(kH)^{-1}$.

The leading order contributions to $\theta_T$ and $\theta_S$ are

$$\theta_T \approx \frac{g\overline{\kappa_T}}{C_P^2\partial_z\overline{S}}\left|\boldsymbol{\nabla}S'\right|^2, \tag{3.77}$$

$$\theta_S \approx \frac{g\overline{\kappa_S}}{C_P\overline{T}\partial_z\overline{S}}\left|\boldsymbol{\nabla}S'\right|^2. \tag{3.78}$$

Thus, for perturbations with $k_z H \gg 1$ and weak dissipation, we have that thermal diffusion and entropy diffusion are equivalent under the identification $\overline{\kappa_S} = \overline{\kappa_T}\overline{T}/C_P$.

## 3.B Eigenvalue Equations and Damping Rates for PI Equations

Recall that for the linearized PI equations $T' = \overline{T}S'/C_P$. This makes temperature and entropy conduction extremely similar. In the limit $kH \gg 1$, the eigenvalue equation for $T$-diffusion is

$$\left[\omega^2\left(1 - i\frac{\overline{\kappa_T}}{\overline{\rho}C_P\omega}\nabla^2\right)\nabla^2 - g\partial_z\frac{\overline{S}}{C_P}\nabla_\perp^2\right]w = 0. \tag{3.79}$$

The eigenvalue equation for $S$-diffusion is

$$\left[\omega^2\left(1 - i\frac{\overline{\kappa_S}}{\overline{\rho}\overline{T}\omega}\nabla^2\right)\nabla^2 - g\partial_z\frac{\overline{S}}{C_P}\nabla_\perp^2\right]w = 0. \tag{3.80}$$

These are equal to each other when $\overline{\kappa_S} = \overline{\kappa_T}\overline{T}/C_P$. This shows that $T$- and $S$- diffusion are equivalent for the PI equations as long as $kH \gg 1$, irrespective of the strength of thermal conduction.

The expression for the perturbation energy is

$$E = \frac{1}{2}\overline{\rho}\,|\boldsymbol{u}|^2 + \frac{1}{2}\frac{g\overline{\rho}}{C_P\partial_z\overline{S}}S'^2, \tag{3.81}$$

and the thermal and entropy damping terms are

$$\theta_T = \overline{\kappa_T}\boldsymbol{\nabla}\left(\frac{gS'}{C_P\overline{T}\partial_z\overline{S}} + \frac{\varpi'}{\overline{T}C_P}\right)\cdot\boldsymbol{\nabla}\left(\overline{T}\frac{S'}{C_P}\right), \tag{3.82}$$

$$\theta_S = \overline{\kappa_S}\boldsymbol{\nabla}\left(\frac{gS'}{C_P\overline{T}\partial_z\overline{S}} + \frac{\varpi'}{\overline{T}C_P}\right)\cdot\boldsymbol{\nabla}S'. \tag{3.83}$$

This is very similar to the FC expressions, except that $T' = \overline{T}S'/C_P$, since there is no $\varpi'$ term in the equation of state. In the limit of $kH \gg 1$, these two expressions are equivalent, since

$$\boldsymbol{\nabla}\left(\overline{T}\frac{S'}{C_P}\right) \approx \frac{\overline{T}}{C_P}\boldsymbol{\nabla}(S'). \tag{3.84}$$

## 3.C Thermal Conduction and Sound Waves

In this chapter, we focus on the differences in IGW damping rates between equation sets and thermal conduction models. However, the FC equations also admit sound waves. Here we demonstrate, using Dedalus, the substantial differences in sound wave damping when using either $T$- or $S$- diffusion.

We solve the linear FC equations for the same background and parameters as in section 3.3. We check the damping rate of each mode against the analytic result given in appendix 3.A. The sound waves are much harder to resolve than IGWs—thus, some of our sound wave damping rates disagree with the analytic damping rates by as much as 20% (with a vertical resolution of 256 modes). However, the differences between $T$- and $S$- diffusion are much larger than this, so we have not repeated the calculation at higher resolution to reduce the errors.

In figure 3.6, we plot the damping rates and oscillation frequencies for sound wave modes, using either $T$- or $S$- diffusion. Although the damping rate increases with increasing $k$ (and increasing oscillation frequency) for $T$-diffusion, the damping rate stays about constant for $S$-diffusion. The oscillation frequencies between the modes agree well because they are only weakly damped.

For sound waves, the damping rate using $S$-diffusion becomes increasing inaccurate as $k$ increases. This is the opposite result as for IGWs. Although the dominant contribution to $T'$ is $S'$ for IGWs, the dominant contribution to $T'$ is the pressure perturbation $\varpi'$ for sound waves. In section 3.4, we show that the ratio of the $\varpi'$ contribution to $T'$, to the $S'$ contribution to $T'$, decreases with increasing $k$ if the modes follow the IGW dispersion relation, but increases with increasing $k$ if the modes follow the sound wave dispersion relation.

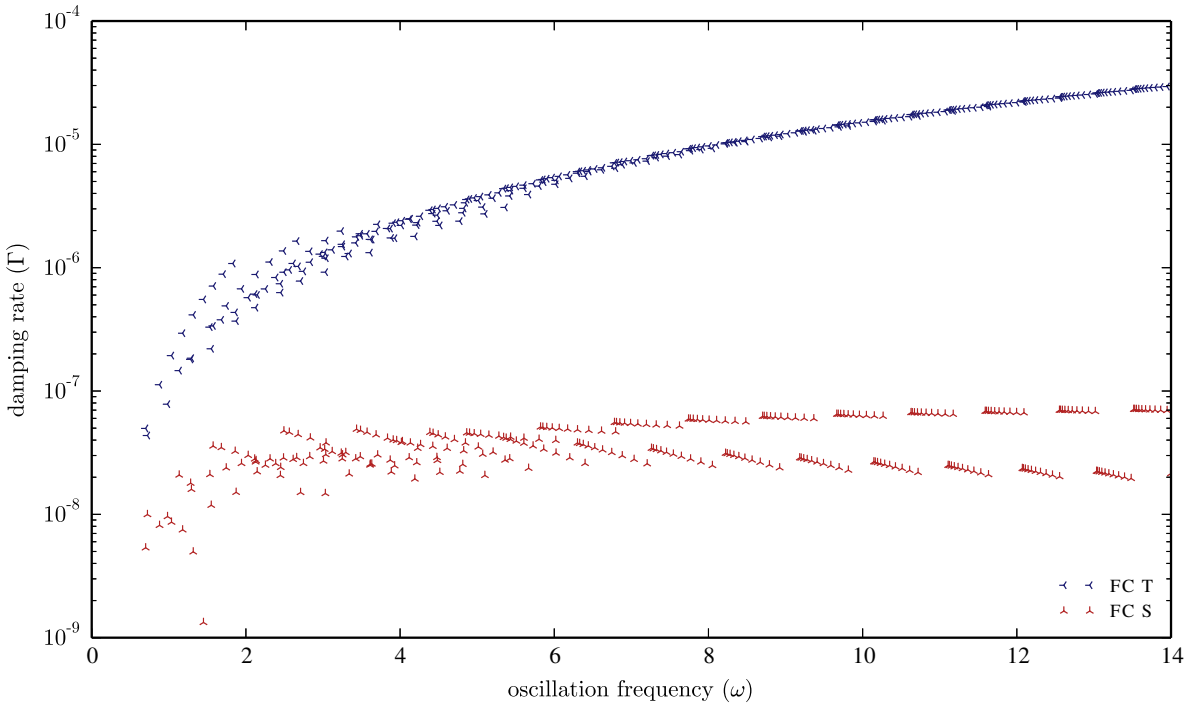


*Figure 3.6*: Damping rates and oscillation frequencies of sound wave modes of the FC equations, using either $T$- or $S$- diffusion. The first ten radial and horizontal modes are shown. Each cluster of modes (most visible at high oscillation frequency) corresponds to a single horizontal mode number. The oscillation frequency increases with increasing wavenumber.

Physically, this is because sound waves are almost adiabatic waves. In the absence of gravity, they are completely adiabatic. On the other hand, as they are pressure-driven waves, they have large pressure perturbations, which correspond to large temperature perturbations. Thus, sound waves are much more efficiently damped with $T$-diffusion than $S$-diffusion.

## 3.D Equation Implementation in Dedalus

Dedalus solves systems of equations which are first order in $z$. Time derivatives are here discretized using an implicit–explicit scheme; equations are written such that terms on the LHS of the equals sign are temporally discretized implicitly (i.e., the term is evaluated in the future), and terms on the RHS of the equals sign are temporally discretized explicitly (i.e., the term is only evaluated in the present and/or past). Only linear terms can be treated implicitly, although they are not required to be.

### 3.D.1 Fully Compressible Equations

We implement the fully compressible equations with temperature diffusion as

$$\begin{aligned}
&\partial_t w + \partial_z T' + \overline{T}\partial_z \Upsilon' + T'\partial_z \log\overline{\rho} \\
&\qquad -\nu\left[\partial_x^2 w + \partial_z w_z + 2\partial_z \log\overline{\rho} w_z + \frac{1}{3}\left(\partial_x u_z + \partial_z w_z\right) - \frac{2}{3}\partial_z \log\overline{\rho}\left(\partial_x u + w_z\right)\right] \\
&\qquad = -T'\partial_z \Upsilon' - u\partial_x w - w w_z \\
&\qquad +\nu\left[u_z\partial_x\Upsilon' + 2w_z\partial_z\Upsilon' + \partial_x w\partial_x\Upsilon' - \frac{2}{3}\partial_z\Upsilon'\left(\partial_x u + w_z\right)\right], \qquad (3.85)\\
&\partial_t u + \partial_x T' + \overline{T}\partial_x\Upsilon' - \nu\left[\partial_x^2 u + \partial_z u_z + \partial_z \log\overline{\rho}\left(u_z + \partial_x w\right) + \frac{1}{3}\left(\partial_x^2 u + \partial_x w_z\right)\right] \\
&\qquad = -T'\partial_x\Upsilon' - u\partial_x u - w u_z \\
&\qquad +\nu\left[2\partial_x u\partial_x\Upsilon' + \partial_x w\partial_z\Upsilon' + u_z\partial_z\Upsilon' - \frac{2}{3}\partial_x\Upsilon'\left(\partial_x u + w_z\right)\right], \qquad (3.86)\\
&\partial_t\Upsilon' + w\partial_z \log\overline{\rho} + \partial_x u + w_z = -u\partial_x\Upsilon' - w\partial_z\Upsilon' \qquad (3.87)\\
&\partial_t T' + w\partial_z\overline{T} + (\gamma-1)\,\overline{T}\left(\partial_x u + w_z\right) - \frac{\chi}{C_V}\left(\partial_x^2 T' - \partial_z\tilde{Q}_z' - \tilde{Q}_z'\partial_z\log\overline{\rho}\right) \\
&\qquad = -u\partial_x T' - w\partial_z T' - (\gamma-1)\,T'\left(\partial_x u + w_z\right) + \frac{\chi}{C_V}\left(\partial_x T'\partial_x\Upsilon' - \tilde{Q}_z'\partial_z\Upsilon'\right) \\
&\qquad\quad + \frac{\nu}{C_V}\left[2\left(\partial_x u\right)^2 + \left(\partial_x w\right)^2 + u_z^2 + 2w_z^2 + 2u_z\partial_x w - \frac{2}{3}\left(\partial_x u + w_z\right)^2\right], \qquad (3.88)\\
&\tilde{Q}_z' + \partial_z T' = 0, \qquad (3.89)\\
&\frac{S'}{C_P} - \frac{T'}{\gamma\overline{T}} + \frac{1}{C_P}\Upsilon' = \frac{1}{\gamma}\left[\log\left(1 + \frac{T'}{\overline{T}}\right) - \frac{T'}{\overline{T}}\right], \qquad (3.90)\\
&w_z - \partial_z w = 0, \qquad (3.91)\\
&u_z - \partial_z u = 0. \qquad (3.92)
\end{aligned}$$

In these equations, $u$ and $w$ are the horizontal and vertical velocity, respectively. The temperature field is decomposed as $T = \overline{T} + T'$, the density field is decomposed as $\log\rho = \log\overline{\rho} + \Upsilon'$, and the entropy field is decomposed as $S = \overline{S} + S'$. The normalized vertical heat flux $\tilde{Q}_z'$ is the vertical component of the heat flux divided by $\chi\rho$. Equations 3.85 & 3.86 are the vertical and horizontal momentum equation respectively, equation 3.87 is the continuity equation, while equation 3.88 is the equation for temperature. Equation 3.89 defines the heat flux, equation 3.90 is the fully non-linear equation of state, while equations 3.91 & 3.92 define quantities which have second vertical derivatives within our first order system. These are equivalent to equations 3.13–3.15. Note that the entropy perturbation solved for in the equation of state (3.90) is only used to enforce the $S' = 0$ boundary condition. The momentum equations and the temperature equation have nonlinear diffusion terms which are treated explicitly.

For the FC equations with entropy diffusion, equations 3.88 & 3.89 are replaced by

$$\begin{aligned}
&\partial_t T' + w\partial_z \overline{T} + (\gamma-1)\,\overline{T}\,(\partial_x u + w_z) - \frac{\chi}{C_V}\left(\overline{T}\partial_x^2\frac{S'}{C_P} - \partial_z\tilde{Q}_z' - \tilde{Q}_z'\partial_z\log\overline{\rho}\right)\\
&\qquad = -u\partial_x T' - w\partial_z T' - (\gamma-1)\,T'\,(\partial_x u + w_z) + \frac{\chi}{C_V}\left(\overline{T}\partial_x\frac{S'}{C_P}\partial_x\Upsilon' - \tilde{Q}_z'\partial_z\Upsilon'\right)\\
&\qquad\quad + \frac{\nu}{C_V}\left[2\,(\partial_x u)^2 + (\partial_x w)^2 + u_z^2 + 2w_z^2 + 2u_z\partial_x w - \frac{2}{3}\,(\partial_x u + w_z)^2\right], \qquad (3.93)\\
&\tilde{Q}_z' + \overline{T}\partial_z\frac{S'}{C_P} = 0. \qquad (3.94)
\end{aligned}$$

Note that $\chi$, $\nu$, and $\gamma$ are assumed to be constant. In both conduction models, we solve for the variables $u, u_z, w, w_z, \Upsilon', T', S', \tilde{Q}_z'$.

### 3.D.2 Pseudo-Incompressible Equations

Our implementation of the PI equations with temperature diffusion is

$$\begin{aligned}
&\partial_t w + \partial_z\varpi' + \overline{\varpi}\partial_z\Upsilon' - \varpi'\partial_z\frac{\overline{S}}{C_P}\\
&\qquad -\nu\left[\partial_x^2 w + \partial_z w_z + 2\partial_z\log\overline{\rho}w_z + \frac{1}{3}\,(\partial_x u_z + \partial_z w_z) - \frac{2}{3}\partial_z\log\overline{\rho}\,(\partial_x u + w_z)\right]\\
&\qquad = -\varpi'\partial_z\Upsilon' - u\partial_x w - ww_z\\
&\qquad +\nu\left[u_z\partial_x\Upsilon' + 2w_z\partial_z\Upsilon' + \partial_x w\partial_x\Upsilon' - \frac{2}{3}\partial_z\Upsilon'\,(\partial_x u + w_z)\right], \qquad (3.95)\\
&\partial_t u + \partial_x\varpi' + \overline{\varpi}\partial_x\Upsilon' - \nu\left[\partial_x^2 u + \partial_z u_z + \partial_z\log\overline{\rho}\,(u_z + \partial_x w) + \frac{1}{3}\left(\partial_x^2 u + \partial_x w_z\right)\right]\\
&\qquad = -\varpi'\partial_x\Upsilon' - u\partial_x u - wu_z\\
&\qquad +\nu\left[2\partial_x u\partial_x\Upsilon' + \partial_x w\partial_z\Upsilon' + \partial_z\Upsilon' u_z - \frac{2}{3}\partial_x\Upsilon'\,(\partial_x u + w_z)\right], \qquad (3.96)\\
&\partial_t\Upsilon' + w\partial_z\log\overline{\rho} + \partial_x u + w_z = -u\partial_x\Upsilon' - w\partial_z\Upsilon', \qquad (3.97)\\
&w\partial_z\log\overline{P} + \gamma\,(\partial_x u + w_z) - \frac{\chi}{C_V\overline{T}}\left(\partial_x^2 T' + \partial_z T_z' + T_z'\partial_z\log\overline{\rho}\right)\\
&\qquad = \frac{\chi}{C_V\overline{T}}\left[\partial_x T'\partial_x\exp\Upsilon' + \left(\partial_x^2 T' + \partial_z T_z' + T_z'\partial_z\log\overline{\rho}\right)(\exp(\Upsilon') - 1) + T_z'\partial_z\exp(\Upsilon')\right]\\
&\qquad\quad + \nu\frac{\exp(\Upsilon')}{C_V\overline{T}}\left[2\,(\partial_x u)^2 + (\partial_x w)^2 + u_z^2 + 2w_z^2 + 2u_z\partial_x w - \frac{2}{3}\,(\partial_x u + w_z)^2\right], \qquad (3.98)\\
&T' + \overline{T}\Upsilon' = \overline{T}\,(\exp(-\Upsilon') - 1 + \Upsilon'), \qquad (3.99)\\
&T_z' - \partial_z T' = 0, \qquad (3.100)\\
&w_z - \partial_z w = 0, \qquad (3.101)\\
&u_z - \partial_z u = 0. \qquad (3.102)
\end{aligned}$$

Equations 3.95 & 3.96 are the vertical and horizontal momentum equation respectively, equation 3.97 is the continuity equation, while equation 3.98 is the constraint equation. Equation 3.99 is the fully nonlinear equation of state, while equations 3.100–3.102 define quantities which have second vertical derivatives within our first order system. These are equivalent to equations 3.20–3.22. Note that the momentum equations and the constraint equation have nonlinear diffusion terms which are treated explicitly.

For the PI equations with entropy diffusion, equations 3.98–3.100 are replaced by

$$\begin{aligned} &w\partial_z \log \overline{P} + \gamma\left(\partial_x u + w_z\right) + \frac{\chi}{C_V \overline{T}}\left[\overline{T}\partial_x^2 \Upsilon' - \partial_z \tilde{Q}_z' - \tilde{Q}_z' \partial_z \log \overline{\rho}\right] \\ &\quad = -\frac{\chi}{C_V \overline{T}}\left[\overline{T}\partial_x \Upsilon' \partial_x \exp(\Upsilon') + \left(\overline{T}\partial_x^2 - \partial_z \tilde{Q}_z' - \tilde{Q}_z' \partial_z \log \overline{\rho}\right)\left(\exp(\Upsilon') - 1\right) - \tilde{Q}_z' \partial_z \exp(\Upsilon')\right] \\ &\qquad + \nu \frac{\exp(\Upsilon')}{C_V \overline{T}}\left[2\left(\partial_x u\right)^2 + \left(\partial_x w\right)^2 + u_z^2 + 2w_z^2 + 2u_z \partial_x w - \frac{2}{3}\left(\partial_x u + w_z\right)^2\right], \end{aligned} \tag{3.103}$$

$$\tilde{Q}_z' + \overline{T}\partial_z \Upsilon' = 0. \tag{3.104}$$

The variables here have the same meaning as for the fully compressible equations. The only additional variables are $\overline{\varpi}$ and $\varpi'$. These are defined as follows. Call the PI pressure perturbation $\pi'$, and recall that $\overline{\beta} = \overline{P}^{1/\gamma}$. Define $\overline{\pi}$ by

$$\overline{\beta}\boldsymbol{\nabla}\left(\frac{\overline{\pi}}{\overline{\beta}}\right) = \boldsymbol{g}\overline{\rho}, \tag{3.105}$$

and define $\pi = \overline{\pi} + \pi'$. Then $\varpi$ is defined as $\varpi = \pi/\rho$, and we can split it up as $\varpi = \overline{\varpi} + \varpi'$. We have that $\overline{\varpi}$ satisfies the equation

$$\overline{\beta}\boldsymbol{\nabla}\left(\frac{\overline{\varpi}}{\overline{\beta}}\right) + \overline{\varpi}\boldsymbol{\nabla}\log\overline{\rho} = \boldsymbol{g}. \tag{3.106}$$

In the PI equations, entropy is proportional to $\Upsilon'$, so the entropy boundary condition becomes $\Upsilon' = 0$ on the top and bottom of the domain. For the PI equations with temperature diffusion, we solve for the variables $u, u_z, w, w_z, \varpi', \Upsilon', T', T_z'$, and for the PI equations with entropy diffusion, we solve for the variables $u, u_z, w, w_z, \varpi', \Upsilon', \tilde{Q}_z'$.

### 3.D.3 Anelastic Equations

Our implementation of the AN equations with temperature diffusion is

$$\partial_t w + \partial_z \varpi' - g\frac{S'}{C_P} - \nu\left[\partial_x^2 w + \partial_z w_z + 2\partial_z \log\overline{\rho} w_z + \frac{1}{3}\left(\partial_x u_z + \partial_z w_z\right) - \frac{2}{3}\partial_z \log\overline{\rho}\left(\partial_x u + w_z\right)\right] = -u\partial_x w - w w_z, \tag{3.107}$$

$$\partial_t u + \partial_x \varpi' - \nu\left[\partial_x^2 u + \partial_z u_z + \partial_z \log\overline{\rho}\left(u_z + \partial_x w\right) + \frac{1}{3}\left(\partial_x^2 u + \partial_x w_z\right)\right] = -u\partial_x u - w u_z, \tag{3.108}$$

$$\begin{aligned}\partial_t S' + w\partial_z \overline{S} - \chi\left[\partial_x^2 \frac{S'}{C_P} + \frac{1}{C_P\overline{T}}\partial_x^2 \varpi' - \frac{1}{\overline{T}}\partial_z \tilde{Q}_z' - \frac{1}{\overline{T}}\tilde{Q}_z'\partial_z \log\overline{\rho}\right] \\ = -u\partial_x S' - w\partial_z S' \\ + \frac{\nu}{\overline{T}}\left[2\left(\partial_x u\right)^2 + \left(\partial_x w\right)^2 + u_z^2 + 2w_z^2 + 2u_z\partial_x w - \frac{2}{3}\left(\partial_x u + w_z\right)^2\right],\end{aligned} \tag{3.109}$$

$$\tilde{Q}_z' + \overline{T}\partial_z \frac{S'}{C_P} + \frac{S'}{C_P}\partial_z \overline{T} + \frac{1}{C_P}\partial_z \varpi' = 0, \tag{3.110}$$

$$\partial_x u + w_z + w\partial_z \log\overline{\rho} = 0, \tag{3.111}$$

$$w_z - \partial_z w = 0, \tag{3.112}$$

$$u_z - \partial_z u = 0. \tag{3.113}$$

Equations 3.108 & 3.107 are the vertical and horizontal momentum equation respectively, equation 3.109 is the entropy equation. Equation 3.110 defines the heat flux, while equation 3.111 is the constraint equation. Equations 3.112 & 3.113 define quantities which have second vertical derivatives within our first order system.

For the AN equations with entropy diffusion, equations 3.109 & 3.110 are replaced by

$$\begin{aligned}\partial_t S' + w\partial_z \overline{S} - \chi\left[\partial_x^2 \frac{S'}{C_P} - \frac{1}{\overline{T}}\partial_z \tilde{Q}_z' - \frac{1}{\overline{T}}\tilde{Q}_z'\partial_z \log\overline{\rho}\right] \\ = -u\partial_x S' - w\partial_z S' \\ + \frac{\nu}{\overline{T}}\left[2\left(\partial_x u\right)^2 + \left(\partial_x w\right)^2 + u_z^2 + 2w_z^2 + 2u_z\partial_x w - \frac{2}{3}\left(\partial_x u + w_z\right)^2\right],\end{aligned} \tag{3.114}$$

$$\tilde{Q}_z' + \overline{T}\partial_z \frac{S'}{C_P} = 0. \tag{3.115}$$

The variables used here have all been defined for the FC & PI equations. One difference, however, is that $\varpi'$ is now a different pressure-type variable. Calling the AN pressure perturbation $P'$, $\varpi' = P'/\overline{\rho}$. This is different from the definition of $\varpi'$ used in the PI equations. In both conduction models, we solve for the variables $u, u_z, w, w_z, \varpi', S', \tilde{Q}_z'$.

# Chapter 4

# A Validated Nonlinear Kelvin-Helmholtz Benchmark for Numerical Hydrodynamics

## 4.1 Introduction

The Kelvin-Helmholtz (KH) instability results from a wide array of velocity-shear profiles in a continuous fluid, or across the interface between two distinct fluids. The instability is ubiquitous in nature, playing important roles in meteorology, oceanography, and engineering. The KH instability plays a particularly prominent role in astrophysical systems ranging in scale from stellar interiors (e. g. Brüggen & Hillebrandt 2001) and protoplanetary disks (e. g. Johansen et al. 2006) to the evolution of the intergalactic medium (e. g. Nulsen 1982, 1986). Physically, the KH instability wraps up coherent sheets of vorticity into smaller, less organized structures. The small scale motion then stretches and cascades to yet smaller scales. The instability therefore plays fundamental roles in fluid mixing and in the transition to turbulence.

Because of its prevalence in nature and its physical significance, KH test problems are commonly used to evaluate the accuracy of different astrophysical hydrodynamics codes (e. g. Springel 2010; Hopkins 2015; Schaal et al. 2015): if a code can properly simulate the KH instability, it is presumed to capture mixing and turbulence in astrophysical simulations. Ideally, such an important test problem should stand against an analytic solution to ensure the veracity (not just reproducibility) of simulation results. Some analytic work addresses the KH instability with a sheet vortex model (Moore 1979), but only for incompressible fluid equations. In the incompressible limit, one can study this problem numerically by approximating the vortex sheet as a finite number of vortices, and then solving for the vortex dynamics (Krasny 1986). However, as we will show below, density variations change the problem substantially. For the compressible Navier-Stokes equations relevant to astrophysics, no analytic description of the nonlinear KH instability currently exists.

Absent a nonlinear analytic prediction, a resolved reference simulation provides the only reasonable approximation of the true solution. Comparing to a well-controlled and high-resolution benchmark gives a proxy for the true error of a given test. Robertson et al. (2010) and McNally et al. (2012) present careful studies of the early evolution of the KH instability. These authors also point out the numeric ill-posededness of contact-discontinuity simulations, in spite of exist-

ing analytical solutions in the linear and/or incompressible regimes. These works emphasize that converged nonlinear simulations require well-resolved initial conditions. One limitation of these studies, however, is that Robertson et al. (2010) and McNally et al. (2012) only provide converged reference simulations for the linear (and possibly weakly nonlinear) phase. In addition, converged nonlinear solutions require solving dissipative equations. Many available astrophysical codes do not implement this essential feature. As a result, these works could only follow the instability for a few e-folding timescales. Furthermore, although almost all astrophysical systems are three-dimensional, test problems are typical run in only two dimensions. Salvesen et al. (2014) performed KH convergence tests in both two and three dimensions. They found that simulations differed dramatically between resolutions in two dimensions, but found little resolution dependence in three-dimensional simulations. Porter et al. (1994) found similar results in three-dimensional turbulence simulations.

Not all works take the benchmark approach, however. In place of a nonlinear reference solution, some authors use apparent small-scale structure as a proxy for the accuracy of their simulations (e.g., Springel 2010; Hopkins 2015). Presumedly, more small-scale structure implies less numerical dissipation, and therefore greater accuracy. We find in the current chapter that this intuition can, in some cases, lead to false conclusions. Mocz et al. (2015) shows that small-scale structure is moving-mesh codes can be due to grid-noise rather than physical effects, and describes methods to mitigate these errors. Some tests also abandon the smooth initial conditions of Robertson et al. (2010) and McNally et al. (2012), even though this choice precludes convergence of even the linear phase of the instability because the linear growth rates increase with wavenumber for an initially discontinuous velocity profile.

In this chapter, we extend the work of McNally et al. (2012) by providing reference solutions for the *strongly nonlinear* evolution of the KH instability. We use a smooth initial condition and explicit diffusion. We conduct simulations using both Athena (a Godunov code), and Dedalus (a pseudo-spectral code that can solve the Navier-Stokes equations of compressible hydrodynamics) and find that both converge to the same reference solutions. We see agreement among different codes and different resolutions, with the validity of the reference solution limited only by (unavoidable) chaotic evolution at late times. We propose that future code tests include this KH instability problem and compare to our validated, converged, reference solutions.

We organize the remainder of the chapter as follows. Section 4.2 describes the equations, initial conditions, and codes used for our simulations. The results comprise two sections. In section 4.3.1 we discuss the simpler simulations with constant initial density. Section 4.3.2 discusses the more complicated simulations with an initial density jump. Section 4.4, summarizes our results.

## 4.2 Methods

### 4.2.1 Equations and Initial Conditions

We solve the hydrodynamic equations, including explicit terms for the diffusion of momentum and temperature:

$$\frac{\partial \rho}{\partial t} + \boldsymbol{\nabla} \cdot (\rho \, \boldsymbol{u}) = 0, \tag{4.1a}$$

$$\frac{\partial}{\partial t}(\rho \, \boldsymbol{u}) + \boldsymbol{\nabla} \cdot (P \, \mathbf{I} + \rho \, \boldsymbol{u} \otimes \boldsymbol{u}) = -\boldsymbol{\nabla} \cdot \boldsymbol{\Pi}, \tag{4.1b}$$

$$\frac{\partial E}{\partial t} + \boldsymbol{\nabla} \cdot [(E + P) \, \boldsymbol{u}] = \boldsymbol{\nabla} \cdot (\chi \rho \boldsymbol{\nabla} T) - \boldsymbol{\nabla} \cdot (\boldsymbol{u} \cdot \boldsymbol{\Pi}), \tag{4.1c}$$

along with the nondimensionalized ideal gas equation of state, $P = \rho T$, with constant ratio of specific heats $\gamma = 5/3$. $\mathbf{I}$ is the identity tensor, $\chi$ is the thermal diffusivity (with units $\mathrm{cm}^2/\mathrm{s}$; $K = n k_\mathrm{b} \chi$ is the thermal conductivity), and

$$\boldsymbol{\Pi} = -\nu\rho \left( \boldsymbol{\nabla u} + (\boldsymbol{\nabla u})^T - \frac{2}{3} \mathbf{I} \boldsymbol{\nabla} \cdot \boldsymbol{u} \right) \tag{4.2}$$

is the viscous stress tensor with viscosity $\nu$ (with units $\mathrm{cm}^2/\mathrm{s}$). We assume both $\nu$ and $\chi$ are constant.

We add a passive scalar to our simulations which we refer to as "dye." The local fraction of dye particles $c$ expresses dye concentration, and initially ranges from 0 to 1. The local conservation of dye is then

$$\frac{\partial}{\partial t}(\rho c) + \nabla \cdot (\rho c \, \boldsymbol{u}) = \rho \frac{dc}{dt} = -\nabla \cdot \boldsymbol{Q}_\mathrm{dye}, \tag{4.3}$$

$$\boldsymbol{Q}_\mathrm{dye} = -\rho \nu_\mathrm{dye} \nabla c, \tag{4.4}$$

where $d/dt$ represents the Lagrangian derivative, and $\nu_\mathrm{dye}$ represents a diffusion coefficient for dye molecules (with units $\mathrm{cm}^2/\mathrm{s}$). These equations conserve the total dye mass $\int \rho \, c \, \mathrm{d}V$.

We define a dye entropy per unit mass $s \equiv -c \, \ln c$, along with its volume integral

$$S \equiv \int \rho \, s \, \mathrm{d}V. \tag{4.5}$$

These evolve such that:

$$\rho \frac{ds}{dt} - \nabla \cdot \left[ (1 + \ln c) \, \boldsymbol{Q}_\mathrm{dye} \right] = \rho \nu_\mathrm{dye} \frac{|\nabla c|^2}{c}, \tag{4.6}$$

$$\frac{dS}{dt} = \int \rho \nu_\mathrm{dye} \frac{|\nabla c|^2}{c} \mathrm{d}V \geq 0. \tag{4.7}$$

The second term on the left-hand side of equation 4.6 represents the entropy flux due to reversible diffusion of the dye. The right-hand side represents entropy generation due to non-reversible dissipation.[1] The volume-integrated entropy $S$ satisfies the following important properties:

1. A fully unmixed fluid with $c = 0$ or $c = 1$ everywhere has zero entropy ($S = 0$).
2. A fully mixed fluid with $c^* = \int \rho\, c \,\mathrm{d}V / \int \rho \,\mathrm{d}V$ maximizes the entropy.
3. $S$ increases monotonically with time if $\nu_{\mathrm{dye}} > 0$, and stays constant otherwise.

We restrict our attention to periodic simulations. This avoids potential difficulties with imposing Dirichlet and/or Neumann boundary conditions. Our initial conditions are:

$$\rho = 1 + \frac{\Delta\rho}{\rho_0} \times \frac{1}{2}\left[\tanh\left(\frac{z - z_1}{a}\right) - \tanh\left(\frac{z - z_2}{a}\right)\right] \tag{4.8a}$$

$$u_x = u_{\mathrm{flow}} \times \left[\tanh\left(\frac{z - z_1}{a}\right) - \tanh\left(\frac{z - z_2}{a}\right) - 1\right] \tag{4.8b}$$

$$u_z = A \sin(2\pi x) \times \left[\exp\left(-\frac{(z - z_1)^2}{\sigma^2}\right) + \exp\left(-\frac{(z - z_2)^2}{\sigma^2}\right)\right] \tag{4.8c}$$

$$P = P_0 \tag{4.8d}$$

$$c = \frac{1}{2}\left[\tanh\left(\frac{z - z_2}{a}\right) - \tanh\left(\frac{z - z_1}{a}\right) + 2\right], \tag{4.8e}$$

where $a = 0.05$ and $\sigma = 0.2$ are chosen so that the initial condition is resolved in all of our simulations. We take $u_{\mathrm{flow}} = 1$ and $P_0 = 10$ so that the flow is subsonic with a Mach number $M \sim 0.25$ in regions with $\rho = 1$ and $M \sim 0.35$ in regions with $\rho = 2$. The size of the initial vertical velocity perturbation is $A = 0.01$. The Athena simulations are initialized with these functions evaluated at cell-centers even though Athena data represents cell-averaged quantities (see Appendix 4.A for more discussion of this effect).

We adopt a rectangular domain with $x$ in $[0, L)$, and $z$ in $[0, 2L)$, with $L = 1$, and $z_1 = 0.5$, $z_2 = 1.5$, with periodic boundary conditions in both directions. The simulations have a horizontal resolution of $N$ grid points (in Athena) or modes (in Dedalus) in the $x$ direction, and $2N$ grid points/modes in the $z$ direction. Our initial condition has a reflect-and-shift symmetry: taking $z \to 2 - z$ and $x \to x + 1/2$ changes the sign of $u_z$ but leaves the other quantities invariant. Thus, the simulations solve for the same flow twice. This is a requirement when using periodic boundary conditions, but also provides a test of whether or not the numerical simulations can preserve the symmetry. Almost all simulations presented here maintain the symmetry. We therefore only show the lower half of the domain. We calculate volume-averaged quantities like the dye entropy or the $L_2$ norm with respect to the entire domain.

In equation 4.8a, the free parameter $\Delta\rho/\rho_0$ represents the density jump across the interface. We study simulations with $\Delta\rho/\rho_0 = 0$ in section 4.3.1 and with $\Delta\rho/\rho_0 = 1$ in section 4.3.2. We refer

[1] Equation 4.6 can be made to look like the analogous equation for heat conduction with the definition of a new "temperature" $T_{\mathrm{dye}} \equiv -\frac{1}{1+\ln c}$

to this change in density as a "jump" throughout, although the transition is smooth, set by the tanh in equation 4.8a. The Reynolds number Re quantifies diffusion,

$$\nu = \chi = \nu_{\rm dye} = \frac{L\Delta u}{\rm Re}, \tag{4.9}$$

where $\Delta u = 2u_{\rm flow}$ is the change in velocity. Note that we set the thermal diffusivity $\chi$ constant; consequently, the thermal conductivity $K \propto \rho$. Throughout the chapter we measure time in units of $L/u_{\rm flow}$, so $t = 1$ corresponds to approximately one turnover time. Equations 4.1–4.9 specify our system, with the free parameters $\Delta\rho/\rho_0$ and Re. In the following section we detail our methods for solving this system of equations.

### 4.2.2 Numerical Methods

We study the KH instability using two open-source codes employing very different numerical methods: Athena & Dedalus.

Athena[2] is a finite-volume Godunov code (Gardiner & Stone 2008; Stone et al. 2008). The scheme represents all field quantities with volume averaged values in each grid element. A Riemann problem solves for fluxes between elements. We use third-order reconstruction with limiting in the characteristic variables to approximate field values at the element walls (Colella & Woodward 1984), the HLLC Riemann solver (Toro 2013), and the CTU integrator (Colella 1990), and super-timestepping for the diffusive terms (Choi et al. 2009; Alexiades et al. 1996). We used the "-O3" compiler flag using Intel 14.0.1.106 and Mvapich2 2.0b on the Stampede supercomputer. We repeated some runs using second-order reconstruction and/or the Roe Riemann solver and/or stricter compiler flags (e.g., "-O2 -fp-model strict") — these choices did not qualitatively affect the solutions. We use a static, uniform mesh, and a CFL safety factor of 0.8.

Athena is second-order accurate in both space and time. The leading-order grid-scale errors are diffusive. For most simulations reported here, we include explicit diffusion. A sufficiently large explicit diffusion can dominate grid-scale errors and allow the simulation to remain close to the true solution. However, higher-order grid-scale errors can introduce non-diffusive effects, such as dispersion. If higher-order errors project onto unstable modes, they can cause large differences in the solution, despite being higher order. The grid-scale errors in Athena respect the reflect-and-shift symmetry of our problem up to floating point accuracy, so even non-converged simulations can maintain the initial symmetry of the flow. In practice, we find all simulations maintain the initial symmetry, except simulations with $\Delta\rho/\rho_0 = 1$ without explicit diffusion. Since Athena's algorithm manifestly preserves this symmetry, we expect the error results from chaotic amplification of floating-point errors.

Dedalus[3] is a pseudo-spectral code (Burns et al. 2016). All field variables are represented as Fourier series, and the simulation solves for the evolution of the spectral-expansion coefficients in time. The code evaluates nonlinear terms on a grid with a factor 3/2 more points than Fourier coefficients; i.e., the 2/3 de-aliasing rule. Lecoanet et al. (2014) (appendix D.1) describes our

[2]Athena is available at https://trac.princeton.edu/Athena/.

[3]Dedalus is available at http://dedalus-project.org.

implementation of the Navier-Stokes equations. Our implementation of the dye evolution equation is

$$\partial_t c - \nu_{\text{dye}} \left(\partial_x^2 c + \partial_z c_z\right) = \\ - u\partial_x c - w c_z + \nu_{\text{dye}} \left(\partial_x \Upsilon' \partial_x c + \partial_z \Upsilon' c_z\right), \tag{4.10a}$$

$$c_z - \partial_z c = 0, \tag{4.10b}$$

where we use the same notation as Lecoanet et al. (2014). For timestepping, we use a third-order, four-stage DIRK/ERK method (RK443 of Ascher et al. 1997) with a total CFL safety factor of 0.6 (i.e., 0.15 per stage). This formulation allows implicit timestepping of sound waves. Thus, our timestep size only adjusts with the flow velocity, not the sound speed. The excellent agreement between the highest resolution Dedalus and Athena simulations shows that high-wavenumber sound waves have negligible influence on the solution.

The pseudo-spectral method produces almost no numerical diffusion. Stability concerns require explicit diffusion in nonlinear calculations. In marginally resolved simulations, discretization errors manifest as Gibbs' ringing, which is prominently visible in snapshots. The numerical method does not explicitly preserve the reflect-and-shift symmetry—numerical errors can put power into the asymmetric modes. However, we find that in resolved simulations these asymmetric modes never grow to large amplitudes. Thus, maintaining this symmetry gives a test for a simulation's fidelity.

## 4.3 Results

This section describes the nonlinear evolution of the KH instability, provides reference solutions, and compares the performance of Dedalus and Athena. Section 4.3.1 considers unstratified simulations with constant initial density; both codes handle this problem easily. Section 4.3.2 concerns simulations with a density jump across the shear interface. This problem shows rich behavior and poses significant numerical challenges. In both cases, a central vortex forms which wraps up material from above and below the initial interface into thin filaments.

### 4.3.1 Unstratified simulations ($\Delta\rho/\rho_0 = 0$)

In this section, we discuss simulations with constant initial density ($\Delta\rho/\rho_0 = 0$). Figure 4.1 visualizes the flow with the dye concentration field of the lower half of the domain for simulations with explicit diffusion at different resolutions and Reynolds number, Re. The flow consists of coherent filaments of unmixed fluid with dye concentration close to zero or one. The filaments twist around the central vortex until they become thin enough to diffuse away. The central vortex stays coherent in all simulations, and exhibits a more gradual dye-concentration gradient than in the filaments. This reflects the smooth velocity and dye initial condition.

The snapshots show the state at $t = 6$. Strong nonlinearity begins at $t \sim 2$, so this corresponds to at least four turnover times after the initial saturation of the instability. The simulations are labeled

*Table 4.1*: List of simulations with $\Delta\rho/\rho_0 = 0$. The character refers to the code used (D for Dedalus, A for Athena, and N for Athena with no explicit diffusion), and the number is the horizontal resolution.

| $\mathrm{Re} = 10^4$ | $\mathrm{Re} = 10^5$ | $\mathrm{Re} = 10^6$ | No explicit diffusion[a] |
|---|---|---|---|
| D512 | D512 | D512 | N1024 |
| A512 | D512dt[b] | D1024 | N2048 |
| A1024 | D1024 | D2048 | N4096 |
| | D2048 | A1024 | |
| | A1024 | A2048 | |
| | A2048 | A4096 | |

[a]Run in Athena.

[b]Run with half the CFL safety factor.

by the code used (A for Athena; D for Dedalus), and their horizontal resolution (see Table 4.1 for a list of simulations with $\Delta\rho/\rho_0 = 0$).

$\mathrm{Re} = 10^5$

Many of the simulations with the same Re but different resolution look similar by eye. To more quantitatively assess convergence, we calculate the $L_2$ norm of the differences between dye concentration fields in different simulations:

$$L_2(c_\mathrm{X} - c_\mathrm{Y}) = \left[\int \mathrm{d}V\, (c_\mathrm{X} - c_\mathrm{Y})^2\right]^{1/2}, \tag{4.11}$$

where $c_\mathrm{X}$ and $c_\mathrm{Y}$ represent the dye concentration fields in two simulations, X and Y. The Athena and Dedalus grids are different, so we use spectrally accurate techniques to interpolate Dedalus solutions to the Athena grid for direct comparison (Appendix 4.A). We argue in Appendix 4.B that all simulations converge to our highest-resolution Dedalus simulations; thus, we assume these simulations are a good approximation to the "true" solution.

Figure 4.2 shows the $L_2$ norm of the difference between dye concentration fields of D2048 and other simulations with $\mathrm{Re} = 10^5$. Because we believe D2048 closely represents the true solution (Appendix 4.B), we call this the $L_2$ norm of the error. Solutions from both codes approach D2048 as resolution increases. At late times, A2048 and D1024 have roughly eight-times smaller errors than A1024 and D512, respectively. That is, both codes exhibit third-order convergence. This indicates that interpolation produces the dominant error in Athena, which is the only third-order part of the algorithm. The Dedalus simulations are spatially resolved, so timestepping produces the dominant error source in the Dedalus simulations, which is also third order. We also plot errors from D512dt, which is run with a horizontal resolution of 512, but with half the CFL safety factor. D512dt is almost as accurate as D1024, showing that the higher accuracy of D1024 is mostly due to taking smaller timesteps. There are certain times (most notably near $t = 3.5$) where the flow develops smaller structures, and extra spatial resolution is required. The errors in quantities other than dye concentration (e.g., density) follow similar behavior to that shown in Figure 4.2.

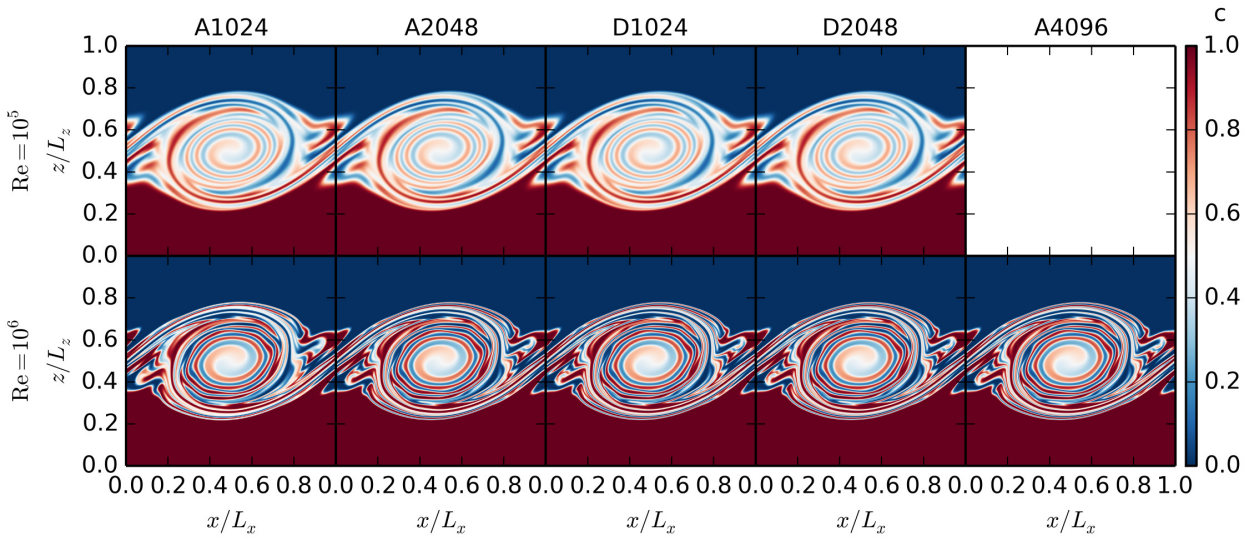


*Figure 4.1*: Snapshots of the dye concentration field in several simulations with $\Delta\rho/\rho_0 = 0$ at $t = 6$. The upper (lower) row shows simulations with Re $= 10^5$ ($10^6$). All the simulations with Re $= 10^5$ are well resolved. Small differences exist between the lower-resolution Athena simulations at Re $= 10^6$ and the highest-resolution Athena simulation & Dedalus simulations (e.g., near $(x, z) = (0.9, 0.6)$, see Figure 4.7).

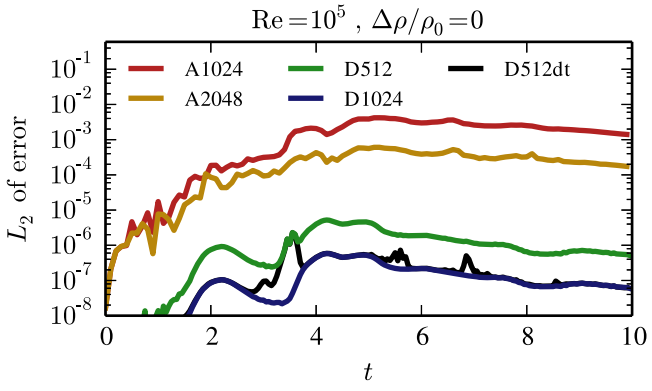


*Figure 4.2*: $L_2$ norm of dye-concentration errors for $\Delta\rho/\rho_0 = 0$ and Re $= 10^5$. We take D2048 as the "true" solution (see Appendix 4.B). Both Dedalus and Athena exhibit third-order convergence. D512dt is run with half the timestep size as D512. Its error is similar to D1024, showing that the higher accuracy of D1024 is mostly due to a smaller timestep size rather than higher spatial resolution.

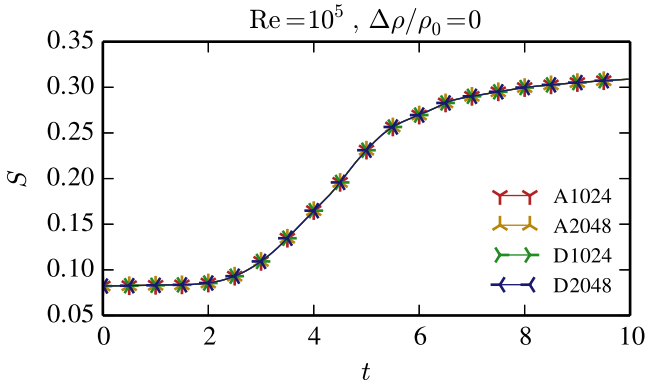


*Figure 4.3*: Volume-integrated dye entropy (equation 4.5) as a function of time for the four simulations with Re = $10^5$ shown in Figure 4.1. All simulations are well resolved, so the dye entropies are almost equal.

We calculate the volume-integrated dye entropy for each simulation (equation 4.5). Figure 4.3 plots the entropy as a function of time. Because all simulations are well resolved, there are no visible differences in the entropy between the different simulations.

Re = $10^6$

The unmixed filaments are much thinner for Re = $10^6$ than for Re = $10^5$, challenging the codes. Unlike the Re = $10^5$ case, some minor visible differences appear between the solutions for Re = $10^6$. The lower-resolution simulations do not fully resolve the flow (one such feature is highlighted in Figure 4.7).

To assess convergence, we again plot the $L_2$ norm of the error in dye concentration with respect to D2048 (Figure 4.4). A1024 has the largest errors of any simulation. At late times, the errors interact nonlinearly, whereas the errors in the higher-resolution Athena simulations stay linear and the temporal variation of the error is the same independent of the magnitude of the error. The ratio of errors of the two higher-resolution Athena simulations is about 6—in between second- and third-order convergence. This suggests that the size of interpolation errors roughly match the size of other errors in the code (e.g., from the Riemann problem or timestepping).

The difference in errors between D512 and D1024 is about 100—much larger than the difference in errors between the Athena simulations. D512 (not shown in Figure 4.1) underresolves the flow and includes some low-amplitude Gibbs' ringing. Increasing the resolution from 512 to 1024 eliminates spatial errors because of the exponential convergence of spectral methods. This allows for very large error reduction with only modest resolution changes. The exponential nature of spectral methods makes convergence practically binary: simulations with Gibbs' ringing are not converged; simulations without Gibbs' ringing very likely are converged.

We plot volume-integrated dye entropy for Re = $10^6$ in Figure 4.5. Like for Re = $10^5$, all well-resolved simulations produce similar entropy. However, the under-resolved A1024 produces slightly more entropy. This agrees with the heuristic that extra numerical diffusion leads to excess

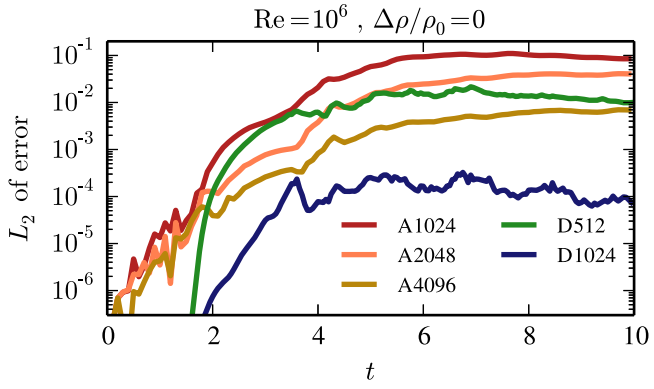


*Figure 4.4*: $L_2$ norm of dye-concentration errors for $\Delta\rho/\rho_0 = 0$ and Re = $10^6$. A1024 is not well resolved so its errors follow a different pattern than the other Athena simulations. The errors in A4096 are smaller than the errors in A2048 by $\approx 6$. The errors in D1024 are smaller than the errors in D512 by about 100. This demonstrates the fast (exponential) convergence of spectral methods.

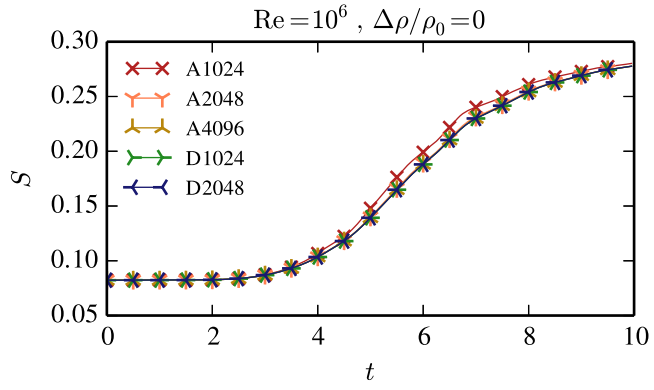


*Figure 4.5*: Volume-integrated dye entropy (equation 4.5) as a function of time for the five simulations with Re = $10^6$ shown in Figure 4.1. The entropy of all simulations are very similar except for A1024; this is another indication that A1024 is not well resolved.

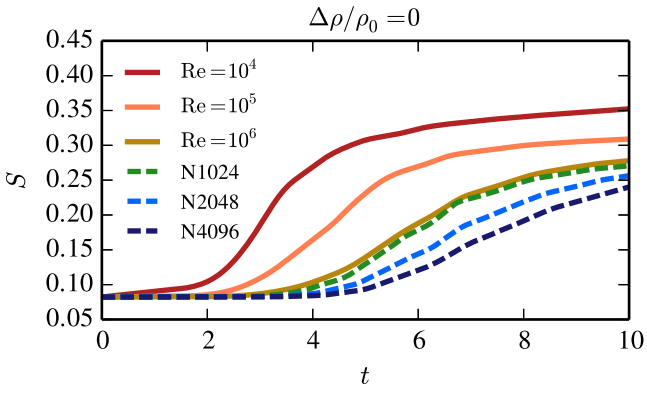


*Figure 4.6*: Volume-integrated dye entropy (see section 4.2.2) as a function of time with $\Delta\rho/\rho_0 = 0$, for three resolved simulations with different Re, as well as three Athena simulations with no explicit diffusion (dashed lines; labeled with N, for no explicit diffusion, and their horizontal resolution). The entropy of N1024 and the simulation with Re $= 10^6$ are very similar. Their flow fields show minor differences (see Figure 4.7). Note that the entropy decreases with increasing resolution in the simulations without explicit diffusion. This is not the case in simulations with an initial density jump (see Figure 4.16).

entropy generation.

**An effective Reynolds number?**

We now describe Athena simulations without any explicit diffusion. These simulations have all three diffusivities equal to zero, i.e., $\nu = \kappa = \nu_{\rm dye} = 0$. An important question is, does the numerical diffusion in Athena act like an explicit diffusion? Put another way, does Athena have an effective Reynolds number at a given resolution for this problem? As we describe below and in section 4.3.2, the answer to this question is very problem dependent.

To test this, we plot the converged volume-integrated dye entropy for several Reynolds numbers, along with the volume-integrated dye entropy for Athena simulations without explicit diffusion (Figure 4.6); simulations run without explicit diffusion are labelled with N. The entropy evolution of N1024 is similar to the entropy evolution for Re $= 10^6$. This might lead one to think that the effective Reynolds number of this Athena simulation is about $10^6$.

However, a closer investigation shows that N1024 and the Re $= 10^6$ simulation have different dye concentration fields which, by chance, result in similar volume-integrated entropies (Figure 4.7). Instead, the dye concentration field of N1024 looks like the dye concentration field of the (under resolved) A1024 simulation with Re $= 10^6$. Figure 4.5 shows A1024 has a higher entropy than the true Re $= 10^6$ solution. By removing the explicit diffusion, the flow evolution remains similar to A1024 (and different from the resolved Re $= 10^6$ solution), but the interfaces between filaments are sharper, which decreases the entropy. The effects of having the incorrect flow field (increasing entropy), but sharper interfaces between filaments (decreasing entropy) happen to cancel out, so the entropy of N1024 is similar to that of Re $= 10^6$.

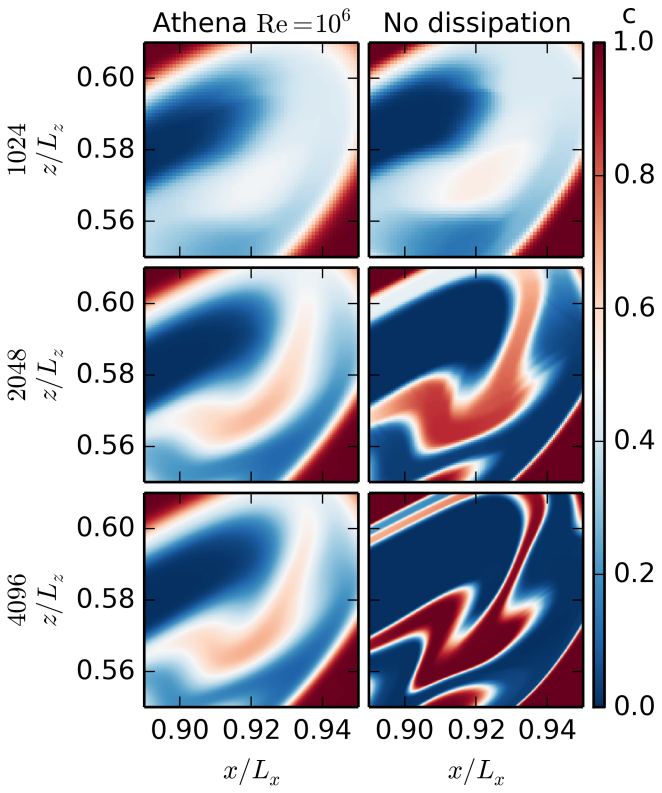


*Figure 4.7*: Snapshots of the dye concentration field between $0.89 < x < 0.95$ and $0.55 < z < 0.61$, at $t = 6$ for $\Delta\rho/\rho_0 = 0$. All simulations use Athena, either with Re = $10^6$ (left column) or no explicit diffusion (right column). The three rows have different resolutions. This zoom-in of Figure 4.1 highlights the differences between simulations at different resolutions—however, for the most part, the simulations look very similar. A2048 & A4096 represent resolved simulations with Re = $10^6$. Although the entropies for N1024 (upper right plot) & A4096 (lower left plot) track each other (Figure 4.6), the dye concentration fields exhibit minor differences.

*Table 4.2*: List of simulations with $\Delta\rho/\rho_0 = 1$. The character refers to the code used (D for Dedalus, A for Athena, and N for Athena with no explicit diffusion), and the number is the horizontal resolution.

| Re = $10^5$ | | No explicit diffusion |
|---|---|---|
| Dedalus | Athena | Athena |
| D2048 | A1024 | N512 |
| D2048r[a] | A2048 | N1024 |
| D2048p[b] | A4096 | N2048 |
| D3072 | A8192 | N4096 |
| D4096 | A16384 | |

[a]Restarted from A2048 at $t = 3.2$.

[b]Different initial perturbation.

Although we have highlighted the differences between N1024 and the converged solutions with Re = $10^6$, it is worth reiterating that the two solutions are in fact remarkably similar. This shows that N1024 roughly has an effective Reynolds number of $10^6$. In detail, however, the remaining modest differences between N1024 and the Re = $10^6$ solution demonstrate that the numerical dissipation in Athena is not exactly equivalent to physical dissipation via viscosity and thermal conduction.

One difficulty with the notion of an effective Reynolds number is that it is extremely problem dependent, even at fixed resolution. In the next section, we introduce a small (by astrophysical standards) density jump into the initial condition. This completely changes the problem by introducing secondary instabilities which enhance mixing, producing very clear differences between resolved simulations and Athena simulations without explicit diffusion (Figure 4.15). For the constant-density problem described here, omitting diffusion produces less entropy. Including a density jump reverses this trend: simulations with only numerical diffusion undergo *more* mixing than simulations with explicit diffusion. Although assigning an effective Reynolds number to Athena simulations without explicit diffusion may be reasonably accurate for the constant-initial-density problem, this does not carry over to the problem with an initial density jump.

### 4.3.2 Simulations with a density jump ($\Delta\rho/\rho_0 = 1$)

Both the qualitative features of the flow and the convergence properties of the simulations change dramatically once we introduce an initial density jump ($\Delta\rho/\rho_0 \neq 0$). Unlike the unstratified case, secondary instabilities of the filaments produce small-scale structures in the flow. These secondary instabilities, and the resulting small-scale features, depend on the resolution and the code used. As a result, simulations with a nonzero density jump require far more computational resources than the unstratified simulations presented in the previous section. We limit the simulations with explicit diffusion to Re = $10^5$—our finite computing budget precludes solutions for Re = $10^6$. The largest simulations required roughly $10^6$ core-hours.

Figure 4.8 shows the dye concentration for different simulations at different times. In both Dedalus simulations, and the highest-resolution Athena simulation, the outer filaments (i.e., those

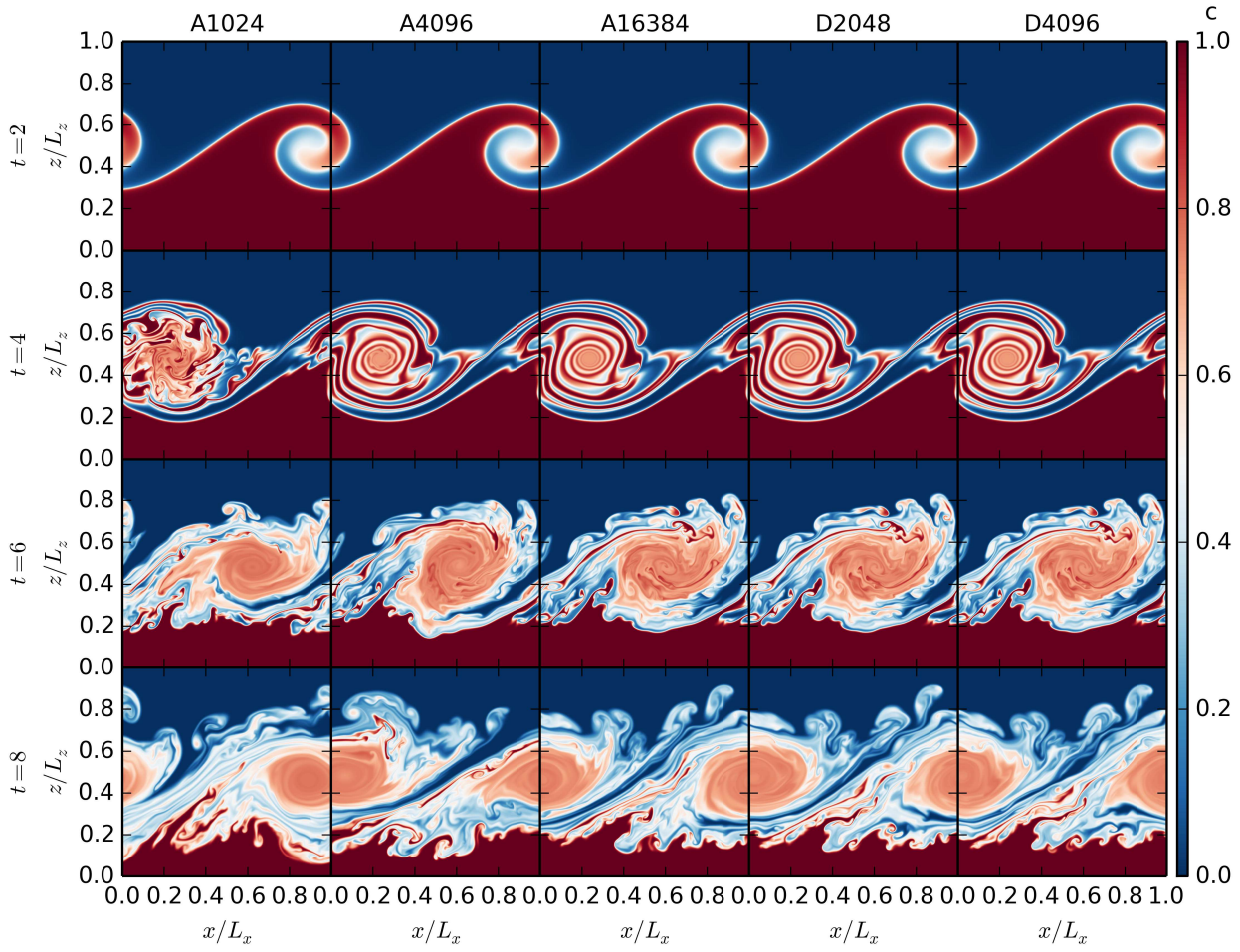


*Figure 4.8*: Snapshots of the dye concentration field in several simulations with $\Delta\rho/\rho_0 = 1$ and Re $= 10^5$. Each row corresponds to a different time. The low-resolution Athena simulations suffer from a secondary instability (seen at $t = 4$) in the middle of the vortex, which is not present in the Dedalus simulations nor A16384. This causes substantial differences at later times. A16384 and both Dedalus simulations stay very similar at late times, although small differences develop from chaos (see section 4.3.2).

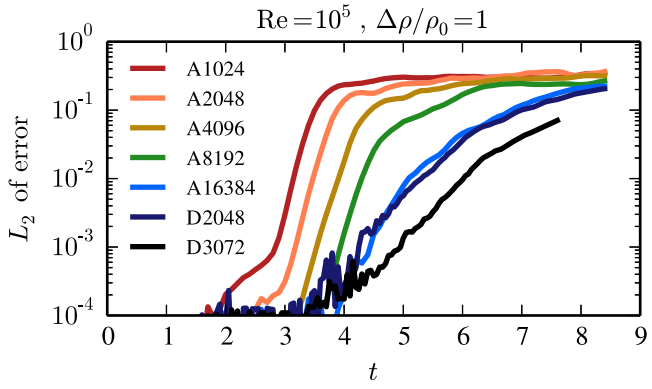


*Figure 4.9*: $L_2$ norm of dye-concentration errors for $\Delta\rho/\rho_0 = 1$ and $\mathrm{Re} = 10^5$. D3072 and D4096 are the closest pair of simulations, suggesting that D4096 is a good approximation to the true solution. All Athena simulations except A16384 diverge away from D4096 exponentially with a rate of 8, suggesting the growth rate of the inner vortex instability (see Figure 4.10) is also 8. The errors in the lower-resolution Dedalus simulation and A16384 grow exponentially with a rate of about 2-3. We interpret this divergence as due to chaos (see section 4.3.2). D3072 has errors smaller than D2048 by $\approx 4$, consistent with third-order convergence set by our choice of timestepping algorithm.

outside the central vortex) become unstable to a sausage-like mode (see the panel in Figure 4.10 for an example). Lower-resolution Athena simulations also undergo a separate instability of the inner filaments of the vortex. We refer to these two instabilities at the outer-filament instability (OFI) and the inner-vortex instability (IVI) (see Figure 4.10 for examples). These instabilities are similar to the baroclinic secondary instabilities discussed in Reinaud et al. (2000); Fontane & Joly (2008). The competition between these two instabilities plays a crucial role in the evolution of the system.

We plot the $L_2$ norm of the error in dye concentration with respect to D4096 in Figure 4.9. As described in Appendix 4.B, we believe D4096 approximates the true solution. The difference between D3072 and D4096 are smaller than the differences between any other pair of simulations. At later times, even the errors between D3072 and D4096 become large. In section 4.3.2 we attribute this late-time behavior to chaos.

Figure 4.9 shows that at early times, the low-resolution Athena simulations diverge exponentially from D4096 with an inferred growth rate of about 8. The IVI produces this divergence. Furthermore, the four Athena simulations with resolutions between 1024 and 8192 are all equally spaced horizontally in Figure 4.9. The horizontal-axis spacing is $\log 2/2$ time units. This suggests that the same instability exists independent of resolution, but the amplitude of the perturbation that seeds the instability drops by 16 when the resolution doubles. Though numerical errors seed the growth, the constant growth rate of the IVI suggests it is a physical instability).

The IVI is a robust feature of low-resolution Athena simulations. Using the Roe integrator, second-order reconstruction, or shifting the initial condition by half a grid point does not affect the development of this instability (as confirmed using the $L_2$ error), but can cause visible differences

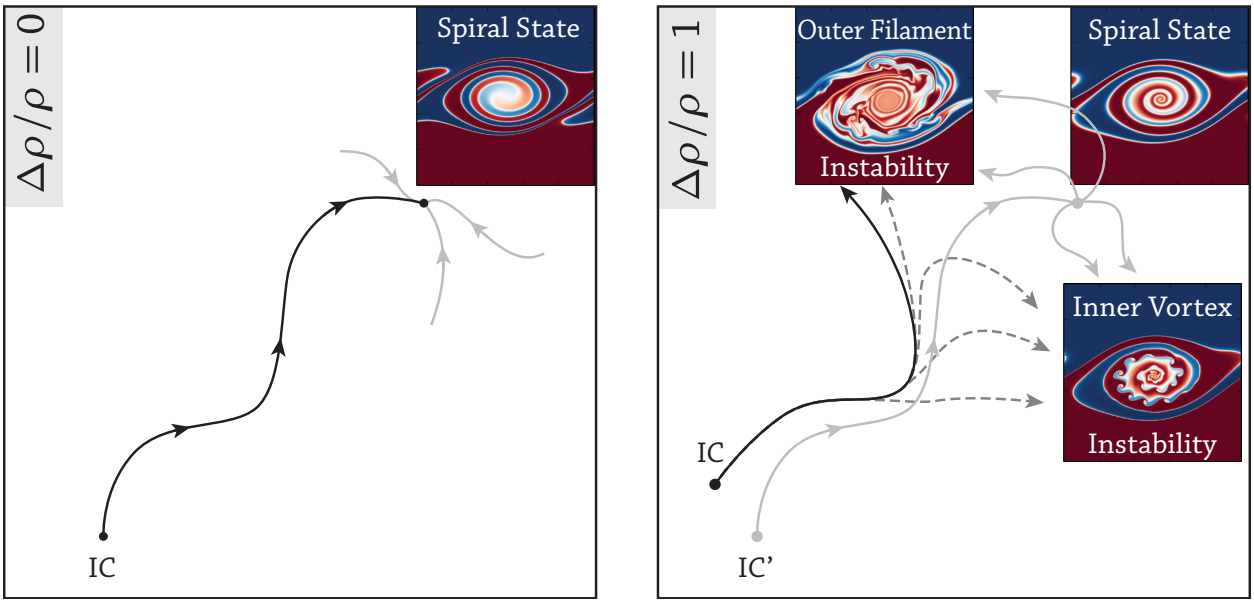


*Figure 4.10*: Schematic phase-space diagram for $\Delta\rho/\rho_0 = 0$ (left) and $\Delta\rho/\rho_0 = 1$ (right). For constant initial density, the system has a stable state with ever-narrowing spiral filaments. We hypothesize that there is an initial condition IC' (right panel) leading to a similar spiral state for $\Delta\rho/\rho_0 = 1$. But this state is now unstable to the outer filament instability (OFI) and the inner vortex instability (IVI). Our chosen initial condition's (IC) trajectory (solid black line) approaches the spiral state, but becomes unstable to the OFI. Errors introduced by the numerical hydrodynamics may cause deviations in the trajectory leading to the IVI (dashed grey lines).

in the flow evolution. This demonstrates that grid-scale errors drive the IVI. Using first-order reconstruction suppresses the IVI, but the enhanced numerical diffusion causes large errors. We have also tried adding low-amplitude (up to $10^{-4}$) white noise to the initial density or pressure. These do not cause any visible changes to the IVI. The flow forgets some of the detailed information of its initial condition (see section 4.3.2).

The highest-resolution Athena simulation (A16384) does not develop the IVI. This demonstrates that the initial condition is in fact stable to the IVI; the problem is well-posed. Rather, numerical errors seed the IVI at some later time, during the evolution of the flow. Although some numerical errors are still inevitably present, A16384 does not develop the IVI because the "base state" of spiralling filaments of unmixed fluid also succumbs to the OFI. In this case, the OFI disrupts the inner vortex before the IVI grows to large amplitudes (see Figure 4.10).

The absence of the IVI is a robust feature of our Dedalus simulations. We confirmed the stability of the base state by re-running D2048 with low-amplitude white noise added to the initial condition; we also re-initialized D2048 from the Athena initial condition. This introduces small but non-random grid-representation differences (section 4.3.2). In both cases, we recover the same evolution. However, we can trigger the IVI in Dedalus with a large ($\sim$ 10% by energy) perturbation to the initial condition (section 4.3.2).

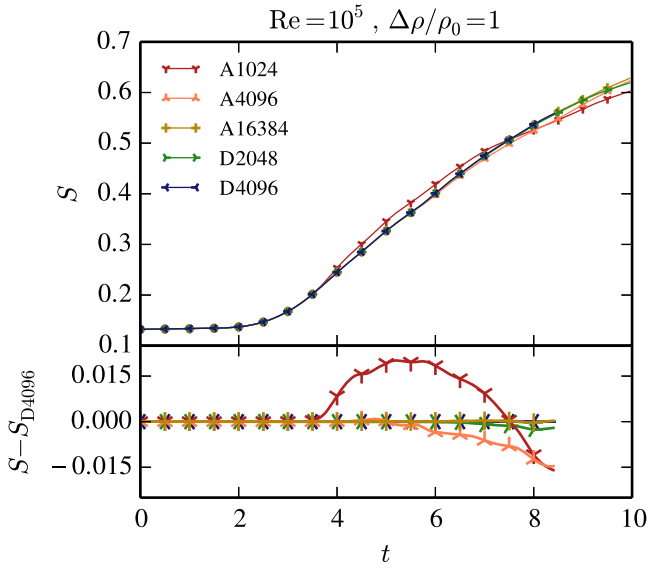


*Figure 4.11*: Volume-integrated dye entropy (equation 4.5) as a function of time for simulations with $\Delta\rho/\rho_0 = 1$ and Re = $10^5$. The top panel plots the entropy, and the bottom panel plots the entropy deviation from D4096. The entropy of all the simulations diverge from D4096, but the less-accurate simulations diverge faster. For each Athena simulation, the entropy initially increases faster than D4096 when it starts to diverge. At later times, the entropy sometimes drops below the entropy of D4096.

Figure 4.10 summarizes the relation between the two secondary instabilities in this problem. For a constant initial density (left panel), the system evolves toward a stable state characterized by spiraling filaments. Small differences in initial conditions, integration algorithms, presence of dissipation, etc., cause only minor changes in the evolution. We hypothesize that a similar spiral state also exists for $\Delta\rho/\rho_0 = 1$, and that it could be reached from some initial condition IC'. However, our simulations demonstrate that the spiral state is now unstable. Thus, small errors lead to the large differences in evolution.

Small perturbations to the hypothetical IC' of Figure 4.10 would lead to trajectories that either develop the OFI or the IVI. However, our chosen initial condition, IC, is squarely in the attracting basin of the OFI. Thus, infinitesimal perturbations to IC will still lead to the OFI. Errors introduced by numerical hydrodynamics cause the codes to not follow the correct trajectory (solid black line). Certain types of errors can cause trajectories to diverge from the correct solution, sometimes toward the IVI (dashed grey lines). Alternatively, sufficiently large initial perturbations can also knock the system into the attracting basin of the IVI (section 4.3.2).

We note that the phase space for this problem is very high dimension, and that the outer filament instability and inner vortex instability represent two (likely non-parallel) unstable directions of the spiral state's stable manifold. Thus, both instabilities can act simultaneously, which sometimes occurs in simulations.

Figure 4.11 shows the volume-integrated dye entropy of the simulations shown in Figure 4.8.

The entropy follows a similar evolution in every simulation. To visualize the small deviations, the bottom panel shows the entropy with reference solution D4096 subtracted off. All the simulations diverge from D4096, but more accurate simulation diverge later, with D2048 and A16384 developing small differences later than any other simulations. The relation between entropy and resolution is more complicated for $\Delta\rho/\rho_0 = 1$ than for $\Delta\rho/\rho_0 = 0$ (Figures 4.3 & 4.5).

Apart from the dye concentration field, many of the other flow quantities follow similar patterns. Figure 4.12 shows several quantities from D4096 at $t = 6$. The mass density is almost the inverse of the dye concentration. This indicates that compression is not an important part of the large-scale dynamics. Lacking mass diffusion, the density shows sharper gradients than the concentration field. Temperature diffusion and rapid sound waves regularize the density evolution. These effects limit large temperature gradients, and keep the flow in local pressure equilibrium.

The velocity divergence field is characterized by a large scale quadrupole centered at the vortex, and large amplitude, small scale features near the boundaries of filaments. The most prominent feature of the vorticity field is the central vortex, which is a remnant of the initial shear. Small-scale vortex sheets and filaments perhaps result from the incomplete roll-up of the initial condition due to secondary instabilities.

Throughout this chapter, we compare different solutions by calculating the $L_2$ norm of the difference between dye concentration fields. We have made similar comparisons between simulations with $\mathrm{Re} = 10^5$ and $\Delta\rho/\rho_0 = 1$ using the $L_1$ norm of the difference between dye concentration fields, and using the $L_2$ norm of the difference between the three other fields shown in Figure 4.12. We find the results to be qualitatively similar in all cases. This is expected given the similarity between the fields.

**Inner-vortex instability**

To determine the origin (physical vs numerical) of IVI, we initialize a Dedalus simulation with horizontal resolution 2048 with the output from A2048 at $t = 3.2$. We call this simulation D2048r. Figure 4.9 shows that A2048 is still in the linear phase of the IVI at this time. In Figure 4.13, we plot the dye concentration field at $t = 3.2$ and $t = 4$ for D2048, A2048, and D2048r. At $t = 3.2$, the simulations all look the same. However, the instability becomes nonlinear by $t = 4$, producing large changes in the dye concentration field. D2048 shows no signs of the IVI. However, D2048r looks almost identical to A2048. The $L_2$ norm of the difference of dye concentration fields between D2048r and D4096 almost exactly follows the norm of the difference between A2048 and D4096.

This shows that the IVI is a physical instability of this system. It is not seen in the Dedalus simulations or the highest-resolution Athena simulation because the initial condition does not project sufficiently onto its unstable modes. Errors in low resolution Athena simulations incorrectly excite perturbations unstable to the IVI. Dedalus simulations, and the highest-resolution Athena simulation, suppress noise well enough the instability never becomes nonlinear. In our phase-space diagram (Figure 4.10), the lower-resolution Athena simulations do not properly follow the black line, and instead meander to the right, becoming unstable to the IVI. D2048r is initialized to the right of IC', so it develops the IVI just like A2048.

As a final test, we started a Dedalus simulation from the output of an Athena simulation at $t = 0$.

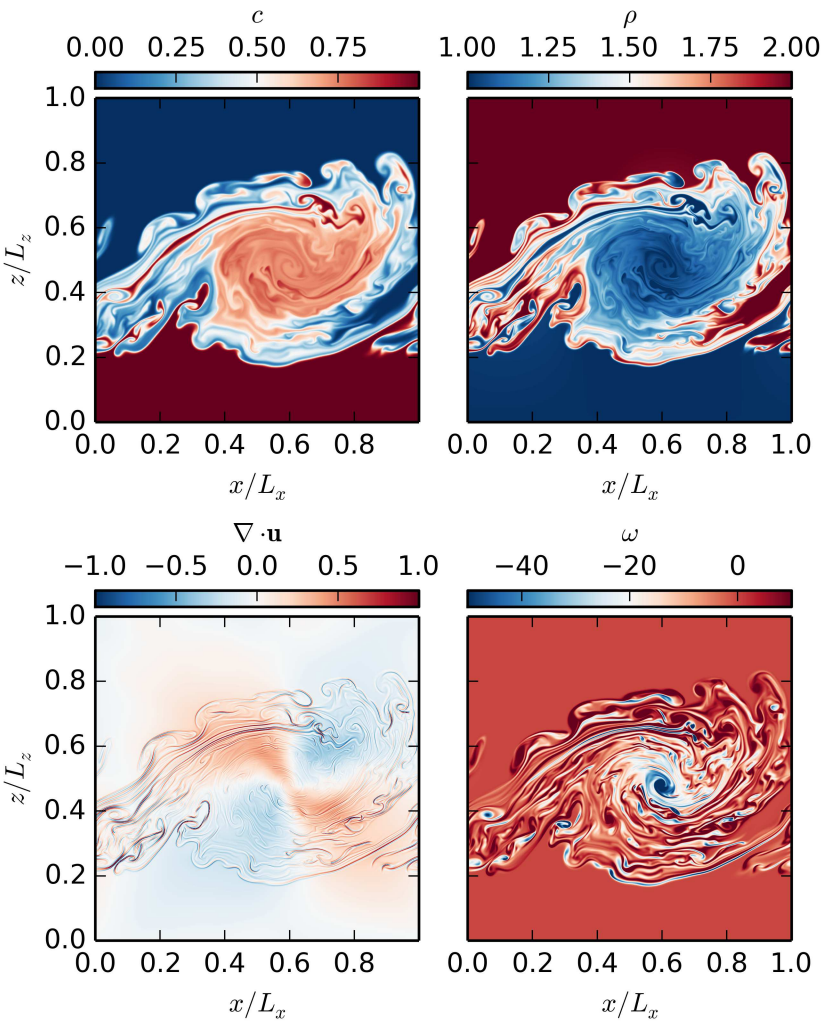


*Figure 4.12*: Plots of dye concentration ($c$), mass density ($\rho$), the divergence of the velocity ($\boldsymbol{\nabla} \cdot \boldsymbol{u}$), and the vorticity ($\omega = \boldsymbol{e}_z \cdot \boldsymbol{\nabla} \times \boldsymbol{u}$) in D4096 with $\Delta\rho/\rho_0 = 1$, Re $= 10^5$ at $t = 6$. The divergence of the velocity and the vorticity are measured in units of $u_{\text{flow}}/L_x$. The dye concentration and mass density fields are almost inverses of each other. The divergence of the velocity is largest at the interfaces between filaments, whereas the vorticity shows the location of vortices.

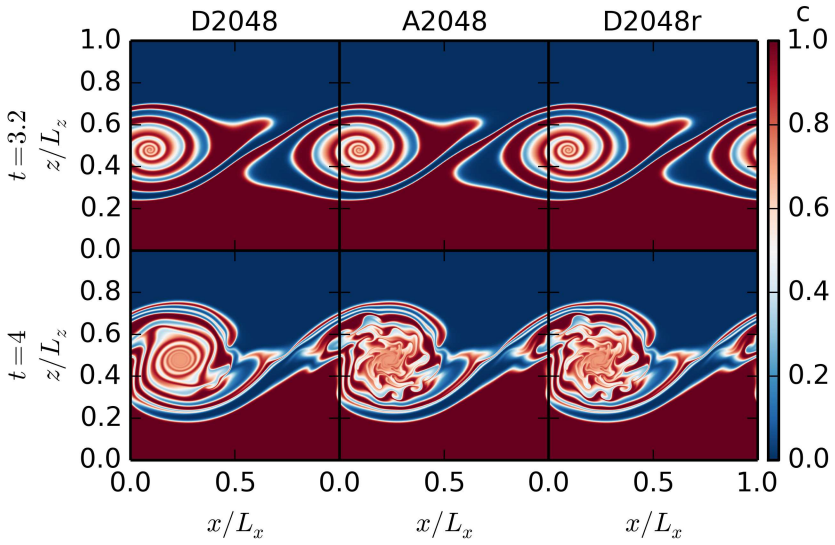


*Figure 4.13*: Snapshots of dye concentration field for Re = $10^5$ and $\Delta\rho/\rho_0 = 1$. D2048r is a Dedalus simulation restarted with the A2048 output at $t = 3.2$. At this time, the inner vortex instability is still in the linear phase, so there are no visible differences between the three simulations. At $t = 4$, the IVI is very nonlinear, producing large differences between D2048 and A2048. This instability also takes place in D2048r, and the dye concentration fields of A2048 and D2048r are nearly identical. This demonstrates that the IVI is physical, but is seeded by errors in the lower-resolution Athena simulations that are not present in the Dedalus simulations or the highest-resolution Athena simulations.

This tests whether dynamical evolution causes the IVI, rather than small differences between the implementation of the initial conditions. Although this introduced root mean squared differences in the horizontal velocity of $\approx 4 \times 10^{-4}$ at $t = 0$, the Dedalus simulation did not develop the IVI.

### Chaos

At around $t \approx 4$, D2048, D3072, and A16384 start to diverge exponentially from D4096 (Figure 4.9). The differences increase with a growth rate of about 2-3, much lower than the growth rate of 8 of the IVI found in the lower-resolution Athena simulations. We interpret the differences between the simulations as due to chaos. The faster divergence discussed in section 4.3.2 is inconsistent with chaos since it is resolution dependent and only seen in low-resolution Athena simulations.

A system is chaotic if small differences between initial conditions grow exponentially in time. To confirm the system is chaotic, we calculate a "local-in-time" Lyapunov exponent (i.e., growth rate). We pick a time and simulation, and look for linearly unstable perturbations. This requires solving an eigenvalue problem. The largest unstable eigenvalue is the Lyapunov exponent. Appendix 4.C details this procedure.

This calculation does not include base-state time evolution (i.e. we consider a "local-in-time" calculation). The most unstable eigenvector at a time $t_0$ might differ significantly from the most unstable eigenvector at a nearby time $t_0 + \Delta t$. Then it would be impossible for perturbations to grow at the Lyapunov exponent over times $\sim \Delta t$. We interpret our "local-in-time" Lyapunov exponents as an upper bound on the growth rate of perturbations due to chaos (up to logarithmic corrections), and as a heuristic measure of the strength of chaos in this problem.

We calculated the Lyapunov exponent for D2048 with $\mathrm{Re} = 10^5$ and $\Delta\rho/\rho_0 = 1$ at two times, $t = 2.5$ and $t = 4.5$. We find Lyapunov exponents of $\lambda_{t=2.5} \approx 2.1$, and $\lambda_{t=4.5} \approx 3.7$. Thus, the exponential growth of differences between either D2048, D3072, or A16384 and D4096 is consistent with chaos. However, the growth rate of the differences between the lower-resolution Athena simulations and D4096 is much larger than the Lyapunov exponent. These differences are inconsistent with chaos, instead being due to the IVI.

The simulations with $\Delta\rho/\rho_0 = 0$ do not appear to diverge from one another in the same way. The highest-resolution Dedalus simulations converge at late times. We also calculate the Lyapunov exponent for D1024 with $\mathrm{Re} = 10^6$ and $\Delta\rho/\rho_0 = 0$ at $t = 6$. We find $\lambda_{t=6} \approx 0.4$. Although this seems inconsistent with our finding that the Dedalus simulations approach each other with time, recall that this "local-in-time" calculation gives an upper bound on the growth rate due to chaos (up to logarithmic corrections). Because the turnover time is 1, a Lyapunov exponent less than 1 suggests that small perturbations cannot grow before the background state changes substantially. To show definitively that the $\Delta\rho/\rho_0 = 0$ solution is not chaotic, one should maximize the amplification of an initial perturbation over several turnover times, e.g., between $t = 6$ and $t = 9$ (for instance, using the adjoint method, e.g., Kerswell et al. 2014).

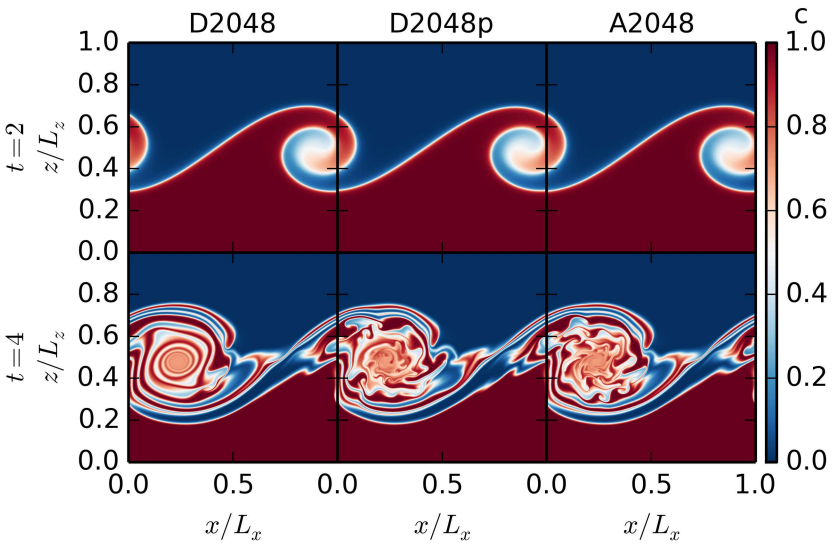


*Figure 4.14*: Snapshots of dye concentration field for Re = $10^5$ and $\Delta\rho/\rho_0 = 1$. D2048p is a Dedalus simulation with an initial vertical velocity that includes power over a range of Fourier modes (equation 4.12), in contrast to the single mode initial conditions focused on throughout the rest of this chapter. At $t = 2$ all solutions look the same, indicating that longest wavelength mode has the largest growth rate. At $t = 4$, D2048p has developed the IVI, as well as other deviations from the Dedalus & Athena simulations away from the vortex.

### Initial condition

Although our chosen initial condition does not lead to the IVI for converged simulations, one might wonder if other initial conditions do lead to this instability. We performed several Dedalus simulations that add low-amplitude white noise to the initial condition (e.g., see section 4.3.2). None of these simulations develop the IVI.

We now consider a simulation in which we include perturbations to the initial condition with order unity amplitude and large wavelengths. Equations 4.8 still hold for all quantities except the vertical velocity, which we now take to be

$$u_z = A\left(\sin(2\pi x) + f(x)\right) \times \left[\exp\left(-\frac{(z-z_1)^2}{\sigma^2}\right) + \exp\left(-\frac{(z-z_2)^2}{\sigma^2}\right)\right], \tag{4.12}$$

where $f(x)$ includes Fourier modes two–ten. Each mode receives a random phase and random amplitude uniformly distributed between -0.05 and 0.05. Thus, $f(x)$ represents about a 10% perturbation to the single sine mode initial condition.

Figure 4.14 shows snapshots of the dye concentration field for this simulation, denoted D2048p, along with D2048 and A2048 for comparison. At $t = 2$, all three simulations look identical. This indicates that the lowest wavenumber Fourier mode grows faster than the other modes included in our initial condition.

By $t = 4$ the perturbations from the other Fourier modes produce significant changes to the dye concentration field. D2048p now displays the IVI. In addition, large differences appear away from the vortex, where the Dedalus and Athena simulations look almost identical. Because the new initial condition does not respect the shift-and-reflect symmetry of the problem, the two half domains have different features (we only show the bottom half).

#### Simulations without explicit diffusion

Lastly, Figure 4.15 compares the resolved simulations at $\mathrm{Re} = 10^5$ with an Athena simulation with horizontal resolution 4096 without explicit diffusion (N4096). The simulation without explicit diffusion exhibits many secondary instabilities early in the evolution (between $t = 2$ and $t = 4$). Unlike the lower-resolution simulations at $\mathrm{Re} = 10^5$, the secondary instability is not limited to the IVI. Instead, instabilities grow throughout the domain at locations of strong shear.

These instabilities shred apart the vortex, leading to vigorous mixing. Figure 4.16 compares the volume-integrated dye entropy of Athena simulations with no explicit diffusion at different resolutions with D4096. Simulations without explicit diffusion produce almost no entropy until $t \approx 3.5$. At this time, the secondary instabilities start to cause diffusion at the grid-scale. This generates entropy more rapidly than the explicit diffusion of D4096 (or any of the other simulations with explicit diffusion). For $t > 5$, the entropy of the simulations without explicit diffusion is larger than the entropy of D4096. Paradoxically, the entropy increases as the resolution increases. Our expectation is that the entropy generation should decrease as Re increases. However, we do not have any resolved simulations with higher Re for comparison, so we cannot present evidence that this additional mixing is spurious. But this problem shows that introducing an explicit diffusion in Athena can *decrease* the diffusion in the simulation.

## 4.4 Conclusion

This chapter describes several converged, nonlinear solutions to the Kelvin-Helmholtz (KH) problem. By using a smooth initial condition and explicit diffusion, we demonstrate that solutions remain virtually identical (for constant initial density) or very similar (for an initial density jump of one) with resolution above a certain threshold. This permits a well-defined reference solution for this problem, against which errors can be accurately estimated. We verify this using two codes, Dedalus and Athena, with very different numerical methods (pseudo-spectral and Godunov, respectively). Previous KH test problems either did not use smooth initial conditions, or did not include explicit diffusion. Absent these two choices, the KH problem cannot be quantitatively compared between codes because the solutions depend sensitively on grid-scale errors and do not converge with increasing resolution.

We first study simulations with a constant initial density (section 4.3.1). We find converged solutions to this relatively easy problem with Reynolds numbers (Re) as high as $10^6$. The solution is characterized by the continual roll-up of the initial vortex sheet, producing alternating filaments of unmixed material (Figure 4.1). We find third-order convergence in both Dedalus & Athena for

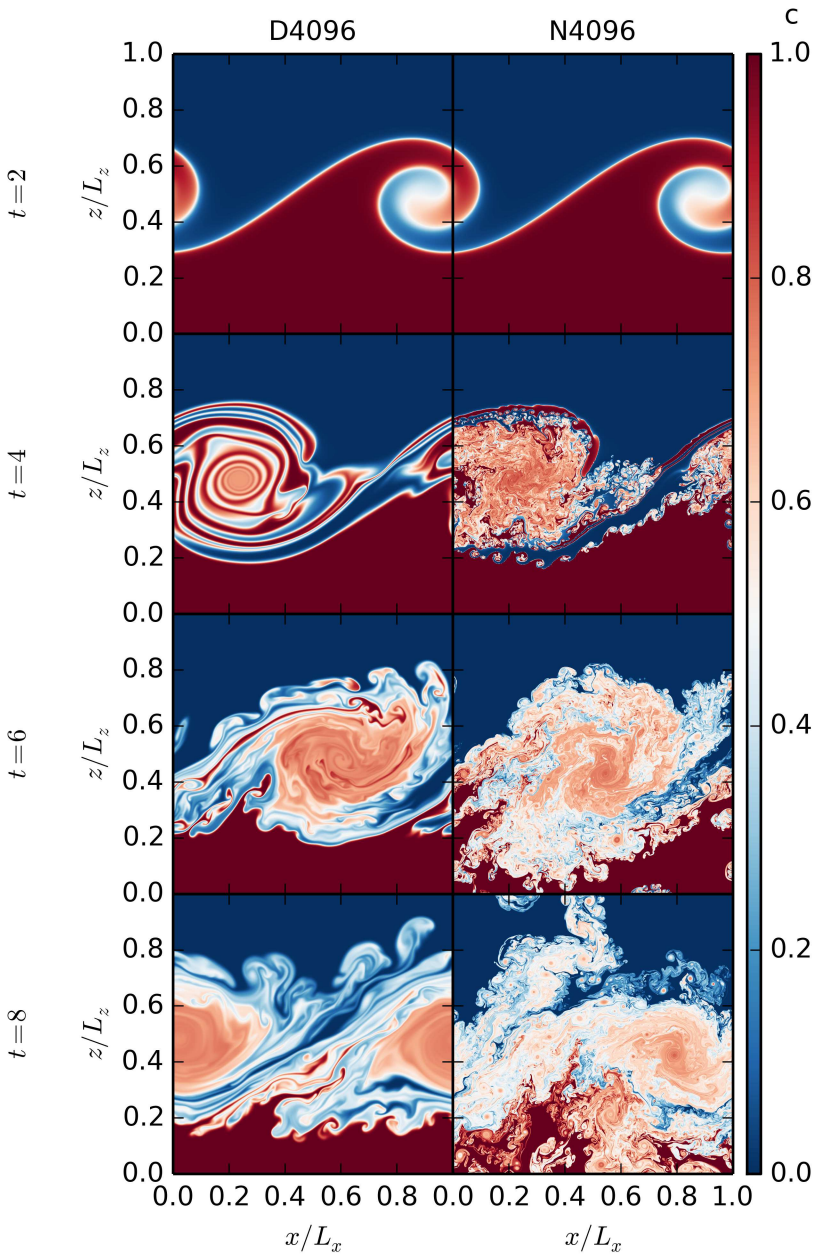


*Figure 4.15*: Snapshots of dye concentration field for $\Delta\rho/\rho_0 = 1$. N4096 is an Athena simulation with no explicit diffusion. For comparison, we also plot D4096 (Re = $10^5$). Secondary instabilities occur very early at many locations in N4096. By $t = 6$, the simulation has broken its initial symmetry (we only plot the bottom half). The secondary instabilities produce significant mixing, leading to greater entropy generation than in simulations with explicit diffusion (Figure 4.16).

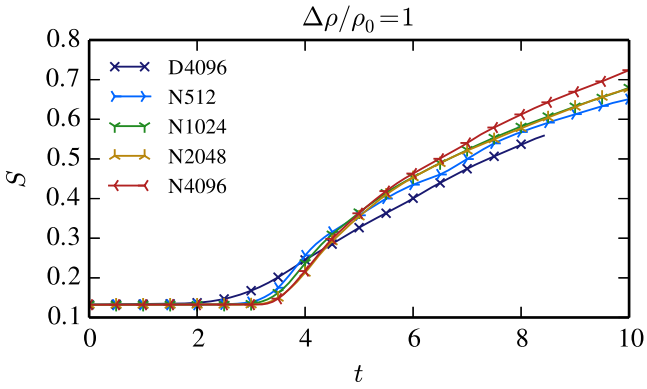


*Figure 4.16*: Volume-integrated dye entropy (equation 4.5) as a function of time for simulations with $\Delta\rho/\rho_0 = 1$. D4096 is run at Re $= 10^5$, and all simulations labeled with N are run with Athena with no explicit diffusion. At early times, the highest-resolution runs without explicit diffusion have the lowest entropy. However, at around $t = 5$, the lower-resolution runs without explicit diffusion have lower entropy. D4096 has the lowest entropy at late times. This indicates that simulations without explicit diffusion have *greater* numerical mixing compared to simulations with explicit diffusion. This becomes more prominent as the resolution increases. By contrast, in the simulations without an initial density jump, explicit diffusion leads to more mixing, and for simulations without explicit diffusion, increasing resolution decreases mixing (Figure 4.6).

simulations with Re $= 10^5$ (Figure 4.2), and better than second-order convergence in both codes for simulations with Re $= 10^6$ (Figure 4.4).

To quantify mixing in the simulations, we calculate the volume-integrated dye entropy as a function of time for several Reynolds numbers, as well as for Athena simulations without explicit diffusion (Figure 4.6). As the Reynolds number increases, the entropy generation decreases monotonically. Similarly, as the resolution of Athena simulations without explicit diffusion increases, the entropy generation also decreases monotonically. The entropy of one Athena simulation without explicit diffusion is very close to the entropy of the Re $= 10^6$ simulation, although the solutions show minor differences (Figure 4.7). These small differences indicate that the numerical diffusion in Athena does not act precisely as a physical diffusion from viscosity and/or thermal conductivity. For certain applications however, assigning an effective Reynolds number to ideal fluid simulations may suffice. This does not appear to be the case for KH simulations with density jumps, as we now discuss.

Including an initial density gradient aligned with the velocity gradient makes the problem much richer (section 4.3.2). The rolled-up vortex-sheet filaments becomes unstable in at least two ways: the inner vortex instability, and/or the outer filament instability (Figures 4.8 & 4.10). The Dedalus simulations and highest-resolution Athena simulation only exhibit the outer filament instability, whereas the lower-resolution Athena simulations also exhibit the inner vortex instability. Adding small amplitude noise to the initial condition does not produce the inner vortex instability in Dedalus, demonstrating that our chosen initial condition is not susceptible to this in-

stability; instead, numerical errors seed the inner vortex instability throughout the evolution of the Athena simulations. It is not surprising that Dedalus is more accurate than Athena for this smooth flow—the Godunov method is designed for simulating flows with shocks. However, it is not well appreciated that the pseudo-spectral method is able to solve the full Navier-Stokes equations with Mach number order unity.

The inner vortex instability was also found in similar ideal simulations of Reinaud et al. (2000). They solved the incompressible, variable density equations. The instability seems to be triggered by the intensification of vorticity by the baroclinic torque. The instability was studied further by Fontane & Joly (2008), who solved for the linear instability modes of a 2D flow snapshot before any secondary instabilities develop (also using the incompressible, variable density equations). They find two types of modes: elliptic modes (which we call the inner vortex instability), and hyperbolic modes (which we call the outer vortex instability). They found no 2D instability for constant initial density. However, if there is an initial density gradient, they find the fastest growing mode is the inner vortex instability. The growth rate increases as the initial density contrast increases. This suggests the instability is enhanced by baroclinicity. However, it is unclear if solving for modes of a snapshot from a simulation is appropriate given the time variability of the background state.

Allowing for 3D perturbations, Fontane & Joly (2008) finds the outer vortex instability is the fastest growing mode in all cases, including in the constant density case. This suggests the 3D dynamics will be completely different. In particular, the constant density case will no longer evolve toward the previously attracting spiral state. Their analysis also suggests the inner vortex instability may be less prominent in the cases with an initial density jump. We thus expect closer agreement between Dedalus and Athena in 3D, and less qualitative differences between simulations with and without initial density jumps.

We use the $L_2$ norm to quantify the difference between dye concentration fields of different simulations, and find the inner vortex instability grows at a rate of $\approx 8$, independent of resolution (Figure 4.9). Furthermore, a Dedalus simulation initialized with an Athena state in the linear phase of the inner vortex instability develops the instability in the same way as Athena (Figure 4.13), demonstrating the physical, rather than numerical, nature of the instability.

Adding a large ($\sim 10\%$ by energy) perturbation with multiple Fourier modes to the initial velocity in Dedalus can seed the inner vortex instability (section 4.3.2). Although this suggests that the inner vortex instability is possibly generic for KH instabilities in astrophysical systems, we believe the single-mode initial condition discussed throughout the rest of this chapter is still particularly valuable for a test problem. Because small numerical errors can produce large differences in the solution, one can assess by eye the fidelity with which a code is solving the fluid equations. This KH test problem is difficult, which we believe makes it interesting. In contrast, an unresolved KH problem is not a good test of fluid codes, because noise due to numerical errors can masquerade as higher-fidelity solutions.

The Dedalus simulations and highest-resolution Athena simulation also diverge from each other exponentially at late times, but with a much smaller growth rate $\approx 2-3$. In section 4.3.2 we calculate the maximum Lyapunov exponent of the flow, and argue that chaos drives the divergence. The Lyapunov exponent represents the maximum possible rate of divergence of solutions due to chaos (up to logarithmic corrections). At late times when the Dedalus simulations and highest-

resolution Athena simulation begin to diverge, the Lyapunov exponent is $\approx 3.7$, so the divergence we see is consistent with chaos. Because the system is chaotic, our solutions are not as accurate as the solutions with constant initial density. We still find power-law convergence in the Dedalus simulations at fixed time (Figure 4.9). However, the amount of time that a solution maintains a fixed level of accuracy increases only logarithmically with resolution.

For the initial condition with a density jump, we also compare a high-resolution Athena simulation without explicit diffusion to our converged (within the limits of chaos) simulations with $\mathrm{Re} = 10^5$. Secondary instabilities pervade the simulation without explicit diffusion (Figure 4.15). The secondary instabilities cause enhanced mixing, and at late times, the simulations without explicit diffusion have higher entropy than the $\mathrm{Re} = 10^5$ simulation (Figure 4.11). Introducing explicit diffusion into Athena can *reduce* the diffusion in the simulation. For this reason, we hypothesize (but cannot prove) that this small-scale structure is likely unphysical, and would not develop for any reasonable initial condition or Reynolds number. This highlights that a solution with more small-scale structure is not necessarily better.

Another possible comparison is to experiments. Unfortunately, the problems described here cannot be studied experimentally because they are two-dimensional, periodic and do not include gravity. Furthermore, the flow is close to sonic and at high Reynolds number. Experimentally, it is far easier to study the incompressible KH instability (Worster 2009). Even with this simplification, results depend sensitively on initial conditions (Slessor et al. 1998). This is reminiscent of difficulties when comparing simulations and experiments of the Rayleigh-Taylor instability (Dimonte et al. 2004), which have only recently been resolved by carefully controlling the initial condition in experiments (Wilkinson & Jacobs 2007; Hutchinson & Rosner 2015).

There has also been substantial efforts to study the KH instability in the atmospheric science community (e.g., Fritts et al. 2009, 2014). They typically study 3D dynamics, and include stable stratification, which can be parameterized by the Richardson number Ri. Fritts et al. (2014) finds the outer vortex instability is the dominant secondary instability in simulations with weak stratification (low Ri), whereas the inner vortex instability is the dominant secondary instability in simulations with strong stratification (high Ri). This is consistent with the calculation of Fontane & Joly (2008) showing the outer vortex instability has a higher growth rate than the inner vortex instability in unstratified flow.

Although we only describe simulations with an initial density ratio of one, we have experimented with larger initial density ratios (e.g., 4). Preliminary investigation suggests that vigorous secondary instabilities become increasingly prominent as the density ratio increases, greatly enhancing mixing. Though it's a common practice to leave out explicit dissipation to model the high Reynolds numbers relevant in astrophysics, our results suggest that including explicit diffusion may provide a very effective way to reduce diffusion in astrophysical simulations with very large density ratios. We stress that these large density ratios are common in astrophysical problems such as star formation or galaxy formation. Our results demonstrate just how subtle and computationally challenging it is to correctly capture mixing in these environments (even restricting ourselves to hydrodynamics, which is likely a poor approximation).

There are many remaining questions left unanswered in this chapter. It is unclear how the Athena algorithm seeds the inner vortex instability. We did not search for the critical perturbation

amplitude that will cause a Dedalus simulation to exhibit the inner vortex instability. Because of limited computer time, we did not find converged Dedalus or Athena simulations with $\Delta\rho/\rho_0 = 1$ and $\mathrm{Re} = 10^6$. Perhaps, contrary to expectation, increasing the Reynolds number of the system does increase the entropy production, as found in the Athena simulations without explicit diffusion. Future work should also test the Galilean invariance of these simulations, test initial conditions with an interface at an angle to the grid, and extend this analysis to larger density ratios.

We hope this study provides a well-posed test problem for future codes used in astrophysics. It would be valuable to carry out this test problem with unstructured/meshless methods (e.g., Springel 2010; Duffell & MacFadyen 2011; Hopkins 2015) to understand their convergence properties on this challenging problem. Introducing smooth initial conditions and explicit diffusion allows us to calculate a converged reference solution and compare between codes. The competing secondary instabilities for initial conditions with a density jump of one provides a stringent test of the fidelity with which a code solves the Navier-Stokes equations, making it a great test problem.

## 4.A Interpolation to a Common Grid

The grid points used in Dedalus and Athena differ slightly. For a periodic simulation between 0 and $L$ with spacing $\Delta x$, the Dedalus grid points are $\{0, \Delta x, 2\Delta x, \ldots, L - \Delta x\}$, whereas the Athena grid points are $\{\Delta x/2, 3\Delta x/s, \ldots, L - \Delta x/2\}$. We use two spectrally accurate methods for interpolating Dedalus and Athena data to a common grid. In several cases we test both methods and find excellent agreement.

Our first method is spectral interpolation. The Dedalus data can be viewed as either $N = L/\Delta x$ values on grid points or $N$ Fourier coefficients. We can pad the Fourier coefficients with zeros and transform to a grid of any uniform spacing. Going from $N$ to $2N$ points, we can compare every other entry to the Athena data. In a second method, we multiply the Fourier coefficients by $\exp(ik_x\Delta x/2)$. A Fourier transform then shifts the grid points by $\Delta x/2$, to align the Dedalus grid with the Athena grid. We follow the same procedure in the $z$ direction.

Throughout this chapter, we treat the Athena data (including initial conditions) as cell-centered data. However, the data are actually volume-averaged. The lowest-order differences between cell-centered and volume-averaged quantities scales as $\sim \Delta x^2$. Thus, any errors associated with these differences should decrease with order 2. In all cases studied here (i.e., Figures 4.2, 4.4, & 4.9), we find better-than second-order convergence. This suggests that differences due to interpreting data as cell-centered rather than volume-averaged is not the dominant source of error.

## 4.B Convergence to a "True" Solution

This chapter describes a series of calculations of the nonlinear evolution of the KH instability, as a function of resolution and Re. Without an analytic solution, we must assess the quality of the solutions carefully. We make two assumptions to help interpret our results.

1. Dedalus and Athena converge to the same solution at fixed Re as the resolution increases. We refer to this unattainable "Platonic ideal" solution as the true solution.

2. The distance (given a choice of norm) between two solutions at different resolutions (for the same code), is larger than the distance between the higher-resolution simulation and true solution.

Our simulations support these assumptions, but it is very difficult, if not impossible, to prove these statements. The existence and uniqueness of solutions to the Navier-Stokes equations remains an active field of research (Fefferman 2000).

To support these assumptions, Figure 4.17 plots the relative differences between simulations with $\mathrm{Re} = 10^6$ and $\Delta\rho/\rho_0 = 0$ at $t = 6$ (described further in section 4.3.1). The top panel assumes our highest-resolution Dedalus solution is the true solution. The bottom panel assumes our highest-resolution Athena solution is the true solution. To assess the deviations, we plot the $L_2$ norm of the difference of dye concentration fields. This allows us to define an error (alternatively a distance) between two solutions X and Y as

$$e(\mathrm{X}, \mathrm{Y}) = L_2(c_X - c_Y), \tag{4.13}$$

where $c_\mathrm{X}$ and $c_\mathrm{Y}$ are the dye concentration fields of solutions X and Y, respectively. Figure 4.17 remains mostly unchanged if we compare lower Reynolds number simulations with $\mathrm{Re} = 10^5$ and $\Delta\rho/\rho_0 = 0$, although the picture is more complicated for $\Delta\rho/\rho_0 = 1$ due to chaos (see section 4.3.2).

Both the Athena simulations and the lower-resolution Dedalus simulations are converging to D2048. The top panel of Figure 4.17 therefore suggests a true solution lives very close to D2048 (assumption (i)). The Athena simulations converge slower than the Dedalus simulations because in Dedalus spatial errors decrease exponentially.

The bottom panel of Figure 4.17 shows that A4096 is a worse approximation to the true solution. This is because the Dedalus simulations are not converging to A4096.

One could argue that perhaps the Athena simulations are converging to a solution near A4096 and the Dedalus simulations are converging to a different solution near D2048. However, this would require the error of the Athena simulations with respect to D2048 to stay constant as the resolution increases, contrary to the top panel. Thus, we believe that both codes are converging to a true solution close to D2048 (assumption (i)).

Presumably if Athena were run at very high resolutions, it would become closer to the true solution than D2048. In this case, we hypothesize that both Dedalus and Athena simulations would converge to this very high-resolution Athena simulation. For the range of resolutions examined in this chapter, our highest-resolution Dedalus simulation is always closest to the true solution.

The main idea behind assumption (ii) is the convergence properties of the algorithms used in Athena and Dedalus. Specifically, both codes are better than first-order accurate. Imagine we somehow know the true solution to our problem, T. If we run a high-resolution simulation, S1, we calculate the error,

$$e(\mathrm{S1}, \mathrm{T}) \equiv E_1. \tag{4.14}$$

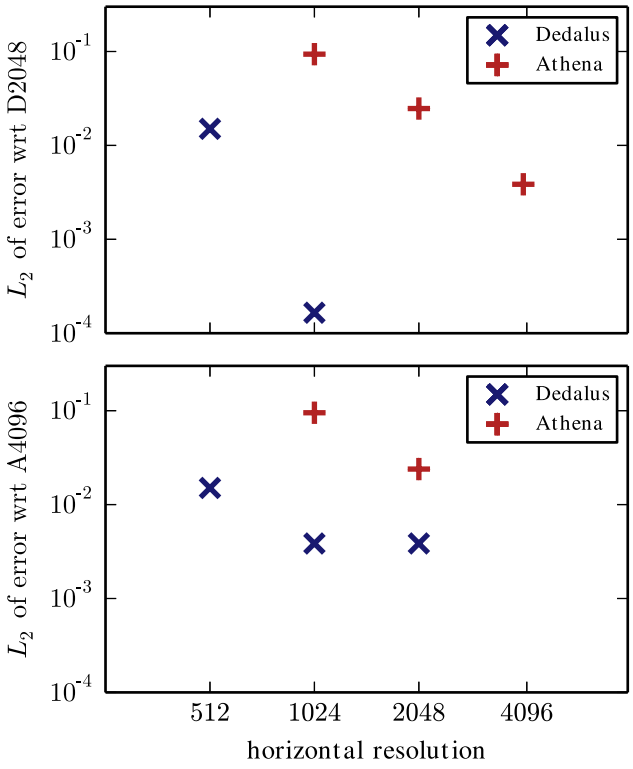


*Figure 4.17*: Differences between different solutions for Re = $10^6$ and $\Delta\rho/\rho_0 = 0$ at $t = 6$. In the top panel, the Dedalus simulation with horizontal resolution 2048 (D2048) is assumed to be the true solution, and in the bottom panel the Athena simulation with horizontal resolution 4096 (A4096) is assumed to be the true solution. The error with respect to the assumed true solution is the $L_2$ norm of the difference of the dye concentration fields (equation 4.13). The top panel shows that both Athena and Dedalus are converging to the high-resolution Dedalus solution, supporting the assumption that it is close to the true solution. In the bottom panel, the Athena solutions are converging to the high-resolution Athena simulation, but the Dedalus solutions are not. This suggests that the Athena solution is further from the true solution than the Dedalus solutions.

Now suppose we run another simulation S2 at double resolution. If S1 and S2 are converging to T, then

$$e(\mathrm{S2}, \mathrm{T}) \equiv E_2 < \frac{E_1}{2}, \tag{4.15}$$

where better-than first-order accuracy implies the inequality. Athena is between second- and third-order accurate, so we expect $E_1/4 \leq E_2 \leq E_1/8$ for Athena. Dedalus is exponentially accurate in space, and third-order accurate in time. Thus, for Dedalus, we should expect $E_2 \leq E_1/8$. Nevertheless, equation 4.15 implies, via the triangle inequality,

$$e(\mathrm{S1}, \mathrm{S2}) > \frac{E_1}{2} > e(\mathrm{S2}, \mathrm{T}), \tag{4.16}$$

which shows that assumption (ii) holds. One can check visually that equations 4.15 & 4.16 hold for the simulations described in Figure 4.17, assuming that T is very close to D2048.

## 4.C Lyapunov exponent calculation

One can write the equations of motion (equations 4.1) as

$$\partial_t U = F(U), \tag{4.17}$$

where $U = (\rho, \boldsymbol{u}, E)$ is the state vector. Then infinitesimal perturbations to $U$ evolve according to the equation

$$\partial_t \delta U = \left.\frac{\delta F}{\delta U}\right|_U \delta U, \tag{4.18}$$

where $\delta F/\delta U$ is the Fréchet derivative, evaluated at $U(t)$.

To calculate the "local-in-time" Lyapunov exponent, we fix the state vector to its value at a specific time $t = t_0$. The maximum Lyapunov exponent is the greatest eigenvalue of $(\delta F/\delta U)_{U(t_0)}$. It is impractical to solve this eigenvalue problem directly—a 2D problem with resolution greater than 1000 in each direction generates very large matrices. Instead, we solve an initial value problem by picking $\delta U(\tau = 0)$, and evolving

$$\partial_\tau \delta U = \left.\frac{\delta F}{\delta U}\right|_{U(t_0)} \delta U, \tag{4.19}$$

where $\tau$ should not be thought of as time, as we have fixed the background state $U$ to $t = t_0$. The maximal Lyapunov exponent is

$$\lambda = \lim_{\tau \to \infty} \log\left(\frac{||\delta U(\tau)||}{||\delta U(0)||}\right), \tag{4.20}$$

for some norm $||\cdot||$. We choose $\sqrt{||\boldsymbol{u}||^2}$. This is equivalent to the power method.

We solve equation 4.19 in Dedalus using two methods. Both methods give very similar Lyapunov exponents. In the first, we directly evolve the linearized equations 4.19. We treat terms independent of $U_0$ implicitly, and treat all other terms explicitly. The second method uses an iteration. On each iteration, we evolve the full equations of motion (equation 4.17) for $U_0 + \delta U_i$ for a time $\Delta t \ll t_0$ to get a state we call $\tilde{U}_i(t_0 + \Delta t)$. The initial perturbation for the next iteration becomes $\delta U_{i+1} \propto \tilde{U}_i(t_0 + \Delta t) - \Delta U_0$, but with norm $10^{-8}$. $\Delta U_0 = U(t_0 + \Delta t) - U(t_0)$ is the change in the unperturbed solution $U_0$ over the time $\Delta t$. We normalize after each iteration to ensure the perturbations stay linear.

In both cases, we initialize the calculation with random noise. After substantial evolution, $\delta U$ undergoes periodic (in $\tau$) variations, on top of exponential growth. In this case, $\lambda$ is the growth averaged over one period.

# Chapter 5

# Turbulent Chemical Diffusion in Convectively Bounded Carbon Flames

## 5.1 Introduction

Super-asymptotic giant branch (SAGB) stars are characterized by the development of a degenerate carbon-oxygen (CO) core and the subsequent ignition of off-center carbon fusion within it. Stellar evolution calculations show that this occurs in stars that have zero-age main sequence masses $\approx 7 - 11\,M_\odot$, with this mass range depending on the metallicity and on modeling assumptions such as the mass loss rate and the efficiency of mixing at convective boundaries.

Carbon ignition initially occurs as a flash, but after one or more of these flashes, a self-sustaining carbon-burning front can develop (see e.g., Siess 2006; Farmer et al. 2015). This "flame" propagates towards the center of the star extremely sub-sonically, as heat from the burning front is conducted inward. The heat from the burning also drives a convective zone above the burning front, and in the quasi-steady-state, the energy released by carbon fusion is balanced by energy losses via neutrino cooling in this convective zone (Timmes et al. 1994). As the carbon-burning flame propagates to the center, it leaves behind oxygen-neon (ONe) ashes. This process creates the core that will become a massive ONe WD or collapse to a neutron star, powering an electron-capture supernova (Miyaji et al. 1980).

However, the presence of additional mixing near the flame can lead to its disruption, preventing carbon burning from reaching the center. There are at least two physical processes that may play a role in this region: (1) mixing driven by the thermohaline-unstable configuration of the hot ONe ash on top of the cooler CO fuel and (2) mixing driven by the presence of a convective zone above the flame via convective overshoot. These processes were investigated by Denissenkov et al. (2013) using 1D stellar evolution models. With a thermohaline diffusion coefficient informed by multi-dimensional hydrodynamics simulations, they concluded that thermohaline mixing was not sufficient to disrupt the flame. However, they did find that the introduction of sufficient convective boundary mixing—using a model of exponential overshooting (Freytag et al. 1996; Herwig 2000)—robustly disrupted the flame, preventing carbon burning from reaching the center. This led to the production of "hybrid C/O/Ne" WDs, in which a CO core is overlaid by an ONe man-

tle. Several groups have begun to model the explosions that would originate from objects with this configuration (Denissenkov et al. 2015; Kromer et al. 2015; Bravo et al. 2016; Willcox et al. 2016).

Is mixing sufficiently vigorous to disrupt the carbon flame? This is a key question for understanding the final outcomes of SAGB stars and the WDs they produce. If the thermal diffusivity $\kappa$ is much larger than the chemical diffusivity $D$, the flame propagates into fresh fuel much more quickly than the fuel and ash can mix, allowing the flame to successfully propagate to the center of the star. We estimate $\kappa/D \sim 10^6$ using the thermal conductivity in MESA (which is drawn from Cassisi et al. 2007) and a chemical diffusivity from Beznogov & Yakovlev (2014). However, convective mixing could produce a *turbulent* diffusivity $D_t$, which is similar to $\kappa$. If this occurs, ash could mix into the fuel, stalling the flame, as was found in Denissenkov et al. (2013).

## 5.2 Carbon Flame Properties

To obtain an example of the structure of a carbon flame, we evolve a star with zero-age main sequence mass of 9.5 $M_\odot$ using revision 6794 of the MESA stellar evolution code[1] (Paxton et al. 2011, 2013, 2015). We used the publicly available inlists of Farmer et al. (2015), who undertook a systematic study of carbon flames in SAGB stars. We did not include the effects of overshoot at the convective boundaries, but did include the effects of thermohaline mixing. The Brunt-Väisälä (buoyancy) frequency profile of the carbon flame is shown in Fig. 5.1. The thermal component dominates the buoyancy frequency. The much smaller compositional component is destabilizing, but Denissenkov et al. (2013) found thermohaline mixing to not affect flame propagation. The flame structure in Fig. 5.1 is similar to that shown in Figure 3 of Denissenkov et al. (2013).

The peak of the buoyancy frequency profile shown in Fig. 5.1 is at a Lagrangian mass coordinate of $M_r = 0.13\,M_\odot$. The properties of the flame change as it propagates, but the following numbers are representative throughout the evolution. The flame velocity is $u = 9 \times 10^{-4}\,\mathrm{cm\,s^{-1}}$; it will take $\sim 10^4$ yr to propagate to the center. The flame width, $\delta$, measured in terms of pressure scale height, $H = 2 \times 10^8$ cm, is $\delta/H \approx 0.03$. The timescale for the flame to cross itself, $t_{\mathrm{cross}} = \delta/u \approx 7 \times 10^9$ s, which is also the timescale for the nuclear burning to occur. The convection zone above the flame has a radial extent of about one pressure scale height $H$, and a convective turnover frequency $\omega_{\mathrm{conv}} \approx 3 \times 10^{-4}\,\mathrm{s^{-1}}$. This implies that there are $\sim 10^5$ convective turnover times in the time it takes flame to cross itself. Thus, over the relatively smaller number of convective turnover times covered by our simulations, $\sim 10^2$, we can treat the flame as effectively stationary. This makes it unnecessary to explicitly include nuclear reactions in our model.

We note that our stationarity assumption is not universally applicable. Convectively bounded oxygen-neon-burning flames, which can also occur in the late evolution of stars in this mass range are thinner, $\delta \sim 10^3$ cm, and have higher velocities, $u \sim 1\,\mathrm{cm\,s^{-1}}$, as a result of the higher energy generation rate (Timmes et al. 1994; Woosley & Heger 2015). Consequently, the time for the flame to traverse its width may be $\lesssim 10$ convective turnover times. Thus it is difficult to anticipate how our simulations carry over to the case of oxygen-neon flames.

[1] MESA is available at http://mesa.sourceforge.net/.

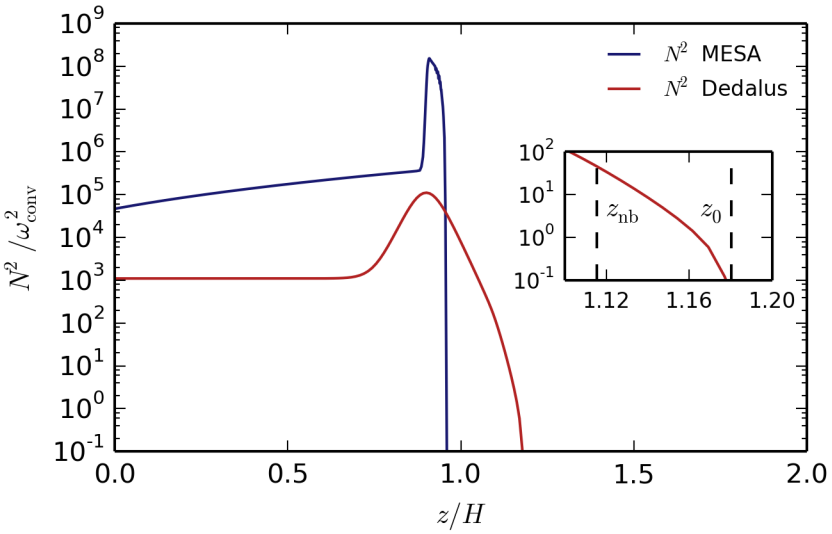


*Figure 5.1*: The blue line shows the buoyancy frequency squared near a carbon flame from a 9.5 $M_\odot$ star evolved in MESA. The red line is the buoyancy frequency squared from the Dedalus simulation R8 (very close to its initial profile, see equation 5.6). Due to computational limitations, the buoyancy frequency in the carbon flame is much lower and the transition between the carbon flame and the convective region is much more gradual, in Dedalus than in the MESA model. These differences both act to enhance the convective mixing via overshoot in Dedalus. The inset shows the neutral buoyancy height $z_{\rm nb}$ and the bottom of the convection zone $z_0$ in the Dedalus simulation. In the MESA model, this region is not resolved, with a width $z_0 - z_{\rm nb} < 3 \times 10^{-3} H$.

The Mach number of the convection is $\approx 4 \times 10^{-5}$, suggesting that compressibility does not play an important role in the convection. To measure the degree of turbulence of the convection, we calculate the Rayleigh number

$$\mathrm{Ra} = \frac{\omega_0^2 H^4}{\nu \kappa}, \tag{5.1}$$

which is the ratio of convective driving to diffusive damping. The variables $\omega_0$ and $H$ represent typical convective frequencies and lengths, and $\nu$ and $\kappa$ are the kinematic viscosity and thermal diffusivity. We estimate the convection driven by a carbon flame to have $\mathrm{Ra} \sim 10^{24}$, using $\nu \sim 5 \times 10^{-2}\,\mathrm{cm^2\,s^{-1}}$ (Itoh et al. 1983) and $\kappa \sim 3 \times 10^{3}\,\mathrm{cm^2\,s^{-1}}$ (Itoh et al. 1987).

Flames maintain coherence because their thermal diffusivity is much larger than their chemical diffusivity. The ratio of these diffusivities is the Lewis number

$$\mathrm{Le} = \frac{\kappa}{D}. \tag{5.2}$$

For carbon flames, we estimate $\mathrm{Le} = 10^6$ (Beznogov & Yakovlev 2014).

## 5.3 Problem Setup

### 5.3.1 Equations & Numerics

We solve the 3D Boussinesq equations (Spiegel & Veronis 1960) using the Dedalus[2] pseudo-spectral code (Burns et al. 2017).

$$\partial_t \boldsymbol{u} + \boldsymbol{\nabla} p - \nu \nabla^2 \boldsymbol{u} + g T \boldsymbol{e}_z = -\boldsymbol{u} \cdot \boldsymbol{\nabla} \boldsymbol{u}, \tag{5.3}$$

$$\partial_t T - \kappa \nabla^2 T = -\boldsymbol{u} \cdot \boldsymbol{\nabla} T + \bar{H}, \tag{5.4}$$

$$\boldsymbol{\nabla} \cdot \boldsymbol{u} = 0, \tag{5.5}$$

where $\boldsymbol{u}$, $p$, and $T$ are the fluid velocity, pressure, and temperature, respectively. $g$ is the gravitational acceleration. We neglecting the compositional effects on buoyancy (and thus thermohaline mixing), and always use $\nu = \kappa$. This is very different from the Prandtl number of stars $\sim 10^{-5}$. However, a Prandtl number of order unity makes the simulations less computationally demanding. The Boussinesq equations are an appropriate model because the convection is low Mach number, and the height of the convection zone is about a scale height.

The simulations are initialized with a temperature profile $T_0(z)$ satisfying $N_0^2(z) = g \mathrm{d}T_0/\mathrm{d}z$, where

$$N_0^2 = -\omega_0^2 + N_{\mathrm{tail}}^2 \frac{1}{2}\left[1 - \tanh\left(\frac{z - z_{\mathrm{fl}}}{\Delta z_{\mathrm{fl}}}\right)\right] + N_{\mathrm{fl}}^2 \cosh\left(\frac{z - z_{\mathrm{fl}}}{\Delta z_{\mathrm{fl}}}\right)^{-2}, \tag{5.6}$$

where $\omega_0^2$ is a characteristic convective frequency, and we take $N_{\mathrm{tail}}^2 = 100\omega_0^2$, $N_{\mathrm{fl}}^2 = 10^4 \omega_0^2$ as approximations to the MESA model. The position of the flame is $z_{\mathrm{fl}} = 0.9H$ and its half-width is $\Delta z_{\mathrm{fl}} = 0.05H$, where $H$ represents a pressure scale height. We plot the time-averaged buoyancy frequency profile of simulation R8 in Fig. 5.1. All simulations have very similar buoyancy frequency profiles, which differ from $N_0^2$ only very close to $z_0$ (defined below). We also include a heating term $\bar{H} = -\kappa \partial_z^2 T_0$ which exactly balances the diffusion of $T_0$. This maintains the flame and convection over the course of our simulations, enforcing the stationary assumption.

Our chosen buoyancy profile differs from the MESA model in two important ways: (1) the peak is at much lower frequencies; and (2) the buoyancy frequency approaches zero much more gradually. This is because it is difficult to resolve the fast buoyancy timescale, and sharp buoyancy gradients numerically. Both these differences should cause more mixing in the model than is realistic (Brummell et al. 2002).

In this chapter, we refer to two important points in the buoyancy profile (see inset in Fig. 5.1). The bottom of the convection zone, where $N^2 = 0$, is denoted $z_0$. We also define the height of neutral buoyancy $z_{\mathrm{nb}}$, the point at which $\langle T(z_{\mathrm{nb}}) \rangle_{x,y,t} = \langle T(z_{\mathrm{top}}) \rangle_{x,y,t}$, where $\langle \cdot \rangle_x$ denotes an average over $x$, and $z_{\mathrm{top}}$ is the top of the domain. Plumes emitted at the top of the convection zone become

[2]Dedalus is available at http://dedalus-project.org.

*Table 5.1*: List of simulations discussed in this chapter. The Rayleigh and Lewis number characterize the diffusion is the simulations (see eqns. 5.1 & 5.2). The resolution is the number of Fourier or Chebyshev modes used in each direction. The CFL safety factor is listed along with our choice of timestepper. The last column is the height at which $\kappa = D_t$, the lowest point at which convective mixing could disrupt a flame. The bottom of the convection zone is $z_0 = 1.180$ and the height of neutral buoyancy is $z_{nb} = 1.116$.

| Name | Ra | Le | Resolution | Timestepper/CFL | $\kappa = D_t$ |
|---|---|---|---|---|---|
| R7 | $10^7$ | 1 | $256^3$ | RK222[a]/1.0 | 1.066 |
| R8 | $10^8$ | 1 | $256^3$ | RK222/1.0 | 1.080 |
| R9 | $10^9$ | 1 | $512^3$ | SBDF2[b]/0.4 | 1.091 |
| R7L3 | $10^7$ | $10^{1/2}$ | $256^3$ | RK222/1.0 | 1.122 |
| R7L10 | $10^7$ | 10 | $256^{3c}$ | RK222/1.0 | 1.143 |

[a]Second order, two-stage Runge-Kutta method (Ascher et al. 1997)

[b]Second order semi-backward differencing (Wang & Ruuth 2008).

[c]The passive scalar field is evolved at $512^3$.

neutrally buoyant at $z_{nb}$. Convective plumes cross $z_0$, but rarely pass below $z_{nb}$. The region between $z_0$ and $z_{nb}$ is the overshoot region.

The simulations are non-dimensionalized using the pressure scale height $H$, and the initial buoyancy frequency in the convection zone $|N_0(z = 2H)| = \omega_0$. These are used to define a Rayleigh number (Eqn. 5.1). Our limited resolution requires diffusivities much larger than in stars, so we can only reach $\mathrm{Ra} = 10^9 \ll 10^{24}$. The simulation self-consistently calculates the convection frequency $\omega_{conv}$ and the height of the convection zone $H_{conv}$. We define $H_{conv}$ using $z_0$ and

$$\omega_{conv} = 2\pi \frac{w_{rms}}{H_{conv}}, \tag{5.7}$$

where $w_{rms}$ is the root-mean-square vertical velocity in the convection zone. We find $H_{conv} \approx 0.83H$ and $\omega_{conv} \sim 0.3\omega_0$.

We solve the equations in cartesian geometry $(x, y, z)$, in the domain $[0, 4H]^2 \times [0, 2H]$. The simulations are periodic in the horizontal directions, and no-slip with zero temperature perturbation at the top and bottom boundaries. All quantities are expanded in a Fourier series in the two horizontal directions. In the vertical direction, quantities are independently expanded in Chebyshev polynomials over the domain $[0, 1.05H]$, and over the domain $[1.05H, 2H]$, with boundary conditions imposed at $z = 1.05H$ to maintain continuity of each quantity and its first vertical derivative. An equal number of Chebyshev modes are used in each vertical sub-domain. 3/2 dealiasing is used in each direction. We use mixed implicit-explicit timestepping, where all the linear terms are treated implicitly, and the remaining terms treated explicitly. The timestep size is determined using the Courant–Friedrichs–Lewy (CFL) condition. Table 5.1 describes the simulations presented in this chapter.

### 5.3.2 Passive Tracer Field

The goal of this work is to estimate turbulent diffusivities associated with convective overshoot. To do this, we solve for the evolution of a passive tracer field $c$

$$\partial_t c - D\nabla^2 c = -\boldsymbol{u} \cdot \boldsymbol{\nabla} c, \tag{5.8}$$

where $D$ is a proxy for chemical diffusivity (and is required for numerical stability). Because $c$ is passive, we can allow $c$ to evolve without including a source term to maintain the flame from diffusing away. This freedom is used to calculate the turbulent diffusivity (similar to Brandenburg et al. 2009). $c$ satisfies zero flux boundary conditions on the top and bottom of the domain, so its volume integral is conserved. It is initialized with

$$c = \frac{1}{2}\left[1 - \tanh\left(\frac{z - 0.8H}{\Delta z_{\rm fl}}\right)\right]. \tag{5.9}$$

## 5.4 Results

After several convective turnover times, the system reaches a statistically steady state. We visualize the convection in Fig. 5.2, plotting 2D vertical slices of the temperature perturbation field and the normalized passive scalar field. The temperature perturbation is $T' = T - \langle T \rangle_{x,y,t}$. We normalize the passive scalar field by subtracting off the volume-average, and setting its value to 1 at the bottom boundary:

$$\tilde{c} = \left(c - \langle c \rangle_{x,y,z}\right) / \left(\langle c(z=0) \rangle_{x,y} - \langle c \rangle_{x,y,z}\right) . \tag{5.10}$$

Fig. 5.2 includes dashed lines at the bottom of the convection zone, $z_0$, and solid lines at the height of neutral buoyancy $z_{\rm nb}$. There is substantial convective overshoot between $z_0$ and $z_{\rm nb}$. However, below $z_{\rm nb}$, the buoyancy perturbations show the long, coherent structures of internal gravity waves. These waves yield negligible mixing. We note the waves are damped more strongly in our simulations than is expected in carbon flames because we use an artificially high thermal diffusivity (see section 5.5).

### 5.4.1 Self-Similar Solution

We now study the evolution of the horizontal average of the passive scalar field, $\bar{c} \equiv \langle c \rangle_{x,y}$. We find that after several convective turnover times, $\bar{c}$ approaches a self-similar solution. Fig. 5.3 shows the evolution of $\bar{c}$ in simulation R8. The profiles collapse to a single curve after subtracting off the volume-average and normalizing the bottom value to unity (i.e., taking the horizontal average of $\tilde{c}$ shown in Fig. 5.2). This indicates that

$$\bar{c}(z,t) - \langle \bar{c} \rangle_z \rightarrow A(t)C(z), \tag{5.11}$$

where $A(t)$ is an amplitude, and $C(z)$ the vertical profile in Fig. 5.3. Furthermore, we find that $A(t) = A_0 \exp(-\lambda t)$ for a constant $\lambda$ that depends on the value of the diffusivities.

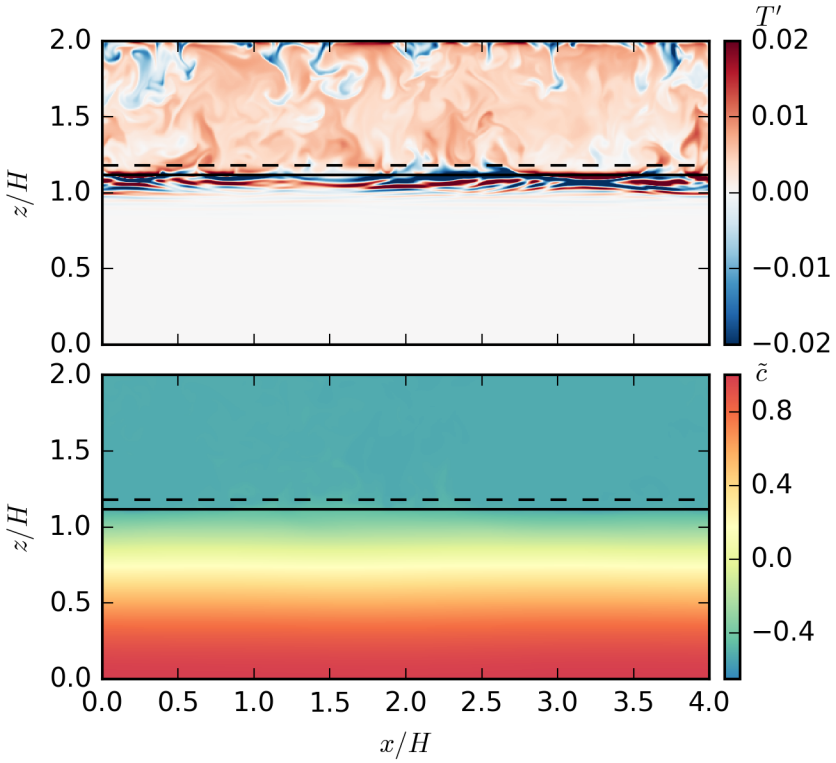


*Figure 5.2*: Two dimensional vertical slices of the temperature perturbation field (top) and the normalized passive scalar field (bottom) in simulation R9. The dashed line shows the bottom of the convection zone, $z_0$, and the solid line shows $z_{\rm nb}$ the neutral buoyancy height. The waves are below $z_{\rm nb}$ and yield negligible mixing.

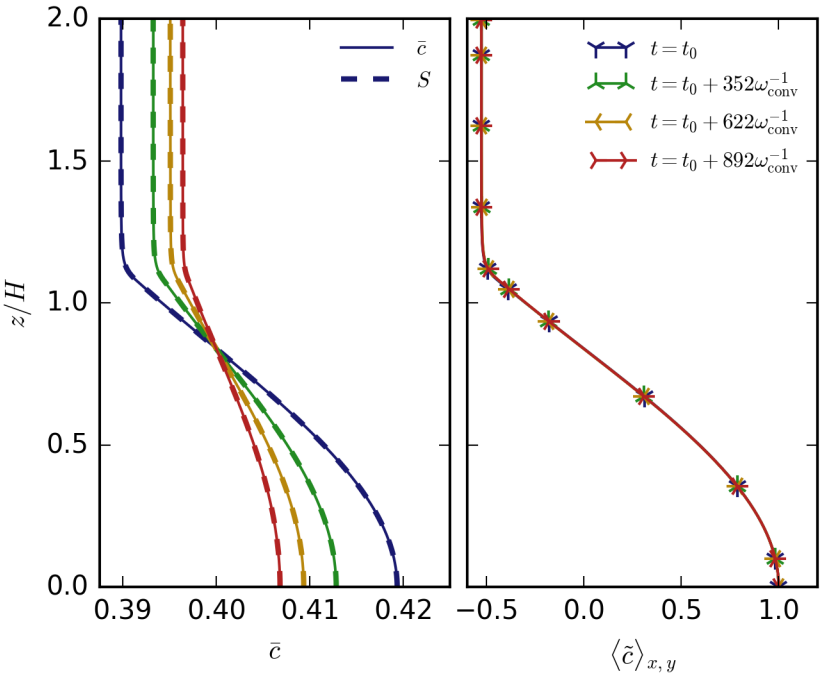


*Figure 5.3*: Horizontal average of the passive scalar field at four times in simulation R8. $\bar{c}$ is also time-averaged around each time for $30\omega_{\mathrm{conv}}^{-1}$. The passive scalar field is attracted to the self-similar solution, $C$ (right panel and equation 5.11). The left panel also shows the solution of the effective diffusion model (equation 5.14). The 1D effective diffusion model matches the 3D simulation.

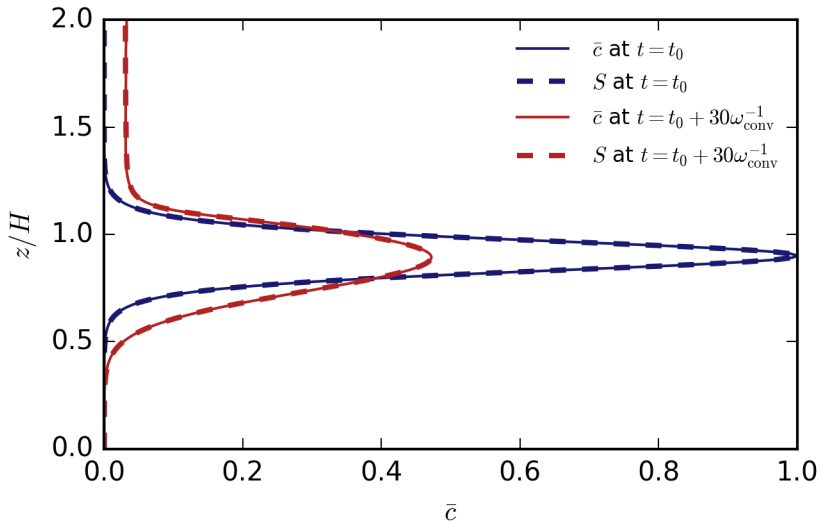


*Figure 5.4*: Horizontal average of the passive scalar field using the convection in simulation R8. $c$ is initialized at $t_0$ to be horizontally uniform, with the vertical profile shown here. The diffusion model equation (5.14) was initialized with the same profile. The 1D effective diffusion model matches the 3D simulation over the entire simulation.

$C$ satisfies the equation

$$-\lambda C - D\partial_z^2 C = -\left\langle \boldsymbol{u}\cdot\boldsymbol{\nabla}\frac{c}{A}\right\rangle_{x,y,t} \tag{5.12}$$

We now assume that the term on the right hand side can be written as an effective diffusion term. This is the Fickian diffusion ansatz (e.g., Brandenburg et al. 2009). Combining with the physical diffusion term on the left

$$-\lambda C = \partial_z(D_\mathrm{t}\partial_z C), \tag{5.13}$$

where $D_\mathrm{t}(z)$ is a new effective diffusivity profile. We can invert equation (5.13) to solve for $D_\mathrm{t}$ in terms of $\lambda$ and $C$. In each simulation, we find that $D_\mathrm{t} = D$ in the stable region, and is large $\sim w_\mathrm{rms}H_\mathrm{conv}$ in the convection zone; as expected, the value of $D_\mathrm{t}$ is not well-constrained in the convection zone, as $\partial_z C$ is very close to zero. In the rest of this chapter, we will replace $D_\mathrm{t}$ with a least-squares fit composed of two error functions, one which approaches $D$ in the flame, and one which approaches $w_\mathrm{rms}H_\mathrm{conv}$ in the convection zone.

### 5.4.2 Effective Diffusivity Model

To show that the convection acts like an effective diffusivity, we solve the model equation

$$\partial_t S(z,t) = \partial_z(D_\mathrm{t}\partial_z S(z,t)). \tag{5.14}$$

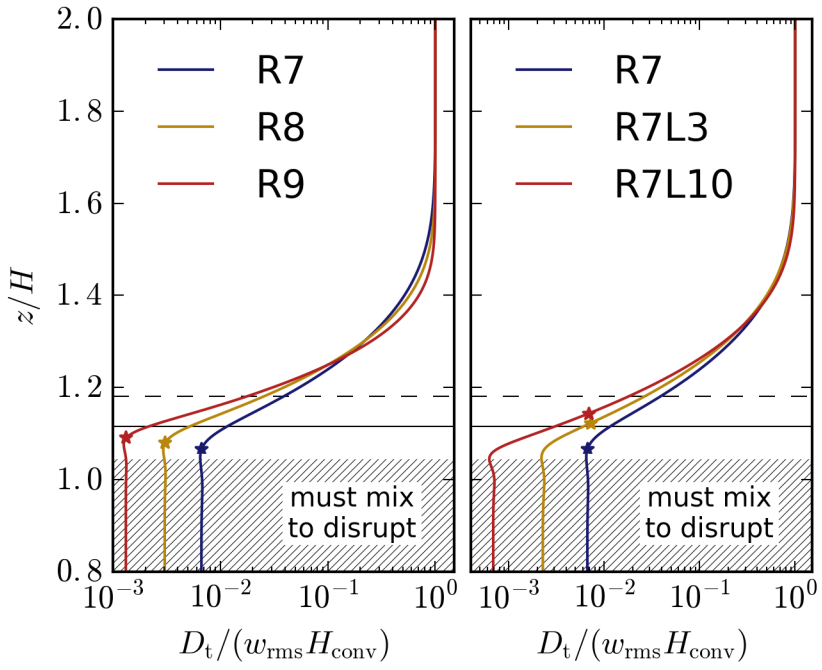


*Figure 5.5*: Effective diffusivity (equation 5.13) as a function of height in each of our simulations. The effective diffusivity is equal to the microscopic diffusivity $D$ below $z = 0.8$. The dashed line shows the bottom of the convection zone, $z_0$, and the solid line shows $z_{\mathrm{nb}}$, the neutral buoyancy height. The height at which $\kappa = D_{\mathrm{t}}$ is marked by an asterisk—mixing can only affect flame propagation above this point. The hatched region shows the region that must be mixed in order to disrupt the flame (section 5.4.4). Since $\kappa > D_{\mathrm{t}}$ in the hatched region, convection will have little effect on flame propagation.

If we initialize $S(z,t)$ with $\langle c(t = t_0)\rangle_{x,y}$ and use our fit for $D_{\mathrm{t}}(z)$, we find that $S \approx A(t)C(z)$, as shown in Fig. 5.3, for every simulation.

As a further test of the diffusion model, we re-initialized simulation R8 with a new passive concentration field profile halfway through the simulation, after the convection is already in a statistically steady state. We also solved equation (5.14) with $S(z,0) = \bar{c}(t = 0)$. Fig. 5.4 shows that $S \approx \bar{c}$ throughout the simulation.

### 5.4.3 Diffusion Profiles

We now describe the effective diffusion profiles $D_{\mathrm{t}}(z)$ in each of our simulations (Fig. 5.5). The effective diffusivity drops from its convective value $w_{\mathrm{rms}}H_{\mathrm{conv}}$ *within* the convection zone. This cannot be attributed to the change in the horizontal average of $w^2$ near $z_0$. In simulation R9, it has dropped two orders of magnitude before reaching the bottom of the convection zone (dashed line).

We are unable to reach the extremely low diffusivities of carbon flames, but we observe trends in the effective diffusivity $D_{\mathrm{t}}$ as Ra and Le increase to more physical values. If $D_{\mathrm{t}} > \kappa$, mixing by overshoot could disrupt the flame. We mark the point where $D_{\mathrm{t}} = \kappa$ in each of the simulations with

an asterisk. As both Ra increases (left panel), and Le increases (right panel), the point at which $D_t = \kappa$ approaches the convection zone. Negligible mixing occurs beyond $z_{nb}$, suggesting that the plumes are not dense enough to penetrate substantially into the flame.

### 5.4.4 Flame Disruption in MESA

We explore the secular effects of mixing on flame propagation in the MESA model via two sets of numerical experiments. First, we set the chemical diffusivity to a constant over the entire flame to determine the ratio $\kappa/D_t$ needed to disrupt a flame. We find the flame is only disrupted if $\kappa/D_t \lesssim 5$ in the flame. This is consistent with our heuristic expectation that $D_t \sim \kappa$ is necessary for flame disruption.

Second, we set the chemical diffusivity to the convective diffusivity $\sim H^2\omega$ in the region of the flame with $N < N_{crit}$. Increasing $N_{crit}$ increases the amount of material in which additional mixing occurs, similar to increasing the overshoot length scale. We find the flame is only disrupted if $N_{crit} \gtrsim 0.1N_{fl}$, where $N_{fl}$ is the peak of the buoyancy frequency. The region below this point is hatched in Fig. 5.5. In all our simulations, $D_t = D$ in this region, indicating no convective mixing. Although convection may mix a small overshoot region, it does not penetrate deep enough into the flame to affect flame propagation.

## 5.5 Conclusions

This chapter describes simulations of an idealized model of convectively bounded carbon flames. The simulations are in the Boussinesq approximation, and assume a Brunt-Väisälä frequency profile motivated by MESA simulations of carbon flames (Fig. 5.1). On the convective timescale, carbon flames are almost stationary, so we do not explicitly include any nuclear burning in our model.

The simulations evolve a passive scalar field which heuristically represents the carbon species fraction. Overshooting plumes mix the passive scalar into the convection zone. The passive scalar field quickly approaches a self-similar solution (equation 5.11; see Fig. 5.3), allowing us to calculate an effective diffusivity profile $D_t(z)$, which captures the extra mixing due to convection. The horizontally averaged 3D evolution of the passive scalar field is very well approximated by the solution of a 1D diffusion equation (equation 5.14; see Fig. 5.4).

We calculate the effective diffusivity profile $D_t(z)$ for each of our simulations (Fig. 5.5). Surprisingly, the diffusivity begins to drop *within* the convection zone (i.e., where $N^2 < 0$). This is very different from the exponential overshoot parameterization derived in the lower Rayleigh number simulations of Freytag et al. (1996), in which the diffusivity starts to decrease at the bottom of the convection zone.

Carbon flames have $\kappa/D \sim 10^6$, but convective mixing can stall a flame if $\kappa \sim D_t$ within the flame. We ran two simulations with $\kappa/D > 1$. We find that as $\kappa/D$ increases (to our maximum value of $10 \ll 10^6$), the height at which $\kappa = D_t$ shifts closer and closer to the convection zone. MESA simulations suggest that a region near the peak of the buoyancy frequency ($N \gtrsim 0.1N_{fl}$)

must be mixed in order to disrupt the flame. None of our simulations show convective mixing in this region. This implies that convective mixing cannot stall a carbon flame and that "hybrid C/O/Ne" WDs are unlikely to be a typical product of stellar evolution.

Convection cannot mix carbon flames because convective plumes must overcome a huge buoyancy barrier to reach the flame. We have neglected important physics in this work, including rotation, magnetism, density stratification, and nuclear burning. However, it seems difficult for these effects to overcome the potential energy barrier, so we do not believe they will change our conclusion.

Internal gravity waves generated by the convection could mix the fluid via breaking. The wave amplitude increases as $\sqrt{N}$ as the waves leave the convection zone and approach the flame. Waves can break if $k_r \xi_r \sim 1$, where $\xi_r$ is the vertical displacement and $k_r$ is the vertical wavenumber. Neglecting damping, theoretical models of internal wave generation by convection (e.g., Lecoanet & Quataert 2013) claim $k_r \xi_r \sim 1$ at the peak of the buoyancy frequency, $N_{\rm fl}$. However, the waves linearly damp due to thermal diffusion (which does not lead to chemical mixing). For carbon flames, we estimate the linear damping to become important near $N_{\rm fl}$, so it is unclear if the waves would break. Furthermore, breaking waves may only mix the unburnt fuel near $N_{\rm fl}$, having little effect on flame propagation.

Given the strong intermittency of convective turbulence, it is also possible that the majority of overshoot mixing may be caused by a few rare but powerful plumes. Although our study cannot rule out this possibility, we note that there are about $\sim 10^6$ convective turnover times in the lifetime of a carbon flame. This is many fewer turnover times than in other astrophysical contexts (e.g., the solar convection zone), so rare events may be less important.

Future work should also study mixing via overshoot in oxygen-neon flames, which is important for understanding whether stars at the top of the SAGB mass range undergo Fe core collapse or electron-capture-induced ONe core collapse (Jones et al. 2014).

# Chapter 6

# Numerical Simulations of Internal Wave Generation by Convection in Water

## 6.1 Introduction

Internal waves are an important non-local transport mechanism in the Earth's atmosphere and in astrophysical fluids. They transport quantities like energy, momentum, and angular momentum from where they are excited to where they damp. Internal wave transport has been invoked to explain such disparate phenomena as the quasi-biennial oscillation (QBO) in the Earth's atmosphere (Baldwin et al. 2001); shear-layer oscillations at the solar tachocline (Talon et al. 2002) and in other stars (Talon & Charbonnel 2005); mass loss during the last year of a massive star's life (Quataert & Shiode 2012; Shiode & Quataert 2014); and synchronization of the rotation of the cores of red giant branch stars (Fuller et al. 2014).

There are many sources of internal waves, including tidal interactions (e.g., Goodman & Lackner 2009), flow over topography, loss of balance (geostrophic adjustment), and convection (Fritts & Alexander 2003). Here we focus on excitation via convection, which is an important source of wave excitation in stars and in the Earth's tropics. Several heuristics are used to explain how internal waves are excited by convection; these include the obstacle effect, the mechanical oscillator effect, and bulk forcing (e.g., Ansong & Sutherland 2010).

The obstacle effect describes the interaction of a horizontal flow over up-flowing plumes. On time scales short in comparison to the plume time scale, the horizontal flow can generate internal waves in the same way that wind generates internal waves over topography (Clark et al. 1986). We restrict ourselves to geometries where there are no mean horizontal flows in the stably stratified region, so the obstacle effect is not important in our simulations. The mechanical oscillator effect refers to excitation by oscillations of the interface between the convective and stably stratified regions (Fovell et al. 1992; Ansong & Sutherland 2010). This is similar to the excitation of sound waves via oscillations in the surface of a drum. In the bulk excitation picture, Reynolds stresses and thermal stresses within the convective region excite internal waves (Goldreich & Kumar 1990; Clark et al. 1986). This is equivalent to the Lighthill (2001) wave excitation theory, and has been applied extensively in the study of sound generation by turbulence (e.g., Lesshafft et al. 2010, and

references within). The main purpose of this chapter is to evaluate the strengths and deficiencies of the interface forcing and bulk excitation mechanisms.

A convenient system for studying convective excitation of internal waves is water near 4°C. Since water has a density maximum at 4°C, a tank cooled to 0°C at the bottom and kept near room temperature at the top is convectively unstable between 0°C and 4°C and stably stratified above 4°C. This experiment was realized by Townsend (1964, 1966), following a suggestion by Malkus. The properties of the penetrative convection have been studied by various authors (e.g., Veronis 1963; Brummell 1993), but not as much attention has been paid to the wave excitation.

There are many numerical simulations of internal wave generation by convection. Moore & Weiss (1973) simulate the water-ice system, and find evidence of internal gravity waves (IGWs). More recently, several authors have studied wave generation in a stable layer adjoining a stratified convective region using the anelastic approximation (e.g., Rogers et al. 2013; Alvan et al. 2014). Rather than simulate both stably stratified and convective regions, Belkacem et al. (2009) and Showman & Kaspi (2013) have coupled simulations of convection (alone) to a theoretical model to estimate wave properties.

The rest of the chapter is organized as follows. In section 6.2.1 we describe the numerical details of the main simulation. Section 6.2.2 presents the broad characteristics of the convectively generated waves. In section 6.3 we discuss the linear damping rates due to diffusion. Sections 6.4 & 6.5 describe simulations of the simulation. We use data from the full simulation to test models of the bulk excitation and interface forcing heuristics. We summarize the main results and conclude in section 6.6.

## 6.2 Full simulation

### 6.2.1 Numerical implementation

We perform simulations of a fluid with a quadratic equation of state using the simple model of fresh water near 4°C of Veronis (1963). The simulations are run using Dedalus (Burns et al. 2015, see `dedalus-project.org` for more information), a general framework for studying partial differential equations, including eigenvalue problems, boundary value problems, and initial value problems (i.e., simulations). It uses a sparse Chebyshev spectral method to solve nearly arbitrary equation sets including algebraic constraints and complex boundary conditions. This flexibility allows us to simulate the water convection problem, as well as simplified linear models representing bulk excitation (section 6.4) and interface forcing (section 6.5). In all cases, we use a two dimensional Cartesian domain with a Fourier grid in the horizontal ($x$) and a Chebyshev grid in the vertical ($z$) directions. Many aspects of the simulation set-up are inspired by the quasi-two dimensional experimental investigation of Le Bars et al. (2015).

We solve the equations

$$\boldsymbol{\nabla}\cdot\boldsymbol{u} = 0, \tag{6.1}$$

$$\partial_t\boldsymbol{u} + \boldsymbol{\nabla}p - \nu\nabla^2\boldsymbol{u} = -\boldsymbol{u}\cdot\boldsymbol{\nabla}\boldsymbol{u} + \boldsymbol{g}\frac{\delta\rho}{\rho_0}, \tag{6.2}$$

$$\partial_t T - \kappa\nabla^2 T = -\boldsymbol{u}\cdot\boldsymbol{\nabla}T - k\,(T - T_{\rm air})\,, \tag{6.3}$$

$$\frac{\delta\rho}{\rho_0} = \frac{\delta\rho(T)}{\rho_0} = -\alpha\,(T - T_0)^2\,, \tag{6.4}$$

where $\boldsymbol{u}, p, T$ are the velocity, pressure, and temperature, respectively. $\delta\rho = \rho - \rho_0$ is the (small) density variation about a typical density of water, $\rho_0$. $\nu, \kappa$ are the viscosity and thermal diffusivity, and $\boldsymbol{g} = -g\boldsymbol{e}_z$ is the gravitational acceleration. Equation 6.1 is the continuity equation and equation 6.2 is the momentum equation. Equation 6.3 is the temperature equation, and includes a Newtonian cooling term $k(T - T_{\rm air})$, which represents heat transfer to the ambient air in the third dimension (the $y$ direction in an $x$–$y$–$z$ coordinate system). The choice of $k$ sets the thermal equilibrium of the system: a small value of $k$ results in a large convective region with only a small stably stratified region, while a large value of $k$ results in a small convective region, with a very large stably stratified region. Our choice of $k$ results in an equilibrium configuration with convective and stably stratified regions of approximately equal size, and corresponds to a heat transfer coefficient of 3.3 W/(m$^2$K). The final equation 6.4 is the equation of state, which is approximated to be quadratic around the density maximum at $T_0 = 4°$C. The diffusivities used in these studies are constant throughout the domain, and correspond to their values for water at $T = 4°$C; here $\mathrm{Pr} = \nu/\kappa = 13.8$. In contrast, the viscosity of water decreases by about a factor of two between $T = 0$ and 25°C, while the thermal diffusivity stays about constant.

The vertical extent of the domain is 0.35 m, and our vertical boundary conditions are no slip, and $T = T_{\rm bot}$, $T = T_{\rm top}$ on the bottom and top, respectively. For the horizontally averaged mode, $\partial_z w = 0$, where $w$ is the vertical velocity. Thus, the conditions $w = 0$ at the top and $w = 0$ at the bottom are redundant. We replace the latter boundary condition with the gauge choice $p = 0$ at the bottom of the domain. We use a resolution of 256 modes and grid points (with no dealiasing) in the vertical direction. Dealiasing is not necessary because the solution is so well resolved that the explicit diffusivities are sufficient for reducing mode amplitudes at high wavenumber to very close to zero. We have repeated portions of the calculation at double resolution, and found negligible differences in the statistics of the flow.

*Table 6.1*: Parameter values used in the simulations.

| parameter | value | parameter | value |
|---|---|---|---|
| $\nu$ | $1.8\times10^{-6}$ m$^2$/s | $\kappa$ | $1.3\times10^{-7}$ m$^2$/s |
| $k$ | $2\times10^{-5}$ s$^{-1}$ | $\alpha$ | $8.1\times10^{-6}$ (°C)$^{-2}$ |
| $T_0$ | 4°C | $T_{\rm air}$ | 21°C |
| $T_{\rm bot}$ | 0°C | $T_{\rm top}$ | 25°C |
| $g$ | 9.8 m/s$^2$ | $z_{\rm int}$ | 0.18 m |

Our horizontal boundary conditions are $u = 0$ and $\partial_x T = \partial_x w = \partial_x p = 0$ on $x = 0$ and $x = 0.2$ m. This allows us to represent $u$ as a sine series in $x$, and $T$, $w$, and $p$ as cosine series in $x$. Plumes rising on the sides of the domain do not exchange heat with the wall, so they lose their buoyancy more slowly than plumes in the center of the domain. Thus, the most stable convective state has plumes rising on the sides of the domain. We use a resolution of 512 sine/cosine modes and grid points (with no dealiasing) in the horizontal direction. We do not dealias in the horizontal direction for the same reason that we do not dealias in the vertical direction.

The time integration uses a split implicit/explicit first-order scheme where certain terms are treated implicitly using forward Euler, and the remaining terms are treated explicitly using backward Euler. We have repeated portions of the calculation with a third order, four-stage DIRK/ERK scheme (Ascher et al. 1997), and found negligible differences in the statistics of the flow. The nonlinear terms, the buoyancy term, and the constant $kT_{\text{air}}$ term in the temperature equation are treated explicitly, and all the other terms are evolved implicitly. The time step is taken to be the lesser of either 0.1 s or the advective Courant–Friedrichs–Lewy (CFL) time given by $0.08 \times \min(\Delta x/u, \Delta z/w)$, where the minimum is taken over every grid point in the domain and $\Delta x$, $\Delta z$ are the grid spacing in the $x$ and $z$ directions, respectively. Typical time steps are $\approx 0.02$ s.

The initial temperature profile is piecewise linear, varying between $T_{\text{bot}}$ at $z = 0$ to $T_0$ at $z = z_{\text{int}} = 0.18$ m, and then to $T_{\text{top}}$ at $z = 0.35$ m at the top of the domain. We also add low amplitude random noise to the temperature field to initiate convection. In this chapter, we analyze the times between 35287 s and 39122 s. This corresponds to a period of about ten convective turnover times, starting about seventy convective turnover times after the beginning of the simulation. We found that ten convective turnover times is long enough to build sufficient statistics to describe both the convection and waves. Although we simulate many convective turnover times, the simulation up to 40000 s corresponds to only 4% of a thermal time, so the thermal structure continues to evolve on long time scales throughout the simulation. Several dimensionless numbers describing the convection in this simulation are given in table 6.2. Because our equations include a Newtonian cooling term, we do not have a constant heat flux through the convection zone. Thus, we calculate the Nusselt number using the average value of $wT$ in the convection zone.

### 6.2.2 Characteristics of convectively generated waves

The convective excitation of waves is depicted in figure 6.1. Panel (*a*) shows the typical state before a major excitation event. The convective region contains two counter-rotating convective cells, with up flows (represented by red cold, buoyant fluid) along the sides of the domain, and a

*Table 6.2*: Dimensionless numbers characterizing the convection in the lower part of the domain. $L_{\text{conv}}$ is taken to be 0.22 m. We use $\langle\cdot\rangle_{x,\ldots}$ to denote an average with respect to the variables listed in the subscript. The $z$ average in the calculation of Nu is only within the convection zone.

| $\text{Ra} = \dfrac{g\alpha T_0^2 L_{\text{conv}}^3}{\nu\kappa}$ | $\text{Re} = \dfrac{u_{\text{rms}} L_{\text{conv}}}{\nu}$ | $\text{Nu} = \dfrac{-\langle wT\rangle_{x,z,t}}{\kappa T_0 / L_{\text{conv}}}$ |
|---|---|---|
| $5.8 \times 10^7$ | 100 | 6 |

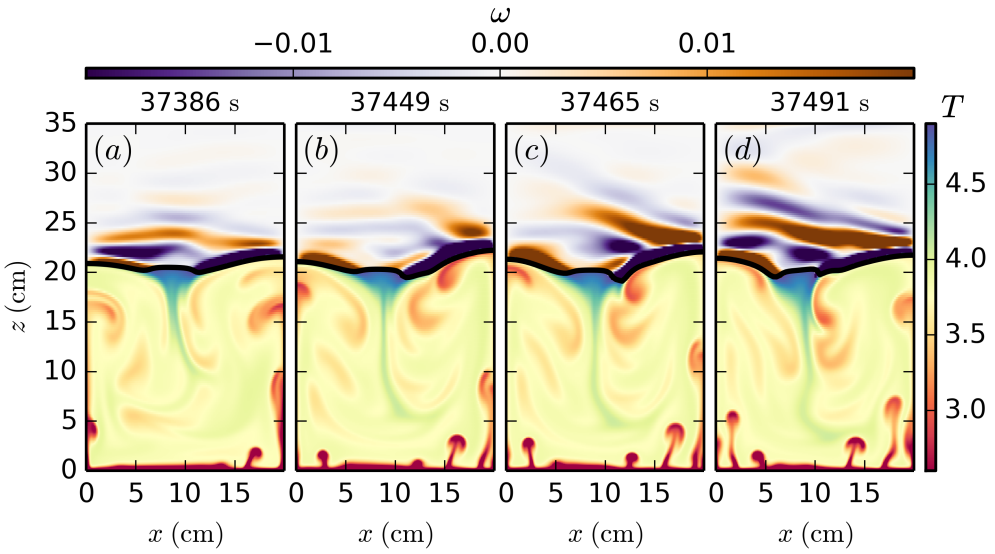


*Figure 6.1*: Four simulation snapshots near $t = 37400$ s. The bottom part of the domain (below the thick black line) shows the temperature field. Recall that below 4°C, cold water (red) is less dense than hot water (blue). The thick black line is the 5°C isotherm and shows the boundary between the convective region (below) and the stably stratified region (above). The top part of the domain (above the thick black line) shows the vorticity field associated with IGWs.

down flow (represented by blue hot, dense fluid) in the center. Because water has a Pr sufficiently higher than one, the thermal boundary layer at the bottom of the domain is unstable to the formation of buoyant plumes. The turnover frequency of the convective cells ($\sim 2 \times 10^{-3}$ Hz) and the plume ejection frequency ($\sim 10^{-2}$ Hz) are the important time scales in the convection zone. The yellow curve in figure 6.2, panel (*c*), shows the kinetic energy spectrum at the top of the convection zone ($z \approx 0.19$ m). Although there is a peak at the turnover frequency, the spectrum is fairly flat between the turnover frequency and the plume ejection frequency. At frequencies higher than the plume ejection frequency, the spectrum falls off rapidly.

Panel (*a*) of figure 6.1 shows a particularly vigorous plume on the right side of the domain at about $z = 0.16$ m. This plume rises into the stably stratified region (water above 4°C) in panel (*b*), moving the interface between the convective and stably stratified regions upwards and generating strong, localized IGWs. The plume is deflected by the stratified fluid above it, and deflects leftwards. This allows the interface to lower (panels *c* & *d*).

Figure 6.1 shows the IGWs generated by the plume in the lower right corner of the stably stratified region propagate toward the upper-left. However, the phase velocity is toward the lower-left—the upper part of the wave packet starts with positive vorticity (panel *b*), but shifts to having negative vorticity (panel *c*), and then positive vorticity again (panel *d*). This is consistent with the IGW dispersion relation, which implies that the group velocity is perpendicular to the phase velocity.

IGWs are continually excited as the plumes detaching from the bottom boundary layer ap-

proach the interface. Viscosity typically damps the waves before they can propagate to the top of the domain. This is depicted in figure 6.2(*a*), a spectrogram of the kinetic energy density, i.e., a plot of $\omega\langle K\rangle_x \equiv 0.5\ \omega\langle|\boldsymbol{u}(\omega, x, z)|^2\rangle_x$ as a function of $\omega$ and $z$, where $\langle\cdot\rangle_x$ denotes a horizontal average. All logarithms in this chapter are base $e$. The frequency spacing of our data is uniform, so at high frequencies, the frequency density becomes large. To improve the statistical power, we smooth the data by convolving with a gaussian with $\sigma_z = 2.5 \times 10^{-3}$ m and $\sigma_{\log\omega} = 0.05$. Figure 6.2 (*a*) also shows the real (black line) and imaginary (white line) parts of the buoyancy (Brunt-Väisälä) frequency, defined by

$$N^2 = \alpha g \frac{\mathrm{d}\left(\langle T\rangle_{x,t} - T_0\right)^2}{\mathrm{d}z}. \tag{6.5}$$

The real part of the buoyancy frequency is the maximum frequency of IGWs, and the imaginary part gives the convection frequency within the convective region.

In the convective region (below $z \approx 0.22$ m), the energy is peaked near the convection frequency at $f \approx 2 \times 10^{-3}$ Hz (figure 6.2 (*c*), yellow line). The convection has power at a broad range of frequencies extending to high frequencies ($> 10^{-1}$ Hz). By contrast, the power in the stably stratified region is localized below the buoyancy frequency (figure 6.2 (*c*), red & blue lines). Although the excitation of internal waves is strongest near the convection frequency, these waves quickly viscously damp. However, higher frequency waves with $f$ between 1–2 $\times 10^{-2}$ Hz have longer damping lengths, and can propagate much further into the stably stratified region.

In a statistically steady state, the viscous damping of waves matches the convective excitation. We use this to estimate the wave flux generated by convection and compare to theoretical predictions. Equating the wave flux to the viscous damping, we find that the flux at a height $z$ in a mode with horizontal wavenumber $k_x$ and frequency $\omega$ is

$$F_{\text{wave}}(z, k_x, \omega) \sim \nu\ell_d(k_x, \omega)|\boldsymbol{k}|^2|\boldsymbol{u}(z, k_x, \omega)|^2, \tag{6.6}$$

where $\ell_d$ is the linear viscous damping length. We discuss the calculation of $\ell_d$ in section 6.3.

To calculate the wave flux, we first calculate the kinetic energy of all modes with frequency $\omega$ as a function of height, $\left\langle|\boldsymbol{u}(z,\omega)|^2\right\rangle_x$. Figure 6.2 (*b*) plots this for three different values of $\omega$. Near the interface at $z = 0.22$ m, the kinetic energy is decreasing exponentially with height. We find that this exponential decay is well fit by $\ell_d$ for a single $k_x$ typically corresponding to a large wavelength mode. In calculating $\ell_d$, we assume that $N$ is constant and equal to 0.08 Hz, a typical value within the stably stratified region. This suggests that most of the energy in waves with frequency $\omega$ is concentrated into a mode with a specific $k_x$ at $z = 0.22$ m. In figure 6.2 (*b*), thin solid lines show the predicted damping for waves with $\omega = 2 \times 10^{-3}$ Hz and wavelength $\lambda_x = 0.4$ m (green); $\omega = 9 \times 10^{-3}$ Hz and $\lambda_x = 0.2$ m (purple); and, $\omega = 2 \times 10^{-2}$ Hz and $\lambda_x = 0.1$ m (orange). These all give good local fits, although the damping rate decreases with height for the two larger values of $\omega$. This is because the waves with $\lambda_x = 0.1$ m or 0.2 m damp more quickly than waves with $\lambda_x = 0.4$ m, so although these lower wavelength waves are dominant at $z = 0.22$ m, they become subdominant higher in the domain.

This shows that the wave flux at $z = 0.22$ m (the position of the convective–stably stratified interface) for a given $\omega$ is dominated by a single $k_x$. In figure 6.3, we plot the flux as a function of

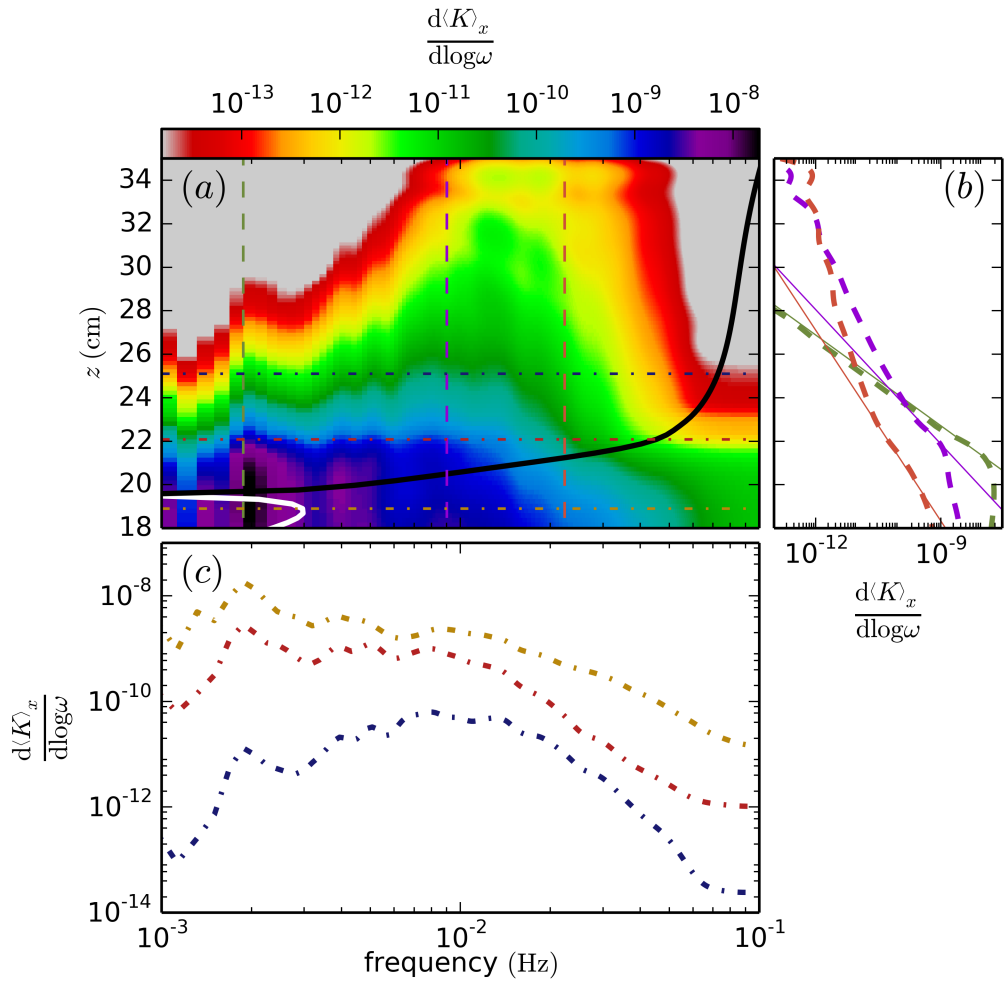


*Figure 6.2*: (*a*): spectrogram of the kinetic energy density. The white curve is the imaginary part of the buoyancy frequency corresponding to the convection frequency. The black curve is the real part of the buoyancy frequency in the stably stratified region. The data has been smoothed to improve statistics (see text for more details). Panels (*b*) & (*c*) plot the kinetic energy density as a function of $z$ (dashed lines) & $\omega$ (dot–dashed) respectively; the vertical and horizontal lines in panel (*a*) are color–coded to correspond to these slices. The thin solid lines in panel (*b*) show the predicted linear damping rates near the convective–stably stratified boundary at $z = 0.22$ m. Within the convection region (panel (*c*), yellow curve), the energy is peaked near the convection frequency. However, these low frequency waves are quickly attenuated, and the stably stratified region is dominated with waves with frequencies $1–2 \times 10^{-2}$ Hz (panel (*c*), blue curve).

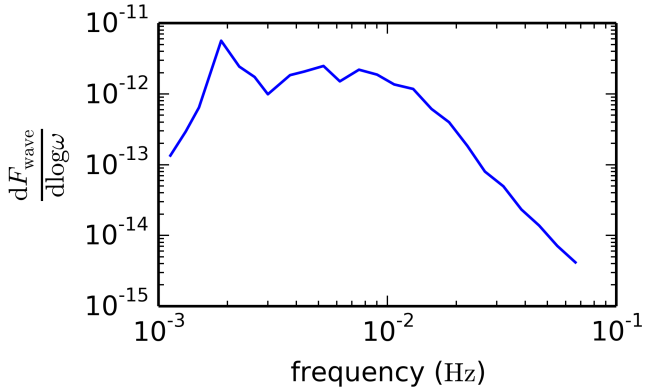


*Figure 6.3*: Wave flux spectrum at $z = 0.22$ m calculated using equation 6.6. We assume that the flux at each $\omega$ is dominated by a single $k_x$, which we determine by comparing the energy decay rate at $z = 0.22$ m to $\ell_d(\omega, k_x)$.

$\omega$, where we assume all the energy is at this special value of $k_x$. Although there is a peak in the wave flux spectrum at the turnover frequency ($2 \times 10^{-3}$ Hz), the spectrum is fairly flat out to the plume ejection frequency ($10^{-2}$ Hz). At higher frequencies, the wave flux decreases as $\omega^{-3}$. The total flux is

$$F_{\text{wave,sim}} \sim 5 \times 10^{-12} \text{ (m/s)}^3. \tag{6.7}$$

The theoretical prediction for the wave flux is $\mathcal{M} u_c^3$ (e.g., Goldreich & Kumar 1990; Lecoanet & Quataert 2013), where $u_c$ is a typical convection velocity and $\mathcal{M}$, the "convective Mach number," is an efficiency factor equal to the ratio of a typical convection frequency to a typical buoyancy frequency. From figure 6.2 (*a*), we estimate $\mathcal{M} \sim 0.03$. If we estimate $u_c \sim \omega_c \ell_c$, where $\omega_c = 2 \times 10^{-3}$ Hz is the turnover frequency and $\ell_c = 0.22$ m is the depth of the convective region, then $u_c = 0.4 \times 10^{-3}$ m/s and

$$F_{\text{wave,theory,1}} \sim 2.5 \times 10^{-12} \text{ (m/s)}^3. \tag{6.8}$$

However, if we assume that $u_c$ is the rms velocity in the convection zone, this gives $u_c = 0.9 \times 10^{-3}$ m/s and

$$F_{\text{wave,theory,2}} \sim 2.5 \times 10^{-11} \text{ (m/s)}^3. \tag{6.9}$$

Thus, the wave flux calculated in the simulations is in the range expected theoretically. This calculation shows that the predicted flux depends sensitively on the assumptions made for various parameters, so we cannot expect more than rough agreement.

## 6.3 Linear damping rates

Wave damping is an important process in the simulation. Rogers & MacGregor (2011); Rogers et al. (2013), and & Alvan et al. (2014) argued that the linear damping rate overestimates the damp-

ing in simulations of convectively excited waves. They attribute the lack of damping to nonlinear interactions. In contrast, we find that linear theory accurately describes the wave damping in our simulation, but only when the full damping rate is used.

The linear damping rate can be derived from the linearized equations of motion in the Wentzel–Kramers–Brillouin (WKB) limit. Zahn et al. (1997) and Press (1981) calculate the damping rate, but only in the quasi-adiabatic or weak dissipation limit, which is not always applicable.

We will describe the damping using an inverse damping length,

$$E(z) = E(z_0) \exp\left(-2 \int_{z_0}^{z} \ell_d^{-1} dz\right), \tag{6.10}$$

where we assume $z > z_0$. In the weak dissipation limit, the inverse damping length due to viscosity is

$$\ell_d^{-1} = \nu \frac{N^3 k_x^3}{\omega^4}. \tag{6.11}$$

For water, viscous damping dominates, while in astrophysical systems, Pr is typically much less than unity, so viscosity is typically less important than thermal diffusivity. Equation 6.11 shows that as $\omega$ goes to zero, the inverse damping length increases as $\omega^{-4}$. This expression for the inverse damping length is valid only in the weak dissipation limit, i.e., when $\omega \gg \nu k^2$. Geophysical and astrophysical systems have very small diffusivities, so this condition is satisfied. However, laboratory experiments and numerical simulations have much larger diffusivities. We find that most modes in our simulation are not in the weak dissipation limit, so we would not expect equation 6.11 to represent the dynamics in the simulation.

The calculation of the linear damping rate in the WKB limit without assuming weak dissipation is more involved, but straightforward. The inverse damping length is

$$\ell_d^{-1} = \operatorname{Im}\left[\frac{(-1)^{3/4}}{\sqrt{2}} \sqrt{-2ik_x^2 - \frac{\omega}{\nu} + \frac{\sqrt{\omega^3 + 4ik_x^2 \nu N^2}}{\nu \sqrt{\omega}}}\right]. \tag{6.12}$$

This reduces to equation 6.11 in the weak damping limit, $\omega \gg k^2 \nu$. Furthermore, the vertical wavenumber also changes from the standard adiabatic result ($k_z = k_x N/\omega$),

$$k_z = \operatorname{Re}\left[\frac{(-1)^{3/4}}{\sqrt{2}} \sqrt{-2ik_x^2 - \frac{\omega}{\nu} + \frac{\sqrt{\omega^3 + 4ik_x^2 \nu N^2}}{\nu \sqrt{\omega}}}\right]. \tag{6.13}$$

In the limit of small $\omega$, the inverse damping length in equation 6.12 approaches

$$\ell_d^{-1} = \sin(7\pi/8) \left(\frac{k_x^2 N^2}{\nu \omega}\right)^{1/4}. \tag{6.14}$$

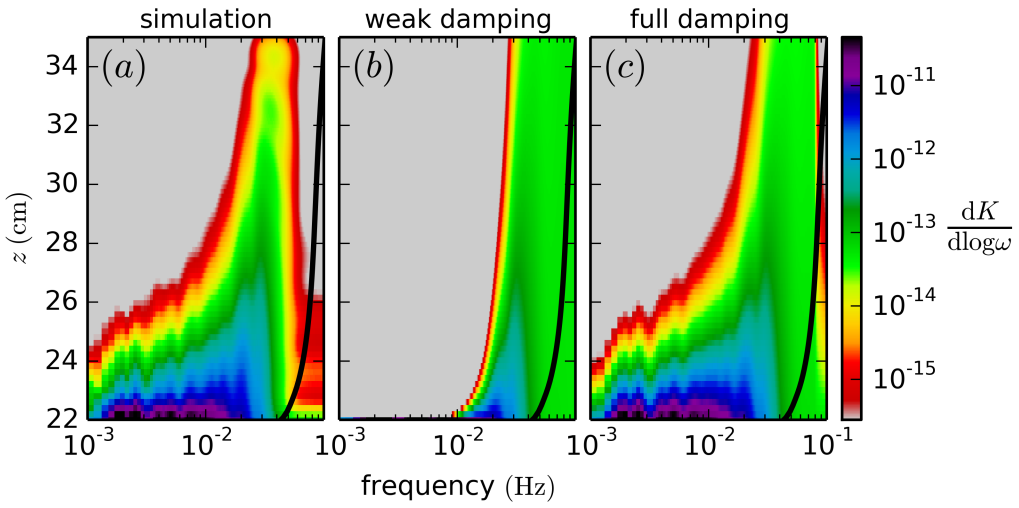


*Figure 6.4*: Spectrograms of kinetic energy in modes with $k_x = 2\pi/0.1$ m$^{-1}$ testing different linear damping formulas. The black line shows the horizontally and temporally averaged buoyancy frequency profile. Panel (*a*): the spectrogram for the simulation result. Panel (*b*): the spectrum from the simulation evaluated at $z = 0.22$ m multiplied by the damping factor (equation 6.10), using the weak dissipation limit expression for $\ell_d^{-1}$ (equation 6.11). Panel (*c*): the spectrum from the simulation evaluated at $z = 0.22$ m multiplied by the damping factor, using the full expression for $\ell_d^{-1}$ (equation 6.12). While the weak damping formula significantly overestimates the damping, the full damping formula accurately describes the damping in the simulation.

In this limit, the inverse damping length increases only as $\omega^{-1/4}$ as $\omega$ goes to zero, much more slowly than in the weak damping limit where $\ell_d^{-1} \sim \omega^{-4}$. For small $\omega$, the weak damping limit predicts the waves are strongly damped. This indicates that the weak damping limit is not appropriate. We find that, although the actual wave damping is less severe than predicted by the weak damping limit, the waves are still strongly damped.

In figure 6.4, we compare these two damping rate calculations with the simulation. Because the inverse damping length depends on the wavenumber, we first filter the simulation data to only include modes with $k_x = 2\pi/0.1$ m$^{-1}$. Panel (*a*) shows the spectrogram of the kinetic energy in these modes in the simulation. Note that there is a factor of $\sim 10$ less energy in this set of modes than in the full simulation (figure 6.2 (*a*)). To simplify the calculation of the damping factor (equation 6.10), we approximate $N$ to be uniform and equal to 0.08 Hz. In panel (*b*), we plot the energy as a function of height using equation 6.10, using the weak dissipation limit for $\ell_d^{-1}$ (equation 6.11), normalizing the wave energy at $z = 0.22$ m using the simulation results (as done in, e.g., Taylor & Sarkar 2007). This greatly overestimates the damping for short wavelength waves ($\omega < 2 \times 10^{-2}$ Hz) because these waves are not in the weak damping limit. This is similar to the results of Rogers & MacGregor (2011); Rogers et al. (2013), and Alvan et al. (2014). We repeat the calculation in panel (*c*), but now use the full expression for $\ell_d^{-1}$ (equation 6.12). When using the full expression without taking the weak dissipation limit, we find that linear theory correctly

describes the damping in the stably stratified region.

## 6.4 Bulk excitation: Reynolds stress forcing

We now test two proposed models of internal wave excitation, first bulk excitation, then interface forcing (section 6.5). We use linear wave models and data from the full simulation to calculate the vertical velocity associated with the wave field. We then compare the wave field in these simplified models with the wave field in the full simulation.

The bulk excitation mechanism is an application of the Lighthill (2001) approach to calculating wave excitation. We decompose the vertical displacement $\xi_z$ into a wave-like component and a convection-like component using the linear eigenfunctions. The wave excitation is given by the projection of the Reynolds stress associated with convection onto the wave-like component by a source term $S$ (Lecoanet & Quataert 2013). This can be written as

$$\nabla^2\left(\partial_t - \nu\nabla^2\right)\partial_t\xi_z + N^2\partial_x^2\xi_z = S \equiv -\nabla^2\left(\boldsymbol{u}\cdot\boldsymbol{\nabla}u_z\right) + \partial_z\left[\left(\partial_{x_i}u_j\right)\left(\partial_{x_j}u_i\right)\right], \tag{6.15}$$

where repeated indices are summed over. We have assumed here that the only important nonlinearity is the Reynolds stress and have neglected the $\boldsymbol{u}\cdot\boldsymbol{\nabla}T$ nonlinearity. Mixing length theory suggests the Reynolds stress term is the most important source term (e.g., Goldreich & Kumar 1990). We also neglect thermal diffusivity because it has a smaller effect than viscosity.

To test the bulk excitation mechanism, we solve equation 6.15, where the source term is calculated directly from the velocities in the full simulation. This is possible by exploiting the flexibility of Dedalus. We solve two problems simultaneously; the full problem described in section 6.2.1, as well as the linear forced problem described here. At every time step, we first evolve the full problem forward. Then we calculate the source term using the velocities in the full problem. With the new source term, we take time step in the linear forced problem, and repeat.

Freund (2001) and Boersma (2005) used a similar approach to study the generation of sound waves by a turbulent jet. In Freund (2001), the linear model is used to study sound waves in the far field, which is too large to be resolved by the jet simulation. In contrast, Boersma (2005) solves the incompressible equations, and uses a linear wave equation to estimate wave generation due to a source term. Neither study is able to compare the predictions of the bulk excitation model with self-consistently generated waves within their simulations, and both limit their analysis to the far field.

We solve the linear problem on the same domain as the full problem, and use the same timestepping scheme. We start the calculation at $t = 34878$ s. The $N^2$ profile we use is a horizontally and time averaged profile, as in figure 6.2($a$), where all negative values of $N^2$ are set to zero so that we can neglect exponentially growing convective modes. The boundary conditions are $\xi_z = 0$ on top and bottom, $\partial_t\partial_z\xi_z = \partial_x u = 0$ on the top, and $\partial_t\partial_z^2\xi_z = \partial_x\partial_z u = 0$ on the bottom, where $u$ is the horizontal velocity. To make sure the source term arises only from the convection and not the existing waves in the simulation, we mask $S$ to include only the convection zone by multiplying it by $0.5\,[1 - \tanh((z - 0.23)/0.01)]$.

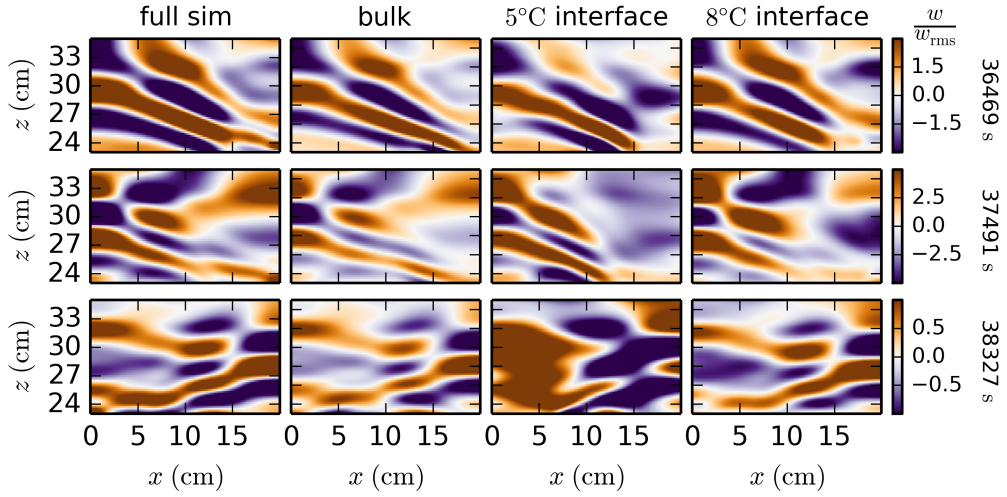


*Figure 6.5*: Snapshots of vertical velocity in the stably stratified region at three different times for the full simulation (first column), bulk excitation simulation (second column), and interface forcing simulations with a 5°C interface (third column) and an 8°C interface (fourth column). The vertical velocities are normalized by the rms vertical velocity at each height. Although there is quite good agreement between the full simulation and the bulk excitation simulation, the interface forcing simulations are not as accurate.

In figure 6.5, we compare the flow pattern between the full simulation and the bulk excitation simulation, as well as two interface forcing simulations described in section 6.5. Because the velocities decrease rapidly with height (see figure 6.1), we normalize the vertical velocity to its rms at each height. At each of the three chosen times, there is very good agreement between the full simulation and the bulk excitation simulation. Note that the second row corresponds to the same time as figure 6.1(*d*). The average amplitude for the bulk excitation simulation is smaller than the average amplitude of the full simulation by a factor of about 0.7. The agreement is quite impressive given the simplified physics in the bulk excitation simulation. The remaining differences might be because we only included the Reynolds stress source term, and not a source term proportional to the $\boldsymbol{u} \cdot \boldsymbol{\nabla} T$ nonlinearity.

To compare quantitatively the two wave fields throughout the simulation, we plot the spectrogram for each simulation in figure 6.6. Again, there is striking agreement between the full simulation and the bulk excitation simulation. We also calculated the correlation of $w/w_{\mathrm{rms}}$ between the two simulations, from 35287 s to 39121 s and from $z = 0.235$ m to 0.349 m. The correlation between the full simulation and the bulk excitation simulation is 96%.

## 6.5 Interface forcing: Mechanical oscillator effect

In this section we present simulations which test interface forcing. We again solve the linear IGW equation, but now force the system with a boundary condition instead of a source term. The moving bottom boundary represents the movement of the interface between the convective and

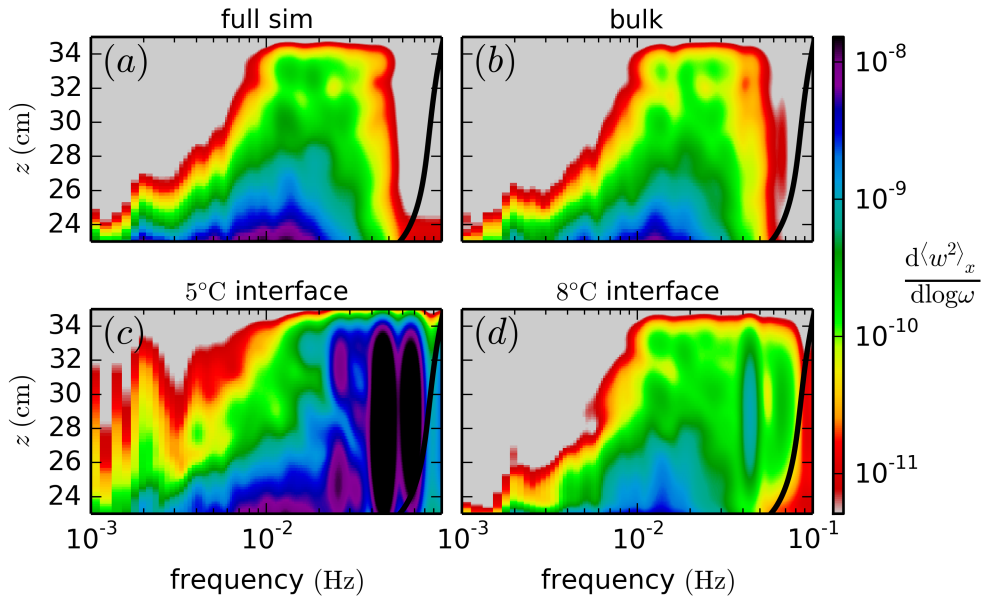


*Figure 6.6*: Spectrogram of vertical velocity squared in four different simulations. The black line shows the horizontally and temporally averaged buoyancy frequency profile. Panel (*a*), full simulation; panel (*b*), bulk excitation simulation; interface forcing simulations with 5°C interface (panel *c*) and 8°C interface (panel *d*). The bulk excitation simulation agrees very well with the full simulation. The interface forcing simulations overestimate the excitation of high frequency waves. This is because the interface forcing cannot detect sweeping motions along the interface, and thus treats the wave excitation as impulsive events which produce high frequency waves.

stably stratified regions in the full simulation. This generates IGWs just as moving the surface of a drum generates sound waves.

First we calculate the interface position as a function of time using data from the full simulation. We calculate two interfaces: a 5°C interface and an 8°C interface. We use 5°C to get very close to the density maximum (4°C), without having to worry about large temperature fluctuations producing unphysical fluctuations in the interface position. The 8°C interface is used because a rising fluid element at 0°C becomes neutrally buoyant when it reaches 8°C, assuming no conductive losses. We calculate the interface position every two hundred time steps (i.e., one fifteenth of a buoyancy period) in the full simulation, calculating the $z$ position at which $T = 5$°C or 8°C at each $x$ position. The interface position at intermediate times is reconstructed via linear interpolation. Calculating the interface position every one hundred time steps (and using linear interpolation for intermediate times) produced no visible changes in the simulation results.

The interface forcing simulations are run on a reduced domain, with $x$ varying from 0 to 0.2 m, but $z$ varying from the mean interface position to 0.35 m. The mean interface position is 0.2096 m for the 5°C interface and is 0.225 m for the 8°C interface. The horizontal resolution in both cases is 512 Fourier modes and grid points (with no dealiasing), and the vertical resolution in both cases is 128 Chebyshev modes and grid points (with no dealiasing). Doubling the vertical resolution of the simulation had no noticeable effect on the wave field.

More specifically, we solve the linear, homogeneous wave equation,

$$\nabla^2 \left(\partial_t - \nu\nabla^2\right) \partial_t \xi_z + N^2 \partial_x^2 \xi_z = 0, \tag{6.16}$$

where $N^2$ is the temporally and horizontally averaged buoyancy frequency, as in section 6.4. Our boundary conditions are as follows. On the bottom, we set $\xi_z = \delta z_{\text{int}}(x,t)$, where $\delta z_{\text{int}}(x,t)$ in the deviation of the interface position from its mean position at that time (i.e., $\langle \delta z_{\text{int}}(x,t)\rangle_x = 0$). This ensures there is zero mass flux into the domain. The second bottom boundary condition is $\partial_t \partial_z^2 \xi_z = \partial_x \partial_z u = 0$. We also tried imposing pressure continuity at the interface as a second boundary condition—this gives qualitatively similar results. The top boundary conditions are $\xi_z = 0$ and $\partial_t \partial_z \xi_z = \partial_x u = 0$.

For timestepping, we use a first order forward Euler/backward Euler scheme. Although the entire equation is linear, we treat the buoyancy term $N^2 \partial_x^2 \xi_z$ explicitly. As mentioned above, the interface position is calculated every two hundred time steps in the full calculation—call this time difference $\Delta t_i$ (which varies, as the time step is set by the CFL condition). The time step for these interface forcing calculations is $\Delta t_i/40$. Thus, the average time step is five times larger than the average time step in the full simulation. Using a smaller timestep of $\Delta t_i/80$ had no noticeable effect on the wave field. The calculation starts at $t = 34878$ s.

Figure 6.5 shows three snapshots of the wave field for the interface forcing simulations using the 5°C interface and the 8°C interface. Although the broad features of the wave field are present, the 5°C interface simulation does not reproduce all the features of the full simulation (the difference is especially striking in the third snapshot at $t = 38327$ s). However, the 8°C interface simulation matches the full simulation fairly well.

As for the bulk excitation simulation, we calculated the correlation of $w/w_{\text{rms}}$ between the full simulation and each of the interface forcing simulations. While the 8°C interface simulation has a

correlation of 81%, the 5°C interface simulation only has a correlation of 31%. Neither come close to matching the 96% correlation of the bulk excitation simulation with the full simulation.

The interface forcing simulations over-excite high frequency waves because they treat the wave excitation as an impulsive process. Large plumes can significantly deflect the interface on short timescales, which excites high frequency waves. In the laboratory experiments of Ansong & Sutherland (2010), dense plumes produce these sorts of large deflections, generating high frequency waves. Michaelian (2002) and Le Bars et al. (2015) also find that high frequency waves are generated when the changing thermal states early in their experiments produce vigorous plumes. In the terminology of astrophysical penetrative convection, these would be termed "penetrating" plumes, rather than typical "overshooting" plumes (e.g., Brummell et al. 2002).

However, most waves are not being generated by these particularly strong, "penetrating" plumes. Instead, they are being generated by the sweeping motion of plumes below the interface, which preferentially generates waves at low frequencies and large horizontal wavelengths. This is accurately captured by the bulk excitation calculation, but not in the interface forcing calculations. If something prevented motions in the convection zone near the interface, there could be waves generated by stresses within the convection zone, even if there are no accompanying interface motions. Because the interface forcing calculations do not know about these sweeping motions, they treat the plumes as an impulsive forcing, generating too many high frequency waves.

Using a higher interface (the 8°C interface) improves the results as the dynamics are better modeled as linear. This is an important check on our numerical implementation of the interface forcing simulations. An interface which is far away from the convection should faithfully reproduce the wave field, but this does not give insight into the wave excitation process since the "interface" motions are dominated by the waves themselves rather than the convection. Instead, this exposes a conceptual problem with the interface forcing picture of wave excitation.

## 6.6 Conclusions

In this chapter we present simulations of convective excitation of internal gravity waves in a fluid with a water-like equation of state. Cold, buoyant plumes near 0°C detach from an unstable boundary layer at the bottom of the domain and are advected by two convective cells to the top of the convective region. As the plumes approach the interface between the convective and stably stratified regions, they generate internal gravity waves (figure 6.1). Although the wave excitation is dominated by low frequency waves matching the convective turnover frequency, these waves are quickly damped as they propagate upwards. Only high frequency waves reach the top of the domain (figure 6.2). Estimates of the wave flux are reasonably consistent with the theoretical estimate of $\mathcal{M}u_c^3$, where $\mathcal{M}$ is the ratio of convection frequency to buoyancy frequency, and $u_c$ is a characteristic convection velocity.

We find that the wave damping with height is in agreement with analytic theory, provided one uses the full expression for the damping length (equation 6.12). Because geophysical and astrophysical waves excited by convection are typically weakly damped by diffusive processes, previous analyses of simulations (e.g., Rogers & MacGregor 2011; Rogers et al. 2013; Alvan

et al. 2014) have used the quasi-adiabatic, or weak dissipation limit (equation 6.11). However, simulations and laboratory experiments have much larger diffusivities than natural systems, and we find that the waves generated in our simulation are mostly not in the weak dissipation limit. Using the full damping expression, we find that low frequency waves have inverse damping lengths proportional to $\omega^{-1/4}$, rather than $\omega^{-4}$ in the weak dissipation limit. This implies that the weak dissipation expression overestimates the wave damping, consistent with previous claims about the failure of linear damping to explain the damping in simulations of convective excited waves. However, we find that the full linear damping rate is able to correctly reproduce the damping in the simulation (figure 6.4).

In addition to this full simulation, we also present three simulations of the simulation. The first tests bulk excitation, where waves are excited by Reynolds stresses within the convective region (section 6.4). We solve the linear wave equation forced by a Reynolds stress source term calculated at each position and time from the convection zone of the full simulation. This accurately reproduces the wave field and spectrum (figures 6.5 & 6.6); the wave field correlation between the bulk excitation and full simulations is 96%. The wave amplitude is underestimated by a factor of 0.7—this may be because we neglect other nonlinear source terms like $\boldsymbol{u} \cdot \boldsymbol{\nabla} T$ in our calculation.

We also run two simulations testing interface forcing (section 6.5). In these simulations, we solve the homogeneous linear wave equation, but force the system with the motions of either the 5°C isotherm or the 8°C isotherm at the bottom of the stably stratified region. The movement of these isotherms is analogous to the oscillations of the surface of a drum pummeled by the mallets of convection. However, this neglects the sweeping motion of plumes below the interface. These simulations thus misinterpret the convective excitation as being due to impulsive, penetrating plumes, which over-excite high frequency waves (figure 6.6). The inability to detect the horizontal motion of sweeping plumes is a fundamental problem of the interface forcing heuristic. In contrast to the 96% correlation between the wave fields in the bulk excitation and full simulations, the 5°C interface forcing and the 8°C interface forcing simulations have a correlation with the full simulation of only 31% and 81%, respectively.

All four simulations presented in this chapter exploit the flexibility of Dedalus. Modifying the classic Boussinesq system to accommodate the nonlinear equation of state of water amounts to changing one line of the simulation script. Furthermore, being able to solve different equations easily makes it practical to test different heuristics by solving model equations using simulation data as input. This represents a novel and fruitful analysis technique.

Although the results presented here are for two dimensional simulations using the unique equation of state of water near 4°C, we expect similar conclusions to hold in 3D, and for fluids with less exotic thermodynamic properties. In future work, we will run similar calculations in 3D at high Rayleigh number, including more physics, such as density stratification and rotation.

# Bibliography


Abramowitz, M., & Stegun, I. 2012, Handbook of Mathematical Functions: with Formulas, Graphs, and Mathematical Tables, Dover Books on Mathematics (Dover Publications)

Alexiades, V., Amiez, G., & Gremaud, P.-A. 1996, Communications in Numerical Methods in Engineering, 12, 31

Almgren, A. S., Bell, J. B., Rendleman, C. A., & Zingale, M. 2006, ApJ, 637, 922

Alvan, L., Brun, A. S., & Mathis, S. 2014, A&A, 565, A42

Ansong, J. K., & Sutherland, B. R. 2010, Journal of Fluid Mechanics, 648, 405

Ascher, U. M., Ruuth, S. J., & Spiteri, R. J. 1997, Appl. Numer. Math., 25, 151

Ascher, U. M., Ruuth, S. J., & Wetton, B. T. R. 1995, SIAM J. Numer. Anal., 32, 797

Balbus, S. A. 2000, ApJ, 534, 420

Baldwin, M. P., Gray, L. J., Dunkerton, T. J., et al. 2001, Reviews of Geophysics, 39, 179

Batchelor, G. K. 1953, Quarterly Journal of the Royal Meteorological Society, 79, 224

Belkacem, K., Samadi, R., Goupil, M. J., et al. 2009, A&A, 494, 191

Beznogov, M. V., & Yakovlev, D. G. 2014, Phys. Rev. E, 90, 033102

Boersma, B. J. 2005, Theoretical and Computational Fluid Dynamics, 19, 161

Braginsky, S. I., & Roberts, P. H. 1995, Geophysical and Astrophysical Fluid Dynamics, 79, 1

Brandenburg, A., Svedin, A., & Vasil, G. M. 2009, MNRAS, 395, 1599

Bravo, E., Gil-Pons, P., Gutiérrez, J. L., & Doherty, C. L. 2016, ArXiv e-prints, arXiv:1603.00641 [astro-ph.SR]

Brookes, J. R., Isaak, G. R., & van der Raay, H. B. 1976, Nature, 259, 92

Brown, B. P., Vasil, G. M., & Zweibel, E. G. 2012, ApJ, 756, 109

Brüggen, M., & Hillebrandt, W. 2001, MNRAS, 320, 73

Brummell, N. H. 1993, Geophysical and Astrophysical Fluid Dynamics, 68, 115

Brummell, N. H., Clune, T. L., & Toomre, J. 2002, ApJ, 570, 825

Brun, A. S., Miesch, M. S., & Toomre, J. 2004, ApJ, 614, 1073

—. 2011, ApJ, 742, 79

Burns, K. J., Vasil, G. M., Oishi, J. S., et al. 2014, In preparation

—. 2015, In preparation

—. 2016, In preparation

—. 2017, In preparation

Calkins, M. A., Julien, K., & Marti, P. 2014, Submitted

—. 2015, Geophysical and Astrophysical Fluid Dynamics, 109, 422

Cassisi, S., Potekhin, A. Y., Pietrinferni, A., Catelan, M., & Salaris, M. 2007, ApJ, 661, 1094
Chan, K. L., & Sofia, S. 1986, ApJ, 307, 222
—. 1989, ApJ, 336, 1022
Charbonnel, C., & Talon, S. 2005, Science, 309, 2189
Choi, E., Kim, J., & Wiita, P. J. 2009, ApJS, 181, 413
Christensen-Dalsgaard, J., Monteiro, M. J. P. F. G., Rempel, M., & Thompson, M. J. 2011, MNRAS, 414, 1158
Clark, T. L., Hauf, T., & Kuettner, J. P. 1986, Quarterly Journal of the Royal Meteorological Society, 112, 899
Clune, T. C., Elliott, J. R., Miesch, M. S., Toomre, J., & Glatzmaier, G. A. 1999, Parallel Computing, 25, 361
Colella, P. 1990, Journal of Computational Physics, 87, 171
Colella, P., & Woodward, P. R. 1984, Journal of Computational Physics, 54, 174
Denissenkov, P. A., Herwig, F., Truran, J. W., & Paxton, B. 2013, ApJ, 772, 37
Denissenkov, P. A., Truran, J. W., Herwig, F., et al. 2015, MNRAS, 447, 2696
Dimonte, G., Youngs, D. L., Dimits, A., et al. 2004, Physics of Fluids, 16, 1668
Dintrans, B., Brandenburg, A., Nordlund, Å., & Stein, R. F. 2005, A&A, 438, 365
Duffell, P. C., & MacFadyen, A. I. 2011, ApJS, 197, 15
Durran, D. R. 1989, Journal of Atmospheric Sciences, 46, 1453
Egbert, G. D., & Ray, R. D. 2000, Nature, 405, 775
Farmer, R., Fields, C. E., & Timmes, F. X. 2015, ApJ, 807, 184
Fefferman, C. L. 2000, The millennium prize problems, 57
Fontane, J. ., & Joly, L. 2008, Journal of Fluid Mechanics, 612, 237
Fourier, J. B. J. 1822, Théorie Analytique de la Chaleur (F. Didot)
Fovell, R., Durran, D., & Holton, J. R. 1992, Journal of Atmospheric Sciences, 49, 1427
Freund, J. B. 2001, Journal of Fluid Mechanics, 438, 277
Freytag, B., Ludwig, H.-G., & Steffen, M. 1996, A&A, 313, 497
Fritts, D. C., & Alexander, M. J. 2003, Reviews of Geophysics, 41, 1003
Fritts, D. C., Wan, K., Werne, J., Lund, T., & Hecht, J. H. 2014, Journal of Geophysical Research (Atmospheres), 119, 8858
Fritts, D. C., Wang, L., Werne, J., Lund, T., & Wan, K. 2009, Journal of Atmospheric Sciences, 66, 1126
Fuller, J., Cantiello, M., Lecoanet, D., & Quataert, E. 2015, ApJ, 810, 101
Fuller, J., Lecoanet, D., Cantiello, M., & Brown, B. 2014, ApJ, 796, 17
Garcia Lopez, R. J., & Spruit, H. C. 1991, ApJ, 377, 268
Gardiner, T. A., & Stone, J. M. 2008, Journal of Computational Physics, 227, 4123
Glatzmaier, G. A. 1984, Journal of Computational Physics, 55, 461
Goldreich, P., & Keeley, D. A. 1977, ApJ, 212, 243
Goldreich, P., & Kumar, P. 1990, ApJ, 363, 694
Goodman, J., & Lackner, C. 2009, ApJ, 696, 2054
Herwig, F. 2000, A&A, 360, 952
Hopkins, P. F. 2015, MNRAS, 450, 53

Hopkins, P. F., Kereš, D., Oñorbe, J., et al. 2014, MNRAS, 445, 581
Hutchinson, M., & Rosner, R. 2015, In preparation
Itoh, N., Kohyama, Y., & Takeuchi, H. 1987, ApJ, 317, 733
Itoh, N., Mitake, S., Iyetomi, H., & Ichimaru, S. 1983, ApJ, 273, 774
Johansen, A., Henning, T., & Klahr, H. 2006, ApJ, 643, 1219
Jones, C. A., Kuzanyan, K. M., & Mitchell, R. H. 2009, Journal of Fluid Mechanics, 634, 291
Jones, S., Hirschi, R., & Nomoto, K. 2014, ApJ, 797, 83
Julien, K., Aurnou, J. M., Calkins, M. A., et al. 2016, ArXiv e-prints, arXiv:1601.08247 [physics.flu-dyn]
Kerswell, R. R., Pringle, C. C. T., & Willis, A. P. 2014, Reports on Progress in Physics, 77, 085901
Krasny, R. 1986, Journal of Fluid Mechanics, 167, 65
Kromer, M., Ohlmann, S. T., Pakmor, R., et al. 2015, MNRAS, 450, 3045
Kumar, P., & Quataert, E. J. 1997, ApJ, 475, L143
Landau, L., & Lifshitz, E. 2013, Fluid Mechanics (Elsevier Science)
Lantz, S. R. 1992, PhD thesis, CORNELL UNIVERSITY.
Le Bars, M., Lecoanet, D., Perrard, S., et al. 2015, Fluid Dynamics Research, 47, 045502
Lecoanet, D., Brown, B. P., Zweibel, E. G., et al. 2014, ApJ, 797, 94
Lecoanet, D., Le Bars, M., Burns, K. J., et al. 2015, Phys. Rev. E, 91, 063016
Lecoanet, D., Parrish, I. J., & Quataert, E. 2012, MNRAS, 423, 1866
Lecoanet, D., & Quataert, E. 2013, MNRAS, 430, 2363
Lecoanet, D., McCourt, M., Quataert, E., et al. 2016, MNRAS, 455, 4274
Lesieur, M. 1990, NASA STI/Recon Technical Report A, 91, 24106
Lesshafft, L., Huerre, P., & Sagaut, P. 2010, Journal of Fluid Mechanics, 647, 473
Lighthill, J. 2001, Waves in Fluids, Cambridge Mathematical Library (Cambridge University Press)
Lou, Y.-Q. 1990, ApJ, 361, 527
Marcus, P. S., Pei, S., Jiang, C.-H., et al. 2015, ApJ, 808, 87
McNally, C. P., Lyra, W., & Passy, J.-C. 2012, ApJS, 201, 18
Meakin, C. A., & Arnett, D. 2007, ApJ, 667, 448
Michaelian, M. 2002, European Journal of Mechanics B Fluids, 21, 1
Miyaji, S., Nomoto, K., Yokoi, K., & Sugimoto, D. 1980, PASJ, 32, 303
Mocz, P., Vogelsberger, M., Pakmor, R., et al. 2015, MNRAS, 452, 3853
Moffatt, H. K. 1978, Magnetic Field Generation in Electrically Conducting Fluids, Cambridge Monographs on Mechanics (Cambridge University Press)
Moore, D. R., & Weiss, N. O. 1973, Journal of Fluid Mechanics, 61, 553
Moore, D. W. 1979, Royal Society of London Proceedings Series A, 365, 105
Niemela, J. J., Skrbek, L., Sreenivasan, K. R., & Donnelly, R. J. 2000, Nature, 404, 837
Nonaka, A., Almgren, A. S., Bell, J. B., et al. 2010, ApJS, 188, 358
Nulsen, P. E. J. 1982, MNRAS, 198, 1007
—. 1986, MNRAS, 221, 377
Ogura, Y., & Phillips, N. A. 1962, Journal of Atmospheric Sciences, 19, 173
Paxton, B., Bildsten, L., Dotter, A., et al. 2011, ApJS, 192, 3

Paxton, B., Cantiello, M., Arras, P., et al. 2013, ApJS, 208, 4
Paxton, B., Marchant, P., Schwab, J., et al. 2015, ApJS, 220, 15
Pedlosky, J. 1992, Geophysical Fluid Dynamics, Springer study edition (Springer New York)
Piro, A. L. 2011, ApJ, 738, L5
Porter, D. H., Pouquet, A., & Woodward, P. R. 1994, Physics of Fluids, 6, 2133
Press, W. H. 1981, ApJ, 245, 286
Quataert, E., Fernández, R., Kasen, D., Klion, H., & Paxton, B. 2016, MNRAS, 458, 1214
Quataert, E., & Shiode, J. 2012, MNRAS, 423, L92
Reinaud, J., Joly, L., & Chassaing, P. 2000, Physics of Fluids, 12, 2489
Robertson, B. E., Kravtsov, A. V., Gnedin, N. Y., Abel, T., & Rudd, D. H. 2010, MNRAS, 401, 2463
Rogers, T. M., & Glatzmaier, G. A. 2005a, MNRAS, 364, 1135
—. 2005b, ApJ, 620, 432
Rogers, T. M., Glatzmaier, G. A., & Jones, C. A. 2006, ApJ, 653, 765
Rogers, T. M., Lin, D. N. C., & Lau, H. H. B. 2012, ApJ, 758, L6
Rogers, T. M., Lin, D. N. C., McElwaine, J. N., & Lau, H. H. B. 2013, ApJ, 772, 21
Rogers, T. M., & MacGregor, K. B. 2011, MNRAS, 410, 946
Rogers, T. M., MacGregor, K. B., & Glatzmaier, G. A. 2008, MNRAS, 387, 616
Salvesen, G., Beckwith, K., Simon, J. B., O'Neill, S. M., & Begelman, M. C. 2014, MNRAS, 438, 1355
Schaal, K., Bauer, A., Chandrashekar, P., et al. 2015, ArXiv e-prints, arXiv:1506.06140
Severnyi, A. B., Kotov, V. A., & Tsap, T. T. 1976, Nature, 259, 87
Shiode, J. H., & Quataert, E. 2014, ApJ, 780, 96
Shiode, J. H., Quataert, E., Cantiello, M., & Bildsten, L. 2013, MNRAS, 430, 1736
Showman, A. P., & Kaspi, Y. 2013, ApJ, 776, 85
Siess, L. 2006, A&A, 448, 717
Slessor, M. D., Bond, C. L., & Dimotakis, P. E. 1998, Journal of Fluid Mechanics, 376, 115
Smith, N., & McCray, R. 2007, ApJ, 671, L17
Spiegel, E. A., & Veronis, G. 1960, ApJ, 131, 442
Spitzer, L. 2013, Physics of Fully Ionized Gases: Second Revised Edition, Dover Books on Physics (Dover Publications)
Springel, V. 2010, MNRAS, 401, 791
Stone, J. M., Gardiner, T. A., Teuben, P., Hawley, J. F., & Simon, J. B. 2008, ApJS, 178, 137
Talon, S., & Charbonnel, C. 1998, A&A, 335, 959
—. 2005, A&A, 440, 981
Talon, S., Kumar, P., & Zahn, J.-P. 2002, ApJ, 574, L175
Taylor, J. R., & Sarkar, S. 2007, Journal of Fluid Mechanics, 590, 331
Timmes, F. X., Woosley, S. E., & Taam, R. E. 1994, ApJ, 420, 348
Toro, E. 2013, Riemann Solvers and Numerical Methods for Fluid Dynamics: A Practical Introduction (Springer Berlin Heidelberg)
Townsend, A. A. 1964, Quarterly Journal of the Royal Meteorological Society, 90, 248
—. 1966, Journal of Fluid Mechanics, 24, 307

Turck-Chièze, S., Couvidat, S., Kosovichev, A. G., et al. 2001, ApJ, 555, L69
Unno, W. 1979, Nonradial Oscillations of Stars (Japan : University of Tokyo Press)
van Driel-Gesztelyi, L., Baker, D., Török, T., et al. 2014, ApJ, 788, 85
Vasil, G. M., Burns, K. J., Lecoanet, D., et al. 2015, ArXiv e-prints, arXiv:1509.07624 [math.NA]
Vasil, G. M., Lecoanet, D., Brown, B. P., Wood, T. S., & Zweibel, E. G. 2013, ApJ, 773, 169
Vasil, G. M., Lecoanet, D., Burns, K. J., Brown, B. P., & Oishi, J. S. 2016, In preparation
Veronis, G. 1963, ApJ, 137, 641
Viallet, M., Baraffe, I., & Walder, R. 2011, A&A, 531, A86
—. 2013, A&A, 555, A81
Wang, D., & Ruuth, S. J. 2008, J. Comp. Math., 26, 838
Weinberg, N. N., Arras, P., Quataert, E., & Burkart, J. 2012, ApJ, 751, 136
Wilkinson, J. P., & Jacobs, J. W. 2007, Physics of Fluids, 19, 124102
Willcox, D. E., Townsley, D. M., Calder, A. C., Denissenkov, P. A., & Herwig, F. 2016, ArXiv e-prints, arXiv:1602.06356 [astro-ph.HE]
Woosley, S. E., & Heger, A. 2015, ApJ, 810, 34
Worster, G. 2009, Understanding Fluid Flow, AIMS Library of Mathematical Sciences (Cambridge University Press)
Zahn, J.-P., Talon, S., & Matias, J. 1997, A&A, 322, 320